Distribution and Metabolism of Antibodies and Macromolecules in Tumor Tissue

By Greg M. Thurber

B.S. Chemical Engineering
Minor Biochemistry and Molecular Biology
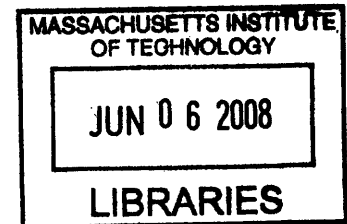The Pennsylvania State University, 2003

Submitted to the Department of Chemical Engineering in Partial Fulfillment of the
Requirements for the Degree of

DOCTOR OF PHILOSOPHY
In Chemical Engineering

At the

Massachusetts Institute of Technology
May 2008
[June 2008]

Signature of Author___

_____
Greg M. Thurber
Department of Chemical Engineering
May 2008

Certified by___

_____
K. Dane Wittrup
C.P. Dubbs Professor of Chemical Engineering and Biological Engineering
Thesis Advisor

Accepted by_____

_____
William M. Deen
Professor of Chemical Engineering
Chairman, Committee for Graduate Students

Distribution and Metabolism of Antibodies and Macromolecules in Tumor Tissue

By Greg M. Thurber

Submitted to the Department of Chemical Engineering on May 22, 2008 in Partial Fulfillment of the Requirements for the Degree of Doctor of Philosophy in Chemical Engineering

ABSTRACT

Tumor targeting drugs that selectively treat cancerous tissue are promising agents for lowering the morbidity and mortality of cancer. Within this field, antibody treatments for cancer are currently being developed for both imaging and therapeutic applications. A major limitation with this class of drugs is the poor distribution and low uptake in tumor tissue. Poor distribution leaves some cells completely devoid of treatment, while others experience marginally toxic concentrations that could foster drug resistance. The low overall uptake in vascularized tumors constrains the therapeutic index and lowers signal to noise ratios for imaging applications. Since antibody therapies are currently used to treat both bulk tumors and residual disease, an understanding of the limitations in targeting prevascular metastases and vascularized tumors is required.

In order to circumvent the current limitations with antibody therapies, the underlying causes must first be determined. In this thesis, the various steps in tumor localization of antibodies are analyzed in order to determine which steps are limiting uptake and distribution. Mathematical models are developed that indicate the distance antibodies and other binding macromolecules will penetrate into tumors and micrometastases. These models can also estimate the maximum uptake and time course of antibody concentration in tumors. The experimental distribution of a CEA binding antibody is measured in tumor spheroids and a mouse xenograft system to validate the model predictions.

Using dimensional analysis of the fundamental transport rates that occur in tumors and micrometastases, two main groups determine the distance antibodies will penetrate in tumor tissue. The clearance modulus indicates whether antibody persistence in the blood is sufficient to allow the drug to reach all cells in the micrometastasis or vascularized tumor. The Thiele modulus, defined for antibody transport in tumors, relates the internalization and catabolism of bound antibodies on cancer cells to the maximum distance the antibodies will reach in the tissue. These groups are related to the overall time course and maximum uptake in tumors, indicating when all cells will be targeted, and what factors determine this limit. These models can aid in experimental design, data interpretation, and strategies to improve uptake.

Thesis Supervisor: Dr. K. Dane Wittrup
Title: C.P. Dubbs Professor of Chemical Engineering and Bioengineering

Acknowledgements

First, I would like to thank my advisor for his excellent advice and expertise over the course of this work. His terrific intellectual input, suggestions, questions, and challenges have guided the project, taught me how to do research, and made this thesis possible. Dane has put together a great lab, where it's both exciting and enjoyable to work. His enthusiasm and patience during the ups and downs of research have been highly motivating and really facilitated the research progress. Finally, beyond the research, I want to thank him for the lessons and advice that will serve for years to come.

I want to thank all the members of the Wittrup lab who have helped me during my time here. From the simple act of loaning material to insightful suggestions, their contributions pervade the following pages. Countless discussions with them have taught me a lot over my graduate career, and it is these people who have made it such a friendly and encouraging atmosphere. This includes former students and postdocs that have helped me early on in my research: Stefan Zajic, Dave Colby, Andy Yeung, Shaun Lippow, Jeff Swers, Balaji Rao, Katarina Midelfort, Andy Rakestraw, Ginger Chao, Wai Lau, Dasa Lipovsek, Andrea Piatesi, Jennifer Cochran, and Pankaj Karande. And the current students, who have helped in the past and will carry on the work, include Shanshan Wu Howland, Steve Sazinsky, Mike Schmidt, Margaret Pawlowski, Annie Gai, Eileen Higham, Ben Hackel, Kelly Davis, David Liu, Chris Pirie, Jordi Mata-Fink, Jamie Spangler, and John Rhoden.

I would especially like to thank my thesis committee members Prof. Bill Deen and Prof. Peter So. I always looked forward to my thesis committee meetings and their constructive input, and their insight constantly provided scope and perspective to the project.

Hyuk-Sang Kwon in Prof. So's lab was a tremendous help with gathering the microscopy data, and Prof. Sangeeta Bhatia and her lab, especially Todd Harris, have been instrumental in making the *in vivo* work happen. Todd in particular was a great help in providing advice and training for the animal studies.

I also want to thank my undergraduate research advisor, Dr. Wayne Curtis. He was the one who plucked me out of the classroom and got me into the laboratory. Without that motivation, I may have never realized how much I enjoy research.

My friends, both at MIT and elsewhere, have provided tremendous support over the years. Whether it's lunchtime coffee in the amphitheatre or a late night break with my roommates, their laughter and support has been refreshing time and time again. Weekend trips and in-town visits from my college friends and those back home have always kept things interesting and new.

My family has been incredible. My mom and dad have been there for me long before there was even the possibility of a thesis, and since then, they have supported me until the end. I also want to thank my older brother, John, for paving the way for me. And for always letting me know that.

My fiancée Melissa has been spectacular over the years with her caring and support. I want to thank her for her love, patience, and support she gave and continues to give each day.

And lastly, I want to give thanks to God, who amazes me every day with His creation.

To my parents, John and Sandy, for their unconditional love and support.
Without them, none of this would have been possible.

And to my beautiful fiancée, Melissa, for always being there.

Table of Contents

Chapter 1 – Introduction

1.1   Background

Cancer is a leading cause of mortality worldwide(1), and the second leading cause of death in the United States(2). Despite intense research, the prognosis for many forms of cancer is still very poor. The disease strikes when cells in the body begin growing uncontrollably, interfering with normal function. Because these cells originate from the host, it is difficult to treat the disease without affecting healthy tissues.

Standard treatment for cancer typically involves surgery to remove the tumor, radiation, and chemotherapy. If the tumor has not spread to the rest of the body (metastasized), surgery of the primary tumor is typically curative. However, when cancer cells disseminate in the vascular and/or lymphatic system, the disease is much more difficult to treat. Radiation and surgery both require knowledge of the location of the disease, but current imaging methods are only capable of detecting masses roughly one centimeter or larger in diameter(3-5). Therefore, chemotherapy is the only option for treating disseminated disease.

Traditional chemotherapeutics are small molecule drugs that are delivered systemically. Most of them work by disrupting DNA replication or other machinery required for cell division, thereby selectively killing rapidly dividing cells. However, normal tissues also undergo cell division, and the chemotherapeutics damage these cells as well, often causing severe side effects, such as nausea, alopecia (hair loss), and extreme fatigue. Due to their poor selectivity, intense, near-lethal courses of drugs are delivered to obtain maximum effect against the neoplastic tissue, followed by breaks in therapy of several weeks to allow the body to recover(6).

The poor selection for cancer cells has led to a variety of research trying to find ways of selectively targeting the cancerous tissue for more effective therapy. This includes, but is not limited to, targeting signaling pathways that are disrupted during the multiple steps of tumorigenesis(7), for example oncogenes such as RAS(8), tumor suppressor genes like p53(9, 10), and angiogenesis receptors(11). Tumor selectivity can also be achieved by enhanced uptake from abnormal tumor physiology(12), eliciting an immune response due to abnormal protein expression(13), and targeting surface antigens that are mal-expressed or up-regulated on cancer cells(14, 15). This thesis focuses on the use of antibodies that specifically bind cancer cell antigens on the surface of tumor cells.

11

1.2   Antibodies as Drugs

Antibodies are proteins produced by the immune system that recognize and associate with foreign proteins and molecules in the body. While there are several classes, the most prevalent in the blood stream is immunoglobulin G (IgG), an approximately 150 kDa 'Y-shaped' protein that contains two identical binding domains and a constant (Fc) region that recruits immune effector cells(16).

Interest in this class of drugs was motivated with the development of monoclonal antibodies(17), allowing the mass production of antibodies with identical specificity. Further progress in protein engineering has allowed researchers to make a variety of smaller fragments of this molecule(18) as well as engineer particular binding specificity, affinity, dissociation rate, stability, reduced immunogenicity, and biological effects(19-22). These techniques have allowed researchers to develop antibodies that bind specifically to antigens that are over-expressed or expressed incorrectly on the surface of cancer cells. This class of drugs then has the ability to bind and concentrate locally in cancer tissue while lowering effects in the normal tissue. There is also flexibility in the type of therapy administered. Current FDA-approved drugs include naked antibodies that can block cell signaling and recruit immune effector cells(14, 23, 24), carry chemical or biological toxins(25), or deliver a radioisotope that emits local radiation to kill the cell(26).

Although much excitement has been created over the use of these molecules to specifically target cancer without the harmful side effects of small molecule drugs, this type of therapy has not fully lived up to its potential. One of the major problems with antibody therapies is their distribution in tumor tissue. Because of their large size (150 kDa for an IgG), the transport of these drugs is severely limited in tumors. Examination of tumors after the systemic delivery of an antibody drug shows large spatial heterogeneities with perivascular and peripheral localization(27-30). Large areas within the tumor contain cancer cells where very little or no drug is present. Not only is the spatial distribution a problem, but the total amount that enters the tumor is also low. The fraction of the injected dose that localizes within a tumor rarely reaches above 0.01% per gram of tissue in humans(31).

Tumor therapy with antibodies is a complex problem, with both pharmacokinetic as well as pharmacodynamic considerations. However, a clear example where uptake is a limiting factor comes from studies on radioimmunotherapy (RIT). In this type of therapy, a radioisotope is conjugated directly to the antibody, and following uptake in tumor sites, the isotope emits radiation locally, giving a higher dose to the tumor than the surrounding tissue. It also has the advantage of being delivered

systemically, as opposed to external beam radiation, so it can target disseminated disease. With short range isotopes, dosage to the surrounding tissue is minimized. The effect of radiation on normal and tumor tissue is well studied(32), and given a sufficient dose, the cancer cells will be killed. However, due to low uptake within solid tumors, results have been poor(33). Full IgG molecules have long circulation times in the plasma, and the dose to bone marrow, which is very sensitive to radiation, is limiting. The use of fragments allows more rapid clearance from the normal tissue, but this results in even lower uptake. A more in depth analysis of clearance versus uptake is discussed in chapters 2 and 4. The challenge with this therapy is delivering sufficient doses to kill the most resistant cancer cells while sparing the most sensitive normal tissues.

A more detailed understanding of the transport of antibodies and antibody fragments is needed to help improve imaging and therapy. Due to the complexity of tumor physiology and targeting, mathematical models are vital to understanding the behavior of these types of drugs. One of the criticisms of this type of modeling is the large heterogeneity found in tumors. While many tumor properties (and and therefore model inputs) are heterogeneous, this analysis focuses on order of magnitude estimates for spatial and temporal distribution. Local values can vary considerably, but an overall understanding of the driving forces and limitations on uptake can be obtained by modeling analysis. Many of the concepts are based on rates that differ by several orders of magnitude (e.g. 100- to 1000-fold differences). Even with the considerable heterogeneity present in tumors, many of these relationships will hold true for most relevant targeting scenarios. From an imaging or therapeutic design perspective, these trends are more useful in identifying ways of circumventing targeting problems, rather than analyzing specific cases that may not be found in other areas of tissue or different tumors.

1.3   Tumor Physiology

In order to understand the basis of the modeling analysis, assumptions, and when these assumptions fail, a brief overview in tumor physiology is necessary. First, there are two different targeting scenarios that will be examined, a micrometastasis that is not yet vascularized, and a vascularized solid tumor. Antibody therapies are being used for both cases, i.e. bulk disease and minimal residual disease(34), so it is important to understand some of the fundamental differences between these clinical targets.

Metastasis occurs when cancerous cells from the primary tumor lose adhesion with the surrounding tissue and travel to a different location within the body. The most common form of metastasis is through the lymph system, and this is used in staging many cancers. Alternatively, cancer cells can enter the circulation and travel a significant distance away from the primary tumor(35). While the lymph system is more amenable to cancer cell survival and local spread(36), metastasis via the vasculature is more difficult to treat, since this route forms distant metastases which cannot be removed by taking larger surgical margins around the primary tumor or removing local lymph nodes.

When a cancer cell begins to grow in a new site, it initially forms a cluster of new cells imbedded in the surrounding normal tissue. These micrometastases continue to divide and grow, fed by the vasculature in the surrounding normal tissue, until their size becomes limited by oxygen transport. The process of angiogenesis has been extensively studied, but some of the earlier work was done in the Rip-TAG mouse model. In this model, oncogenes are expressed by the β cells in the islets of the pancreas. Although the cells become tumorigenic, they cannot grow beyond 100 to 200 μm in diameter until they have recruited their own blood supply by the process of angiogenesis(37). Larger clusters of cells can exist, but they suffer from central necrosis due to these transport limitations, so only cells near the surface remain viable(38).

Normal tissues in the body have well organized vascular and lymphatic structures. This efficient transport system provides adequate exposure of most tissues to systemically delivered drugs, including the tissue surrounding a metastasis. Fluid balance in the tissue prevents edema (swelling) and ensures that the interstitial pressure remains close to zero (Figure 1.1 A, left). According to Starling's hypothesis, fluid is filtered from the capillary due to a higher sum of hydrostatic and osmotic pressures (effective pressure) at the arterial end (Figure 1.1 B, left). Hydrostatic pressure decreases along the length of the capillary, and the low permeability of vessels to proteins causes an increase in osmotic pressure. Towards the venous end, the effective capillary pressure is less than the interstitial pressure, so fluid is reabsorbed into the vessel lumen(39, 40). The remaining fluid is taken up by local lymph vessels, which often contain a negative pressure. These closed end vessels are held open by attachment to the surrounding cells and are highly permeable to macromolecules and cells of the immune system(41). Capillaries and lymph vessels are adequately spaced so that delivery of oxygen and nutrients and removal of waste products is efficiently carried out in the tissue. Although capillaries are not highly permeable to macromolecules, the pressure differences allow convection between the tissue and vessels, which is typically more important than diffusion for these large molecules.

A more extensive look at the convective and diffusive contributions to macromolecular permeability of capillaries is given by Rippe and Haraldsson(42). Here, the authors use a two-pore model to analyze the transport of proteins and fluid across the capillary wall. The capillary membrane is assumed to consist of a series of small pores, roughly 4-6 nm in radius, and large pores, approximately 20-40 nm. The large pores are thought to have a low reflection coefficient, so that the hydrostatic pressure drives filtration of fluid and macromolecules across these pores. Osmotic absorption of fluid through the more selective small pores counterbalances some of this fluid flow. These conditions allow the circulation of fluid across the capillary wall even in situations of zero fluid filtration. The good fit between two-pore experimental predictions and data is used to argue that active transcytosis across capillary walls is insignificant compared to the passive mechanisms of transport from the blood to tissue.

The physiology of solid tumors is very different than the well organized structure of normal tissue. While much of this lies outside the scope of this thesis, several factors are important in understanding the unique state of convection and diffusion within tumors as well as the origin of some of the heterogeneity present in this type of tissue.

The biology of cancer is exceedingly complex, but it is important to understand how this can impact the distribution of antibodies. A limited overview of some of the major tumor cell types and biological effects can illustrate the complexity in tumor tissue composition and signaling. Cancerous tissue consists of multiple cell types, namely the cancer itself and many types of supporting stromal cells. These include endothelial cells that form the vascular structure, inflammatory cells such as macrophages, and connective cells such as fibroblasts. In extreme cases, cancer cells are in the minority, such as Hodgkin's disease, where they make up 1% of the tumor. There is immense complexity in the signaling, cross-talk, and interaction of tumor tissue, essentially encompassing all healthy cell signaling pathways in a pathological manner. Many of these pathways operate during wound healing, but are constitutively activated. For example, carcinoma cells may release platelet derived growth factor (PDGF), which recruits fibroblasts and monocytes. The monocytes differentiate in the tissue to become macrophages (tumor associated macrophages or TAMs). In hypoxic areas, these cells, along with some tumor cells, release vascular endothelial growth factor (VEGF) to recruit endothelial cells. PDGF also causes some fibroblasts (carcinoma associated fibroblasts or CAFs) to release matrix metalloproteases (MMPs), which degrade extracellular matrix (ECM), releasing more growth factors and allowing movement of cells within the tumor. Recruitment and differentiation of fibroblasts into myofibroblasts leads to the increased secretion of ECM components, and increased

15

collagen can lead to 'hard' desmoplastic tumors. ((37) and references therein) Some of these variations, such as heterogeneity of diffusion through different ECM compositions or variations in vascular density, will directly affect antibody targeting, but others have a smaller impact. While these different cell types have a large biological influence on the tumor, they essentially behave as antigen negative cells from an antibody targeting perspective. This is advantageous, since it may result in fewer differences between antibody pharmacokinetics in animal models and the clinic. In contrast, small molecule drugs that act by inhibiting one or several of these pathways are highly dependent on the other activated pathways in the tumor, and animal models like tumor xenografts are notoriously easier to treat than clinical tumors. These differences will have to be kept in mind when studying antibody pharmacodynamics, however, since there may be major differences in tumor cell response to the antibody, immune effector cell recruitment, tumor growth, metastasis, etc.

Although the presence of these cell types and many of the biological interactions do not have a direct impact on targeting, the interaction with the vasculature has major implications. Several signaling molecules increase the vascular permeability, which is useful in wound healing by increasing the local amount of clotting factors and providing access to white blood cells. One of the most important players is vascular endothelial growth factor (VEGF), also known as vascular permeability factor. This molecule has a dual role of recruiting endothelial cells for angiogenesis and inducing vascular leak(43). The role in angiogenesis has a direct effect on targeting of antibodies, since the vasculature is the major source for antibody entering the tumor. The effects of increased permeability, however, are more complicated.

VEGF increases permeability of fluid and small solutes by inducing the formation of fenestrations in the blood vessel wall and disrupting cell-cell adhesion, which allows large molecules through intercellular junctions(43). The increased fluid permeability causes large amounts of fluid to leave the vessel due to the higher hydrostatic pressure inside. By allowing increased passage of large molecules, the normal osmotic gradient across the vessel is lowered, so re-absorption by the vessel is significantly reduced. Normally, excess fluid in the interstitium is removed by the lymphatic system, but tumors largely lack functional lymphatics(36). Fluid pressure builds up within the interstitium until the pressure gradient across the blood vessel wall is low enough that little fluid exits the vessels(44). This elevated interstitial pressure has profound implications for antibody targeting (Figure 1.1).
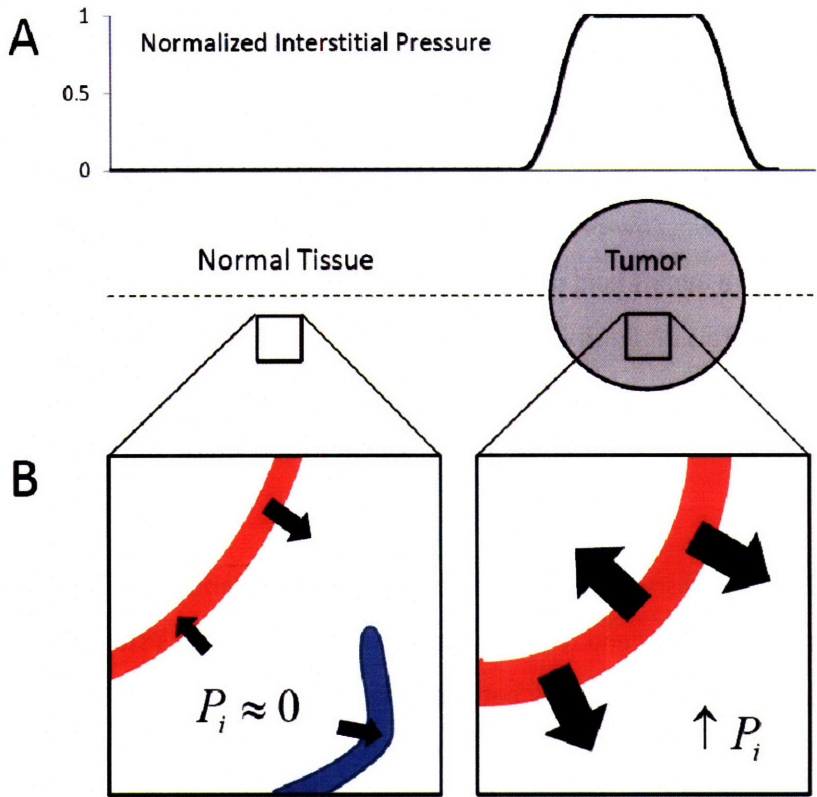
Figure 1.1 – Elevated Interstitial Pressure in Solid Tumors. A) The normalized interstitial pressure gradient is plotted for the dotted line below the graph that crosses through the normal tissue and center of the tumor. When the normalized pressure gradient is equal to one (in the tumor), the hydrostatic and osmotic pressure gradients inside and outside the capillaries are in balance, so there is no net fluid flow across the vessel wall. The pressure gradient at the tumor periphery can lie within or outside the edges of the tumor depending on conditions at the tumor boundary. This elevated interstitial pressure is a result of the local fluid balance in the tissue. B) In normal tissues, a large hydrostatic pressure gradient at the beginning of capillaries causes net fluid filtration. As the proteins in the plasma become more concentrated and the pressure drops along the length of the capillary, reabsorption of interstitial fluid occurs. The remainder of the fluid that is not reabsorbed is taken up by low pressure, closed-end lymph vessels (left). In solid tumors, permeability factors increase the fluid flow across the vessel wall and lower the osmotic pressure difference. With increased fluid extravasation and decreased absorption, fluid builds up in the tissue. The only escape for fluid is from the tumor periphery, but poor hydraulic conductivity in tumors from high cell and extracellular matrix densities allows this only at the tumor periphery(45). The interstitial fluid pressure is elevated in the remainder of the tissue, preventing more fluid extravasation from the vessels.

Elevated interstitial pressure is present in most solid tumors and is correlated with poor prognosis(44). It has also been implicated in blood vessel collapse, which reduces the number of capillaries that can deliver drug to the tumor. Since the source of the elevated pressure is from the hydrostatic pressure in the blood vessel, it is unlikely that elevated interstitial directly causes tumor

blood vessel collapse. However, the lack of higher pressure in the vessel keeping it open may make it more susceptible to collapse, and solid stress from rapidly dividing tumor cells surrounding the capillary can close the vessel. This leads to large necrotic regions cut-off from the vascular supply. If the cell density is reduced, for example with radiation therapy, these vessels may reopen, increasing tumor perfusion(46). This mechanism may also be why low-pressure, functional lympatics cannot operate in tumors. The increase in interstitial pressure means fluid does not flow from the vessel to interstitium, so convection across the vessel wall is severely diminished. Large molecules are typically transported by convection due to their low diffusion coefficients, so the lack of convection severely restricts their transport. These molecules therefore rely primarily on diffusion to cross the vessel wall and transport through the tumor interstitium(47).

High permeability also contributes to the disruption of blood flow in tumor capillaries. In healthy tissue, a steady pressure gradient from the arterial end to the venous end directs flow consistently along the length of the vessel. High permeability allows cross-talk between the interstitial and capillary pressures, which may slow blood flow and divert it to the tumor periphery(48). This poor flow is exacerbated by the poorly formed vessel structures, including bifurcations, dead-ends, and loop structures(49). The inflammatory response may cause leukocytes to stick to the vessel walls, temporarily blocking flow(50), and malfunctioning arteriole shunting may also temporarily cut off the blood supply to certain areas(51). Finally, some vessels may operate in a partially collapsed state(52), with minor fluctuations causing transient opening and closing of the vessels. This all leads to transient hypoxia in the tumor, where certain regions are cut-off from the blood supply for varying lengths of time. Chronic hypoxia also occurs from extensive collapse of vessels as discussed above, as well as the poor recruitment of vessels initially (lack of sufficient angiogenesis). This insufficient access to the blood supply leads to hypoxic regions in the tumor, which are more resistant to radiation and some chemotherapy(53). Lack of oxygen also causes pH gradients within the tumor and changes in metabolism(54, 55). Regions far from active blood vessels cannot survive, and larger tumors often contain extensive regions of necrosis.

Antibodies have the potential to significantly improve cancer therapy by selectively treating cancer cells while reducing exposure in the normal tissues of the body. There are a variety of obstacles to their efficient uptake and distribution throughout tumors caused by the unique physiology in malignant tissue. The following chapters describe a mechanistic modeling approach that can be used to understand antibody distribution in tumors and how it can be improved.

References

1.   Cancer Fact Sheet: World Health Organization; 2006. Report No.: N^{0}297.
2.   Heron M. Deaths: Leading Causes for 2004: Center for Disease Control; 2007.
3.   Heicappell R, Muller-Mattheis V, Reinhardt M, et al. Staging of pelvic lymph nodes in neoplasms of the bladder and prostate by positron emission tomography with 2- F-18 -2-deoxy-D-glucose. European Urology 1999;36:582-7.
4.   Kumar R, Alavi A. Clinical applications of fluorodeoxyglucose-positron emission tomography in the management of malignant melanoma. Current Opinion in Oncology 2005;17:154-9.
5.   Saisho H, Yamaguchi T. Diagnostic imaging for pancreatic cancer - Computed tomography, magnetic resonance imaging, and positron emission tomography. Pancreas 2004;28:273-8.
6.   Katzung B, editor. Basic and Clinical Pharmacology. 9 ed. New York: McGraw-Hill Companies; 2004.
7.   Hanahan D, Weinberg RA. The hallmarks of cancer. Cell 2000;100:57-70.
8.   Friday BB, Adjei AA. K-ras as a target for cancer therapy. Biochimica Et Biophysica Acta-Reviews on Cancer 2005;1756:127-44.
9.   Roth JA. Adenovirus p53 gene therapy. Expert Opinion on Biological Therapy 2006;6:55-61.
10.   Ventura A, Kirsch DG, McLaughlin ME, et al. Restoration of p53 function leads to tumour regression in vivo. Nature 2007;445:661-5.
11.   Shih T, Lindley C. Bevacizumab: An angiogenesis inhibitor for the treatment of solid malignancies. Clinical Therapeutics 2006;28:1779-802.
12.   Bartlett DW, Su H, Hildebrandt IJ, Weber WA, Davis ME. Impact of tumor-specific targeting on the biodistribution and efficacy of siRNA nanoparticles measured by multimodality in vivo imaging. Proceedings of the National Academy of Sciences of the United States of America 2007;104:15549-54.
13.   Yee C, Greenberg P. Modulating T-cell immunity to tumours: New strategies for monitoring T-cell responses. Nature Reviews Cancer 2002;2:409-19.
14.   Plosker GL, Figgitt DP. Rituximab - A review of its use in non-Hodgkin's lymphoma and chronic lymphocytic leukaemia. Drugs 2003;63:803-43.
15.   Albanell J, Baselga J. Trastuzumab, a humanized anti-HER2 monoclonal antibody, for the treatment of breast cancer. Drugs of Today 1999;35:931-46.
16.   Kindt TJ, Goldsby RA, Osborne BA. Kuby Immunology. 6th ed. New York: W. H. Freeman and Company; 2007.
17.   Kohler G, Milstein C. Continuous cultures of fused cells secreting antibody of predefined specificity. Nature 1975;256:495-7.
18.   Wu AM, Senter PD. Arming antibodies: prospects and challenges for immunoconjugates. Nature Biotechnology 2005;23:1137-46.
19.   Gai SA, Wittrup KD. Yeast surface display for protein engineering and characterization. Current Opinion in Structural Biology 2007;17:467-73.
20.   Boder E, Wittrup KD. Yeast surface display for screening combinatorial polypeptide libraries. Nature Biotechnology 1997;15:553-7.
21.   Maynard J, Georgiou G. Antibody engineering. Annual Review of Biomedical Engineering 2000;2:339-76.
22.   Skerra A. Alternative non-antibody scaffolds for molecular recognition. Current Opinion in Biotechnology 2007;18:295-304.
23.   Carter P, Presta L, Gorman CM, et al. Humanization of an Anti-P185her2 Antibody for Human Cancer-Therapy. Proceedings of the National Academy of Sciences of the United States of America 1992;89:4285-9.

24.   Clynes RA, Towers TL, Presta LG, Ravetch JV. Inhibitory Fc receptors modulate in vivo cytoxicity against tumor targets. Nature Medicine 2000;6:443-6.

25.   Kratz F, Abu Ajaj K, Warnecke A. Anticancer carrier-linked prodrugs in clinical trials. Expert Opinion on Investigational Drugs 2007;16:1037-58.

26.   Hernandez M, Knox S. Radiobiology of radioimmunotherapy: targeting CD20 B-cell antigen in non-Hodgkin's lymphoma. International Journal of Radiation Oncology Biology Physics 2004;59:1274-87.

27.   Shockley TR, Lin JK, Nagy JA, Tompkins RG, Yarmush ML, Dvorak HF. SPATIAL-DISTRIBUTION OF TUMOR-SPECIFIC MONOCLONAL-ANTIBODIES IN HUMAN-MELANOMA XENOGRAFTS. Cancer Research 1992;52:367-76.

28.   Adams G, Schier R, McCall A, et al. High Affinity Restricts the Localization and Tumor Penetration of Single-Chain Fv Antibody Molecules. Cancer Research 2001;61:4750-5.

29.   Dennis MS, Jin HK, Dugger D, et al. Imaging tumors with an albumin-binding Fab, a novel tumor-targeting agent. 2007;67:254-61.

30.   Juweid M, Neumann R, Paik C, et al. Micropharmacology of Monoclonal-Antibodies in Solid Tumors - Direct Experimental-Evidence for a Binding-Site Barrier. 1992;52:5144-53.

31.   Welt S, Divgi CR, Real FX, et al. QUANTITATIVE-ANALYSIS OF ANTIBODY LOCALIZATION IN HUMAN METASTATIC COLON CANCER - A PHASE-I STUDY OF MONOCLONAL ANTIBODY-A33. Journal of Clinical Oncology 1990;8:1894-906.

32.   Hall E, Giaccia A. Radiobiology for the Radiologist. 6th ed: Lippincott Williams and Wilkins; 2006.

33.   Koppe MJ, Bleichrodt RP, Oyen WJG, Boerman OC. Radioimmunotherapy and colorectal cancer. British Journal of Surgery 2005;92:264-76.

34.   Minchinton AI, Tannock IF. Drug penetration in solid tumours. Nature Reviews Cancer 2006;6:583-92.

35.   Pantel K, Brakenhoff RH. Dissecting the metastatic cascade. Nature Reviews Cancer 2004;4:448-56.

36.   Swartz MA, Skobe M. Lymphatic function, lymphangiogenesis, and cancer metastasis. Microscopy Research and Technique 2001;55:92-9.

37.   Weinberg RA. The Biology of Cancer. 1st ed: Garland Science; 2006.

38.   Sutherland R. Cell and Environment Interactions in Tumor Microregions: The Multicell Spheroid Model. Science 1988;240:177-84.

39.   Michel CC. One hundred years of Starling's hypothesis. News in Physiological Sciences 1996;11:229-37.

40.   Silverthorn DU, Ober WC, Garrison CW, Silverthorn AC. Human Physiology: Prentice Hall; 2001.

41.   Swartz MA. The physiology of the lymphatic system. Advanced Drug Delivery Reviews 2001;50:3-20.

42.   Rippe B, Haraldsson B. Fluid and protein fluxes across small and large pores in the microvasculature. Application of two-pore equations. Acta Physiol Scand 1987;131:411-28.

43.   Weis SM, Cheresh DA. Pathophysiological consequences of VEGF-induced vascular permeability. 2005;437:497-504.

44.   Heldin CH, Rubin K, Pietras K, Ostman A. High interstitial fluid pressure - An obstacle in cancer therapy. Nature Reviews Cancer 2004;4:806-13.

45.   Baxter L, Jain RK. Transport of Fluid and Macromolecules in Tumors: 1. Role of Interstitial Pressure and Convection. Microvascular Research 1989;37:77-104.

46.   Hilmas D, Gillette E. MORPHOMETRIC ANALYSES OF THE MICROVASCULATURE OF TUMORS DURING GROWTH AND AFTER X-IRRADIATION. Cancer 1974;33:103-10.

47.   Pluen A, Boucher Y, Ramanujan S, et al. Role of tumor-host interactions in interstitial diffusion of macromolecules: Cranial vs. subcutaneous tumors. Proceedings of the National Academy of Sciences of the United States of America 2001;98:4628-33.

48. Baish JW, Netti PA, Jain RK. Transmural coupling of fluid flow in microcirculatory network and interstitium in tumors. Microvascular Research 1997;53:128-41.

49. Ahlstrom H, Christofferson R, Lorelius L. Vascularization of the continuous human colonic cancer cell line LS 174 T deposited subcutaneously in nude rats. APMIS 1988;96:701-10.

50. Honess DJ, Kitamoto Y, Rampling MR, Bleehen NM. Nicotinamide and pentoxifylline increase human leucocyte filterability: A possible mechanism for reduction of acute hypoxia. 1996;74:S236-S40.

51. Dewhirst MW, Kimura H, Rehmus SWE, et al. Microvascular studies on the origins of perfusion-limited hypoxia. British Journal of Cancer 1996;74:S247-S51.

52. Galie M, D'Onofrio M, Montani M, et al. Tumor vessel compression hinders perfusion of ultrasonographic contrast agents. Neoplasia 2005;7:528-36.

53. Vaupel P, Thews O, Hoeckel M. Treatment resistance of solid tumors - Role of hypoxia and anemia. Medical Oncology 2001;18:243-59.

54. Helmlinger G, Yuan F, Dellian M, Jain RK. Interstitial pH and pO_2 gradients in solid tumors *in vivo*: High-resolution measurements reveal a lack of correlation. Nature Medicine 1997;3:177-82.

55. Helmlinger G, Sckell A, Dellian M, Forbes N, Jain RK. Acid Production in Glycolysis-impaired Tumors Provides New Insights into Tumor Metabolism. Clinical Cancer Research 2002;8:1284-91.

Chapter 2 – Theory of Antibody Spatial Distribution in Tumor Tissue

2.1   Importance of Spatial Distribution in Imaging and Therapy

The heterogeneous localization of systemically delivered antibodies in tumor tissue has been recognized for over twenty years(1). This chapter focuses on mathematical models that describe the transport of antibodies from the circulation to the tumor tissue, highlighting the reasons for this uneven distribution. Once the underlying causes are obtained, a discussion on methods to circumvent these limitations is presented.

The presence of spatial heterogeneity in tumors is detrimental to the therapeutic outcome. Not only will some cells completely escape therapy, able to repopulate the tumor once treatment is finished, but some regions will contain marginally toxic concentrations, able to foster the development of drug resistance. Any treatment where cell killing is faster than cell growth can have a positive therapeutic outcome, i.e. shrinking of the tumor. A more effective treatment will be able to reach a larger number of cells, reducing the treatment time, lowering the chance of spread during this period, and cutting the chances of developing drug resistance.

The resolution of imaging modalities such as PET and SPECT are lower than the roughly 100 μm distance between tumor blood vessels, so spatial heterogeneity has less of a direct impact on tumor imaging. However, it is important to understand the impact spatial heterogeneity has on total uptake within a vascularized tumor, which determines the signal to noise ratio that is achievable. Also, understanding uptake in small tumors is important for developing more sensitive imaging modalities, ones which are potentially able to locate tumors smaller than the current roughly 1 cm limit of detection(2-4).

2.2   Model Development

Mathematical modeling is a critical tool in understanding the distribution of antibody drugs in tumors. The complexity of antibody targeting is readily apparent from the multiple transport steps involved and variation in the factors that determine uptake. Systemically delivered antibody must distribute in the plasma volume, flow to the site of the tumor, extravasate across the blood vessel wall, diffuse between the cells, and bind to the target antigen. During this time it is being cleared from the

plasma, diffusing or flowing by convection from the surface of the tumor, and being internalized by the cancer cells themselves. Many of these factors vary between systems by several orders of magnitude, such as the dose, plasma clearance rate, and antigen internalization rate, making it difficult to generalize from a few experiments. It is virtually impossible to accurately control conditions with *in vivo* models, so experimentally varying parameters to determine their effect on uptake is impractical. Intra-tumor and inter-tumor variability blurs trends and masks some of the general principles that dictate localization. While it is important to be mindful of the variability and heterogeneity present in tumors that affect the uptake, this should not stand as an insurmountable barrier to analysis. Mathematical models provide quantitative insight into the fundamental factors controlling the distribution of these drugs. Complete control over simulation parameters allows in-silico experiments to determine trends and trade-offs. Even the variability present in tumors can be assessed by using a range of parameter values to see the effect on the outcome. These model simulations are a powerful tool to use in conjunction with experimental investigation.

Throughout the development of these models, the term antibody will be used to describe any binding macromolecule. This includes IgG molecules, antibody conjugates, antibody fragments, and smaller binding proteins. Although the parameter values change for the different sizes, the basic principles are the same. With some further adjustments, the approach could be adapted for analyzing the diffusion, binding, and cellular processing of many small molecule drugs and larger nanoparticles, which also show heterogeneous distribution in solid tumors(5, 6).

This modeling exercise will examine two contrasting cases of antibody targeting in order to develop a general theory for the uptake and distribution of antibodies in tumor tissue. The first case applies to residual disease, where micrometastases are present that are imbedded in normal tissue. These metastases are at the prevascular stage, where oxygen and nutrients must diffuse inwards from the surrounding tissue. The second case is for a vascularized tumor. Once a primary tumor or metastasis develops the ability to recruit its own vascular supply, the size of the mass can grow beyond its previous surface transport limited size. The tumor vasculature is able to supply oxygen and nutrients to an expanding mass of cancerous cells.

a. Micrometastases

The micrometastasis will be treated as a spherical clump of tumor cells (figure 2.1). The transport of all molecules occurs from the surface of the metastasis, and the lack of vasculature means

diffusion is the only mode of transport. For simplicity, the tissue is treated as a pseudo-homogenous medium. Diffusion around and between the cells is handled by measuring the effective diffusion coefficient in the tissue. The accessible volume is factored in by the void fraction, which adjusts for the interstitial concentrations that determine the binding and dissociation rates. Despite the heterogeneities found in tumor tissue, diffusion has been found to be consistent with experimental data of transport *in vitro* and *in vivo*(7-10).
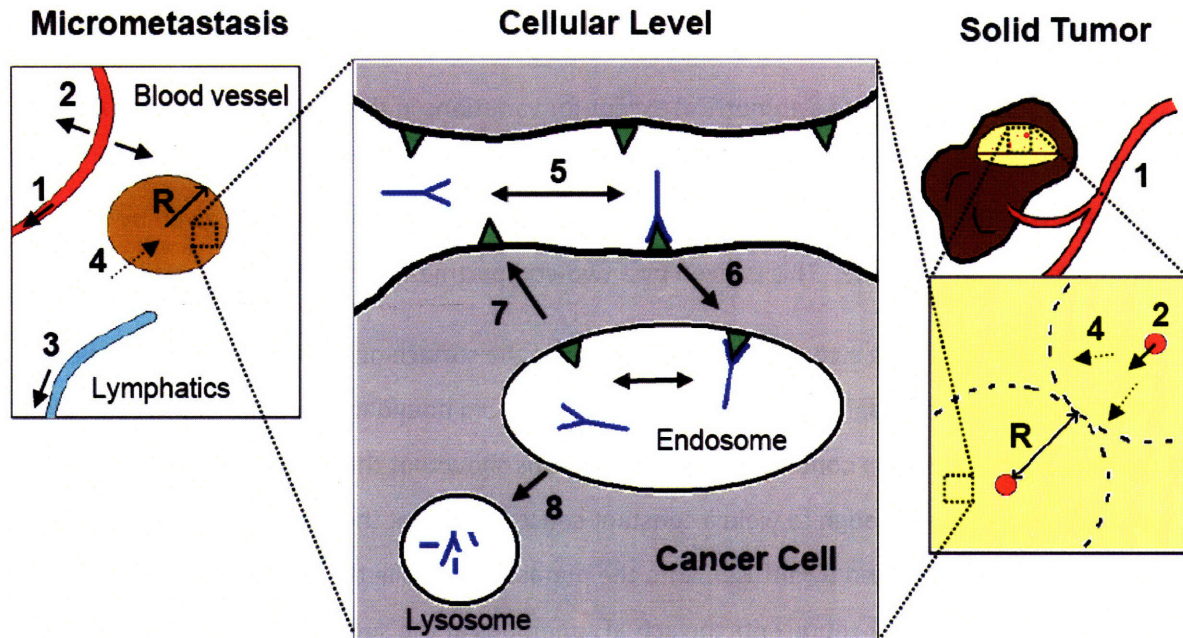
Figure 2.1 – Geometry of the model system for antibody distribution. The spherical representation of a micrometastasis is illustrated on the left, while the cross section of a capillary shows the cylindrical analysis for vascularized tumors on the right. Within the tissue for both models, antibody diffuses and binds antigen. Some of the major rates used in the modeling are clearance from the plasma (1), extravasation from blood vessels (2), normal tissue clearance by lymphatic drainage (3), diffusion in the tumor tissue (4), binding (5), internalization (6), recycling (7), and degradation (8). The distance antibody must travel is based on the radius of the micrometastasis or around a tumor blood vessel (R).

The equations describing this transport are presented below and in the appendix (section 2).

$$\frac{\partial [Ab]}{\partial t} = D\nabla^2[Ab] - \frac{k_{on}}{\varepsilon}[Ab][Ag] + k_{off}[B] \qquad \text{2.1}$$

$$\frac{\partial [B]}{\partial t} = \frac{k_{on}}{\varepsilon}[Ab][Ag] - k_{off}[B] - k_e[B] \qquad \text{2.2}$$

$$\frac{\partial [Ag]}{\partial t} = R_s - \frac{k_{on}}{\varepsilon}[Ab][Ag] + k_{off}[B] - k_e[Ag] \qquad\qquad 2.3$$

Where [Ab] is the free antibody concentration, [B] is the bound antibody-antigen complex concentration, [Ag] is the free antigen concentration, D is the diffusion coefficient in tumor tissue, ∇^2 is the Laplacian, k_{on} is the binding rate, ε is the void volume, k_{off} is the dissociation rate constant, k_e is the endocytosis rate, and R_s is the antigen synthesis rate. A list of all the symbols used in the thesis can be found in the Appendix, Section 1.

The transport is considered symmetrical except for variations in the radial distribution. A no-flux (Neumann) boundary condition is used at the center of the spheroid. The surface of the micrometastasis will have a defined concentration, i.e. a Dirichlet boundary condition, given by the concentration in the normal tissue. This is given by a two-compartment model for transport in the body.

The validity of assuming a constant concentration at the surface of micrometastases has been analyzed by Banerjee and colleagues(11). They argue that a Robin boundary condition more accurately represents the surface boundary condition. Their simulations show that the source term and diffusion in normal tissue are not fast enough to yield a constant concentration at the surface, and the concentration is actually depleted by diffusion into the metastasis. While this more sophisticated boundary condition likely better represents the actual conditions at the surface, the magnitude of the uptake rate is similar in both cases. The more recent estimates for diffusion coefficients, which are the faster of the two rates used in their paper, yield less of a difference than older estimates of this rate. Convection in the surrounding normal tissue is also ignored, but convection in the radial direction would lower this transport limitation at the surface.

b. Vascularized Tumors

The above equations and boundary conditions describe the model for micrometastases. The transport in solid tumors must be analyzed in a different manner. Antibodies in solid tumors localize primarily around the tumor blood vessels, the transport system for the tumor. Here, the model will focus primarily on the distribution around these blood vessels. Due to the shape of tumor capillaries, a cylindrical model will be used, similar to a Krogh cylinder. An inner cylinder represents the tumor capillary, where the concentration inside is equivalent to the plasma concentration. A cylindrical annulus of tissue surrounding the capillary is used to represent the cancer cells. The outer radius represents half of the intercapillary distance, where cells beyond this radius are supplied by an adjacent

26

capillary. The concentration of antibody is a function of the radius only, so it follows the same equations as given above (where the Laplacian is for a cylinder, not a sphere). Justification for ignoring variations along the length of the capillary is given later (Chapter 4). A no-flux boundary condition is used at the outer radius so no antibody crosses this boundary (figure 2.1).

The Krogh cylinder was first used to analyze the transport of oxygen in tissue. August Krogh noted the regular, parallel spacing of blood vessels in muscle tissue, and used this to justify the cylindrical arrangement of vessels. In fact a series of these cylinders, stacked more like a hexagonal array, describes the spatial orientation quite well to first approximation. Using this cylindrical annulus to describe the geometry of the system, he analyzed the diffusion rates of oxygen and the distance it must travel in order to adequately supply the muscle tissue. For reference, he found that in warm-blooded animals, the outer radius, R, was 10-15 microns, such that all cells are within 1-2 cell diameters of a capillary in this type of tissue(12).

The Krogh cylinder model has been criticized as overly simplifying the vascular structure. Most tissues lack such a regular array of vessels, and exchange with larger vessels is completely ignored. The no flux condition used at the outer radius isolates each cylinder so that exchange between vessels is not allowed. The vascular network in solid tumors is even more disorganized and heterogeneous than normal tissue. The stochastic distribution of tumor blood vessels results from their haphazard recruitment by tumors cells as they continue to grow uncontrollably beyond the limits imposed by oxygen diffusion. In solid tumors, there is a wide range in the intercapillary distance(13), half of which is the maximum distance cells are found from the nearest vessel. Given the heterogeneous nature of tumor blood vessels, the use of a Krogh cylinder must be justified.

Histological examination of antibody distribution after systemic delivery shows perivascular distribution. The antibody rarely reaches beyond 1 or 2 cell diameters away from the capillary(14-16). In these situations, the no-flux boundary condition, also known as a non-interacting boundary condition, is justified since antibody never reaches the outer radius, and the boundary condition does not affect the distribution. Low affinity or non-binding antibodies may be able to reach the outer radius since they are not slowed by binding. However, in the center of a tumor, the blood vessel is surrounded by other capillaries. The transport from the surrounding capillaries occurs in a similar manner, and antibody that reaches half the intercapillary distance will be met by antibody originating from the adjacent capillary. The symmetry assures that the net-flux across this boundary is zero, which is identical to the no flux condition; this is also known as a mirror boundary condition. In some regions, the intercapillary distance

27

may be large, but this can be taken into account by using a larger outer radius, R. In the case of low affinity or non-binding antibodies near the surface of the tumor, the no-flux condition across the outer radius does not hold. This will be treated with a separate term for surface effects found in Chapter 4.

With large doses, a significant portion of the tumor may become saturated, and the above assumptions may fail. Areas that have a high vascular density will become saturated before adjacent areas with few blood vessels. Antibody will then diffuse from these areas into the avascular regions. However, as will be shown later in the compartmental model, this will not greatly affect the total uptake in the tumor when extravasation, not diffusion, is limiting. For now, the no-flux boundary condition at the outer surface will be used with knowledge of the above caveats.

c. Effects of Tumor Physiology

The unique physiology of tumors described in Chapter 1 has several implications on antibody uptake. Some of these properties directly affect targeting, while others have minimal influence, so they must be discussed in more detail.

Tumor blood flow can affect targeting in several ways. First, poor flow limits the amount of blood that perfuses the vascularized tumor. However, studies show that the amount of antibody exiting the vessels is so small that the concentration within the plasma is not affected (17, 18). Transient cessation of flow, such as that cause by arteriole shunting(19), temporary vessel collapse(20, 21), or blockage from leukocytes (22), would limit blood flow to certain vessels. However, as long as the antibody is not cleared from the plasma at a rate much faster than this transient hypoxia (usually on the order of several minutes(23, 24)), the temporary cessation of flow has little impact. Vessels would fill with the plasma concentration while they were open, and the low extravasation rate would ensure little depletion occurred within the vessel while it was not flowing. Vessels that are closed for long periods of time, on the same order as clearance from the blood, would not be effective at delivering antibody. In this case, the vessel can be treated as non-functional, and cells would have to be targeted by adjacent functional vessels. This increases the distance, R, between functional capillaries that must be reached in order to target all cells. Permanently disabled vessels cannot deliver oxygen, which would cause local necrosis. From a practical standpoint, only the viable cells need to be targeted for effective therapy.

The non-cancerous cell types present in tumors have profound biological effects, but since they lack target antigen on their surface, they are not bound by the antibody drug. Since binding reduces the amount of free antibody available to transport through the tissue, slowing targeting, the antigen

negative cells in the tumor actually lack this impediment to transport and have little direct impact on targeting. If they are completely antigen negative and present in large amounts, they could reduce the overall antigen concentration, thereby increasing the distance antibodies can target.

In summary of the model development, micrometastases will be analyzed as a spherical mass of cells, imbedded in normal tissue. Antibody localization occurs only by diffusion from the surrounding normal tissue. The distribution in solid tumors is analyzed around the tumor capillaries using a Krogh cylinder. Antibody is supplied by the blood plasma but does not cross the outer radius of the cylinder. Due to uniformly elevated interstitial pressure, transport in the cylinder is treated by diffusion only.

2.3   Previous Models and Current Approach

Several models have been used previously to examine the transport of antibodies in tumor tissue(17, 25-29). Fujimori and colleagues showed that binding alone can cause heterogeneous distribution of antibodies on length scales less than 100 microns (microdistribution)(26). They coined the term 'binding site barrier' to describe the phenomena where antibodies are immobilized close to their site of entry. This 'barrier' is often misrepresented, however, and it is not the result of any physical or structural impedance to antibody transport. Rather, it is a dynamic boundary that is caused by a balance of factors, including affinity, diffusion, and internalization. Baxter and Jain(17) simulated distribution on a macroscopic scale in 1 cm diameter tumors. They examined the role of elevated interstitial pressure including tumor convection and spatial variation in extravasation. In a subsequent model(29), they showed binding and internalization are further detrimental to antibody distribution. Rippley and Stokes(27) used a microscopic model to analyze the effects of cellular interactions on the distribution around blood vessels. The well-studied kinetics of transferrin were used as the model therapeutic, and binding, internalization, and recycling were shown to have a large influence on distribution. Using a similar model and measuring parameters for transferrin-toxin conjugates, Wenning and Murphy(28) quantitatively described cell killing in multicell tumor spheroids. They went on to generalize conditions where spheroid penetration is limited by internalization and describe trade-offs between affinity and dose. Graff and Wittrup(25) described a reductionist model of penetration, binding, and retention. Simple analytical expressions demonstrated the interplay between dose, affinity, diffusivity, antigen concentration, clearance, and internalization.

For each of the models, the relevant differential equations were solved numerically, and the solutions for various cases were presented graphically. These simulations are a valuable resource for

exploring system behavior by in silico experimentation. However, these simulations can only practically capture several base case scenarios. Given a system with different parameters, more simulations must be run to determine the behavior. This is not ideal for lending insight into the fundamental behavior of the system. The simulations do not give principles and concepts that can easily be extended to different scenarios. Analytical solutions are more suited for these types of results, where the outcome is an explicit function of the system properties. Unfortunately, even with assuming ideal spherical and cylindrical geometry, the targeting scenarios are too complex for analytical solutions. The series of coupled, non-linear, partial differential equations cannot be solved in most cases. Even with simplifying assumptions, the resulting infinite series solutions are complex and require a computer to visualize, defeating their purpose. Section 11.b and c of the appendix present two such solutions. The first solution gives the distribution of a low affinity antibody in a sphere with no catabolism, and the second provides the solution for uptake in a Krogh cylinder with a constant plasma concentration (constant infusion) and no catabolism. Unfortunately, these series solutions provide little insight into the general behavior of antibody distribution.

Given the limited utility of analytical solutions and difficulty in generalizing the numerical simulations, a different approach was chosen to analyze the distribution of antibodies in tumor tissue. Dimensional analysis is a powerful technique that can provide insight into complex systems by conceptually comparing and contrasting the behavior of the system in different regimes and yielding quantitative results. As an example, one of the most common dimensionless numbers in the field of engineering is the Reynolds number, which describes flow as being either laminar or turbulent given a small or large magnitude. The current theory develops several dimensionless numbers that describe the qualitative distribution of antibodies in tumor tissue. From a practical standpoint, two of these numbers in particular describe which cells in a tumor will be targeted by antibody, and the parameters required to evaluate the numbers can be estimated from the literature or obtained by *in vitro* experiments. In this way, experiments can be designed and analyzed with a better understanding of the expected results.

In order to reduce the complex problem of antibody distribution to its simplest form, it will be parsed into two components: 1) transport; and 2) clearance. The mechanisms and timescales of each are fundamental in controlling the distance an antibody will permeate through tumor tissue under a given set of conditions. It is the balance between these processes of uptake and loss that governs how far antibody penetrates into a tumor.

2.4   Transport

a.   Diffusion

Diffusion is the dominant mode for antibody transport in tumor tissue. Although fluid flow in the blood vessel lumen carries the drug inside the tumor or to the surrounding normal tissue, once it extravasates from the vessel, random Brownian motion dominates and causes a net flow of molecules from high concentration to low concentration. Due to uniformly elevated interstitial pressure, diffusion is the dominant mode of transport in solid tumors(30). Convection is explicitly ignored in both the micrometastases and tumors. Models(17) and measurements(31) of convection in tumors show that it is very slow, on the order of 0.17 µm/s at its highest value in the tumor periphery. A convection-diffusion model examining transport around a capillary shows this rate is slow enough that it does not affect the distribution on the intercapillary length scale(32). Therefore, transport in both the micrometastasis and vascularized tumor models will only consist of diffusion of the antibody.

b.   Convection

While convection is slow enough that it does not affect the movement within the interstitium to a significant extent, it can increase the rate of extravasation from the blood vessels. Baxter and Jain(17) showed increased peripheral uptake caused by fluid filtration around the outer edge of the tumor using a convection-diffusion model. This occurrence will be examined closer to illustrate the effect this has on transport.

The high permeability and lack of functional lymphatics in tumors causes a large amount of fluid to build up in the tissue. This fluid must exit through the tumor surface, causing a net outward movement of fluid in the tissue. For tumors isolated in a body cavity, such as the lumen of the intestine, the pressure at the surface is roughly zero. The pressure gradient drops from near vascular pressure to zero in a relatively short distance close to the surface. In the tumor center, the elevated interstitial pressure causes little fluid to extravasate, whereas near the periphery, the lower interstitial pressure allows fluid to escape. However, for tumors surrounded by normal tissue, the lymphatics are not able to completely drain this fluid immediately at the tumor surface, and the interstitial pressure does not drop until a distance outside of the tumor(17). In this case, the interstitial pressure is elevated at the tumor surface, there is no increase in extravasation within the tumor, and convection occurs only in the surrounding stroma. In fact, the pressure profiles measured within a subcutaneous tumor show the pressure gradient occurs almost entirely in the surrounding skin(33).

31

The rate of extravasation via convection versus extravasation from diffusion is known as the Peclet number. In the Baxter and Jain convection-diffusion model(17), the Peclet number was much greater than 1 near the surface. However, they could not measure the rate of convection versus diffusion, so based on estimates of Rippe and Haraldsson(34), they assumed that permeability measurements made in a rabbit ear chamber(35) were 0%, 1%, or 10% diffusive. Rippe and Haraldsson's estimate is looking at a two-pore model, where convection can occur across large pores even in the absence of net filtration by reabsorption of fluid through small pores. This occurs via the difference in the reflection coefficient across the large and small pores. Fluid flow is determined by a balance between the hydrostatic and osmotic pressure gradients across the vessel wall. Typically, the oncotic pressure is higher inside the capillary due to the high concentration of plasma proteins. In a two-pore model, the large pores in the capillary are not able to maintain this oncotic pressure gradient, so the larger hydrostatic pressure in the vessel forces fluid out of the large pores. This extra fluid is then reabsorbed by the small pores. These smaller pores are more prevalent in number, and the oncotic pressure gradient is greater than the hydrostatic pressure gradient due to the large reflection coefficient and high concentration of plasma proteins in the blood. This volume circulation occurs in the absence of net flow (figure 2.2). The convection across the large pores carries macromolecules with it, which dominates the transport in a two pore model. In this case, diffusion only makes a minor contribution. Convection can therefore occur in the center of a tumor even in the absence of net fluid filtration. However, the Baxter and Jain model uses a one pore model that only treats convection from the net movement of fluid from the vasculature to the interstitium. This results in the overall extravasation rate in the center of the tumor in the Baxter and Jain model being 0%, 1%, or 10% of what was measured in the rabbit ear chamber. Their early model may therefore overestimate the contribution of extravasation from fluid flow exiting the vessels (convective extravasation).

1 Pore Model   2 Pore Model

$p_i = 11 \quad mmHg$ $p_v = 15 \quad mmHg$ $p_i = 11 \quad mmHg$

$\Pi_i = 15 \quad mmHg$ $\Pi_v = 20 \quad mmHg$ $\Pi_i = 15 \quad mmHg$

$\sigma = 0.8$ $\sigma_{large} \approx 0$

Capillary Lumen

$$Flow = L_p S(\Delta p - \sigma \Delta \Pi)$$
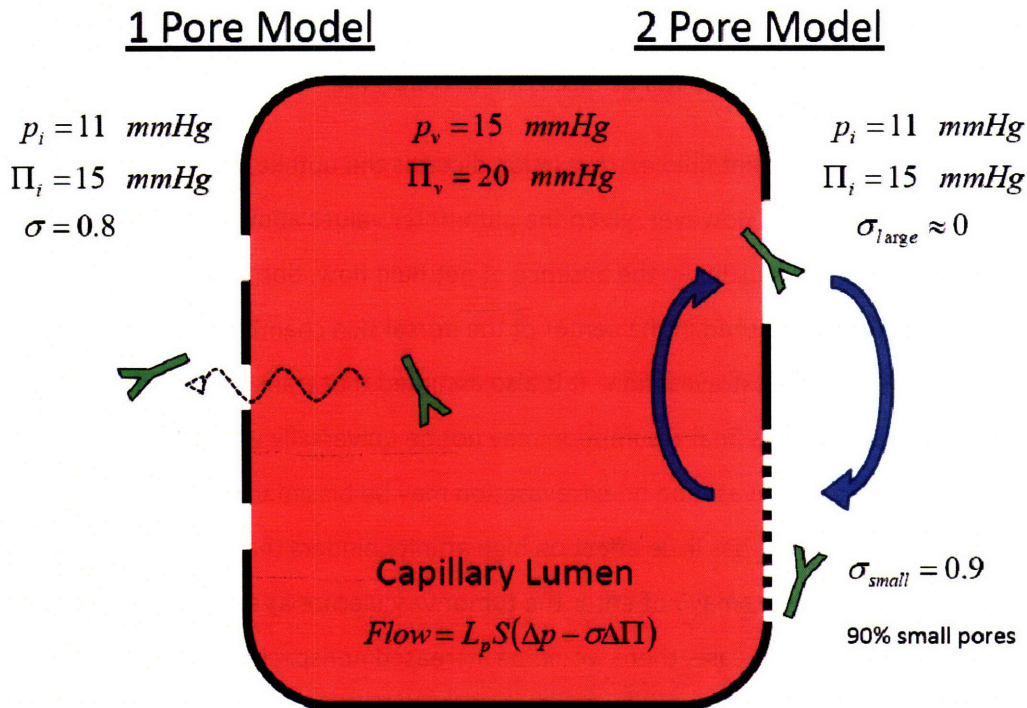
$\sigma_{small} = 0.9$

90% small pores

Figure 2.2 – Models of capillary permeability. Using a single pore model, the larger hydrostatic pressure within the vessel is completely balanced by the higher osmotic pressure inside the capillary. In this case, there is no net flow, and macromolecules must diffuse in and out of the vessel (left). As will be shown later, a lower interstitial pressure near the surface of a tumor may allow convection from the vessels in this location. For a two pore model, the reflection coefficient varies between the large and small pores. The lack of an osmotic pressure gradient over the large pores causes fluid to exit the large pores, carrying macromolecules with it. The large osmotic pressure gradient over the small pores causes the reabsorption of fluid, yielding no net fluid filtration. For the two pore model, convection over the large pores dominates the transport. Macromolecules cannot easily cross the small pores, resulting in a bias for macromolecules exiting the vessel. The current model assumes diffusive transport (left), where the increased permeability of tumor capillaries lowers the osmotic pressure gradient, and transport is not biased in either direction.

For the current model, the values measured in the center of the tumor are assumed to be diffusive and occur even in the absence of net fluid flow. In a subsequent model using a dorsal skin chamber(36), Baxter and Jain argued that due to the experimental setup, where measurements are taken near the center of the tumor window that is impermeable to fluid, the permeability values are primarily diffusive. In addition, the assumptions with pore sizes and osmotic pressure gradients for the two pore model may not be justified given the increased permeability from VEGF signaling and collapse of the osmotic pressure gradient(20). Assuming the permeability measurements are mostly convective inflates the Peclet number 10 to 100-fold (in the case of assuming 10% or 1% of the measured

permeability is from diffusion) or an infinite amount when assuming no diffusion occurs. Therefore, diffusion likely dominates for many tumors, as will be discussed in chapter 4.

There are probably cases where net fluid extravasation dictates the uptake in tumors, as described by the Baxter and Jain model. However, given the parameter values above, diffusive extravasation, or at least convection occurring in the absence of net fluid flow, dominates in the tumor. For the current analysis, the values measured in the center of the dorsal skin chamber are used as the permeability in the absence of net fluid extravasation. It is also assumed that transport is equal in both directions, given its diffusive nature. This final assumption may not be universally valid if the two pore model best describes the situation. Intravasation or extravasation may be biased under certain conditions. For example, although a bias has little effect on high affinity binders that are cleared by internalization, unbound macromolecules may not enter the tumor vasculature as easily due to outward convection across the large pores. In this case, there would be increased nonspecific uptake as unbound antibody takes longer to enter smaller pores or leave the tumor surface, which may be some distance away.

c. High Affinity Antibodies

The transport of antibodies is affected by their binding. As these molecules diffuse between cells, they associate with their particular antigen, immobilizing them on the surface of the cell. This depletes the number of free antibodies and slows penetration into the tumor mass. Antibody affinity is determined by the association rate and dissociation rate to the target. For monovalent interactions, the K_d is simply:

$$K_d \equiv \frac{k_{off}}{k_{on}}$$

2.4

There are four qualitatively different behaviors of transport and binding, depending on the rate of binding and dissociation. These four scenarios are outlined in figure 2.3, and they will be discussed throughout the chapter. The most common scenario for high affinity binders is a fast-on, slow-off rate which is often enhanced by avidity (multiple binding sites). The two moderate affinity cases are the fast-on, fast-off binders and the slow-on, slow-off case. Finally, for molecules with a slow-on and fast-off rate, they only form a few transient complexes and are treated as non-binding antibodies.
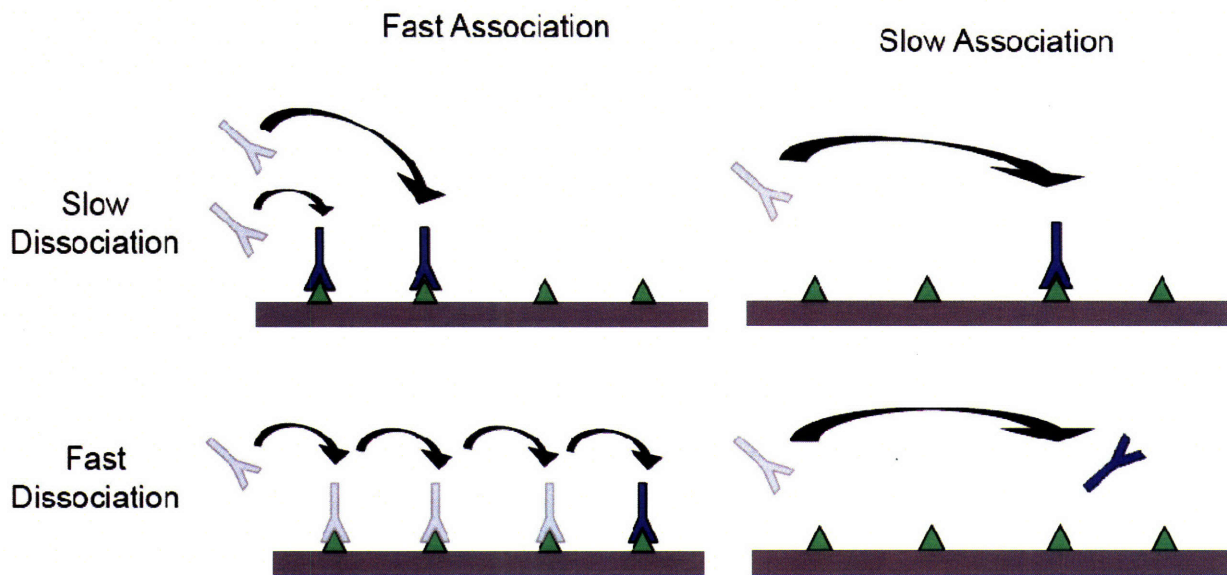
Figure 2.3 – Qualitative binding behavior of antibodies. Most antibodies have fast association rates, and for high affinity binders, their dissociation rates are very slow (top left). Lower affinity binders typically maintain fast association rates but quickly dissociate, allowing them to diffuse deeper into the tissue (bottom left). Binders with slow association rates can diffuse through tissue without binding initially, but once they form a complex, they remain anchored in place (top right). For antibodies that associate slowly and then quickly fall off the antigen, very few complexes form, and they behave as non-binding antibodies (bottom right).

Most antibodies have a high affinity for their target, which in this case means their dissociation constant (K_d) is much less than their concentration in the tissue. Their association rates are often very fast compared to the rate of free diffusion, and so free antibody binds immediately to any free antigen, saturating each cell layer before diffusing to the next cell layer.

This qualitative behavior can be demonstrated using a dimensionless number defined as the binding modulus (see Appendix section 3):

$$\text{Binding modulus} \equiv \frac{k_{on}\left(\frac{[Ag]}{\varepsilon}\right)R^2}{D} \qquad\qquad 2.5$$

where R is distance.

The association rate and antigen concentration determine the binding rate, and the diffusion coefficient over the distance squared provides the diffusion rate for free antibody. This dimensionless number, a Damkohler number, describes the distance over which antibody gradients occur in the tissue. For example, diffusion coefficient for IgGs in tissue vary, but a typical value is 10 μm^2/s(8, 10, 30, 37, 38).

Association rates are on the order of 10^5 /M/s(39), and effective antigen concentrations ([Ag]/ε) have magnitudes around 5 μM(40). When the binding modulus is approximately equal to one, the rate of binding is equal to the rate of diffusion, so this gives a rough estimate of the distance an antibody travels before binding. In this situation, the distance R is approximately 5 μm. Put in terms of time scales, an antibody binds free antigen after approximately 2 seconds, and the antibody diffuses an average distance of 5 μm in this time. Since the distance is less than the diameter of a cell, the antibody will bind the current cell layer before diffusing on to the next. Once all of the antigen is saturated on the first cell layer, antibody will be able to diffuse beyond this saturated region to the next layer. Simulations varying the binding rate show that the profile becomes a sharp gradient as the binding modulus increases (figure 2.4). In this case, the Krogh cylinder radius is used to calculate the modulus.
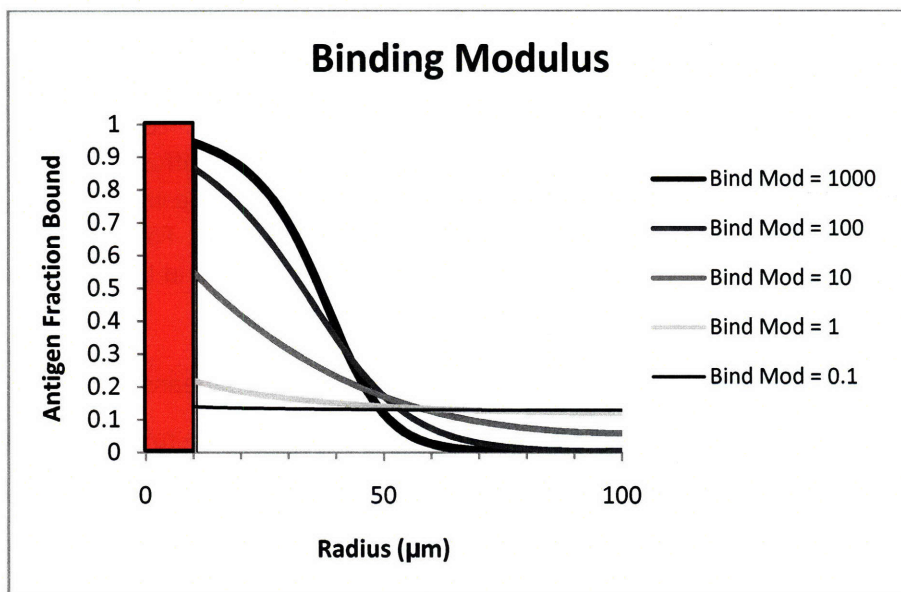

Figure 2.4 – Binding modulus in a vascularized tumor (Krogh cylinder). The red bar on the left represents the capillary (covering the first 10 μm), and the lines describe the antigen saturation for various values of the binding modulus. The level of antigen binding was determined using a numerical simulation of antibody distribution in a Krogh cylinder (Appendix section 2 equations) using an IgG with ε = 0.1, D = 14 μm²/s, [Ag] = 280 nM, and a constant dose of 1 μM. Using a cell diameter of 10 μm, this constant dose is able to target approximately three cell layers from the capillary. The association rate ranged from 5x10⁵/Ms to 50/Ms to vary the binding modulus. For a typical IgG, the binding modulus is on the order of 1000, giving heterogeneous distribution.

The rapid association kinetics result in 'shrinking core' transport. From a chemical engineering perspective, this transport situation is similar to the rapid reaction of oxygen in a catalyst pellet, which is much faster than diffusion, allowing a pseudo-steady state to develop(41). The shrinking core

assumption allows the complex transport situation to be simplified and solved analytically. This same analysis is valid for high affinity antibodies with rapid association rates. Other methods will be used for lower affinity (i.e. reversible) binding interactions and slower association rates.

2.5 Antibody Clearance

a. Systemic Clearance

Intravenously delivered antibody rapidly distributes in the plasma volume, then slowly exchanges with the extracellular space in the body. Antibodies are hydrophilic drugs, in contrast to some small molecule drugs, which are lipophilic and can cross cell membranes and distribute in the fatty tissues of the body(42). Uniform distribution in the plasma volume is obtained very quickly after injection. Dispersion in the circulatory system is rapid due to large variances in the length of capillary beds, velocity differences as a function of blood vessel radius, and recirculation due to the closed nature of the system(43). Fluctuations in the plasma concentration cease quickly after only a couple circulation times (e.g. approximately 1 min for a human)(44), therefore a bolus dose is assumed to instantly and uniformly disperse in the plasma volume.

The plasma concentration of antibodies and their fragments follow a biexponential decay, which is generally well described by a two-compartment system. The initial rapid, or distribution, phase occurs due to redistribution from the plasma volume to the extracellular space in normal tissues. The second, or clearance, phase occurs as the antibody is removed from the body, for example by uptake in the liver and endothelial cells, or filtration by the kidney. Table 2.1 illustrates typical clearance curves for various antibodies and fragments.

Whole Body Pharmacokinetic Parameters	alpha	beta	% α	Ref.
Mouse IgG in Mouse	1 day	7 days	70%	(45)
Human IgG in Mouse	1.2 hr	6.81 days	66%	(46)
Human IgG in Human	12.74 hrs	86.92 hrs	43%	(47)
scFv in mouse	0.05 hr	3 hrs	80%	(48)
scFv in human	0.42 hrs	5.32 hrs	90%	(49)

Table 2.1 – Typical biexponential clearance values for IgG and scFv

Whole IgG molecules clear slowly from the plasma, with a β-phase half life of elimination typically on the order of several days (48, 50, 51). This extended serum persistence is the result of salvage recycling by FcRn (52) and exclusion from renal filtration due to large molecular size. Over days and weeks, non-specific pinocytosis will capture soluble IgG molecules in the plasma and interstitial fluid, trapping them in endosomes. The FcRn receptor binds the Fc region of an IgG under the acidic conditions in the endosome prior to being directed to a lysosome. The receptor-antibody complex is then recycled back to the surface, where the neutral pH releases the IgG outside of the cell. The role of FcRn in Ig circulation has been captured in physiologically based pharmacokinetic (PBPK) models (53, 54). By contrast, smaller antibody fragments such as Fabs, scFvs, and diabodies clear more rapidly with half times of minutes to hours (48, 55, 56). This rapid clearance occurs primarily through the kidneys as these molecules are below the ~60-70 kDa size cutoff for glomerular filtration(57). Conjugation of polyethylene glycol (PEG) chains to antibody fragments can increase their hydrodynamic radius above the kidney filtration cutoff and greatly reduce systemic clearance rates (58, 59). Plasma clearance rates of antibody fragments may also be reduced by covalent or non-covalent linkage to albumin or Fc domains that are able to mediate FcRn recycling (55, 56, 60, 61). Other recombinant antibody fragment formats such as Fab_2 (~110 kDa), minibodies (~75 kDa), and tetrabodies (~110-130 kDa) exhibit intermediate clearance rates as they are large enough to avoid rapid renal filtration but lack the Fc domain for salvage recycling (48, 62, 63).

Systemic clearance can also occur via the antibodies specific interaction with a particular target. This can occur via binding and/or degradation by the tumor tissue itself (64) or expression in healthy tissues in the body(65, 66). This phenomena is called "target mediated drug disposition" or TMDD(67, 68). The endocytic clearance in tumor or normal tissue was required to adequately describe the systemic clearance of an anti-EGFR antibody(64), anti-CD4(65) and anti-CD11a(66). These are saturable effects, so they are significant with low doses relative to the total target size. Therefore, they are most important with large volume disease and with target expression on normal tissues.

b. Local Clearance

Internalization and catabolism of antibodies in tumor tissue can exert a local effect as well as the systemic effect on distribution. As antibody enters the tumor tissue and binds antigen, the internalization of the target can cause degradation of the complex, slowing penetration into the tissue and limiting retention on the cell surface.

The internalization rate for cell bound antibodies depends on the properties of the target antigen. For rapidly cycling receptors, such as those controlled by clathrin coated pit mediated endocytosis, the half life can be in minutes, whereas more stable antigens may remain on the surface for hours to days(64, 69-72). Constitutive turn-over of the membrane surface occurs over several hours, so antigens that remain on the surface longer, such as A33, must be actively retained there(73). Antibodies complexed with extracellular matrix proteins may remain in the tumor for more extended periods of time but will be turned over by proteases and degradation of the extracellular matrix. Mattes and coworkers demonstrated that for many antibodies, the local endocytic turn-over is faster than dissociation, so binding is effectively irreversible on the cell surface(72). This is true for many bivalent IgG molecules due to their avidity, but this is not always true with monovalent binders, depending on the affinity. This will be discussed later in the chapter.

After antibodies are internalized on the surface, they may be recycled back to the surface with the bound antigen, reducing the net uptake rate(74). Assuming a pseudo-steady state develops between the surface and internal antibody, the overall rate of endocytosis is a function of the relative rates of recycling and degradation after equilibration (see Appendix section 14):

$$k_e = \frac{k_i}{\left(\dfrac{k_r}{k_{\deg}}\right) + 1}$$

2.6

where k_i is the internalization rate from the surface to the endosome, k_r is the rate of recycle from the endosome, and $k_{\deg}$ is the rate antibodies are directed to the lysosome for degradation.

2.6 Limitations to Antibody Localization

Targeting all the antigen within a tumor, thereby saturating the amount of antibody in the tissue, is a difficult task to achieve, although this is desirable from a therapeutic standpoint. Even if all of the antigen within the tumor cannot be saturated, targeting all cells at a subsaturating concentration would be beneficial in some cases by eliminating regions that completely escape therapy. However, when the mechanisms of antibody clearance are faster than transport, this will not be achieved. If the antibody is cleared from the circulation faster than the time required to saturate the tumor or micrometastasis, some cells will escape targeting. Similarly, if the local endocytosis of the antibody complexes is faster

than antibodies can transport into the tissue, then antibody cannot bind all of the cells. These two scenarios can be predicted by dimensionless ratios of the transport and clearance rates.

a. Systemic clearance versus antibody transport

For many antibody fragments and binding molecules, systemic clearance places a major role in determining the depth of penetration into tumor tissue. Although IgGs are cleared slowly, many fragments and other protein binders are quickly filtered by the kidney. In other instances, a clearing agent may be used to speed up clearance before imaging or delivery of a secondary agent. A finite amount of time is required for the antibody to extravasate, diffuse through the cells, and bind antigen, and if the plasma level drops quickly, antibody will not be able to target very many cells.

Using the shrinking core kinetics discussed above, the time required to saturate a spherical micrometastasis, with a constant surface concentration and ignoring local clearance (see Appendix Section 4a.i) is:

$$t_{sat} = \frac{R_{met}{}^2 \left([Ag] \middle/ \varepsilon \right)}{6D[Ab]_{surf}} \qquad\qquad 2.7$$

where R_{met} is the radius of the metastasis and $[Ab]_{surf}$ is the surface concentration. If the antibody is removed prior to this time, only the peripheral cells will be targeted. However, this is for a constant concentration at the surface. For *in vivo* situations, the surface concentration (in the surrounding normal tissue) will rise as antibody extravasates into the normal tissue interstitium, then fall as it is cleared from the plasma and tissues. The overall exposure time of the antibody is based on the biexponential clearance parameters in the tumor. For a plasma concentration:

$$[Ab]_{plasma} = [Ab]_{plasma,0} \left(A \exp\left(-k_\alpha t\right) + B \exp\left(-k_\beta t\right) \right) \qquad\qquad 2.8$$

where A, B, k_α, and k_β are the biexponential decay constants. $[Ab]_{plasma,0}$ is the initial plasma concentration, and t is time. The exposure time can be measured by the area under the curve of a plasma concentration profile, normalized to the initial concentration:

$$t_{clearance} \equiv \left(\frac{A}{k_\alpha} + \frac{B}{k_\beta} \right) = \frac{1}{\ln(2)} \left(A \cdot t_{1/2,\alpha} + B \cdot t_{1/2,\beta} \right) \qquad\qquad 2.9$$

The ratio of the time required for saturation to the time antibody remains in the plasma is defined as the clearance modulus:

$$\Gamma \equiv \frac{R^2 \left([Ag] \middle/ \varepsilon \right)}{D[Ab]_{surf} \left(\dfrac{A}{k_\alpha} + \dfrac{B}{k_\beta} \right)} = \frac{\text{penetration time}}{\text{clearance time}} \qquad\qquad 2.10$$

The surface concentration varies between micrometastases and solid tumors. For micrometastases, the normal tissue concentration surrounding the metastasis is the relevant value, and for solid tumors, it is the concentration just outside the capillary wall. Expressions for these concentrations will be given later, but derivations for each specific case can be found in Appendix sections 4a and 4b. The 6 found in the saturation time is a shape factor for a sphere, and it appears in the exact solution for a high affinity binder in a micrometastasis for both the clearance modulus and Thiele modulus (see Appendix sections 4a.ii and 5a.ii). However, when the theory is generalized to low affinity binders and presented for both solid tumors and micrometastases, the shape factor is not included since it does on appear in these other scenarios. The area under the concentration-time curve, or AUC, is often measured in pharmacokinetics, so the clearance modulus for high affinity binders can also be expressed as:

$$\Gamma \equiv \frac{R^2 \left([Ag] \middle/ \varepsilon \right)}{D\left(AUC_{surf} \right)} \qquad\qquad 2.11$$

This allows the clearance modulus to be extended to cases where an infusion is given first, or multiple doses are used. If the clearance modulus is less than one, antibody will remain in the plasma long enough to saturate to the given radius, R. Values greater than one mean the plasma level drops too quickly, and no free antibody remains in the blood to target more antigen. The concept is illustrated graphically in figure 2.5. This dimensionless group was obtained by integrating over infinite time, so the sample time may also affect the results. Uptake of an IgG typically occurs over several days, so examining a tumor after only a few hours will yield different results.
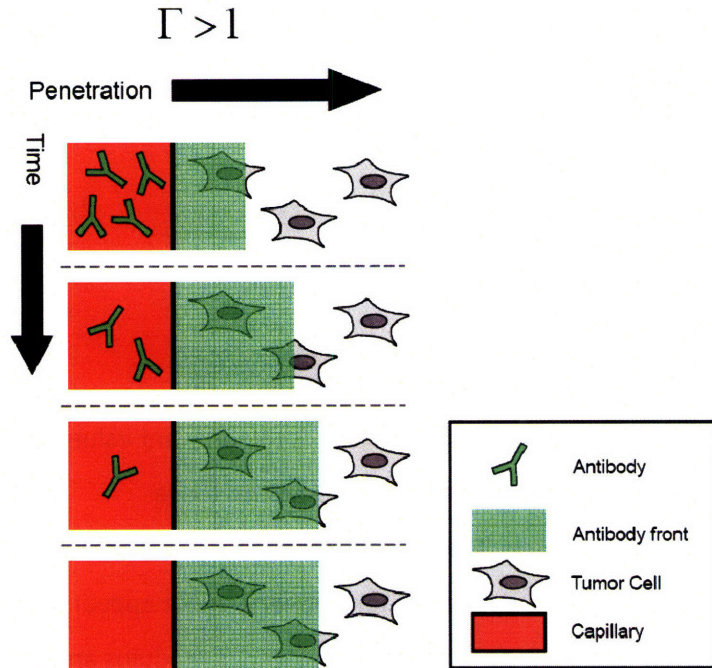
Figure 2.5 – Clearance modulus under sub-saturating conditions. The concentration of free antibody in the blood drops over time, lowering the amount of antibody that enters the tissue. As the concentration falls, the rate at which the antibody front progresses through the tissue slows until it stops once there is no free antibody in the plasma.

The scaling analysis above can be compared to numerical simulations of antibody distribution in micrometastases and vascularized tumors. The numerical simulations show that the simple clearance modulus captures the behavior of uptake and clearance from the plasma. The clearance modulus can then be used to predict the maximum distance of penetration for various doses in mice and humans (figure 2.6).
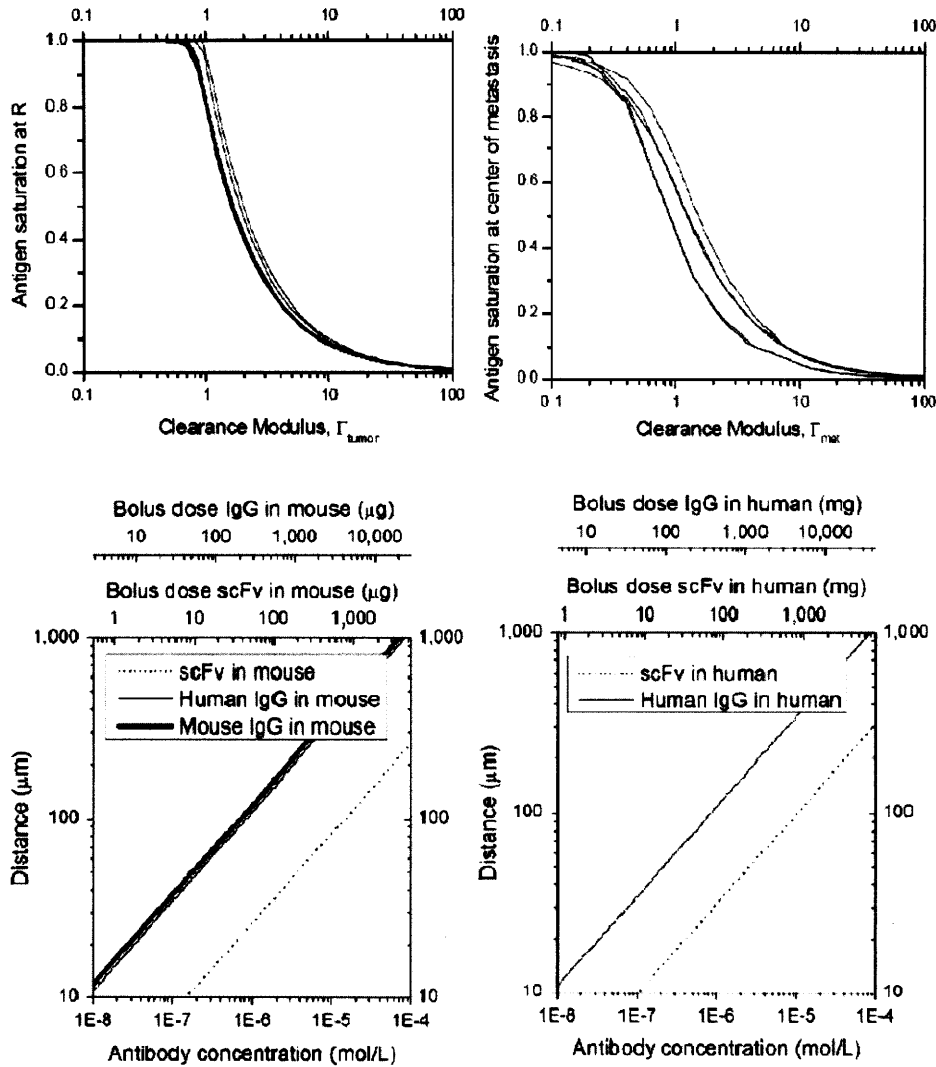
Figure 2.6 – Clearance modulus simulations. Numerical simulations using a Krogh cylinder (top left) or spherical metastasis (top right) were run varying the clearance values for IgG and antibody fragments in mouse and human (Appendix section 2). The maximum fraction of antigen saturation at a radius of 100 μm was graphed while varying the dose with no internalization. Typical parameter values were used for the simulations as published(75). Using these values in the clearance modulus, the maximum distance of penetration when limited by systemic clearance is shown for a mouse (bottom left) and human (bottom right) by setting the modulus equal to one and solving for R.

b. Local clearance versus antibody transport

The clearance modulus predicts when systemic clearance occurs before all of the cells are targeted. For slow clearing IgGs, constant drug infusions, or multiple doses, the plasma concentration remains elevated over an extended period of time, so the area under the curve is larger than the saturation time. This satisfies the clearance modulus criteria. However, local clearance can be limiting in these cases. As antibody diffuses into the tissue and binds antigen, the complex may be turned over

43

on the cell surface at different rates. Free antigen is either synthesized or recycled back to the cell surface and is able to internalize more antibody, providing a constitutive route for endocytic clearance. If the rate at which antibodies are degraded in the tissue is faster than antibody transport over a given distance, then cells beyond this distance will not be targeted.

If systemic clearance from the plasma is ignored, the local uptake and clearance will reach a steady state in the tumor. The ratio of the penetration time to the internalization time is defined as the Thiele modulus squared in tumor tissue:

$$\phi^2 \equiv \frac{k_e R^2 \left([Ag]\big/\varepsilon\right)}{D[Ab]_{surf}} = \frac{\text{penetration time}}{\text{catabolism time}} \qquad\qquad 2.12$$

From an engineering perspective, this is a zero-order Thiele modulus. The high affinity antibody saturates the antigen, so the zero order rate constant is the endocytosis rate multiplied by the antigen concentration. The shape factor is not included, although it is a 6 in the denominator for a sphere (Appendix Section 5a.ii) and is lumped into the surface concentration for a cylindrical annulus (Appendix Section 5b.ii). The Thiele modulus is defined as the square root of this ratio since this dimensionless number appears directly in the first order solution, where it was first applied historically (see reference(76) and Appendix Section 8a.iii).

When the value of the Thiele modulus is greater than one, endocytic consumption is faster than transport into the tissue, and antibody will not reach the distance R. If the value is less than one, then transport is faster than internalization on the cells, and antibody will target this distance. This concept is illustrated in figure 2.7.
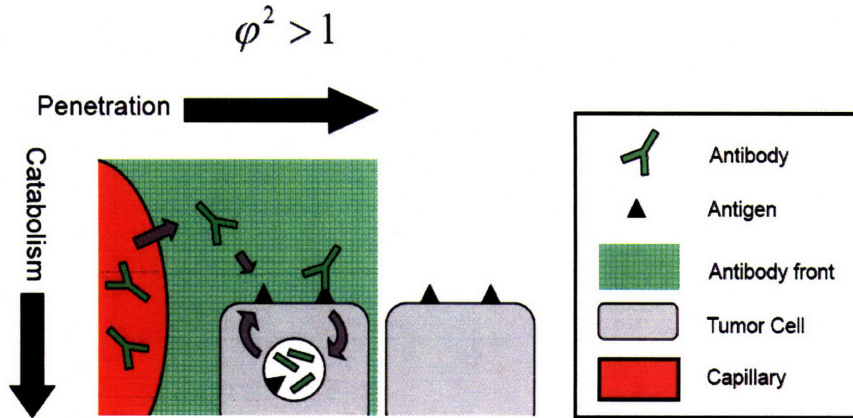
Figure 2.7 – Thiele modulus in sub-saturating conditions. With a constant or slowly clearing agent, there is a continuous supply of antibody entering the tissue. As it binds to its target, the complexes will be internalized at a rate dependent on the antigen. Newly synthesized or recycled antigen will replace the complex on the surface, providing a continuous route of local clearance. If the rate that the antibody is catabolized is equal to the rate it enters the tissue, the antibody front will not be able to progress past this distance.

Knowing the Thiele modulus is approximately one at the maximum targeted distance, this value can be determined by setting the modulus equal to one and solving for the radius of penetration.

$$R \approx \sqrt{\frac{D[Ab]_{surf}}{k_e([Ag]/\varepsilon)}} \qquad\qquad 2.13$$

The penetration distance into the tumor tissue can be increased by using larger doses or a smaller molecule with a faster diffusion coefficient. The target antigen also plays a critical role by determining the concentration in the tissue as well as the endocytsosis rate. More slowly internalized antigens will allow better penetration, but this may be detrimental for therapies that require internalization, such as immunotoxins.

To validate the analytical scaling analysis, numerical simulations were carried out with a constant plasma concentration. The dose was varied to change the Thiele modulus value, and the fraction of antigen saturated at a distance of 100 μm was monitored to determine saturation. Figure 2.8 shows that the antigen is saturated when the Thiele modulus approaches one. The lower graphs indicate the dose and concentration required to target a particular distance with different internalization rates in mouse and man.
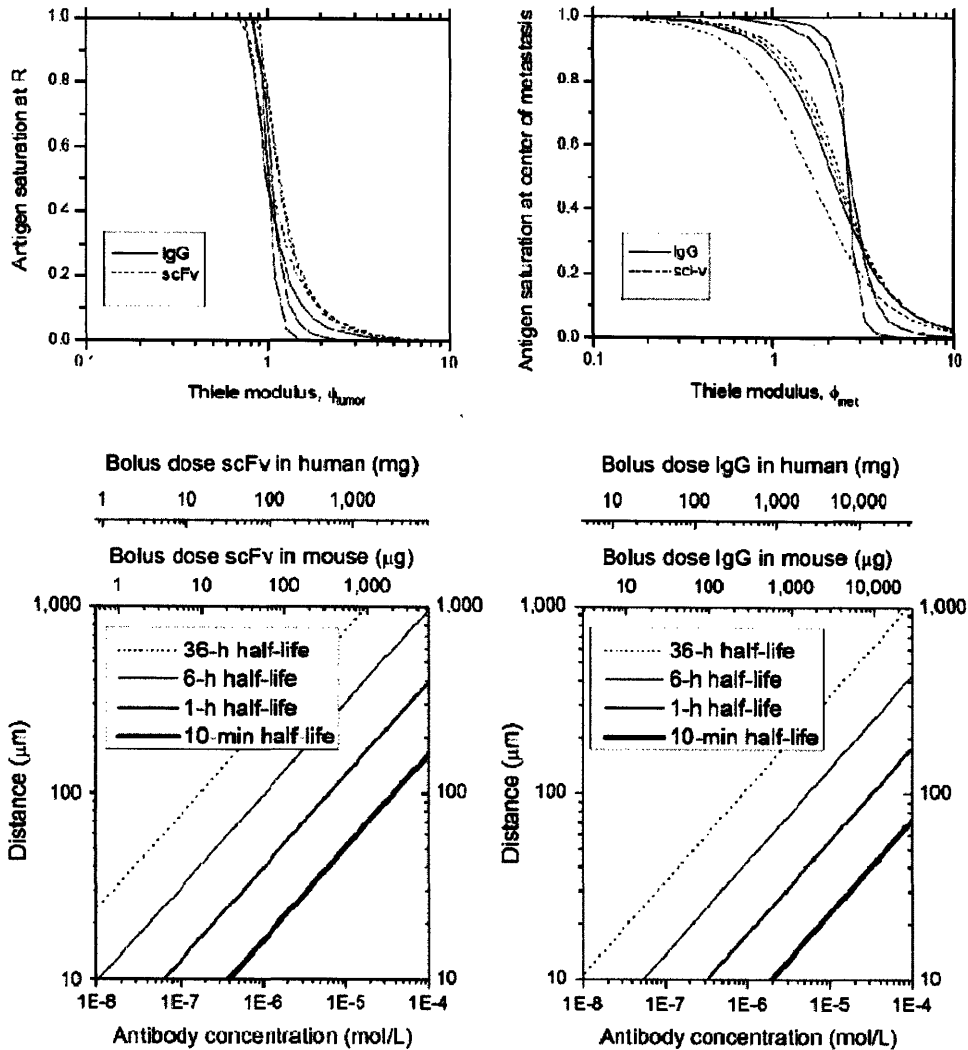
Figure 2.8 – Thiele modulus simulations. Numerical simulations examining the distribution of IgG and antibody fragments using a Krogh cylinder (top left) or spherical metastasis (top right) were performed with constant plasma concentrations and non-zero internalization rates (Appendix section 2 equations). As the Thiele modulus drops below one, the antigen at a 100 μm radius becomes saturated. Typical parameter values were used for the simulations(75). Using the Thiele modulus, the maximum distance of penetration based on cellular internalization and degradation is shown for an scFv (bottom left) and IgG (bottom right) by setting the modulus equal to one. Even for a 6 hour half life on the surface, doses in humans are exceedingly large.

It is important to note that the clearance modulus and Thiele modulus deal with two separate limitations to uptake. When developing the clearance modulus, it was assumed that there was no internalization on the cell surface, and when deriving the Thiele modulus, there was no clearance from the plasma. In targeting scenarios, both systemic and local clearance occur simultaneously, making the requirements even more stringent for saturation. Numerical simulations are able to show how the

values change under these more realistic conditions. Figure 2.9 shows a contour map of the Thiele and clearance modulus when both internalization and plasma clearance occur together. Only in the region to the lower left is the antigen saturated.
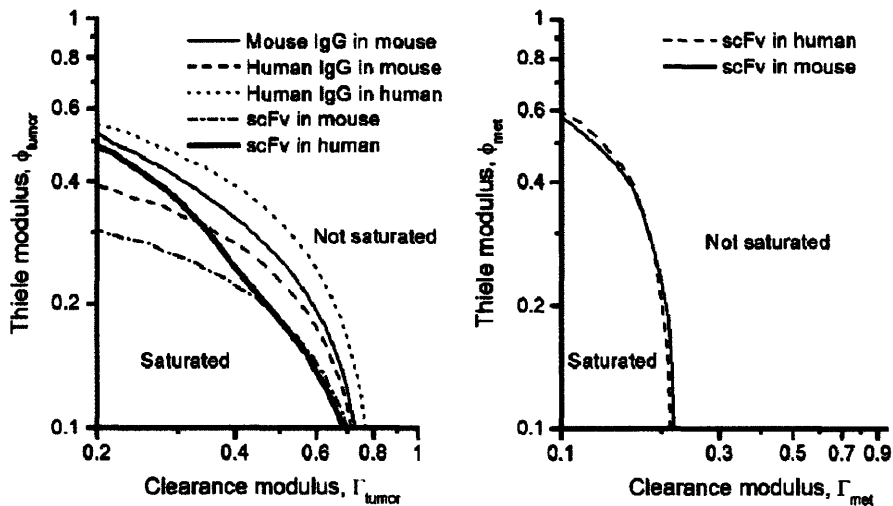

Figure 2.9 – Saturation with both systemic and local clearance. A contour plot shows the values required to saturate 95% of the antigen at a given distance in a solid tumor (left) and micrometastasis (right) using a numerical simulation (Appendix section 2 equations) where both local and systemic clearance occur. The antibody concentration (dose) was changed to vary the value of the clearance modulus, and the internalization rate was varied to independently change the Thiele modulus.

To compare the model predictions for the Thiele modulus with experimental data, studies that were minimally affected by clearance were chosen. Two published papers looking at anti-HER2 scFv and IgGs were examined. Independent estimates for the various parameters were obtained from the literature (table 2.2). In the first paper(14), the kidney's were removed to eliminate the rapid renal clearance found with these small scFvs. For the second paper(77), multiple doses of the slowly cleared IgG maintained an elevated plasma concentration through the study.

47

Parameter	Adams et al.	Baselga et al.	References
Model	Nephrectomized Mouse Xenograft	Multiple Dose Mouse Xenograft	
R	'300 µm'	100 µm	(13)
K_d	15 pM	5 nM	(14), (77)
R_{cap}	5 µm	10 µm	(21, 36)
D	80 µm^2/s	14 µm^2/s	(25)
P	5x10^{-9} m/s	3x10^{-9} m/s	(36)
Ag	0.15 µM	0.13	(29, 77, 78)
epsilon	0.3	0.1	(79)
Ab	2 µM	varies	2 mL plasma volume or 78 mL/kg for mice; 3.5 L for human
$k_{endocytosis}$	2.2x10^{-4} /s	2.2x10^{-4} x 0.15 = 3.3x10^{-5} /s	(40, 74, 80)

Table 2.2 – Literature parameters for model comparison with experimental data

A sample histology image of a high affinity scFv was given by Adams et al. on anephric mouse xenografts. The numerical simulation shows a high concentration near the capillary, marked in yellow, with a rapidly falling concentration with increasing radius. Setting the Thiele modulus to one and solving for the radius, the scFv is predicted to target a distance less than 40 µm. To get a more quantitative estimate of the experimental radius of penetration, the intensity of the red channel was measured in concentric rings around the capillary. This was normalized to the highest intensity red signal in the image. The experimental fractional saturation matched closely to what was predicted by the model, although there are fluctuations due to the series of cell layers around the capillary (figure 2.10).
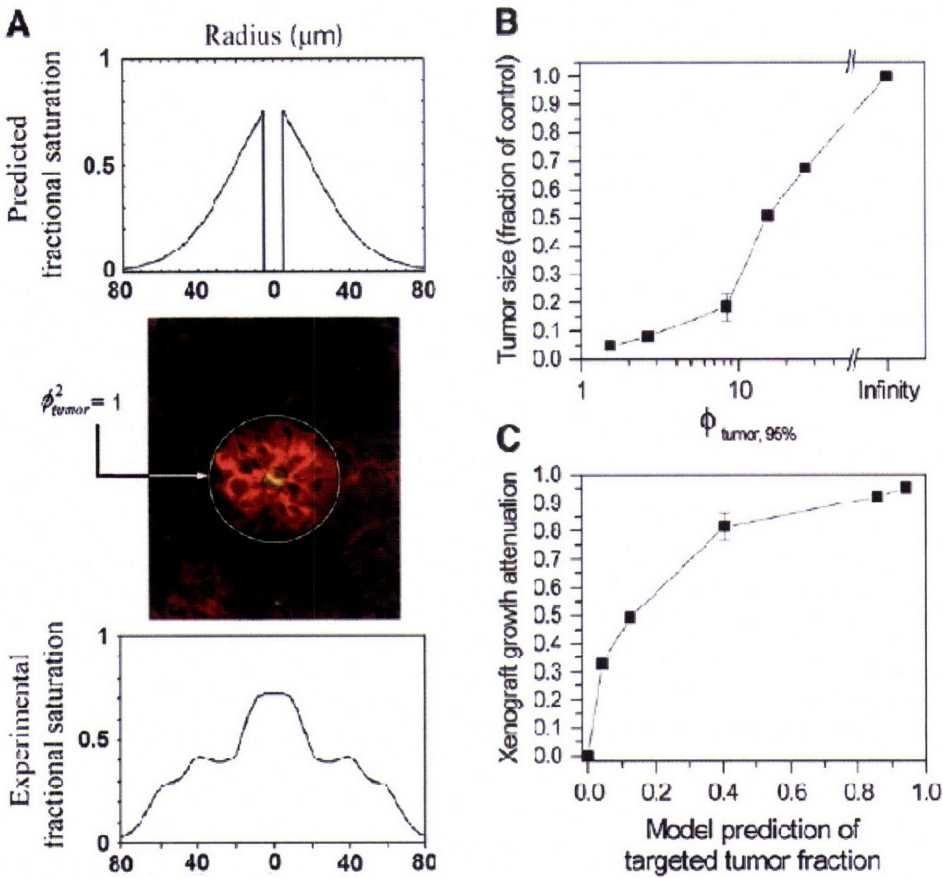
Figure 2.10 – Model comparison to experimental data. A comparison of the model numerical simulation using Appendix section 2 equations (A – top), histological image (A – middle), and image analysis of the antibody staining (A – bottom) is shown on the left. In the image, the capillary is in yellow, the scFv is in red, and the green circle defines the limit of penetration given by setting the Thiele modulus to one. The tumor size of an anti-HER2 IgG (trastuzumab) treated xenograft is plotted versus the Thiele modulus. This is using a conservative estimate of 100 μm for the Krogh cylinder radius (B). Using measured values of the maximum intercapillary distance(13) and the penetration distance given by setting the Thiele modulus to one, the growth attenuation is plotted versus the targeted tumor fraction (C). More details can be found in reference(75).

Model predictions were also compared with anti-HER2 antibody (trastuzumab) treated xenografts. The mice received multiple injections of antibody over the course of the experiment to maintain elevated plasma levels. The tumor volume was then measured for mice treated at various doses. The results are shown in figure 2.10. As the dose is increased, the Thiele modulus drops, and tumor size decreases. Using a conservative estimate of 100 μm for the maximum Krogh cylinder radius, the tumor size approaches zero as the Thiele modulus approaches 1. Baish et al. have measured the maximum distance between vessels in solid tumors(13). Using these values and the maximum radius of penetration given by the Thiele modulus, the growth attenuation (control tumor size minus experimental tumor size normalized to the control) is plotted. As the fraction of the tumor that is

targeted approaches 100%, the tumor size approaches zero. This demonstrates the relationship between the Thiele modulus, targeting, and therapy in this system.

2.7   Micrometastases versus Vascularized Tumors

Antibodies are used to treat both bulk tumors and residual disease(5, 81), which involves targeting prevascular metastases and vascularized tumors. For micrometastases, the only uptake occurs from the surrounding tissue through the surface of the cancer cell mass. In solid tumors, uptake can occur from the outer surface, but the smaller surface area to total tumor volume causes uptake from the tumor vasculature to dominate in most cases.

The normal tissue surrounding a micrometastasis is well vascularized, with normal convection occurring via Starling's hypothesis as well as diffusive transport. The healthy cells are directly adjacent to the cancer cells, so there are no barriers to uptake from the surface. The lack of binding in the normal tissue means adequate free antibody is available to diffuse in from the surface. The concentration in the normal tissue is therefore the appropriate surface concentration. Using a two-compartment model for the plasma and normal tissue concentration:

$$[Ab]_n = [Ab]_{plasma,0}\left(\kappa\left(\frac{Ae^{-k_\alpha t}}{\gamma-k_\alpha}+\frac{Be^{-k_\beta t}}{\gamma-k_\beta} \right) - \kappa\left(\frac{A}{\gamma-k_\alpha}+\frac{B}{\gamma-k_\beta} \right)e^{-\gamma t} \right) \qquad 2.14$$

where κ is the capillary extravasation coefficient for normal tissue, and γ is the lymphatic drainage constant for normal tissue. This provides the concentration surrounding the metastasis as a function of time. For micrometastases, the surface concentration is:

$$[Ab]_{surf} = \frac{\kappa}{\gamma}[Ab]_{plasma} \approx [Ab]_{plasma} \qquad 2.15$$

when the normal tissue concentration equilibrates with the plasma concentration over time.

For vascularized tumors, the situation is very different. Here, the antibody must cross the tumor capillaries directly into the tumor tissue. Whereas in the micrometastasis case, multiple capillaries surrounding the vessel could contribute to the surface concentration as antibody diffuses without binding in the normal tissue, here each vessel is isolated. The capillary wall is made up of an endothelial

50

sheet that separates the blood in the lumen from the tissue outside. Since these large hydrophilic molecules cannot cross the plasma membrane, they must diffuse between the cells or through fenestrations. Fortunately, the action of VEGF and other signaling molecules increases the permeability of these vessels.

The antibody concentration just outside the capillary vessel is dependent on the rate of extravasation and the rate of diffusion away from the wall. The flux of antibodies (mol per surface area per time) can be defined using the permeability(35):

$$flux = \frac{P}{\varepsilon}\left([Ab]_{plasma} - [Ab]_{surf}\right) \qquad 2.16$$

where P is the permeability and $[Ab]_{surf}$ is the concentration just outside of the capillary. From an engineering perspective, the permeability is simply a mass transfer coefficient for the blood vessel wall. The extravasation time for the tumor will be equal to the permeability multiplied by the surface area for extravasation divided by the tumor volume. This average value, expressed in terms of a Krogh cylinder is:

$$\text{Extravasation time} = \frac{\pi R^2 L}{2\pi R_{cap} L \cdot P} = \frac{R^2}{2PR_{cap}} \qquad 2.17$$

Antibody will be diffusing away from the capillary wall to the binding/reaction front according to the rate of free diffusion:

$$\text{Diffusion time} = \frac{R^2}{D} \qquad 2.18$$

The ratio of these two times provides an estimate of whether antibody uptake is limited by extravasation or diffusion in the tumor. This is known as the Biot number, which is a ratio of internal to external transport limitations in a multiphase system(82):

$$Bi \equiv \frac{2PR_{cap}}{D} = \frac{\text{Diffusion time}}{\text{Extravasation time}} \qquad 2.19$$

For large values of the Biot number, the diffusion time is much slower than extravasation, so the surface concentration of antibody will be roughly equivalent to the plasma concentration. For very small values, diffusion away from the capillary wall is much faster than extravasation, resulting in

51

surface concentrations well below the plasma concentration. Using values measured *in vivo* with xenograft tumors, the permeability for an IgG is approximately 3×10^{-3} μm/s(36), the capillary radius, which is slightly larger than those found in healthy tissue, is approximately 10 μm(21), and the diffusion coefficient is roughly 14 μm^2/s(25). The Biot number is therefore 0.004 for an IgG. This value, which is much less than one, indicates that extravasation is limiting in solid tumors, and the surface concentration will be much less than the plasma concentration.

The surface concentration can be expressed as a function of the Biot number and the plasma concentration. By scaling the boundary condition at the capillary wall (see Appendix Section 5b), the surface concentration for a solid tumor is:

$$[Ab]_{surf} = \frac{[Ab]_{plasma}}{\left(1 + \frac{1}{Bi}\right)}$$

2.20

This same result is obtained when scaling the capillary wall conditions by examining the clearance modulus with a high affinity antibody, using a total mass balance for the Thiele modulus, and looking at transport in an infinite medium around a cylinder, which allows the restrictions on binding and diffusion to be relaxed (Appendix Sections 6a, b, and c). To further confirm this relationship, numerical simulations were carried out varying all 3 parameters in the Biot number. As long as antibody does not reach the outer radius, the relationship holds (see Appendix Section 6d).

For the very small Biot numbers found in solid tumors:

$$[Ab]_{surf} \approx Bi[Ab]_{plasma}$$

2.21

When plugging this into the clearance and Thiele modulus for high affinity binders, the diffusion coefficients cancel out, leaving the permeability as the limiting factor. Conceptually, it is important to note that since permeability is limiting, the concentration that tumor cells are exposed to is several orders of magnitude less than that found in the plasma. This is often difficult to directly observe, since binding can increase the total concentration (bound plus free antibody) to very high levels due to high antigen concentrations. If a 1 μM dose is given in the plasma, the free antibody concentration outside the capillary may only be 1-10 nM. However, a high affinity binder could saturate a 1 μM antigen, giving a much higher overall signal. A qualitative way to confirm this result is to examine non-binding fluorescently tagged molecules at early times after delivery. When extravasation is limiting, the

concentration in the plasma is much higher than the concentration just outside the vessel, as seen with *in vivo* imaging(83). If diffusion were limiting, the fluorescence intensity would decay at some distance outside of the capillary, not all at the vessel wall.

Another important point to note is that with this low permeability, not much antibody extravasates from the blood. This means that the concentration is not depleted along the length of the capillaries in the tumor. In fact, in an isolated tumor perfusion study, albumin was used as a "non-extravasating" tracer since the concentration leaving the tumor is virtually identical to that entering in this experimental setup(18). (Note this is not the case for small molecules and oxygen.) This justifies ignoring gradients along the length of the capillary.

The above analysis shows that permeability is the limiting factor in transporting large hydrophilic molecules to vascularized tumors. It is important to contrast this with oxygen and small molecules in solid tumors. There are four major steps in the delivery of molecules from the circulation. The molecules must: 1) flow to the tumor, 2) extravasate across the vessel wall, 3) diffuse in the tissue, and 4) bind/react at the given site within the tissue. For oxygen, poor blood flow caused by transient cessation and unsteady flow force the oxygen tension to drop along the length of vessels (transient hypoxia). This is a limit in the first step described above. In poorly vascularized areas, the distances between vessels are so large that the diffusion of oxygen cannot reach all the tissue, regardless of the blood flow in the vessel. This occurs in areas of chronic hypoxia and is a limitation in the 3rd step above(19). While extravasation is limiting for large macromolecules, this step is often not discussed with oxygen transport because it appears to limit oxygenation. In contrast to macromolecules, which show sharp differences between the vascular concentration and interstitial concentration, oxygen profiles do not show a large drop outside the vessel(84). An example where the last step, i.e. binding/reaction, is limiting would be oxygen transport in well-oxygenated normal tissue. Here, blood flow is sufficient, transport across the endothelial wall occurs very quickly, and the vascular spacing is close enough that diffusion is adequate for oxygen to reach all the tissue; this is not the case in solid tumors. When examining uptake of small molecule drugs, Heijn et al. found that a diffusion limitation (step 3 described above) best described the experimental data(18). The blood flow and estimated permeability were much higher than the measured uptake in the tumor, yet not all the cells were targeted, which rules out limitations by steps 1, 2, and 4 respectively and implicates diffusion limitations. In a previous experiment, Jain et al. found that blood flow is sometimes limiting(85).

2.8 Effect of Affinity on Targeting

a. Antibody Distribution

Up until now, only the distribution of high affinity binders has been considered. This was defined where the affinity of the antibody was higher (i.e. the K_d was lower) than the antibody concentration in the tumor. IgGs and other multivalent binders typically behave like high affinity antibodies, since their multiple binding sites allow quick reattachment after any single site dissociates. For example, an scFv with a 320 nM dissociation constant can exhibit an effective affinity in the pM range when it is reformatted as a (bivalent) IgG due to avidity(86). Protein engineering techniques such as directed evolution using phage and yeast surface display have created high affinity binders with picomolar K_d values and generated families of antibodies with a range in affinities(39, 87), so it is important to understand the role of affinity in distribution and uptake.

The affinity of an antibody for its target is important in determining both its microdistribution and retention in a tumor. Experimental (14, 88, 89) and theoretical analyses (26, 29, 90) have shown that lower affinity antibodies have a more homogeneous distribution in tumor tissue. Antibodies typically have fast association rates, so it is primarily the dissociation rate that determines the overall affinity(39). The better penetration and more homogeneous distribution of lower affinity antibodies is due to their ability to dissociate from the antigen and diffuse farther in the tissue (see figure 2.3). This has associated costs, however. Since permeability is independent of antigen binding, and this is the limiting step in uptake, lower affinity does not increase the amount of antibody that enters the tumor, it only affects the distribution in the interstitium. The affinity does affect the retention in the tumor, however, so lower affinity antibodies may not be retained as long as high affinity binders. This occurs through intravasation of free antibody or loss from the tumor surface. This loss is not as significant for vascularized tumors as it is for micrometastases, since the low permeability not only limits uptake in the tumor but also slows the loss of unbound antibody as well.

The affinity at which an antibody transitions from a high affinity binder with a saturation front to a low affinity binder with gradual or undetectable gradients in the tissue can be predicted based on theoretical considerations. With their fast association rate, both high and low affinity antibodies bind quickly when they contact unbound antigen. High affinity and/or multivalent antibodies become irreversibly immobilized if the internalization rate of the antigen is faster than the dissociation rate ($k_{off} <$ k_e), which is often the case(72). Lower affinity antibodies are able to dissociate prior to internalization

($k_{off} > k_e$), allowing them to diffuse farther in the tissue. The sharp gradient present with high affinity binders is replaced by a more gradual gradient at sub-saturating concentrations from this repetitive binding and dissociation.

With very low antibody concentrations, the amount of antigen bound is linearly proportional to the antibody concentration. This typically occurs in solid tumors, since the low permeability reduces the concentration in the tumor interstitium by several orders of magnitude. Using this assumption, the transport time of diffusion with binding can be calculated. Here, the characteristic time for transport to a distance R (see Appendix 8c.ii) is:

$$t_{transport} = \frac{R^2 \left([Ag]/\varepsilon\right)}{D \cdot K_d} \qquad 2.22$$

where K_d is the equilibrium dissociation constant for the antibody. This is assuming K_d is less than $[Ag]/\varepsilon$, since otherwise the antibody would behave as a non-binder (with the dissociation constant larger than both the antibody and antigen concentrations). In the case of a non-binder, the transport time is simply the time for free diffusion, or R^2/D.

Incorporating the transport time for a low affinity binder compared to the clearance time, the clearance modulus for a low affinity antibody becomes (Appendix 8c.ii):

$$\Gamma \equiv \frac{R^2 \left([Ag]/\varepsilon\right)}{D([Ab]_{surf} + K_d)\left(\dfrac{A}{\alpha} + \dfrac{B}{\beta}\right)} \qquad 2.23$$

If the K_d is small, the clearance modulus reverts to the high affinity case. When K_d is much larger than the surface concentration, the surface concentration can be ignored, giving the ratio between low affinity penetration time and clearance time (see Appendix 8b):

$$\Gamma \equiv \frac{R^2 \left([Ag]/\varepsilon\right)}{D \cdot K_d \left(\dfrac{A}{\alpha} + \dfrac{B}{\beta}\right)} \qquad 2.24$$

In this case, the continuous binding and dissociation may be able to yield a homogenous distribution. It is important to note that this does not mean the tissue is saturated. It only means that antibody will be

able to reach the distance R. Even with a large K_d, if the dose is high enough that $[Ab]_{surf}$ is greater than K_d, the tissue will be saturated layer after layer, since the saturation front moves through the tissue faster than the low affinity antibodies can bind, dissociate, and diffuse. It is therefore the larger value of these two values, not an absolute value of either, that matters. Figure 2.11 illustrates the antibody concentration surrounding a capillary as a function of time with a clearance modulus of 10 and 0.1 for a low affinity binder. The contour lines extended outward for the value less than one, indicating antibody reaches the outer distance R. However, looking closely at the scale, the concentration is sub-saturating throughout the tissue even though the dose is identical.
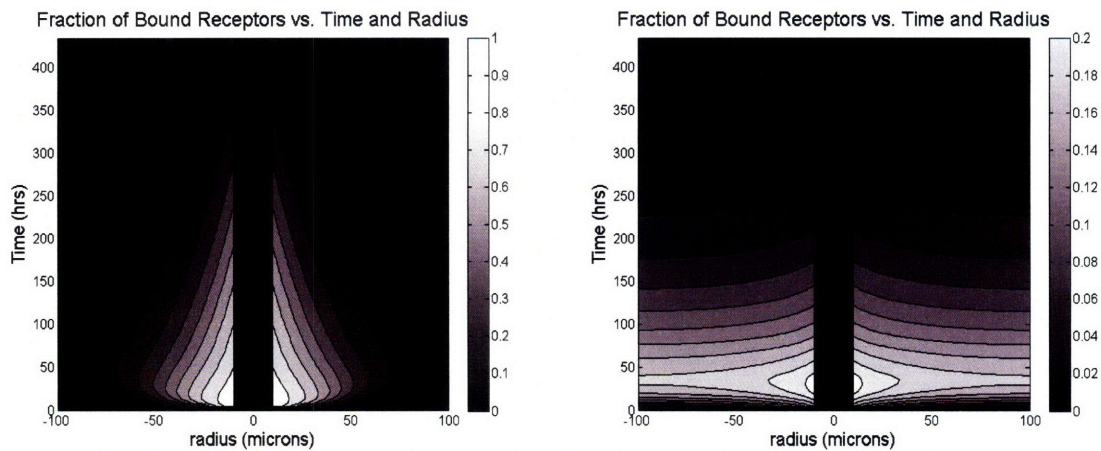

Figure 2.11 – Clearance modulus for a low affinity antibody. A contour plot of antibody concentration is shown for a numerical simulation (Appendix section 2 equations) in a Krogh cylinder with the capillary in the center. The graph on the left shows an antibody where the K_d is too small to lower the clearance modulus below one; using K_d in the denominator, the clearance modulus is 10. This results in a heterogeneous distribution, shown by the high concentration near the center (capillary) and low concentrations at the outer edge of the Krogh cylinder. The graph on the right illustrates an antibody where the clearance modulus drops to 0.1 due to the larger K_d. The contour lines extend to the outer edge of the Krogh cylinder, showing an equal concentration as a function of radius. Note the change in scale between the two graphs, since lower affinity antibodies achieve less fractional saturation of antigen. The parameter values are: D = 14 $\mu m^2/s$, k_{on} = 10^5/Ms, R_{Krogh} = 100 μm, [Ag] = 300 nM, $[Ab]_{plasma}$ = 3 μM, ε = 0.1, R_{cap} = 10 μm, P = 3×10^{-3} $\mu m/s$, k_e = 1.3×10^{-5}/s, clearance values were for a human IgG in human(75), and the affinity is varied.

Similar to the case for clearance, the Thiele modulus for antibodies becomes (Appendix 8c.i):

$$\varphi^2 \equiv \frac{k_e R^2 ([Ag]/\varepsilon)}{D([Ab]_{surf} + K_d)}$$

2.25

In the case of the general Thiele modulus, a low affinity results in less antigen bound by antibody as it internalizes. This lowers the level of endocytic consumption, allowing a more homogeneous distribution. When K_d is much greater than $[Ab]_{surf}$, the solution becomes (Appendix 8a):

$$\varphi^2 \equiv \frac{k_e R^2 ([Ag]/\varepsilon)}{D \cdot K_d}$$

2.26

This expression is a first order Thiele modulus, and the solution in a sphere can be found exactly (Appendix 8a.iii). When this value is less than 1, antibody will reach all the cells in the tissue. However, it does not mean that all the cells are saturated, just that some antibody has reached the center. This is shown graphically for a Krogh cylinder in figure 2.12.
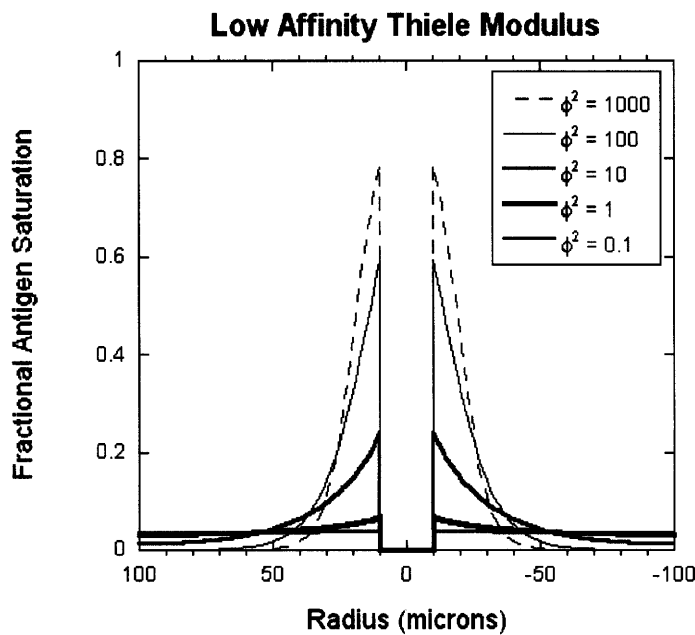

Figure 2.12 – Thiele modulus for a low affinity antibody. The steady state distribution for antibodies with decreasing affinity is shown with their corresponding Thiele modulus values for a numerical simulation (Appendix section 2 equations). As the K_d value increases, the Thiele modulus drops below one, fractional saturation decreases, and the distribution reaches a homogeneous level throughout the Krogh cylinder. The parameter values are: D = 14 $\mu m^2/s$, k_{on} = 10^5/Ms, R_{Krogh} = 100 μm, [Ag] = 500 nM, $[Ab]_{plasma}$ = 500 nM, ε = 0.1, R_{cap} = 10 μm, P = 3×10^{-3} $\mu m/s$, k_e = 1.3×10^{-5}/s, and the affinity is varied.

For antibodies that bind slowly, the binding modulus, as given before, indicates whether the antibody will distribute homogeneously in the tissue, whether it is limited by catabolism (Appendix section 8a.i) or clearance (Appendix 8b.iv). This is assuming free diffusion is faster than clearance, which is generally the case.

b. Antibody Saturation

It is very important to note that these moduli for low affinity binders do not indicate that the antigen is saturated to the given distance. It only indicates that binding does not prevent the molecules from reaching that distance. In general, this means the fraction of antigen bound by antibody on each cell will be less than 100%. When compared to clearance, the fraction of free antibody is increased, allowing it to diffuse deeper in the tissue. For catabolism, less antibody is bound to the cell surface, lowering the amount that is internalized and catabolized. From a chemical engineering perspective, a first order Thiele modulus only means the concentration throughout the tissue is equal to the surface concentration, and if this is a sub-saturating concentration, then none of the tissue is saturated.

The importance of the fractional saturation of antigen on each cell depends on the application. Therapeutic effector functions that require high receptor occupancy such as signal inhibition and ADCC may be ineffective when combined with sub-saturating low affinity binders(91), while potent therapeutics such as alpha emitter radionuclides and some immunotoxins may be able to kill the majority of cells with delivery of a small number of antibody molecules (86, 92, 93).

In general, the fraction bound in the tissue scales as:

$$\frac{[B]}{[Ag]} = \frac{[Ab]_{surf}}{\dfrac{k_{off}+k_e}{k_{on}}+[Ab]_{surf}}$$

2.27

For most antibodies, the binding rate is much faster than internalization at typical doses, so:

$$\frac{[B]}{[Ag]} \approx 1$$

2.28

With low affinity antibodies, where $k_{off} \gg k_e$:

$$\frac{[B]}{[Ag]} = \frac{[Ab]_{surf}}{K_d+[Ab]_{surf}}$$

2.29

If the antibody binds slowly, where $k_e \gg k_{off}$:

$$\frac{[B]}{[Ag]} = \frac{k_{on}[Ab]_{surf}}{k_e + k_{on}[Ab]_{surf}}$$

2.30

For slow binding antibodies, the clearance rate must also be taken into consideration (Appendix 8b.iv). These concentrations provide an estimate for the fraction of antigen bound on the *targeted cells*. It is important to differentiate this from the total fraction of antigen bound in the *tissue*. For example, with a high affinity antibody, the expression above indicates that 100% of the antigen is saturated. This is valid for the cells within the reaction/binding front. Beyond this distance, none of the antigen will be bound, so a low dose may only target 10% of the tumor cells. The fraction of the total antigen in the tissue that is bound is therefore 10%. It is important to specify that this is 100% of the antigen bound on 10% of the cells, not 10% of the antigen bound on 100% of the cells.

Although the low affinity cases were derived assuming a linear binding regime, conceptually, they can also be viewed as the high affinity case adjusted for the fraction of antigen that is bound at saturation (Appendix 8d.i). For instance, multiplying the high affinity clearance modulus by the fraction bound:

$$\Gamma = \frac{R^2([Ag]/\varepsilon)}{D[Ab]_{surf}\left(\dfrac{A}{\alpha}+\dfrac{B}{\beta}\right)}\left(\frac{[Ab]_{surf}}{K_d +[Ab]_{surf}}\right) = \frac{R^2([Ag]/\varepsilon)}{D([Ab]_{surf}+K_d)\left(\dfrac{A}{\alpha}+\dfrac{B}{\beta}\right)}$$

2.31

Similarly for the Thiele modulus:

$$\varphi^2 = \frac{k_e R^2([Ag]/\varepsilon)}{D[Ab]_{surf}}\left(\frac{[Ab]_{surf}}{K_d +[Ab]_{surf}}\right) = \frac{k_e R^2([Ag]/\varepsilon)}{D([Ab]_{surf}+K_d)}$$

2.32

From this perspective, it is easier to see why the transition occurs slowly from the high to low affinity cases. Another useful construct is a more dynamic view of lower affinity antibodies (Appendix 8d.ii). The linear binding regime yields the low affinity transport time from an equilibrium standpoint, but the same result can be derived by more heuristic means. The characteristic distance an antibody diffuses before binding is given when the binding modulus approaches one. With a fast dissociation rate, the antibody is able to release before being internalized and can diffuse deeper in the tissue. The time required to 'reach' a certain distance is simply the distance the antibody travels on each 'jump' multiplied by the waiting period for the antibody to dissociate between each 'jump.' This waiting period

is given by the dissociation rate of the antibody. (See figure 2.3.) The transport time for a low affinity antibody is then:

$t_{transport}$ = (number of jumps to distance R)(time per jump)

$$t_{transport} = \left(\frac{k_{on}\left(\frac{[Ag]}{\varepsilon}\right)R^2}{D} \right)\left(\frac{1}{k_{off}} \right) = \frac{\left(\frac{[Ag]}{\varepsilon}\right)R^2}{K_d \cdot D}$$

2.33

c. Antibody Retention

The affinity of an antigen for its target not only affects the distribution in the tissue, but also the retention. While the affinity does not have a major impact on the amount of antibody entering tumor tissue, its affect on the retention time can ultimately determine the uptake at the time of measurement. Several groups have demonstrated this tradeoff experimentally showing increased tumor uptake with increasing affinity in a variety of tumor models (88, 94-96), although this increase plateaus at very high affinities (14).

The retention of high affinity antibodies is ultimately determined by the internalization and catabolism on the tumor cells. With a fast binding rate and slow dissociation, these antibodies are internalized before they dissociate. The fate of the antibody label also becomes important, since this is often used as the measure of the antibody concentration, even if the antibody becomes degraded. For imaging or therapeutic approaches utilizing radiolabeled antibodies, degradation of the antibody frees the radioisotope allowing it to diffuse away from the cell and potentially out of the tumor. This loss can occur on the order of hours for radioiodinated antibodies or more slowly for radiometal conjugates and other residualizing labels (97-101). This phenomenon has been used to determine antibody internalization rates in various organs (102).

Low affinity antibodies are slightly more complicated. The rapid dissociation rate that allows them to distribute more homogeneously also allows them to exit the tissue once the surface concentration drops below that present in the tumor. The lower the affinity, the more rapid they are able to clear from the tissue. There is a distinction between micrometastases and vascularized tumors, however. In the micrometastasis, the surrounding normal tissue clears more quickly than the metastasis due to the functional lymphatics and adequate blood vessel supply. There is no barrier between the

metastasis and normal tissue, so the antibody diffuses out with little impediment. The rate at which the antibody leaves is also proportional to the K_d as given by the transport time above, so antibodies with very little affinity will diffuse out of the tissue at a much faster rate than those with higher affinity. With vascularized tumors, the capillary wall again stands between the plasma and tumor tissue. Assuming that diffusion is the primary cause of transcapillary transport, the low permeability works in reverse. Although there may be a higher concentration of free antibody in the tissue, the rate at which this intravasates and enters the plasma is slow. Therefore, lower affinity antibodies will be retained for a longer period of time in the tumor than in the normal tissue. This enhanced retention, part of an EPR (enhanced permeation and retention) effect is often seen in tumors(103).

The retention of slow binding antibodies is also more complicated than high affinity binders. Here, the relevant rates are the binding rate, trans-capillary transport, and clearance from the plasma. It is assumed that the binding rate is slow enough to yield a homogeneous concentration in the tissue. For sub-saturating concentrations, if the binding rate in the tissue is faster than the transport rate across the endothelium, the antibody will reach equilibrium in the tissue. Formally:

$$\text{If } \frac{k_{on}\left(\left[Ag\right]\middle/\varepsilon\right)R^2}{2PR_{cap}} \gg 1 \tag{2.34}$$

then equilibrium is reached, and a compartmental model (see Chapter 4) can be used. For micrometastases, or if the binding is slower than transcapillary transport, the endothelial barrier is irrelevant, so the competition is between plasma clearance versus binding.

$$\text{If } k_{on}\left(\left[Ag\right]\middle/\varepsilon\right)\left(\frac{A}{\alpha}+\frac{B}{\beta}\right) \gg 1 \tag{2.35}$$

then a significant fraction of the antibody will be retained. Otherwise, the clearance from the plasma occurs before any of the antibody can bind, and it behaves similar to a non-binder. This case is for a sub-saturating dose, so it is assumed the free antigen concentration changes very little, and this is the concentration of interest. If the goal is to saturate the tissue, then antibody must be in excess, and the time-scale for saturation is given by the antibody concentration.

In this case, for a micrometastasis, if $k_{on}[Ab]_{surf}\left(\dfrac{A}{\alpha}+\dfrac{B}{\beta}\right)\gg 1$ 2.36

the tissue will be saturated. Although this section is more concerned with retention than saturation, it is important to note when the antibody or the antigen concentration should be used (Appendix 8b.iv).

2.9   Buckingham Pi Analysis

Dimensional analysis leads to a variety of dimensionless groups that describe the behavior of the system. The Buckingham Pi theorem provides a limit on the total number of independent dimensionless groups that can be formed in a given problem. The theorem states that given n variables (e.g. D, k_e, etc.) formed by k fundamental dimensions (e.g. length), the maximum number of linearly independent Pi groups is (n-k).

The variables that describe this system are k_{on}, k_{off}, D, R, $[Ag]/\varepsilon$, $[Ab]$, R_{cap}, k_e, $t_{clearance}$, P, and t_{sample}. For simplicity, the void fraction has been lumped with the antigen concentration to keep all the concentrations on the same (interstitial) basis, and the clearance parameters A, B, k_α, and k_β were lumped into $t_{clearance}$ since differences between the alpha and beta phases are not explicitly examined. The t_{sample} variable is introduced to emphasize how the time of measurement affects the results. The three fundamental dimensions are length, time, and moles (always as concentration in this analysis). The eight dimensionless groups are given in table 2.3 (Appendix 9).

#	Name	Group	Param.	Ratio
1	Thiele modulus	$\dfrac{k_e R^2\left([Ag]/\varepsilon\right)}{D[Ab]}$	k_e, R, D	$\dfrac{\text{Catabolism rate}}{\text{Penetration rate}}$
2	Clearance modulus	$\dfrac{R^2\left([Ag]/\varepsilon\right)}{D[Ab]t_{clearance}}$	$t_{clearance}$	$\dfrac{\text{Clearance rate}}{\text{Penetration rate}}$
3	Biot number	$\dfrac{2PR_{cap}}{D}$	P	$\dfrac{\text{Extravasation rate}}{\text{Diffusion rate}}$
4	Low affinity number	$\dfrac{R^2\left([Ag]/\varepsilon\right)}{D\cdot K_d\cdot t_{clearance}}$	k_{off}	$\dfrac{\text{Clearance rate}}{\text{Low affinity penetration rate}}$
5	Binding modulus	$\dfrac{k_{on}R^2\left([Ag]/\varepsilon\right)}{D}$	k_{on}	$\dfrac{\text{Binding rate}}{\text{Diffusion rate}}$
6	Geometry ratio	$\dfrac{R}{R_{cap}}$	R_{cap}	$\dfrac{\text{Tumor volume}}{\text{Capillary volume}}$
7	Saturation number	$\dfrac{\left([Ag]/\varepsilon\right)}{[Ab]}$	[Ab], [Ag]	$\dfrac{\text{Antigen conc.}}{\text{Antibody conc.}}$
8	Sampling time ratio	$\dfrac{t_{sample}}{t_{clearance}}$	t_{sample}	$\dfrac{\text{Sampling time}}{\text{Clearance time}}$

Table 2.3 – Buckingham Pi Analysis. Given the 11 parameters and 3 dimensions that define this system, there are 8 linearly independent Pi groups. The name of the group and definition are given in the first columns. The last two columns define the major parameter that is introduced with the particular group, along with the ratio of rates or parameters that the group describes.

These dimensionless groups are linearly independent, but they are not unique. For example, the ratio of the Thiele modulus (defined for a micrometastasis) to the Biot number yields the Thiele modulus in a vascularized tumor. Another important dimensionless group is the pretargeting number:

$$\frac{\phi^2}{\Gamma} = k_e\left(\frac{A}{k_\alpha} + \frac{B}{k_\beta}\right) = \frac{\text{catabolism rate}}{\text{clearance rate}} \qquad 2.37$$

This ratio describes whether catabolism by the cells or clearance from the plasma is limiting saturation of the tissue. The ratio is also has special significance in describing the distribution of antibody after maximum uptake, which is important for pretargeting.

Pretargeting strategies are multi-step therapies. In these types of therapies, a bispecific agent is administered first, such as an antibody where one half binds the cancer antigen and the other half binds a radioisotope (104). Another example is ADEPT (antibody directed enzyme prodrug therapy), where the antibody is conjugated to an enzyme that converts a non-toxic prodrug into a toxic form at the site of the tumor(105). The primary agent is delivered, allowed to target the tumor, then clears from the plasma. A secondary agent, in this case a radioisotope or prodrug, is delivered, which is converted to a toxic drug (for ADEPT) or retained specifically at the tumor site (radioisotope). These therapies combine the specificity obtained by antibodies with the more rapid transport properties of small molecules. For these strategies to work, however, the timing and doses of each agent are important. Experimental results must also be analyzed carefully. For example, if the secondary agent is limiting, the signal in the tumor may appear to be saturated even if the primary agent is given at a sub-saturating dose(106). Mathematical models are very helpful for analyzing these more complicated therapies.

If the pretargeting ratio is small, clearance from the plasma occurs much faster than catabolism in the tissue. After maximum uptake, the antibody will be rapidly cleared from the tissue, leaving all the saturated cells to decay at the same rate (figure 2.13 top). After the concentration in the plasma has decayed sufficiently, the secondary agent can be delivered. At this point, all the targeted cells still retain some antibody at their surface, albeit a lower amount due to decay. If this pretargeting number is greater than one, a different scenario develops. Here, the catabolism rate is so fast, an equilibrium distribution develops with the plasma as it decays (figure 2.13 bottom). The Thiele modulus describes this equilibrium distance. For example, if the antibody targets 40 μm at a 1 μM plasma dose, by the time the plasma concentration decays to 250 nM, the antibody will only be targeting out to 20 μm. Antibody beyond this distance will be completely degraded, whereas cells within this distance will remain saturated due to the supply from the plasma. Since the plasma concentration often needs to reach a certain level before the secondary agent can be delivered (to avoid binding or conversion in the plasma), different strategies are required in the two cases. For a pretargeting number less than one, the largest dose up to saturation of the tumor should be given. This will maximize the number of cells targeted when the secondary agent is delivered. For pretargeting numbers greater than one, a larger dose will not help. Increasing the dose will require a longer waiting period, so the same distance will be

64

targeted once the plasma level drops to the maximum acceptable plasma dose for secondary agent delivery. In this scenario, a clearing agent would be beneficial to artificially increase the clearance after maximum targeting is achieved (107).

$$\frac{\phi^2}{\Gamma} \ll 1$$
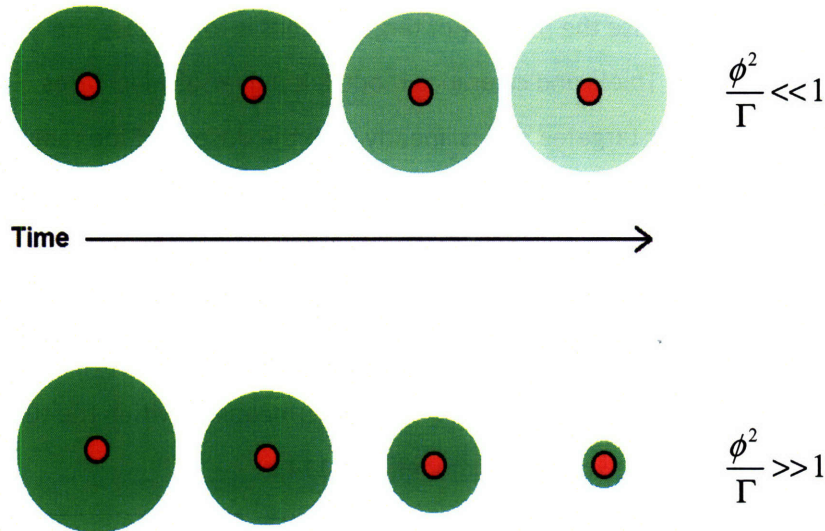
$$\frac{\phi^2}{\Gamma} \gg 1$$

Figure 2.13 – Pretargeting number. The pretargeting number is the ratio between the Thiele and Clearance moduli. This value qualitatively describes the loss of antibody from the tumor. If the value is much less than 1, the antibody quickly clears from the plasma after targeting, and the antibody is degraded evenly over time through the targeted region (top). If, however, antibody catabolism is fast compared to clearance, a pseudo-steady state develops, where antibody in the outer regions is completely degraded, but the slowly decreasing plasma concentration is sufficient to maintain targeting to a shrinking region around the capillary (bottom).

2.10   Methods to Improve Distribution

The dimensional analysis for antibody targeting provides insight into methods to improve spatial distribution. For example, decreasing the Thiele or clearance modulus is predicted to increase the penetration of antibodies in tumor tissue. However, since either systemic clearance or endocytic clearance can limit uptake, reducing one parameter may be insufficient. For example, if endocytic uptake is limiting, saturation cannot be achieved by increasing the plasma circulation alone. The small Biot number highlights a major reason why vascularized tumors are more difficult to target than residual disease. In fact, Minchinton and Tannock pointed out that trastuzumab, when used as an adjuvant

therapy, reduces recurrence by 50%, whereas only 25% of women with advanced disease respond(5). Several of the more important parameters that can improve spatial distribution are discussed below.

a. Antibody Dose

One of the most direct approaches to increase the number of targeted cells is to increase the antibody dose. Since this appears in both the Thiele and clearance moduli, it universally increases uptake in the tumor. The fraction of the tumor targeted scales linearly with the dose (and the radius of targeting scales by the square root due to geometry). Several groups have demonstrated that the uptake is approximately linear until saturation is reached(108-111). The %ID/g remains constant until all available binding sites are taken, then decreases as antibody with no available binding sites is cleared faster from the tumor(110, 111). High doses also show better spatial distribution and increased homogeneity(89, 112). These doses are often very large due to the poor permeability within the tumor, requiring several hundred micrograms in a mouse xenografts model(113, 114).

Naked antibody has a high maximum tolerated dose (MTD), and it is administered in multiple grams per kilogram of body weight during IVIG therapy(115, 116). Unfortunately, this is often impractical for cancer therapy, due to conjugated toxins or radioisotopes, which drastically lower the MTD(117). The cost of highly pure monoclonal antibodies can also be limiting(118).

For imaging applications, increasing the dose is not always useful. While targeting larger fractions of cancer cells increases the signal, this is typically offset by the increased background from the plasma and normal tissues(119). Highly sensitive detection methods, such as PET, lower the requirement for the minimum amount of targeting. The signal to noise ratio is more important for imaging, so increased tumor retention and faster plasma and normal tissue clearance is often more critical.

b. Antigen Selection

Antigen selection influences several factors in antibody distribution and therapeutic efficacy, including the distribution and concentration of the antigen in the tissue, internalization kinetics, and tumor specificity. High antigen concentrations reduce the distance antibody penetrates in tumor tissue, as seen by the Thiele and clearance moduli. Antigens expressed at lower levels would therefore be targeted more uniformly. However, these levels may be insufficient for the therapeutic effect; the flux into the cell may be too low for antibodies that must be internalized, such as immunotoxins. Ideally the

amount on the cell surface would be just above the threshold for cytotoxicity. In some instances, antigen heterogeneity results in some cells expressing little antigen, even if saturation is achieved(120). The level of antigen expression is also important for Fc effector functions, since even ADCC requires a minimum amount of antibody on the surface(86, 121). More potent therapeutics will be able to successfully target and treat cells with lower antigen expression levels. Alternatively, targeting multiple cancer antigens or using therapies with bystander effects may improve therapy(122, 123).

The rapid internalization of some antigens limits their penetration into the tissue as well as their retention on targeted cells. The surface concentration is important for pretargeting therapies and ADCC, where the Fc region must interact with effector cells(121). Antibodies against more stable antigens, such as tight junction proteins, extracellular matrix components, or trapped necrotic debris(124) may be ideal for targeting. Antibodies that effectively recycle can reduce the amount of endocytic consumption (see Appendix 14 and (124)), and some antibodies downregulate the amount of surface antigen, effectively reducing the antigen concentration(125). While slower internalization rates are beneficial to the distribution of antibodies, there may be trade-offs with antibodies that must be internalized. These trade-offs have been considered in previous mathematical models(28).

The specificity of antigen for neoplastic tissues is also an important issue. Some cancer antigens are expressed in normal tissues or shed into the plasma(126), which can not only change the systemic clearance but may also cause dose-limiting side effects in other organs. These regions are often targeted quickly due to healthy vascular structure and convective flow in normal tissues. This can be exploited by delivering a large dose of 'cold' or unlabeled antibody to initially saturate these plasma and/or normal tissue binding sites prior to delivery the toxic load for the tumor(127, 128).

c. Systemic Clearance

For many antibody fragments, clearance from the plasma severely restricts uptake in the tumor. Reducing this rate would allow more time for antibody to extravasate in the tumor. This is a major reason why long circulating molecules, such as IgGs have high uptake levels, on the order of 20-40 %ID/g (51, 129, 130), whereas small fragments have much lower concentrations, around 1-5 %ID/g (48, 49, 51, 130, 131).

Several methods have been employed to increase plasma retention. This includes attaching polyethylene glycol (PEG) to increase the molecular size above the roughly 50-60 kDa limit for kidney

filtration(131-133). Similarly, attaching albumin to anti-Her2 targeting Fab fragments reduced plasma clearance, increased total tumor uptake, and improved distribution(15). In a systematic manner, Kenanova and colleagues demonstrated a direct relationship between serum persistence and tumor uptake using a series of scFv-Fc constructs with Fc mutations to manipulate the systemic clearance(134).

There are trade-offs with increasing antibody size. Therapeutics that are directly conjugated to toxic moieties may exhibit higher systemic toxicities with longer plasma circulation times(135, 136). Smaller fragments have large void fractions and higher diffusivities, allowing better penetration in the tissue(137). For solid tumors, these smaller fragments also show a small but significant increase in the permeability across the vessel wall(83). Plasma clearance is typically beneficial for imaging agents as well, since it reduces the background in normal tissues. Clearance that is too rapid reduces the specific signal, however, so Wu and colleagues explored optimal fragment sizes to obtain the best signal to noise ratio (138, 139).

d. Increasing Transcapillary Flux

A major limitation for solid tumors is the rate at which antibodies escape the blood vessels to enter the interstitium. The slow extravasation rate causes slow localization of the antibodies, results in the surface concentration being several orders of magnitude below the plasma concentration, and limits the total amount of antibody taken up by the tumor. Increasing the transcapillary flux would also likely increase clearance from unbound antibody in the tumor, lowering the EPR effect and increasing specificity mediated by binding.

Some intrinsic properties of the antibody affect the permeability across the vasculature. One of the most important is the antibody size. Smaller fragments have increased permeabilities, although molecular shape is likely to play a role(83). The capillary endothelium also has a negative charge, so antibody charge is an important factor(34, 140, 141). Positively charged molecules may help, but these may also clear more rapidly, accumulating in the kidney or liver(142, 143).

The properties of tumor vasculature ultimately determine the permeability of the endothelial structure. Permeability enhancing cytokines such as VEGF, IL-2, and TNF increase the flux of molecules crossing the endothelial barrier. Exogenous delivering of these agents may increase permeability(144, 145), although the mechanisms may be saturated in the tumor already (146). Because it is likely that a small hydrostatic and/or osmotic pressure gradient is necessary between the vessel and interstitium to

prevent vessel collapse, permeability cannot be increased indefinitely. More permeable vessels may also increase the incidence of metastasis(147, 148), but modulating the permeability will likely be done in conjunction with therapy, which should easily target cells escaping to the plasma.

Other blood flow modifying agents and techniques include anti-VEGF therapies and pharmacological agents that modify blood pressure(149, 150). Increased blood pressure increases the hydrostatic pressure in the vessels, which can increase convection and could open previously collapsed vessels. The increased convection is likely short lived, since interstitial pressure profiles rapidly adjust to the vascular pressure(151, 152). The effect of anti-VEGF therapies is more complicated. These therapies function in part by 'normalizing' the vessel properties, such as decreasing permeability, increasing pericyte coverage, and lowering vessel diameter(153-157). Jain and colleagues showed that the restored pressure gradients increase blood flow and distribution of small molecule drugs in the tissue. This is important for oxygen (which is critical in radiation therapy(158)) and small molecules, where poor blood flow and transient cessation of flow can limit efficacy. They argued that restored convection allowed albumin to travel farther away from the capillary(155), but the total uptake of this macromolecule was lower due to decreased permeability. This is different than the results found by Nakahara and colleagues(159). Their results show that the number of blood vessels was reduced dramatically (80-90%), but the uptake was only lowered 60-70%. Therefore, uptake was better on a per vessel basis. However, they noted that there was a large amount of antibody still contained in the vessel lumens, so the increased signal may have been from antibody remaining in the plasma. These experiments were carried out after 7 days of anti-VEGF treatment, so this may have missed the 'normalization window' seen with this type of treatment. In both cases, however, the total amount of antibody entering the tissue is lower upon anti-VEGF treatment. While there may be therapeutic benefits to combining anti-VEGF therapy with antibody delivery, from a pharmacokinetic standpoint, it appears to lower uptake by decreasing permeability and lowering the blood vessel surface area for transport.

A final method that has been explored for increasing transcapillary flux involves utilizing proteins that are actively transcytosed across the vessel wall. This can involve interaction with specific receptors on the endothelium. Schnitzer and colleagues have isolated an antibody specific for the lung caveolae that is rapidly transported into the lung following systemic administration(160). Albumin may be actively trafficked across the vasculature through interactions with receptors(161, 162). If transcytosis can be selectively obtained in the tumor, this could provide another layer of specificity. Ultimately,

these mechanisms must be able to transport a large flux of antibodies across the endothelium to significantly increase tumor localization.

References

1.	Weinstein JN, Eger RR, Covell DG, et al. The pharmacology of monoclonal antibodies. Ann N Y Acad Sci 1987;507:199-210.
2.	Heicappell R, Muller-Mattheis V, Reinhardt M, et al. Staging of pelvic lymph nodes in neoplasms of the bladder and prostate by positron emission tomography with 2- F-18 -2-deoxy-D-glucose. European Urology 1999;36:582-7.
3.	Kumar R, Alavi A. Clinical applications of fluorodeoxyglucose-positron emission tomography in the management of malignant melanoma. Current Opinion in Oncology 2005;17:154-9.
4.	Saisho H, Yamaguchi T. Diagnostic imaging for pancreatic cancer - Computed tomography, magnetic resonance imaging, and positron emission tomography. Pancreas 2004;28:273-8.
5.	Minchinton AI, Tannock IF. Drug penetration in solid tumours. Nature Reviews Cancer 2006;6:583-92.
6.	Kirpotin DB, Drummond DC, Shao Y, et al. Antibody targeting of long-circulating lipidic nanoparticles does not increase tumor localization but does increase internalization in animal models. Cancer Research 2006;66:6732-40.
7.	Deen WM. Hindered Transport of Large Molecules in Liquid-Filled Pores. AIChE Journal 1987;33:1409.
8.	Berk DA, Yuan F, Leunig M, Jain RK. Direct in vivo measurement of targeted binding in a human tumor xenograft. Proc Natl Acad Sci U S A 1997;94:1785-90.
9.	Brown EB, Boucher Y, Nasser S, Jain RK. Measurement of macromolecular diffusion coefficients in human tumors. Microvasc Res 2004;67:231-6.
10.	Davies Cde L, Berk DA, Pluen A, Jain RK. Comparison of IgG diffusion and extracellular matrix composition in rhabdomyosarcomas grown in mice versus in vitro as spheroids reveals the role of host stromal cells. Br J Cancer 2002;86:1639-44.
11.	Banerjee RK, Sung C, Bungay PM, Dedrick RL, Van Osdol WW. Antibody penetration into a spherical prevascular tumor nodule embedded in normal tissue. Annals of Biomedical Engineering 2002;30:828-39.
12.	Krogh A. The number and distribution of capillaries in muscles with calculations of the oxygen pressure head necessary for supplying the tissue. Journal of Physiology 1919;52:409-15.
13.	Baish JW, Gazit Y, Berk DA, Nozue M, Baxter LT, Jain RK. Role of tumor vascular architecture in nutrient and drug delivery: an invasion percolation-based network model. Microvasc Res 1996;51:327-46.
14.	Adams G, Schier R, McCall A, et al. High Affinity Restricts the Localization and Tumor Penetration of Single-Chain Fv Antibody Molecules. Cancer research 2001;61:4750-5.
15.	Dennis MS, Jin HK, Dugger D, et al. Imaging tumors with an albumin-binding Fab, a novel tumor-targeting agent. 2007;67:254-61.
16.	Steffen AC, Orlova A, Wikman M, et al. Affibody-mediated tumour targeting of HER-2 expressing xenografts in mice. European Journal of Nuclear Medicine and Molecular Imaging 2006;33:631-8.
17.	Baxter L, Jain RK. Transport of Fluid and Macromolecules in Tumors: 1. Role of Interstitial Pressure and Convection. Microvascular Research 1989;37:77-104.
18.	Heijn M, Roberge S, Jain RK. Cellular membrane permeability of anthracyclines does not correlate with their delivery in a tissue-isolated tumor. 1999;59:4458-63.

19.   Dewhirst MW, Kimura H, Rehmus SWE, et al. Microvascular studies on the origins of perfusion-limited hypoxia. British Journal of Cancer 1996;74:S247-S51.

20.   Boucher Y, Jain RK. Microvascular Pressure Is the Principal Driving Force for Interstitial Hypertension in Solid Tumors: Implications for Vascular Collapse. Cancer Research 1992;52:5110-4.

21.   Hilmas D, Gillette E. MORPHOMETRIC ANALYSES OF THE MICROVASCULATURE OF TUMORS DURING GROWTH AND AFTER X-IRRADIATION. Cancer 1974;33:103-10.

22.   Honess DJ, Kitamoto Y, Rampling MR, Bleehen NM. Nicotinamide and pentoxifylline increase human leucocyte filterability: A possible mechanism for reduction of acute hypoxia. 1996;74:S236-S40.

23.   Chaplin DJ, Olive PL, Durand RE. Intermittent Blood-Flow in a Murine Tumor - Radiobiological Effects. Cancer research 1987;47:597-601.

24.   Eskey CJ, Koretsky AP, Domach MM, Jain RK. H-2-Nuclear Magnetic-Resonance-Imaging of Tumor Blood-Flow - Spatial and Temporal Heterogeneity in a Tissue-Isolated Mammary Adenocarcinoma. Cancer research 1992;52:6010-9.

25.   Graff CP, Wittrup KD. Theoretical analysis of antibody targeting of tumor spheroids: importance of dosage for penetration, and affinity for retention. Cancer Res 2003;63:1288-96.

26.   Fujimori K, Covell D, Fletcher J, Weinstein J. A Modeling Analysis of Monoclonal Antibody Percolation Through Tumors: A Binding-Site Barrier. The Journal of Nuclear Medicine 1990;31:1191-8.

27.   Rippley RK, Stokes CL. Effects of cellular pharmacology on drug distribution in tissues. Biophysical journal 1995;69:825-39.

28.   Wenning LA, Murphy RM. Coupled cellular trafficking and diffusional limitations in delivery of immunotoxins to multicell tumor spheroids. Biotechnology and bioengineering 1999;62:562-75.

29.   Baxter L, Jain RK. Transport of Fluid and Macromolecules in Tumors: 3. Role of Binding and Metabolism. Microvascular Research 1991;41:5-23.

30.   Pluen A, Boucher Y, Ramanujan S, et al. Role of tumor-host interactions in interstitial diffusion of macromolecules: Cranial vs. subcutaneous tumors. Proceedings of the National Academy of Sciences of the United States of America 2001;98:4628-33.

31.   Butler TP, Grantham FH, Gullino PM. BULK TRANSFER OF FLUID IN INTERSTITIAL COMPARTMENT OF MAMMARY-TUMORS. Cancer Research 1975;35:3084-8.

32.   Baxter LT, Jain RK. TRANSPORT OF FLUID AND MACROMOLECULES IN TUMORS: 4. A MICROSCOPIC MODEL OF THE PERIVASCULAR DISTRIBUTION. Microvascular Research 1991;41:252-72.

33.   Boucher Y, Baxter LT, Jain RK. INTERSTITIAL PRESSURE-GRADIENTS IN TISSUE-ISOLATED AND SUBCUTANEOUS TUMORS - IMPLICATIONS FOR THERAPY. Cancer Research 1990;50:4478-84.

34.   Rippe B, Haraldsson B. Fluid and protein fluxes across small and large pores in the microvasculature. Application of two-pore equations. Acta Physiol Scand 1987;131:411-28.

35.   Gerlowski L, Jain RK. Microvascular Permeability of Normal and Neoplastic Tissues. Microvascular Research 1986;31:288-305.

36.   Yuan F, Dellian M, Fukumura D, et al. Vascular Permeability in a Human Tumor Xenograft: Molecular Size Dependence and Cutoff Size. Cancer Research 1995;55:3752-6.

37.   Nugent LJ, Jain RK. Extravascular diffusion in normal and neoplastic tissues. Cancer Res 1984;44:238-44.

38.   Clauss MA, Jain RK. Interstitial transport of rabbit and sheep antibodies in normal and neoplastic tissues. Cancer Res 1990;50:3487-92.

39.   Schier R, McCall A, Adams GP, et al. Isolation of picomolar affinity Anti-c-erbB-2 single-chain Fv by molecular evolution of the complementarity determining regions in the center of the antibody binding site. Journal of Molecular Biology 1996;263:551-67.

40.   Worthylake R, Opresko LK, Wiley HS. ErbB-2 amplification inhibits down-regulation and induces constitutive activation of both ErbB-2 and epidermal growth factor receptors. Journal of Biological Chemistry 1999;274:8865-74.

41.   Fogler HS. Elements of Chemical Reaction Engineering. 3rd ed: Prentice-Hall; 1999.

42.   Katzung B, editor. Basic and Clinical Pharmacology. 9 ed. New York: McGraw-Hill Companies; 2004.

43.   Dokoumetzidis A, Macheras P. A Model for Transport and Dispersion in the Circulatory System Based on the Vascular Fractal Tree. Annals of Biomedical Engineering 2003;31:284-93.

44.   Karalis V, Dokoumetzidis A, Macheras P. A Physiologically Based Approach for the Estimation of Recirculatory Parameters. The Journal of Pharmacology and Experimental Therapeutics 2004;308:198-205.

45.   Larson SM, Brown JP, Wright PW, Carrasquillo JA, Hellstrom I, Hellstrom KE. Imaging of Melanoma with I-131-Labeled Monoclonal-Antibodies. Journal of Nuclear Medicine 1983;24:123-9.

46.   Lin YS, Nguyen C, Mendoza JL, et al. Preclinical pharmacokinetics, interspecies scaling, and tissue distribution of a humanized monoclonal antibody against vascular endothelial growth factor. Journal of Pharmacology and Experimental Therapeutics 1999;288:371-8.

47.   Scott AM, Lee FT, Jones R, et al. A phase I trial of humanized monoclonal antibody A33 in patients with colorectal carcinoma: Biodistribution, pharmacokinetics, and quantitative tumor uptake. Clinical Cancer Research 2005;11:4810-7.

48.   Milenic DE, Yokota T, Filpula DR, et al. Construction, Binding-Properties, Metabolism, and Tumor Targeting of a Single-Chain Fv Derived from the Pancarcinoma Monoclonal-Antibody Cc49. Cancer Research 1991;51:6363-71.

49.   Begent RHJ, Verhaar MJ, Chester KA, et al. Clinical evidence of efficient tumor targeting based on single-chain Fv antibody selected from a combinatorial library. Nature Medicine 1996;2:979-84.

50.   Lobo ED, Hansen RJ, Balthasar JP. Antibody pharmacokinetics and pharmacodynamics. J Pharm Sci 2004;93:2645-68.

51.   Williams LE, Wu AM, Yazaki PJ, et al. Numerical selection of optimal tumor imaging agents with application to engineered antibodies. Cancer Biother Radiopharm 2001;16:25-35.

52.   Ghetie V, Ward ES. Transcytosis and catabolism of antibody. Immunol Res 2002;25:97-113.

53.   Garg A, Balthasar JP. Physiologically-based pharmacokinetic (PBPK) model to predict IgG tissue kinetics in wild-type and FcRn-knockout mice. J Pharmacokinet Pharmacodyn 2007.

54.   Ferl GZ, Wu AM, DiStefano JJ, 3rd. A predictive model of therapeutic monoclonal antibody dynamics and regulation by the neonatal Fc receptor (FcRn). Ann Biomed Eng 2005;33:1640-52.

55.   Holt LJ, Herring C, Jespers LS, Woolven BP, Tomlinson IM. Domain antibodies: proteins for therapy. Trends Biotechnol 2003;21:484-90.

56.   Holliger P, Hudson PJ. Engineered antibody fragments and the rise of single domains. Nat Biotechnol 2005;23:1126-36.

57.   Deen WM, Lazzara MJ, Myers BD. Structural determinants of glomerular permeability. 2001;281:F579-F96.

58.   Chapman AP, Antoniw P, Spitali M, West S, Stephens S, King DJ. Therapeutic antibody fragments with prolonged in vivo half-lives. Nat Biotechnol 1999;17:780-3.

59.   Yang K, Basu A, Wang M, et al. Tailoring structure-function and pharmacokinetic properties of single-chain Fv proteins by site-specific PEGylation. Protein Eng 2003;16:761-70.

60.   Nguyen A, Reyes AE, 2nd, Zhang M, et al. The pharmacokinetics of an albumin-binding Fab (AB.Fab) can be modulated as a function of affinity for albumin. Protein Eng Des Sel 2006;19:291-7.

61.   Muller D, Karle A, Meissburger B, Hofig I, Stork R, Kontermann RE. Improved pharmacokinetics of recombinant bispecific antibody molecules by fusion to human serum albumin. J Biol Chem 2007;282:12650-60.

62.   Hu S, Shively L, Raubitschek A, et al. Minibody: A novel engineered anti-carcinoembryonic antigen antibody fragment (single-chain Fv-CH3) which exhibits rapid, high-level targeting of xenografts. Cancer Res 1996;56:3055-61.

63.   Willuda J, Kubetzko S, Waibel R, Schubiger PA, Zangemeister-Wittke U, Pluckthun A. Tumor targeting of mono-, di-, and tetravalent anti-p185(HER-2) miniantibodies multimerized by self-associating peptides. J Biol Chem 2001;276:14385-92.

64.   Lammerts van Bueren JJ, Bleeker WK, Bogh HO, et al. Effect of target dynamics on pharmacokinetics of a novel therapeutic antibody against the epidermal growth factor receptor: implications for the mechanisms of action. Cancer research 2006;66:7630-8.

65.   Ng CM, Stefanich E, Anand BS, Fielder PJ, Vaickus L. Pharmacokinetics/pharmacodynamics of nondepleting anti-CD4 monoclonal antibody (TRX1) in healthy human volunteers. Pharm Res 2006;23:95-103.

66.   Ng CM, Joshi A, Dedrick RL, Garovoy MR, Bauer RJ. Pharmacokinetic-pharmacodynamic-efficacy analysis of efalizumab in patients with moderate to severe psoriasis. Pharm Res 2005;22:1088-100.

67.   Mager DE. Target-mediated drug disposition and dynamics. Biochemical Pharmacology 2006;72:1-10.

68.   Mager DE, Jusko WJ. General pharmacokinetic model for drugs exhibiting target-mediated drug disposition. J Pharmacokinet Pharmacodyn 2001;28:507-32.

69.   Liu H, Rajasekaran AK, Moy P, et al. Constitutive and antibody-induced internalization of prostate-specific membrane antigen. Cancer research 1998;58:4055-60.

70.   Bryan JN, Jia F, Mohsin H, et al. Comparative uptakes and biodistributions of internalizing vs. noninternalizing copper-64 radioimmunoconjugates in cell and animal models of colon cancer. Nucl Med Biol 2005;32:851-8.

71.   Matzku S, Brocker EB, Bruggen J, Dippold WG, Tilgen W. Modes of binding and internalization of monoclonal antibodies to human melanoma cell lines. Cancer research 1986;46:3848-54.

72.   Kyriakos RJ, Shih LB, Ong GL, Patel K, Goldenberg DM, Mattes MJ. The fate of antibodies bound to the surface of tumor cells in vitro. Cancer research 1992;52:835-42.

73.   Ackerman M, Chalouni C, Schmidt M, et al. A33 antigen displays persistent surface expression. Cancer Immunology, Immunotherapy 2008.

74.   Austin C, Maziere A, Pisacane P, et al. Endocytosis and Sorting of ErbB2 and the Site of Action of Cancer Therapeutics Trastuzumab and Geldanamycin. Molecular Biology of the Cell 2004;15:5268-82.

75.   Thurber GM, Zajic SC, Wittrup KD. Theoretic criteria for antibody penetration into solid tumors and micrometastases. J Nucl Med 2007;48:995-9.

76.   Thiele EW. Relation between Catalytic Activity and Size of Particle. Industrial and Engineering Chemistry 1939;31:916-20.

77.   Baselga J, Norton L, Albanell J, Kim YM, Mendelsohn J. Recombinant humanized anti-HER2 antibody (Herceptin (TM)) enhances the antitumor activity of paclitaxel and doxorubicin against HER2/neu overexpressing human breast cancer xenografts. Cancer Research 1998;58:2825-31.

78.   Lyng H, Haraldseth O, Rofstad EK. Measurement of cell density and necrotic fraction in human melanoma xenografts by diffusion weighted magnetic resonance imaging. Magnetic Resonance in Medicine 2000;43:828-36.

79.   Krol A, Nagaraj S, Dewhirst M, Yuan F. Available volume fraction of macromolecules in tumor tissues. Faseb Journal 2000;14:A167-A.

80.   Hendriks BS, Opresko LK, Wiley HS, Lauffenburger D. Coregulation of epidermal growth factor receptor/human epidermal growth factor receptor 2 (HER2) levels and locations: Quantitative analysis of HER2 overexpression effects. Cancer Research 2003;63:1130-7.

81.   Romond EH, Perez EA, Bryant J, et al. Trastuzumab plus adjuvant chemotherapy for operable HER2-positive breast cancer. 2005;353:1673-84.

82.   Blanch HW, Clark DS. Biochemical Engineering: CRC Press; 1997.

83.   Dreher MR, Liu WG, Michelich CR, Dewhirst MW, Yuan F, Chilkoti A. Tumor vascular permeability, accumulation, and penetration of macromolecular drug carriers. Journal of the National Cancer Institute 2006;98:335-44.

84.   Torres IP, Leunig M, Yuan F, Intaglietta M, Jain RK. Noninvasive Measurement of Microvascular and Interstitial Oxygen Profiles in a Human Tumor in Scid Mice. 1994;91:2081-5.

85.   Jain RK, Wei J, Gullino PM. PHARMACOKINETICS OF METHOTREXATE IN SOLID TUMORS. Journal of Pharmacokinetics and Biopharmaceutics 1979;7:181-94.

86.   Tang Y, Lou J, Alpaugh RK, Robinson MK, Marks JD, Weiner LM. Regulation of antibody-dependent cellular cytotoxicity by IgG intrinsic and apparent affinity for target antigen. 2007;179:2815-23.

87.   Graff C, Chester K, Begent R, Wittrup KD. Directed Evolution of an Anti-Carcinoembryonic Antigen scFv with a Four-Day Monovalent Dissociation Half-time at 37 °C. Protein Engineering, Design, & Selection 2004;17:293-304.

88.   Kievit E, Pinedo HM, Schluper HM, Haisma HJ, Boven E. Comparison of monoclonal antibodies 17-1A and 323/A3: the influence of the affinity on tumour uptake and efficacy of radioimmunotherapy in human ovarian cancer xenografts. British journal of cancer 1996;73:457-64.

89.   Blumenthal RD, Fand I, Sharkey RM, Boerman OC, Kashi R, Goldenberg DM. The effect of antibody protein dose on the uniformity of tumor distribution of radioantibodies: an autoradiographic study. Cancer Immunol Immunother 1991;33:351-8.

90.   Thurber G, Schmidt M, Wittrup KD. Factors determining antibody distribution in tumors. Trends in Pharmacological Sciences 2008;29:57-61.

91.   Schoeberl B, Eichler-Jonsson C, Gilles ED, Muller G. Computational modeling of the dynamics of the MAP kinase cascade activated by surface and internalized EGF receptors. Nature Biotechnology 2002;20:370-5.

92.   Zhou HN, Randers-Pehrson G, Waldren CA, Vannais D, Hall EJ, Hei TK. Induction of a bystander mutagenic effect of alpha particles in mammalian cells. 2000;97:2099-104.

93.   Couturier O, Supiot S, Degraef-Mougin M, et al. Cancer radioimmunotherapy with alpha-emitting nuclides. 2005;32:601-14.

94.   Adams GP, Schier R, McCall AM, et al. Prolonged in vivo tumour retention of a human diabody targeting the extracellular domain of human HER2/neu. British journal of cancer 1998;77:1405-12.

95.   Zuckier LS, Berkowitz EZ, Sattenberg RJ, Zhao QH, Deng HF, Scharff MD. Influence of affinity and antigen density on antibody localization in a modifiable tumor targeting model. Cancer research 2000;60:7008-13.

96.   Adams GP, Schier R, Marshall K, et al. Increased affinity leads to improved selective tumor delivery of single-chain Fv antibodies. Cancer research 1998;58:485-90.

97.   Yao Z, Garmestani K, Wong KJ, et al. Comparative cellular catabolism and retention of astatine-, bismuth-, and lead-radiolabeled internalizing monoclonal antibody. J Nucl Med 2001;42:1538-44.

98.   van Schaijk FG, Broekema M, Oosterwijk E, et al. Residualizing iodine markedly improved tumor targeting using bispecific antibody-based pretargeting. J Nucl Med 2005;46:1016-22.

99.   Michel RB, Ochakovskaya R, Mattes MJ. Antibody localization to B-cell lymphoma xenografts in immunodeficient mice: importance of using residualizing radiolabels. Clin Cancer Res 2002;8:2632-9.

100.   Mattes MJ, Griffiths G, Diril H, Goldenberg D, Ong G, Shih L. Processing of Antibody-Radioisotope Conjugates after Binding to the Surface of Tumor Cells. Cancer 1994;73:787-93.

101.   Press OW, Shan D, HowellClark J, et al. Comparative metabolism and retention of iodine-125, yttrium-90, and indium-111 radioimmunoconjugates by cancer cells. Cancer Research 1996;56:2123-9.

102.   Ferl GZ, Kenanova V, Wu AM, DiStefano JJ. A two-tiered physiologically based model for dually labeled single-chain Fv-Fc antibody fragments. 2006;5:1550-8.

103. Noguchi Y, Wu J, Duncan R, et al. Early phase tumor accumulation of macromolecules: a great difference in clearance rate between tumor and normal tissues. Japanese Journal of Cancer Research 1998;89:307-14.

104. Goldenberg DM, Sharkey RM, Paganelli G, Barbet J, Chatal JF. Antibody pretargeting advances cancer radioimmunodetection and radioimmunotherapy. J Clin Oncol 2006;24:823-34.

105. Bagshawe KD, Sharma SK, Begent RH. Antibody-directed enzyme prodrug therapy (ADEPT) for cancer. Expert Opin Biol Ther 2004;4:1777-89.

106. van Schaijk FG, Oosterwijk E, Soede AC, et al. Pretargeting of carcinoembryonic antigen-expressing tumors with a biologically produced bispecific anticarcinoembryonic antigen x anti-indium-labeled diethylenetriaminepentaacetic acid antibody. Clinical Cancer Research 2005;11:7130S-6S.

107. Lin Y, Pagel JM, Axworthy D, Pantelias A, Hedin N, Press OW. A genetically engineered anti-CD45 single-chain antibody-streptavidin fusion protein for pretargeted radioimmunotherapy of hematologic malignancies. Cancer Res 2006;66:3884-92.

108. Liu G, He J, Dou S, Gupta S, Rusckowski M, Hnatowich DJ. Further investigations of morpholino pretargeting in mice--establishing quantitative relations in tumor. Eur J Nucl Med Mol Imaging 2005;32:1115-23.

109. Sharkey RM, Karacay H, Richel H, et al. Optimizing bispecific antibody pretargeting for use in radioimmunotherapy. Clin Cancer Res 2003;9:3897S-913S.

110. Koppe MJ, Soede AC, Pels W, et al. Experimental radioimmunotherapy of small peritoneal metastases of colorectal origin. Int J Cancer 2003;106:965-72.

111. Kranenborg MH, Boerman OC, Oosterwijk-Wakka JC, de Weijert MC, Corstens FH, Oosterwijk E. Two-step radio-immunotargeting of renal-cell carcinoma xenografts in nude mice with anti-renal-cell-carcinoma X anti-DTPA bispecific monoclonal antibodies. Int J Cancer 1998;75:74-80.

112. Juweid M, Neumann R, Paik C, et al. Micropharmacology of Monoclonal-Antibodies in Solid Tumors - Direct Experimental-Evidence for a Binding-Site Barrier. 1992;52:5144-53.

113. Fenwick J, Philpott G, Connett J. Biodistribution and histological localization of anti-human colon cancer monoclonal antibody (MAb) 1A3: the influence of administered MAb dose on tumor uptake. International Journal of Cancer 1989;44:1017-27.

114. Ong G, Mattes MJ. Penetration and Binding of Antibodies in Experimental Human Solid Tumors Grown in Mice. Cancer Research 1989;49:4264-73.

115. Haskin JA, Warner DJ, Blank DU. Acute renal failure after large doses of intravenous immune globulin. 1999;33:800-3.

116. Ratko TA, Burnett DA, Foulke GE, Matuszewski KA, Sacher RA. Recommendations for off-label use of intravenously administered immunoglobulin preparations. University Hospital Consortium Expert Panel for Off-Label Use of Polyvalent Intravenously Administered Immunoglobulin Preparations. Jama 1995;273:1865-70.

117. Behr TM, Behe M, Stabin MG, et al. High-linear energy transfer (LET) alpha versus low-LET beta emitters in radioimmunotherapy of solid tumors: Therapeutic efficacy and dose-limiting toxicity of Bi-213- versus Y-90-labeled CO17-1A Fab ' fragments in a human colonic cancer model. Cancer Research 1999;59:2635-43.

118. Norum J. Cetuximab in the treatment of metastatic colorectal cancer: a model-based cost-effectiveness analysis. 2006;18:532-7.

119. Wu AM, Senter PD. Arming antibodies: prospects and challenges for immunoconjugates. Nature Biotechnology 2005;23:1137-46.

120. Frykholm G, Glimelius B, Richter S, Carlsson J. Heterogeneity in Antigenic Expression and Radiosensitivity in Human Colon-Carcinoma Cell-Lines. In Vitro Cellular & Developmental Biology 1991;27:900-6.

121.   Lustig HJ, Bianco C. Antibody-Mediated Cell Cytotoxicity in a Defined System - Regulation by Antigen, Antibody, and Complement. Journal of Immunology 1976;116:253-60.

122.   Liao SK, Meranda C, Avner BP, et al. Immunohistochemical phenotyping of human solid tumors with monoclonal antibodies in devising biotherapeutic strategies. Cancer Immunol Immunother 1989;28:77-86.

123.   Mothersill C, Seymour C. Radiation-induced bystander and other non-targeted effects: Novel intervention points in cancer therapy? 2006;6:447-54.

124.   Epstein AL, Chen FM, Taylor CR. A novel method for the detection of necrotic lesions in human cancers. Cancer Res 1988;48:5842-8.

125.   Friedman LM, Rinon A, Schechter B, et al. Synergistic down-regulation of receptor tyrosine kinases by combinations of mAbs: Implications for cancer immunotherapy. Proceedings of the National Academy of Sciences of the United States of America 2005;102:1915-20.

126.   Ballesta AM, Molina R, Filella X, Jo J, Gimenez N. Carcinoembryonic Antigen in Staging and Follow-up of Patients with Solid Tumors. 1995;16:32-41.

127.   Prinssen HM, Molthoff CF, Verheijen RH, et al. Biodistribution of 111In-labelled engineered human antibody CTM01 (hCTM01) in ovarian cancer patients: influence of prior administration of unlabelled hCTM01. Cancer Immunol Immunother 1998;47:39-46.

128.   Knox SJ, Goris ML, Trisler K, et al. Yttrium-90-labeled anti-CD20 monoclonal antibody therapy of recurrent B-cell lymphoma. Clin Cancer Res 1996;2:457-70.

129.   Flynn AA, Boxer GM, Begent RH, Pedley RB. Relationship between tumour morphology, antigen and antibody distribution measured by fusion of digital phosphor and photographic images. Cancer Immunol Immunother 2001;50:77-81.

130.   Sharkey RM, Motta-Hennessy C, Pawlyk D, Siegel JA, Goldenberg DM. Biodistribution and radiation dose estimates for yttrium- and iodine-labeled monoclonal antibody IgG and fragments in nude mice bearing human colonic tumor xenografts. Cancer research 1990;50:2330-6.

131.   Kubetzko S, Balic E, Waibel R, Zangemeister-Wittke U, Pluckthun A. PEGylation and multimerization of the anti-p185HER-2 single chain Fv fragment 4D5: effects on tumor targeting. J Biol Chem 2006;281:35186-201.

132.   Delgado C, Pedley RB, Herraez A, et al. Enhanced tumour specificity of an anti-carcinoembrionic antigen Fab' fragment by poly(ethylene glycol) (PEG) modification. British journal of cancer 1996;73:175-82.

133.   Li L, Yazaki PJ, Anderson AL, et al. Improved biodistribution and radioimmunoimaging with poly(ethylene glycol)-DOTA-conjugated anti-CEA diabody. Bioconjug Chem 2006;17:68-76.

134.   Kenanova V, Olafsen T, Williams LE, et al. Radioiodinated versus radiometal-labeled anti-carcinoembryonic antigen single-chain Fv-Fc antibody fragments: optimal pharmacokinetics for therapy. Cancer research 2007;67:718-26.

135.   Behr TM, Memtsoudis S, Sharkey RM, et al. Experimental studies on the role of antibody fragments in cancer radio-immunotherapy: Influence of radiation dose and dose rate on toxicity and anti-tumor efficacy. Int J Cancer 1998;77:787-95.

136.   DeNardo SJ, Richman CM, Albrecht H, et al. Enhancement of the therapeutic index: From nonmyeloablative and myeloablative toward pretargeted Radioimmunotherapy for metastatic prostate cancer. Clinical Cancer Research 2005;11:7187S-94S.

137.   Yokota T, Milenic D, Whitlow M, Schlom J. Rapid Tumor Penetration of a Single-Chain Fv and Comparison with Other Immunoglobulin Forms. Cancer Research 1992;52:3402-8.

138.   Sundaresan G, Yazaki PJ, Shively JE, et al. 124I-labeled engineered anti-CEA minibodies and diabodies allow high-contrast, antigen-specific small-animal PET imaging of xenografts in athymic mice. J Nucl Med 2003;44:1962-9.

139.   Kenanova V, Olafsen T, Crow DM, et al. Tailoring the pharmacokinetics and positron emission tomography imaging properties of anti-carcinoembryonic antigen single-chain Fv-Fc antibody fragments. Cancer research 2005;65:622-31.

140.   Melkko S, Halin C, Borsi L, Zardi L, Neri D. An antibody-calmodulin fusion protein reveals a functional dependence between macromolecular isoelectric point and tumor targeting performance. 2002;54:1485-90.

141.   Dellian M, Yuan F, Trubetskoy VS, Torchilin VP, Jain RK. Vascular permeability in a human tumour xenograft: molecular charge dependence. British journal of cancer 2000;82:1513-8.

142.   Tabata Y, Kawai T, Murakami Y, Ikada Y. Electric charge influence of dextran derivatives on their tumor accumulation after intravenous injection. 1997;4:213-21.

143.   Onda M, Kreitman RJ, Vasmatzis G, Lee B, Pastan I. Reduction of the nonspecific animal toxicity of anti-Tac(Fv)-PE38 by mutations in the framework regions of the Fv which lower the isoelectric point. J Immunol 1999;163:6072-7.

144.   Khawli LA, Hu P, Epstein AL. NHS76/PEP2, a fully human vasopermeability-enhancing agent to increase the uptake and efficacy of cancer chemotherapy. Clin Cancer Res 2005;11:3084-93.

145.   LeBerthon B, Khawli LA, Alauddin M, et al. Enhanced tumor uptake of macromolecules induced by a novel vasoactive interleukin 2 immunoconjugate. Cancer Res 1991;51:2694-8.

146.   Halin C, Niesner U, Villani ME, Zardi L, Neri D. Tumor-targeting properties of antibody-vascular endothelial growth factor fusion proteins. Int J Cancer 2002;102:109-16.

147.   Galaup A, Cazes A, Le Jan S, et al. Angiopoietin-like 4 prevents metastasis through inhibition of vascular permeability and tumor cell motility and invasiveness. Proc Natl Acad Sci U S A 2006;103:18721-6.

148.   Criscuoli ML, Nguyen M, Eliceiri BP. Tumor metastasis but not tumor growth is dependent on Src-mediated vascular permeability. Blood 2005;105:1508-14.

149.   Burke D, Davies MM, Zweit J, et al. Continuous angiotensin II infusion increases tumour: normal blood flow ratio in colo-rectal liver metastases. 2001;85:1640-5.

150.   Kinuya S, Yokoyama K, Kawashima A, et al. Pharmacologic intervention with angiotensin II and kininase inhibitor enhanced efficacy of radioimmunotherapy in human colon cancer xenografts. 2000;41:1244-+.

151.   Netti PA, Hamberg LM, Babich JW, et al. Enhancement of fluid filtration across tumor vessels: Implication for delivery of macromolecules. 1999;96:3137-42.

152.   Netti PA, Baxter LT, Boucher Y, Skalak R, Jain RK. Time-dependent behavior of interstitial fluid pressure in solid tumors: implications for drug delivery. Cancer research 1995;55:5451-8.

153.   Inai T, Mancuso M, Hashizume H, et al. Inhibition of vascular endothelial growth factor (VEGF) signaling in cancer causes loss of endothelial fenestrations, regression of tumor vessels, and appearance of basement membrane ghosts. 2004;165:35-52.

154.   Jain RK. Normalization of tumor vasculature: An emerging concept in antiangiogenic therapy. Science 2005;307:58-62.

155.   Tong R, Boucher Y, Kozin S, Winkler F, Hicklin D, Jain RK. Vascular Normalization by Vascular Endothelial Growth Factor Receptor 2 Blockade Induces a Pressure Gradient Across the Vasculature and Improves Drug Penetration in Tumors. Cancer research 2004;64:3731-6.

156.   Turetschek K, Preda A, Novikov V, et al. Tumor Microvascular Changes in Antiangiogenic Treatment: Assessment by Magnetic Resonance Contrast Media of Different Molecular Weights. Journal of Magnetic Resonance Imaging 2004;20:138-44.

157.   Yuan F, Chen Y, Dellian M, Safabakhsh N, Ferrara N, Jain RK. Time-dependent vascular regression and permeability changes in established human tumor xenografts induced by an anti-vascular endothelial growth factor vascular permeability factor antibody. Proceedings of the National Academy of Sciences of the United States of America 1996;93:14765-70.

158.   Hall E, Giaccia A. Radiobiology for the Radiologist. 6th ed: Lippincott Williams and Wilkins; 2006.

159.   Nakahara T, Norberg SM, Shalinsky DR, Hu-Lowe DD, McDonald DM. Effect of inhibition of vascular endothelial growth factor signaling on distribution of extravasated antibodies in tumors. Cancer Research 2006;66:1434-45.

160.   McIntosh D, Tan X, Oh P, Schnitzer J. Targeting endothelium and its dynamic caveolae for tissue-specific transcytosis *in vivo*: A pathway to overcome cell barriers to drug and gene delivery. Proceedings of the National Academy of Science, USA 2002;99:1996-2001.

161.   John TA, Vogel SM, Tiruppathi C, Malik AB, Minshall RD. Quantitative analysis of albumin uptake and transport in the rat microvessel endothelial monolayer. Am J Physiol Lung Cell Mol Physiol 2003;284:L187-96.

162.   Tiruppathi C, Naqvi T, Wu Y, Vogel SM, Minshall RD, Malik AB. Albumin mediates the transcytosis of myeloperoxidase by means of caveolae in endothelial cells. Proc Natl Acad Sci U S A 2004;101:7699-704.

Chapter 3 – Experimental Distribution of Antibodies in Tumor Spheroids

3.1 Introduction

Fluorescently or radiolabeled antibodies can be used to track their distribution in tumor tissue. These labels facilitate measurement of the concentration and movement in tumors; however, there are several challenges. Manipulating the conditions *in vivo* to analyze the distribution is very difficult, so an *in vitro* model system, such as a tumor spheroid, offers many advantages, like better control over experimental conditions and easier access to the sample for data collection. The choice of label is also important and typically involves three main options: radiolabeling, indirect detection (e.g. labeling the Fc region, FLAG tag, etc. in histology slides), and fluorescent labeling. Radiolabeling has several advantages, notably its sensitivity at low concentrations and the option for *in vivo* imaging. However, it is challenging to use autoradiography to detect the localization on the intercapillary length scale, which utilizes destructive sampling. Indirect detection also destroys the sample, so the same spheroid cannot be followed in time, and the secondary detection is more laborious. Fluorescently labeled antibodies can easily be detected at the relevant concentrations over the cellular and tissue length scale using fluorescence microscopy techniques, they have fewer safety regulations due to the lack of ionizing radiation, and the non-destructive imaging allows the molecules to be followed in real time.

The size of the fluorescent tags used is small compared to the macromolecule, so the effect is negligible on the overall diffusion and binding. For example, the molecular weight of fluorescein is 0.3 kDa (332 g/mol), whereas an scFv and IgG are ~30 kDa and ~150 kDa. This is an issue for small molecules, where an organic dye would be similar in size to the drug itself. In these cases, the drug must be fluorescent (e.g. doxorubicin) or is typically radiolabelled(1). Similar size issues can arise when tagging macromolecules with quantum dots, which are the same magnitude in size as a large protein. For these reasons, small fluorescent dyes were used to tag the antibodies studied in the *in vitro* tumor spheroid system.

Tumor spheroids offer a system that can be easily manipulated and controlled *in vitro* (e.g. the temperature, concentration, access to imaging) but is more representative of *in vivo* cell and tissue behavior than monolayer culture. Their three dimensional structure replicates many of the gradients present in tumors, such as oxygen and glucose, and causes the cells to secrete more extracellular matrix(2). Whereas in monolayer culture all the cells have equal access to drugs in the surrounding media, the 3D spheroids allow the study of diffusion and binding within the tissue as it penetrates

towards the center. These spheroids can be generated by several techniques, such as shaker flasks(2), the hanging drop method(3), or high throughput 96 well plate techniques(4).

3.2   Previous Spheroid Studies

Several studies of antibody targeting have been done in tumor spheroids using various methods. Studies by Sutherland and colleagues showed that antibodies against carcinoembryonic antigen (CEA) yielded limited penetration into multi-cellular spheroids, similar to that seen *in vivo*, even though histology shows antigen is present throughout the spheroid(5). The same results were seen when using radiolabeled antibodies for cell killing(6). Further experiments demonstrated that antibody distribution was better with Fab fragments rather than full IgGs (although the determining factors, such as affinity/avidity, diffusion coefficient, and/or molecular size were not fully elucidated), and distribution was more homogeneous with cell lines having lower antigen density(7), although these were all carried out at 4^0C. In a later paper by Langmuir et al., a lower affinity antibody was shown to have better distribution in the spheroid, although retention was poor after the antibody was removed(8). The results were qualitatively similar when Hjelstuen and colleagues targeted a melanoma associated antigen expressed on osteosarcoma cells in spheroids. A high affinity antibody bound the cells layer after layer over time, whereas the lower affinity antibody penetrated deeper, gradually filling up the binding sites(9). The authors compared autoradiograph studies with confocal imaging, finding analogous results. However, with the intact spheroid and fluorescence imaging, they could only detect antibody up to 60 μm from the surface(10). This was avoided in a setup used by Myrdal and Foster, where the spheroid was first allowed to attach to the coverslip, creating a hemispheroid on the coverglass with a 'physical slice' through the spheroid rather than relying on the optical sectioning properties of the confocal microscope(11). Studies by Ballangrud and colleagues examined several other antigens, demonstrating that prostate specific membrane antigen (PSMA) and human epidermal growth factor receptor 2 (HER-2) targeting antibodies had the same qualitative behavior. The high affinity antibody against PSMA binds and penetrates cell layer after layer over time(12). Using trastuzumab to target HER-2, the authors found that the antibody did not penetrate to the center of the spheroids after 5 hours(13). The penetration of antibodies is not a binary process where it either does or does not reach the center, however. Uptake is dependent not only on the particular antibody and antigen chosen, but the dose, antigen density, and affinity. This indicates the utility of mathematical models to predict the penetration distance under various conditions(14).

The spheroid system is useful for a variety of experiments and has been used to explore the penetration of small molecules(15), two-step targeting approaches(16), and cellular and tissue trafficking of immunotoxins(17). While some parameters such as diffusion coefficients may vary *in vivo*(18), and the system does not capture all the barriers present in tumors, such as elevated interstitial pressure, blood flow, permeability, and vascular density(19), the precise control over conditions makes this system very useful for studying transport issues.

3.3   Carcinoembryonic Antigen

Carcinoembryonic antigen (CEA) is a 180 kDa glycerophosphatidylinositol (GPI) linked membrane protein present in the fetal gut and on the luminal side of healthy colonocytes. It is also expressed on a majority of advanced stage colon cancers and a variety of other cancer types including breast, pancreas, and lung(20). It was initially thought this antigen was present only in the developing colon and was re-expressed sporadically in cancers, giving rise to its name. However, further research showed that it is present on the apical side of the healthy adult colon, but it is isolated from the bloodstream. During tumorigenesis, the polarity of the cells is lost, exposing this antigen to the vasculature. Expression in the tissues is very heterogeneous, with some cells expressing very high levels and others very little CEA. This has led some investigators to explore the use of drugs to increase CEA expression of some cells(21). The antigen is extensively shed and is fairly stable in the bloodstream, leading to increased plasma levels in cancer patients, although this level is typically less than 1 nM(22). Its primary clinical use is providing an early measure of recurrence after resection of colon cancer tumors(20), although it cannot be used as an initial screen, since background levels vary too widely in the population.

CEA is a member of the immunoglobulin superfamily and is inserted into one leaflet of the plasma membrane through its GPI tail. Although the exact role of CEA is unknown, it has been shown to function as an adhesion molecule(20, 23), and may have a role in innate immunity(20). While endogenous phospholipase C has been shown to cleave the protein from colonic crypts, it can also be shed in a membrane bound form. Studies have shown that 90% of the CEA found in human feces is membrane bound, likely shed by exfoliation and extrusion of colonic epithelial cells(24). While many studies of CEA have focused on the synthesis and shedding of the antigen(25), and it is often referred to as a "non-internalizing antigen"(26-28), a couple references report evidence of the internalization of the antigen(29, 30). This agrees with early work on anti-CEA immunotoxins, which showed increased toxicity even when using a toxin that must be internalized for its effect(22). Early in the development of anti-CEA antibodies, it was discovered that many of the antibodies were cross reactive with other cell

81

surface antigens, such as one given the name 'non-specific cross-reactive antigen,' or NCA. It is important to test newly developed antibodies for specificity against these homologous surface proteins(31).

Due to its overexpression on tumor cells, anti-CEA antibodies have been investigated for a variety of therapy and imaging approaches, including radioimmunotherapy (RIT), pretargeted radioimmunotherapy (PRIT), antibody directed enzyme prodrug therapy (ADEPT), PET, and SPECT(32-35). There have also been several clinical trials using anti-CEA antibodies(36, 37), and an anti-CEA Fab fragment labeled with technetium-99 (arcitumomab) was approved for imaging CEA positive tumors, although it is no longer available(38).

3.4   Materials and Methods for Tracking Anti-CEA scFvs in LS174T Tumor Spheroids

The diffusion, binding, and distribution of antibody single chain variable fragments (scFvs) against CEA were studied in tumor spheroids. Although the behavior of full IgG antibodies compared to scFvs is quantitatively different (due to differences in the diffusion coefficient, void fraction, and bivalent binding), these differences are captured in the theoretical model. Qualitatively, these types of molecules transport in a similar fashion, allowing predictions for both antibodies, antibody fragments, and other binding macromolecules. The experiments were carried out in part to validate the modeling results presented earlier.

Parameters for the model were measured independently in order to validate the model without fitting uptake data. All experiments were carried out at 37°C using a tissue culture incubator or heated microscope stage unless otherwise indicated. The number of antigens per cell was measured using an Alexa-488 (Invitrogen, Carlsbad, CA) labeled anti-CEA antibody M111147 (Fitzgerald Industries, Concord, MA). LS174T cells (ATCC, Manassas, VA) were labeled along with Quantum Simply Cellular beads (Bangs Laboratories, Fishers, IN) according to the manufacturer's instructions. Flow cytometry was done on a Coulter EPICS XL flow cytometer. Cell density was determined by counting Hoechst33342 stained nuclei (Invitrogen, Carlsbad, CA) in a known volume of tissue under the microscope. Combined with antigens per cell, this gives the overall concentration of antigen in the tumor ([Ag]).

To assess spheroid void fraction (ϵ), an irrelevant non-binding scFv (4M5.3 which binds fluorescein) was fluorescently labeled and allowed to diffuse into a spheroid. Using a two-photon microscope, the fluorescent intensity inside the spheroid was compared with the fluorescent intensity outside the spheroid. The two photon microscope was used rather than confocal imaging to avoid

artifacts from light scattering. Assuming the accessible volume outside the spheroid is 100%, the effective void fraction inside the spheroid could be found by a simple ratio.

The scFvs were secreted from yeast and purified by metal affinity and size exclusion chromatography as described previously(39). Briefly, yeast strain YVH10 was transformed with a plasmid containing the disulfide stabilized sm3E or shMFE plasmid. The disulfide stabilized variants were used to prevent the formation of spontaneous dimers, which resulted in the lower affinity variant exhibiting a higher apparent affinity. Yeast were selected from a plate, cultured in 5 mL tubes overnight, and inoculated in a 1 L culture in baffled Tener flasks using SD-CAA media with Pen-strep. After 2 days of growth at 30^0C, the OD_{600} was approximately 10. The cells were spun down and transferred to 1 L of YPG non-selective media in 2 L unbaffled glass flasks. Secretion was carried out for 2 days at 37^0C. Afterwards, the supernatant was concentrated using 10 kDa MWCO filters, purified using a Talon anti-His resin batch procedure, and concentrated. Gel filtration was carried out on Superdex 75 and Superdex 200 columns in series. This setup was easily able to separate monomers, dimers, and higher order aggregates. The fractions were then collected, pooled, and concentrated. Reducing and non-reducing SDS-PAGE showed a single, monovalent band of the expected molecular weight. Competitive binding to the surface of LS174T cells was used to verify the affinity and specificity of binding to CEA. After fluorophore conjugation and dialysis, thin layer chromatography was used to verify the absence of free fluorophore. One μL of labeled antibody stock is pipetted onto glass backed 250 μm thick ultra pure silica gel thin layer chromatography plates (Silicycle, Quebec, Canada), allowed to dry, and incubated vertically in a sealed chamber with one edge in a saturated 70% ethanol aqueous solution. After 10-15 minutes, the plate was removed, dried, and imaged on a fluorescent imager. The free dye travels with the mobile phase, while the protein remains adhered to the original spot. The scFv concentrations were measured by absorption 280 ($[Ab]_{surf}$).

The diffusion coefficient (D) was measured using a non-binding irrelevant scFv. Since free diffusion within the spheroids is rapid relative to diffusion with binding, it was not possible to adjust the microscope settings after the addition of the non-binding antibody. To circumvent this problem, spheroids (attached to a coverslip) were preincubated with sm3E-597, and the microscope parameters (z-axis, laser intensity, z-stack settings, etc.) were setup first using the red channel. A non-specific scFv (4M5.3) labeled with Alexa-488 (green channel) was mixed in the well at a 250 nM concentration on the microscope stage, and images were taken every 15 seconds until fluorescence within the spheroid stopped increasing. The high concentration was required since, in the absence of binding, there is no

increase in the local concentration. For analysis, a circular region of interest was drawn around the periphery of the spheroid, and a radial average intensity was found for each time point. This average was adjusted to give the total volumetric uptake of material. The diffusion coefficient was fit using least squares to the series solution for uptake(40) truncated at 11 terms. Analysis by adjusting the signal for volumetric effects and comparing to the volumetric uptake in a sphere yielded the same result as comparing the area intensity to the area averaged uptake (Appendix section 11a). The internalization rate for CEA binders (k_e) was calculated(41), and the radius of the spheroids (R) was measured from the microscopic image.

Spheroids were grown by the hanging drop method(3) using microwell trays (Nunc, Rochester, NY). Subconfluent LS174T cells were trypsinized, and a 20 μL drop containing ~500 cells was transferred to wells in a microwell plate (Figure 3.1, left). The plates were inverted and incubated in EMEM plus 10% FBS at 37°C and 5% CO_2. After incubation upside down for 2 days, the cells formed compact spheroids (center image). Direct imaging of these spheroids complicates results due to higher scattering in the center of the spheroid than in the periphery. After cells were allowed to attach to glass coverslip bottom dishes for 2 days, the spheroids flattened into a hemi-sphere shape. To better picture the shape, a spheroid was dislodged with a needle and held on edge (image on right). The depth in the direction perpendicular to the glass coverslip ('z' direction) must be the same order as the radius. If not, diffusion from the top of the spheroid will cause saturation premature to the conditions predicted by the theory when using the larger radius (as measured in the x-y direction) as the length scale.
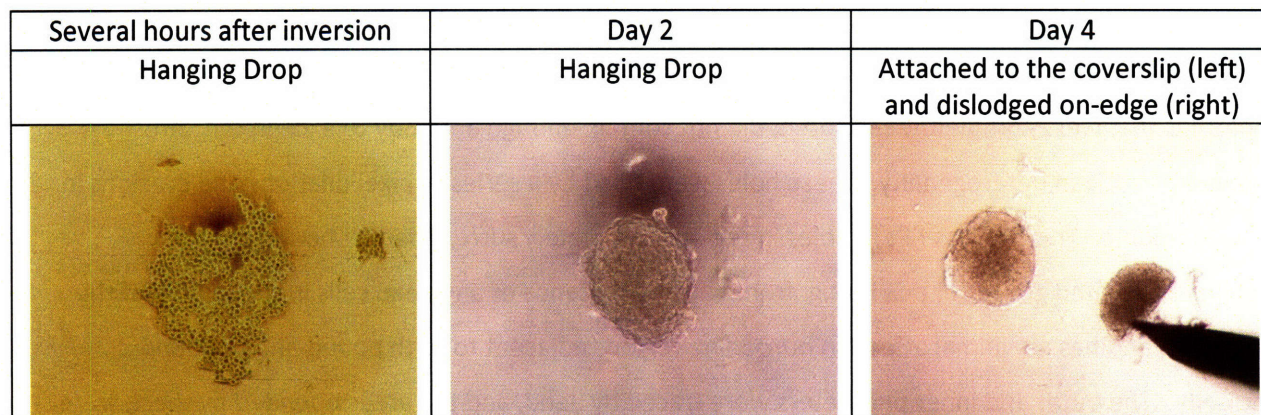
Several hours after inversion	Day 2	Day 4
Hanging Drop	Hanging Drop	Attached to the coverslip (left) and dislodged on-edge (right)

Figure 3.1 – LS174T spheroids were created using the hanging drop method. Approximately 500 cells were pipetted in 20 μL into a well, and inverted. After several hours, gravity causes the cells to collect in the bottom of the drop (left). The cells adhere to each other, drawing into a compact spheroid after 2 days (center). The spheroids are then moved to a glass coverslip bottom dish and allowed to adhere to the surface for 2 days. At this point, the bottom layer of cells is firmly adhered to the surface, but the spheroid maintains its hemisphere shape as shown by a spheroid dislodged and held on edge by a needle (right).

Fluorescent scFv was added to the wells for a defined time before or during imaging. The purified proteins were labeled with Alexa-488, Alexa-594, or Alexa-647 (Invitrogen) according to the manufacturer's instructions. A molecular ratio (MR) of 12 gave approximately 1-2 dyes per protein. Single chain antibody fragments (sm3E with a K_d = 30 pM and shMFE, K_d = 8 nM(39)) were incubated with spheroids for a given period of time. Images were taken on a Zeiss confocal microscope (Zeiss, Thornwood, NY) or Zeiss microscope with Spectra-Physics Ti-Sa laser for two-photon imaging. The confocal and two-photon microscopes allowed images to be taken in the presence of antibody in the bulk solution, yielding uninterrupted sequential images.

Analysis of imaging data from spheroids labeled with fluorescent antibody had several complicating factors including antigen heterogeneity, free antibody in the bulk solution, noise, autofluorescence, and spheroids that were not perfectly round. In order to obtain a single average distance for antibody penetration, the images were processed using a semi-automated routine in the following manner. First the image was despeckled to reduce the number of lone 'hot' pixels from noise, autofluorescence, and bulk antibody. A binary mask was created by thresholding the image at a low level just above the signal intensity from background noise and autofluorescence. Regions where the local fluorescent antibody concentration was increased due to binding exceeded this threshold and

were captured in the mask. The initial despeckling step helped eliminate the number of pixels that falsely exceeded the threshold due to aforementioned reasons. Some areas of the image, even in spheroids that were completely saturated, did not contain enough antibody to exceed this threshold because of antigen heterogeneity. These holes were filled by a series of pixel dilations and erosions in equal numbers. This process fills in holes in regions completely surrounded by bound antibody, eliminates isolated groups of pixels (e.g. from autofluorescence of any dead cells in the middle of the spheroid), and has a minimal effect on borderline regions adjacent to both bound and unbound antibody. The outer and inner perimeters were traced by hand, and the areas bounded by these were measured. The outer (spheroid) radius and inner (antibody front) radius were calculated from these areas by assuming a circular shape. All steps were automated and identical for all spheroids except for tracing the spheroid perimeters. Green fluorescent beads (Duke Scientific, Fremont, CA) were added to the wells to serve as internal controls. Although they had no direct impact on analysis of the data, consistent fluorescence intensity of these beads verified exposure conditions were constant across all experiments. The fluorescent beads sometimes merged with the outer perimeter and this area had to be excluded. More rarely, regions inside the spheroid that were autofluorescent due to dead cells would merge with the antibody front and were also excluded. This autofluorescence showed up in several fluorescent channels and could be distinguished from antibody signal which appears exclusively in the designated fluorophore channel. All image analysis was done in ImageJ (NIH). An example image and corresponding mask are illustrated in figure 3.2.
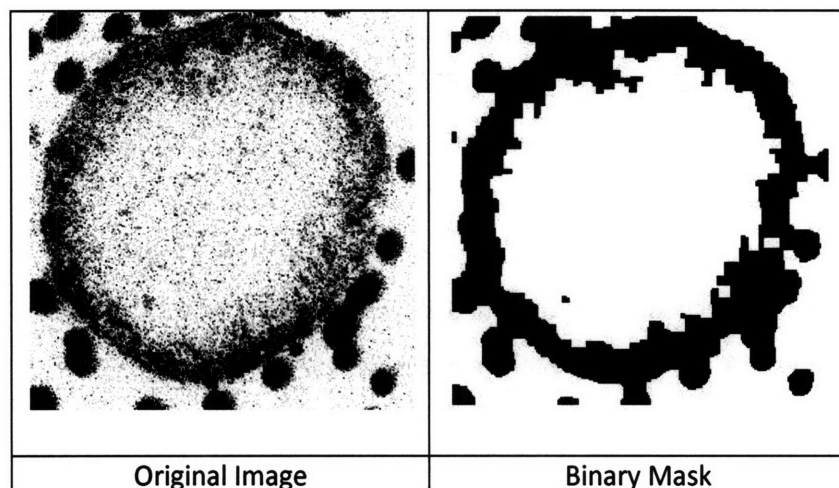
| Original Image | Binary Mask |

Figure 3.2 – An example of the image processing is shown above. A fluorescent image from the two-photon microscope is picture on the left, showing the increased intensity around the periphery. Fluorescent beads serving as an internal control for intensity surround the outside of the spheroid, and the center contains some gray regions due to autofluorescence (left). After processing the image (described in text), the binary mask is used to measure the outer and inner radii of the labeled spheroid (right). The original image and images in different color channels were used in conjunction with the mask to distinguish the beads and areas of autofluorescence.

This type of analysis is not valid for lower affinity or non-binding antibodies. In these cases, the scFv does not diffuse into the spheroid in a shrinking core manner (saturating cell layer after layer), so it is not possible to quantify the penetration depth in this way. The difference between the high and low affinity antibodies provides an example of how antigen saturation alone is not sufficient to describe antibody distribution. If a spheroid has 10% of its antigen saturated, this does not indicate whether 10% of the cells have 100% of their antigen bound, 100% of the cells have only 10% of their surface antigen complexed, or some combination in between.

For immunohistochemistry, spheroids were grown in a similar manner except they were not allowed to adhere to the coverglass. Fluorescent antibody (sm3E-488) was added directly to the drops, and the spheroids were incubated for an additional 48 hours. Individual spheroids were moved to Eppendorf tubes, centrifuged briefly to remove the media, and fixed with 250 µL Cytofix (BD Biosciences) for 3 hours at 4°C. After removing the fixative and washing in PBS, spheroids were suspended in 100 µL HistoGel and processed by the MIT Center for Cancer Research Histology lab.

Unstained sections from the center of the spheroids were then labeled with fluorescent antibody. The sections were first deparaffinized with 2x5 min washes in xylene, 2x3 min washes in 100%

87

ethanol, 1 min in 95% ethanol, 1 min in 70% ethanol, and rinsed in distilled water. For epitope retrieval, plates were boiled in Citrate-EDTA (10 mM citric acid, 2 mM EDTA, 0.05% Tween 20, pH 6.2) for 20 min and allowed to cool for 20 min. The plates were then blocked (2% FBS, 1% BSA, 0.1% Triton X-100, 0.05% Tween 20 in PBS) for 30 min on a rocker at room temperature. The scFv was already fluorescently tagged, so only an anti-CEA antibody was needed to label antigen. The non-competing antibody M85151a (Fitzgerald Industries) was incubated in PBS with 0.1% BSA at room temperature for 1 hour followed by 2x3 min washes in PBS-BSA. Images were taken on a widefield Deltavision microscope with filters appropriate for FITC and Cy5.

3.5   Anti-CEA scFv Results

The internalization rate of CEA bound antibodies must be determined in order to calculate the Thiele modulus. Endocytosis of a GPI linked protein is not surprising, since the well studied folate receptor is a GPI-linked protein that traffics folate across the membrane(42). One method of obtaining the rate of endocytosis is to saturate the surface of cells with a short incubation on ice to stop internalization, then warm them to 37^0C and measure the surface versus total fluorescence. For these experiments, a moderately differentiated colon adenocarcinoma cell line, LS174T, was chosen. LS174T cells are a commonly used CEA positive cell line, first isolated from a non-metastatic tumor(43). The cells were labeled with sm3E-488 on ice to saturate the surface, and then moved to a 37^0C incubator. At each time point, cells were dissociated with Gibco cell dissociation buffer, labeled with anti-His-PE to detect the His tag present on the surface accessible fraction, and analyzed using flow cytometry. (Cell dissociation buffer was used, although experiments indicated trypsin did not degrade a detectable fraction of the surface antigen.) The results are shown in figure 3.3, top. The surface signal drops slightly faster than the total signal, indicating a slow internalization rate. With a 4 day dissociation half life from the antigen, it is likely the drop in primary antibody signal is due to shedding(39). The experiment was carried out with the lower affinity shMFE, but the total signal is lost within the first hour due to rapid dissociation. The fluorescence in the media could be precipitated by TCA, indicating it was not due to fast degradation (data not shown). Due to the lower sensitivity of fluorescence, this required a large amount of antibody and number of cells.
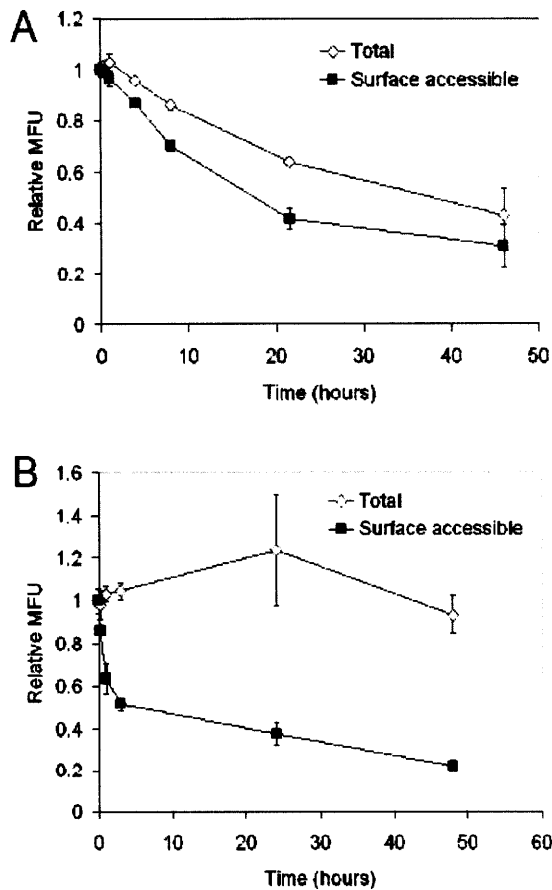
Figure 3.3 – The retention of antibody and scFv complexes on the surface of LS174T cells is shown for a high affinity scFv (A) and IgG M85151a (B) against CEA. The cells were labeled at 4^{0}C to saturate the surface, antibody was removed, and the cells were incubated at 37^{0}C for various times. At each time point, an anti-His tagged antibody (for the scFv) or an anti-Fc antibody (for the IgG) were used to label the surface accessible fraction, and both signals were normalized to the initial time point. The total antibody signal decays gradually over two days for the high affinity scFv, with the internal signal decaying at a slightly faster rate, indicating a slow net internalization (top). The IgG displays a different behavior, with a rapid drop in the surface accessible signal and virtually no change in total signal. This indicates the IgG is rapidly internalized from the cell surface (bottom).

The same experiment was carried out with an anti-CEA IgG, clone M85151a, figure 3.3 bottom. This clone was shown to down-regulate the amount of antigen on the surface. Subsequent experiments showed that this antibody causes rapid internalization, likely due to binding multiple epitopes per CEA molecule(41). Here, the primary signal does not decrease, since much of it is internalized and remains within the cell, but the secondary label decreases rapidly as clustering drives internalization. Microscope images of the cells show a large portion of antigen inside the cell that is not labeled with surface antibody, whereas cells incubated at 4^{0}C show only colocalization at the surface (figure 3.4).

89

Imaging experiments were performed to see if the mechanism of internalization could be pinpointed (figure 3.4). Various fluorescent dyes were used to test for colocalization with the anti-CEA scFvs. Although some colocalization is present with several of these markers, none are complete. The lack of a cytoplasmic domain probably results in the non-specific turn-over of CEA with the plasma membrane. Since no trafficking mechanism is 100%, CEA likely ends up in multiple compartments(44).
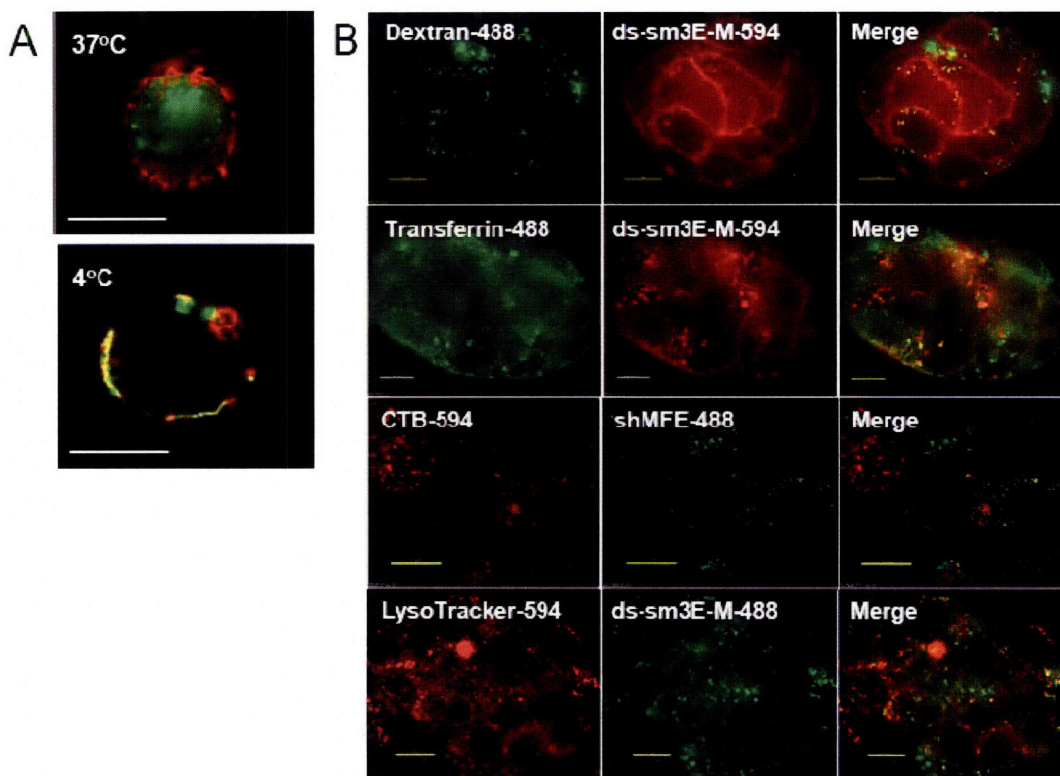

Figure 3.4: Imaging anti-CEA antibody uptake. A: Anti-CEA antibodies are trafficked into intracellular pools at 37°C. Trypsinized LS174T cells were surface labeled with Alexa-488 labeled IgG M85151a on ice and incubated for 24 hours at 4°C or 37°C. Cells were then labeled with goat-anti-mouse-PE and imaged on a deconvolution microscope. When incubated at 37°C a significant fraction of the 488 labeled anti-CEA antibodies are endocytosed into an intracellular pool where they are not labeled by the secondary antibody. Scale bar, 20 μm. B: Internalized anti-CEA antibodies partially colocalize with markers of endocytosis. LS174T cells were incubated overnight at 37°C with fluorescently labeled anti-CEA scFvs. Cells were then washed and incubated for 1 hour with fluorescently labeled markers of endocytic and lysosomal pathways. Dual label images were taken on a deconvolution microscope. The anti-CEA scFv shows partial but incomplete colocalization with all endocytic pathway markers. Each image is a cluster of 5-10 adherent LS174T cells. Scale bar, 10 μm.

Diffusion and binding of fluorescently tagged scFv molecules in tumor spheroids was monitored using confocal or multi-photon fluorescence microscopy, and the distance of penetration of these molecules was then compared to theoretical predictions. The scaling criteria used for these predictions consist of two moduli, which are ratios of parameters that capture fundamental rates (clearance, diffusion, internalization, etc.) that determine antibody and antibody fragment distribution. To make accurate predictions of antibody penetration with the clearance modulus and Thiele modulus criteria(45), all the pertinent parameters were measured independently in LS174T spheroids. The individual parameters, as outlined in Materials and Methods, were determined experimentally, and are presented in figure 3.5. Cell density is in line with previous estimates in other systems(12, 46), although it may be slightly higher in these spheroids than in solid tumors due to high viability and lack of other cell types. Antigen density is also in agreement with reported values(47), although variability on individual cells is high. The void fraction is slightly lower than previous estimates for scFv(48), likely due to the high cell density.

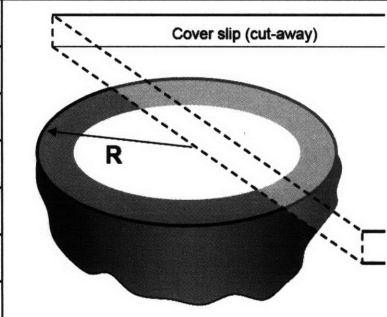| Parameter	Value	Abs Error	
Cell density	7.23×10^8 cell/mL	+/- 1.87×10^8	
Ag/cell	3.88×10^5 Ag/cell	+/- 4.7×10^3	
Antigen density	4.68×10^{-7} M	+/- 1.27×10^{-7}	
Epsilon	0.1537	+/- 0.011	
Diffusivity	33.1 μm^2/s	+/- 20.7	
k_e	1.23×10^{-5} s^{-1}	+/- 3.06×10^{-6}	

Figure 3.5. Experimental imaging setup and measured parameter values. Spheroids were allowed to attach to the coverglass and form a hemisphere shape. All the parameter values were measured separately to give an independent theoretical prediction for scFv distribution, and these were used in the analytical and numerical simulations.

The diffusion coefficient is lower than previously published values(14), and this value is averaged over the entire spheroid which incorporates the effects of extracellular matrix, tortuosity, and constriction between cells. The normalized intensity for the uptake of a non-binding scFv in 4 different spheroids is presented below (figure 3.6). The free diffusion coefficient measured in this way most closely captures the diffusion rate within the spheroids. Other techniques, such as FRAP, are typically done on the space between cells. While this captures any changes in diffusion due to extracellular

matrix proteins, it does not capture changes in the effective diffusion coefficient caused by the tortuous path and constriction in space between cells. Averaging the coefficient across the entire spheroid, however, includes these effects. The void fraction, which was measured separately, does not affect the time frame for uptake. However, it does affect the total flux of antibody entering the spheroid, so it is important when considering binding within the spheroid.
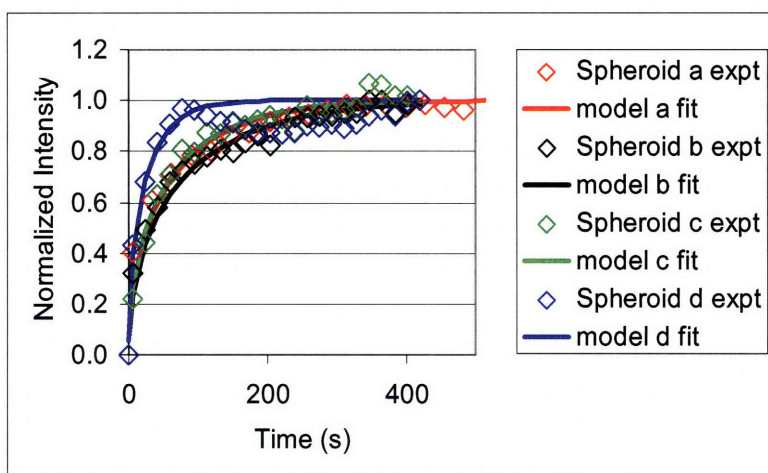

Figure 3.6 – A non-binding scFv (4M5.3), prewarmed to 37^0C, was added to a spheroid on a heated microscope stage at time zero, and confocal images were taken until the fluorescence intensity stopped increasing. After background subtraction and normalization to long time periods, the fluorescence intensity in the circular region of interest was measured over time. The diffusion coefficient was fitted to these data using the series solution for uptake in a sphere (Appendix 11a).

Live cell imaging of fluorescently labeled scFvs allowed the collection of dynamic diffusion and binding data. These spheroids are highly scattering, so even two-photon microscopy was not able to image in the center of the spheroids without geometric artifacts and low signal to noise. (When imaging an equatorial slice of a sphere, light from the periphery travels through the less scattering media, while light from the center must pass through the highly scattering tissue giving falsely lower signal in the center.) In order to circumvent this problem, the spheroids were first allowed to attach to coverslips. After sufficient time for attachment, diffusion of scFvs between the coverslip and the spheroid is negligible, as seen previously(11). This results in a 'physical slice' (the coverslip) through the spheroid (figure 3.5). The optical slicing ability of the two-photon microscope was used to image deeper into the spheroid to verify that scFv was not diffusing more rapidly near the coverslip.

a. Exposure Time (AUC) – Clearance Modulus

Antibody penetration into tumor tissue *in vivo* is predicted to be a function of exposure time and concentration, or the area under the curve (AUC)(14, 45). In this *in vitro* system, there is no clearance of the antibody fragment, so the concentration is constant over time. The AUC in this spheroid system is just the concentration outside the spheroid multiplied by the incubation time. In other words, spheroids need to be incubated for a sufficient period of time in order for the antibody to reach the center, and this time is a function of spheroid size, diffusion coefficient, antigen, and antibody concentrations. In the absence of antibody metabolism, this penetration time is predicted to be(14):

$$t_{sat} = \frac{R^2 \left([Ag] \middle/ \varepsilon \right)}{6D[Ab]_{surf}}$$
3.1

Figure 3.7 shows experimental images of dynamic penetration of scFv into a spheroid. Using 100 nM concentration of sm3E, the antibody fragment saturated the spheroid after 95 minutes of incubation (predicted time from the above formula is 57 min). This is in contrast to a non-binding scFv (4M5.3) that reaches 90% of total signal in 3 minutes due to lack of binding (above) or lower concentrations of sm3E that do not penetrate after 48 hours (and are theoretically predicted to never reach the center, because endocytic consumption exceeds diffusive flux). With such rapid penetration, antibody internalization (~15 hr half life) has a negligible effect on the saturation time. Although saturation is predicted to occur faster than measured in the experiment, much of this may be due to non-specific sticking of the antibody fragment. At concentrations above ~20 nM, scFv begins to adhere to the surface of cells (data not shown), requiring more scFv to diffuse into the spheroid in order to specifically bind the antigen.

For an order of magnitude estimate of the effects of non-specific sticking, the antigen concentration can simply be increased to account for the non-specific binding. Since the saturation time is increased roughly 50% over the model prediction, this means that the antigen concentration, which now includes specific and non-specific components, is approximately 50% larger, yielding roughly 200,000 non-specifically bound scFvs at a 100 nM concentration. At concentrations around 20 nM, the non-specific sticking is not detectable. If the non-specific binding is assumed to be linear in terms of concentration, this means it is not detectable at 40,000 antibodies per cell. In other words, when non-specific sticking falls below 10% of the specific binding sites per cell, it can no longer be detected, which is arguably reasonable for this system.
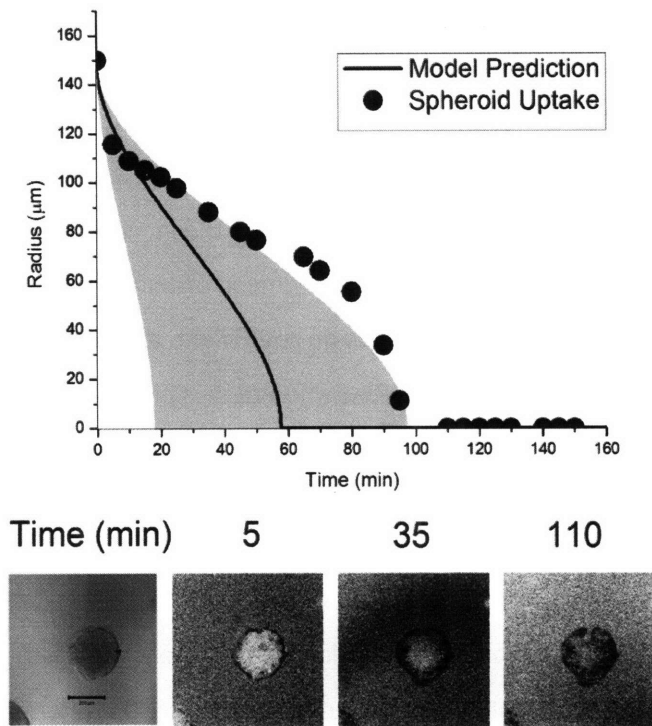
Figure 3.7. Live sm3E Diffusion with Binding in Spheroids. Top: The solid black dots mark the radius of the moving scFv front as a function of time. The black line indicates the theoretical prediction for a shrinking core (Appendix section 4a.i), and the gray shaded area marks plus and minus one standard deviation from the theoretical prediction due to error in the experimentally measured parameters. Bottom: A Differential Interference Contrast (DIC) image and three fluorescence images at various time points are shown. The high background is due to the 100 nM fluorescent scFv present in the bulk solution. Scale bar = 200 μm.

b. Internalization – Thiele Modulus

Looking at the above saturation time predicted by the clearance modulus, low doses of sm3E will reach every cell given sufficient exposure time. However, the Thiele modulus predicts that there is a threshold dose required to overcome internalization and metabolism of the surface bound antibody fragments to saturate all cells at steady state. Spheroids were incubated at low doses of sm3E for long periods of time (48 hours), and the radius of antigen saturation was measured. The experimental threshold dose required for saturation closely matches the theoretical prediction (figure 3.8, left). In all cases, the scFv was in excess at least 10-fold over antigen to avoid depletion in the bulk solution. The antibody concentrations were less than 20 nM, so non-specific binding was not detectable.
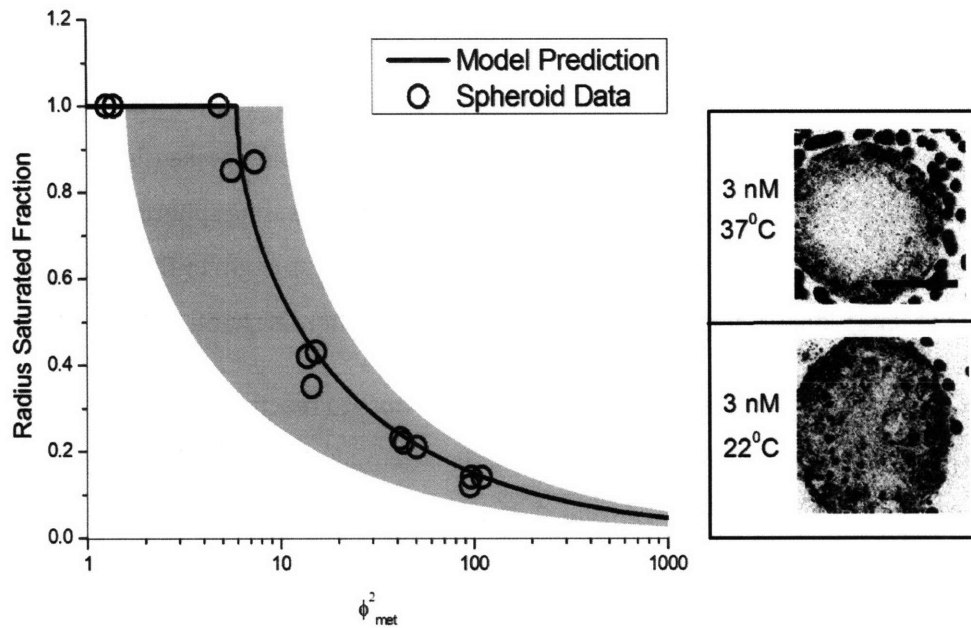
94

Figure 3.8. Steady State Spheroid Depth of Saturation. Left: The saturated fraction of the radius [(R_{tumor} − $r_{antibody\ front}$)/R_{tumor}] is plotted as a function of the Thiele modulus. The open circles indicate measured values for individual spheroids, and the black line is the theoretical prediction (Appendix section 5a.ii). The gray shaded area indicates plus and minus one standard deviation from the theory due to uncertainty in the experimentally measured parameters. Complete saturation occurs at $\varphi^2 = 6$ because the geometric shape factor of 6 (for spheres) which arises in the exact solution is not included in the Thiele modulus. Right: Images of two spheroids incubated at different temperatures are shown. Antibody fragment reaches the center at room temperature when internalization is reduced. The dark circles surrounding the spheroids are the green fluorescent beads serving as internal controls. Scale bar = 200 μm.

To further demonstrate that the lack of penetration is due to the slow internalization and degradation of scFv bound to antigen, spheroids were incubated at room temperature for 48 hours at identical concentrations. Internalization is significantly diminished at room temperature (data not shown), and antibody is able to reach the center (Figure 3, right). In the absence of internalization, a reduction in temperature would actually be expected to *decrease* the penetration distance by reducing the diffusion coefficient(49).

Since carcinoembryonic antigen is internalized with an approximately 15 hour half life, at longer incubation times, a steady state develops. The amount of antibody diffusing into the spheroid equals the amount of antibody being internalized on all saturated cells. Higher concentrations increase the

amount of antibody entering the spheroid, more cells become saturated, and this increases the amount of antibody internalized. For time periods shorter than this half life, antibody is still penetrating deeper into the spheroid in a manner dependent on the clearance modulus. This fact was used to isolate the clearance modulus effect by using high concentrations for the live spheroid uptake (figure 3.7). There is also an upper limit on labeling times caused by practical concerns. Incubating spheroids longer than 48 hours increases problems with growth and attachment. Some spheroids begin to flatten and spread out on the coverglass at times longer than 48 hours, losing their hemispheroid shape.

Because of the need to incubate cells longer than 15 hours to reach steady state and constraints on incubating cells greater than 48 hours at 37°C, it is difficult to make comparisons between room temperature and 37°C at time periods longer than 2 days. In fact, the two lowest concentrations of antibody used (1 nM and 0.5 nM) were not high enough to saturate the spheroids even without internalization (room temperature incubations). However, the penetration distance of antibody in these cases was still farther than the corresponding concentrations at 37°C and in agreement with the estimate for shrinking core penetration. When these spheroids were incubated for extended periods of time at room temperature (where growth and attachement are not a problem), the antibody eventually reached the center (data not shown). Comparing the room temperature and $37^{0}C$ results at 48 hrs to experimental predictions:
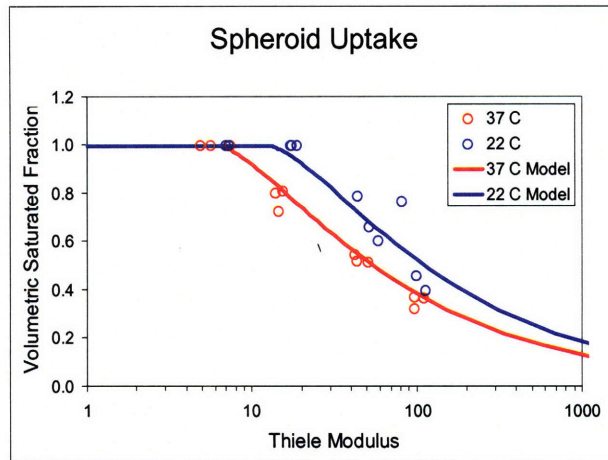
Figure 3.9 – LS174T spheroids were incubated with 7, 3, 1, and 0.5 nM antibody either at 37^0C or room temperature (~22^0C) for 48 hours. The volume fraction of cells saturated with antibody was measured as given above, and individual spheroids are marked with open circles. The steady state (maximum) distance of penetration as given by the Thiele modulus (Appendix 5a.ii) is compared to the uptake at 37^0C, while the penetration at room temperature is compared to the prediction by the clearance modulus (Appendix 4a.i) in the absence of internalization at 22^0C. Although the lowest two concentrations at room temperature did not reach the center after 2 days, they did reach the center at more extended periods of time, since without internalization, there is no limit to the depth of penetration.

Although the Thiele modulus would be zero for spheroids where there is no internalization, with the concentrations used and incubation time of 48 hours, the blue line predicts the fraction of the spheroid that would be saturated according to the clearance modulus. Only the two lowest concentrations have not completely saturated the spheroid, but the lack of internalization allows a greater fraction of cells to be labeled at this time point.

c. Affinity and Retention

Low affinity antibody fragments are predicted to have more homogenous distribution in tumor tissue(50), and this has been verified experimentally(51). To examine this effect in the spheroid system, a lower affinity variant of the sm3E scFv was used. This scFv, designated shMFE, has a dissociation constant of 8 nM versus the 30 pM dissociation constant of sm3E. There are only 2 amino acid changes between these scFvs, so affinity is the primary difference(39). As shown in figure 3.10, the 'low' affinity shMFE has a much more homogenous distribution in the spheroid compared to the bottom panel, which shows the heterogeneous distribution of the high affinity scFv. However, also note that the concentrations for shMFE are much higher than for sm3E in order to bind a significant fraction of

antigen. At the highest shMFE concentration (100 nM), the free scFv in the bulk is approaching the

antigen concentration in the spheroid (500 nM). This distribution is in agreement with numerical

simulations of antibody and antibody fragment penetration (figure 3.10, right). The disulfide stabilized

version of shMFE had to be used, since without this disulfide bond stabilizing the two domains, the

apparent affinity is much higher. This is likely due to the spontaneous formation of dimers.

Experiments with the dimers showed more heterogeneous distribution, (data not shown) indicating

avidity causes low affinity interactions to behave more like high affinity antibodies.
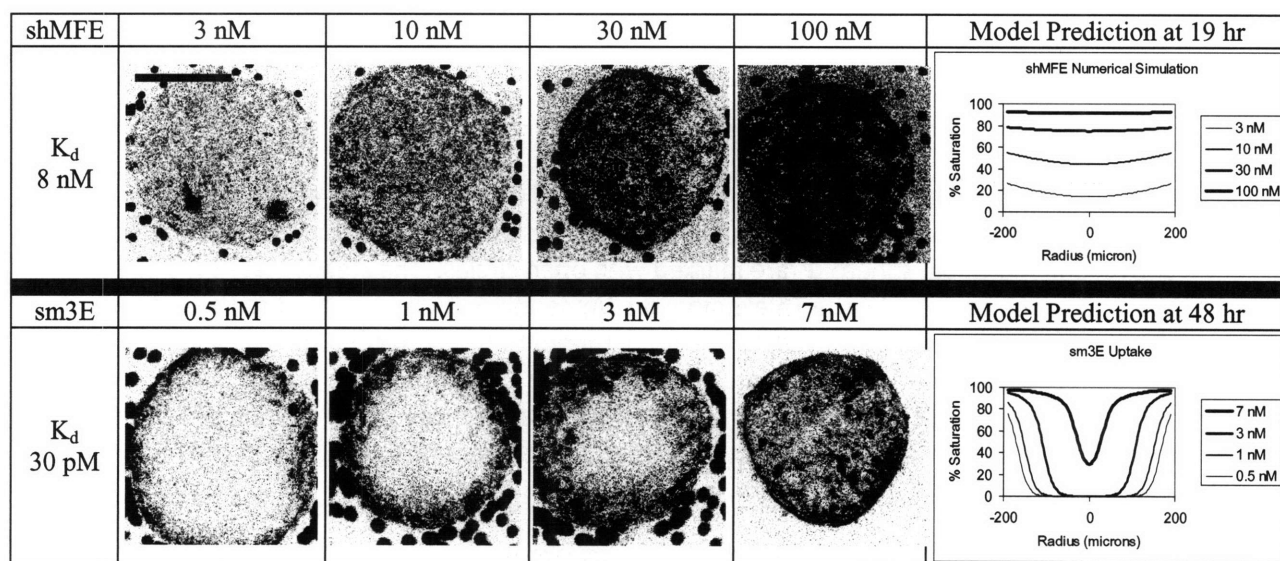
Figure 3.10 - Low Affinity versus High Affinity Distribution. Top: Images of spheroids exposed to various concentrations of shMFE for 19 hours are shown alongside the model predictions from numerical simulations (right). The high background is caused by fluorescent scFv in the bulk solution. Bottom: Spheroids were incubated with different concentrations of sm3E for 48 hours. Notice the concentrations are much lower for the high affinity scFv. Numerical simulation predictions are shown on the right. The numerical simulations used Appendix section 2 equations for diffusion and binding in a sphere. All images are adjusted to the same level of contrast. Scale bar = 200 μm.

Although numerical simulations are useful, scaling analyses can also be used to determine the

affinity necessary for a more homogenous distribution. If $[Ab]_{surf}$ is replaced with K_d in the clearance or

Thiele modulus terms, this scaling parameter determines whether antibody will reach a given radius(52).

Note that for low affinity antibody fragments, this does not mean antigen is saturated to this radius. It

only means that by repetitive binding, dissociation, and diffusion, some scFv was able to reach the given

radius.

$$\varphi^2 = \frac{k_e R^2 \left({[Ag]}/{\varepsilon} \right)}{D\left(K_d + [Ab]_{surf}\right)}$$

3.2

$$t_{center} = \frac{R^2 \left({[Ag]}/{\varepsilon} \right)}{D\left(K_d + [Ab]_{surf}\right)}$$

3.3

As affinity increases from that of shMFE to sm3E, the model predicts that the distribution will become increasingly heterogeneous as more scFv is bound at the higher affinities.

Due to the fact that a higher proportion of low affinity scFvs are not bound, they may not be adequately retained after the free antibody fragment is removed from the surface of the spheroid. The persistence of scFv in the spheroid after free scFv was removed from the bulk was directly tested in the spheroids. Spheroids were incubated with 20 nM sm3E or shMFE for 2.5 hours to quickly bind antigen. The dose was kept low to minimize non-specific sticking, and the time was short to minimize internalization during the binding phase, although this results in incomplete saturation. After this brief incubation, the media was exchanged to remove free antibody fragment, and the spheroids were incubated for 48 hours. Figure 3.11 shows the images after this 'wash out' period. The high affinity sm3E has a much stronger signal after 48 hours. The Alexa488 dye used in these studies remains inside the cells for an extended period of time after internalization (data not shown). Therefore, much of the signal that is seen may be from internalized antibody for both sm3E and shMFE. Numerical simulations provide further insights into this experiment. The high affinity sm3E remains bound such that very little diffuses out of the spheroid, and the total signal is high. After 2 days, the antigen turn-over (15 hr half life) has internalized a significant fraction of antibody fragment, but 15% still remains on the surface. The results are much different for the low affinity scFv. The rapid release and low fraction of bound scFv allows more homogenous penetration, but it also allows the antibody fragment to diffuse out of the spheroid. After 48 hours, much of the total signal is gone. The signal that does remain has all been internalized, and less than 0.5% of the antigen is predicted to be bound on the surface.
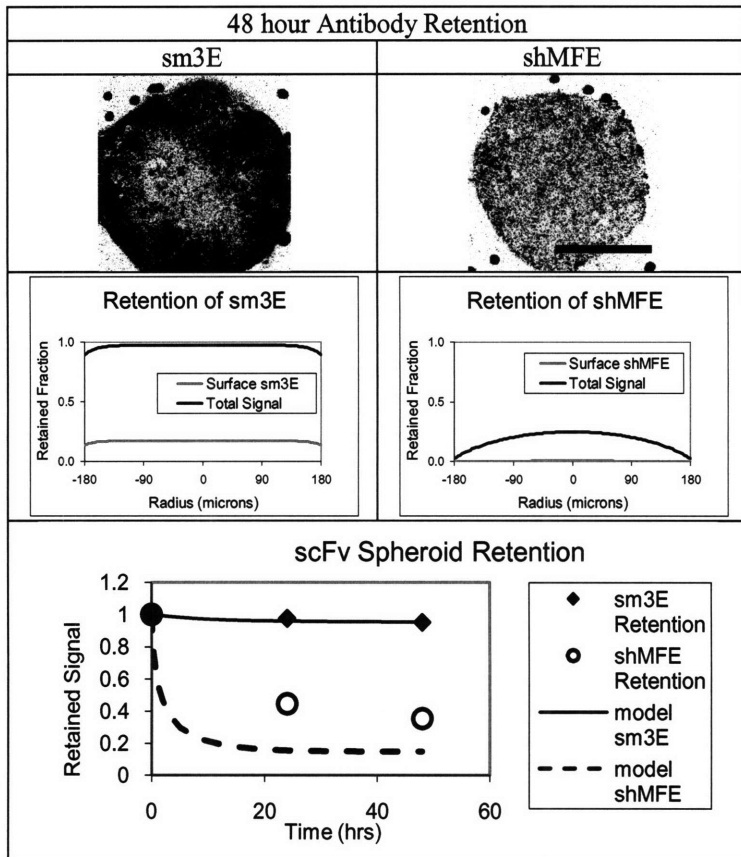
Figure 3.11 - Spheroids were incubated at 20 nM concentration for 2.5 hours, free scFv was removed, and they were incubated for 48 hours in plain media. Top: Images were taken of two spheroids after the 48 hour 'washout' period. Scale bar = 200 µm. Middle: Results of a numerical simulation where the spheroids were initially at equilibrium with 20 nM scFv, then moved to scFv free media for 48 hours. Bottom: Time course of retention for sm3E and shMFE in tumor spheroids. Average fluorescence of the entire spheroid was normalized to the initial signal after the 2.5 hr incubation. These spheroids were incubated in 100 nM scFv to ensure saturation at the initial time point. Numerical simulations used the equations in Appendix section 2 for diffusion in a sphere. The signal was integrated over the spheroid to yield the total retained signal for the bottom graph.

To validate the microscope imaging techniques used, spheroids were grown continually in a hanging drop without attachment to plates. They were incubated with sm3E, fixed, and analyzed by immunohistochemistry (IHC). In this setup, antigen could be labeled independently using a non-competing IgG in addition to the fluorescent scFv to look at colocalization. The top panels in figure 3.12 show sm3E, antigen, and merged images at three different concentrations. Looking at the scFv fluorescence, the two highest concentrations have $\varphi^2 < 6$ and are predicted to be saturated, in agreement with the images. The lowest concentration has peripheral fluorescence indicative of the lack

of penetration to the center of the spheroid. The heterogeneity of antigen on individual cells seen in flow cytometry is clearly apparent in the antigen density.
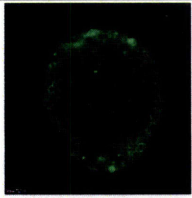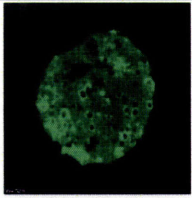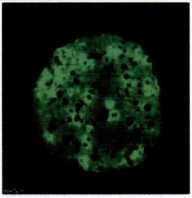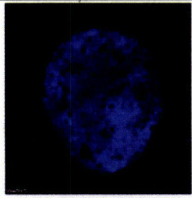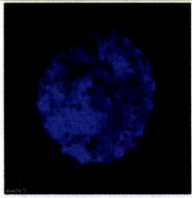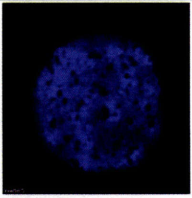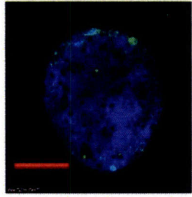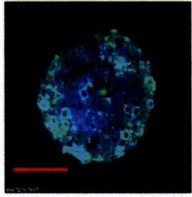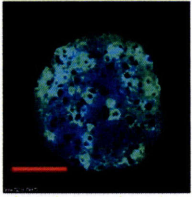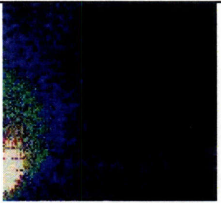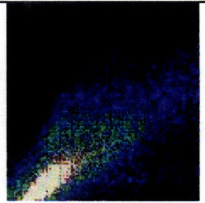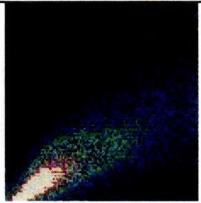
	1 nM $\varphi^2_{met} = 16.7$	3 nM $\varphi^2_{met} = 4.7$	10 nM $\varphi^2_{met} = 1.8$
Ab			
Ag			
Merge			
Pearson Correlation Coefficient	0.35	0.80	0.82
Intensity Scatter Plot Y = Ag X = Ab			

Figure 3.12 - Immunohistochemistry Analysis of Antibody Fragment Penetration. Top: Spheroids were incubated in suspension with 3 different concentrations of green fluorescent sm3E scFv for 48 hours. The spheroids were then processed for IHC and labeled with a non-competing anti-CEA antibody (blue fluorescence). The two highest concentrations have $\varphi^2 < 6$ and are predicted to be saturated. Bottom: Pearson Correlation coefficients were calculated for the fluorescence intensity of sm3E and antigen. Pixels with no fluorescence in either channel (background) were excluded from the analysis. Scatter plots of the fluorescent pixels are shown for all three images. Scale bar = 100 μm.

To quantitatively examine colocalization between antibody fragment and antigen, dot plots were created to evaluate the Pearson correlation coefficient. In this way, absolute intensity of either channel (microscope settings, differences in tags, etc.) does not influence the results. A major increase in the Pearson correlation coefficient occurs once the spheroid is saturated. Some correlation is

expected for the unsaturated spheroid, as there should be colocalization near the surface in the region where scFv is able to penetrate.

3.6   Discussion of anti-CEA scFvs

The tumor spheroid model system for measuring scFv penetration provides valuable insights into key aspects of antibody tumor targeting. Antibody distribution is dependent on a variety of parameters, and penetration to the center of a spheroid is not simply a binary result. The dose, antigen density, spheroid size, incubation time, and all the other parameters that appear in the clearance and Thiele moduli impact the results. The spheroids used here most closely resemble pre-vascular micrometastases in normal tissue. Other physiological barriers, such as lowered concentrations in normal tissue and inefficient extravasation across tumor capillaries, are not reproduced in the spheroid model system. Therefore the *in vitro* results do not directly mimic the *in vivo* results. Nevertheless, the fundamental processes of diffusion, binding, and endocytosis that determine distribution in spheroids are expected to closely replicate those acting *in vivo*.

The distribution of scFvs in these spheroids lacks a major barrier to penetration in solid tumors, namely the capillary wall, as well as systemic clearance. Spheroid saturation is therefore not sufficient to predict *in vivo* saturation, but since the transport barriers in the spheroid system also exist *in vivo*, it is a necessary condition that a spheroid be saturated in order for the corresponding tumor to be saturated. Due to elevated interstitial pressure, convection in the tumor is negligible, and the dominate mode of transport is diffusion(53), similar to the spheroids. Therefore, although the supply of antibodies is severely limited compared with these spheroids (and the surface concentrations are very low), the distribution is expected to follow the same principles. Poor extravasation of macromolecules in tumors(54) results in concentrations outside the tumor capillary that can be 100-1000 fold below that found in the plasma(55). The modeling results can then be modified in order to account for these additional complications present in vascularized tumors *in vivo*. For example, given a 1 µM dose of antibody in the plasma and a Biot number of 0.004, the approximate tissue concentration would be 4 nM, so the penetration distance would be similar to a spheroid exposed to a 4 nM concentration. This much lower concentration is one reason why saturation of a CEA spheroid occurs in less than 2 hours at a 100 nM dose (above), but several days with concentrations in the micromolar range are required to

saturate a tumor *in vivo*(56). Modeling for the case of solid tumors as compared to spheroids and metastases has been carried out previously and shown to agree with published data(45).

These experiments have demonstrated that two simple model scaling criteria can predict the distribution of antibody fragments in spheroids. The clearance modulus, which predicts the exposure time required to saturate spheroids, and the Thiele modulus, which predicts the concentration required to overcome internalization in order to reach the center of a spheroid, are criteria that quantitatively capture the major determinants in antibody distribution.

Experiments with high affinity scFvs show steep gradients as the 'core' of unbound antigen 'shrinks' when antibody binds the outer layers of cells. Conceptually, these high affinity antibodies bind at saturating concentrations 'from the outside in' (figure 3.10, bottom). Most IgG molecules travel through tumor tissue in this "shrinking core" fashion (saturating cell layer after cell layer) due to their rapid binding to free antigen, slow diffusion coefficients(14), and slow dissociation caused by multivalent interactions. They are often internalized before they have a chance to dissociate and diffuse farther into the tissue(57) resulting in "shrinking core" penetration with effectively irreversible binding. However, with newer protein engineering techniques (scFvs, Fabs, single domain antibodies, alternative protein scaffolds), these new proteins, which are often smaller and monovalent, can exhibit 'non-shrinking core' transport in tumor tissue.

Lower affinity scFvs display a more diffuse gradient, yielding more homogenous labeling of the spheroids with lower amounts of bound antibody; conceptually, they bind antigen at sub-saturating concentrations 'from the bottom up' (figure 3.10, top). If a significant fraction of antigen must be bound for the desired effect, however, much higher concentrations have to be used with the lower affinity fragments. As mentioned previously, antibody and antibody fragment concentrations in solid tumors are often very low *in vivo*. The rapid dissociation and high fraction of unbound scFv allows the lower affinity monovalent scFv to penetrate more homogenously(55). Increasing the valency would hinder complete dissociation and result in distributions similar to higher affinity binders. Unfortunately it is the same ability to rapidly dissociate that allows scFv to diffuse back out of the tissue once the surrounding concentration has dropped.

The poor retention of lower affinity binders has implications for both imaging and pretargeting therapies. As systemic antibody is cleared from the circulation, the total signal of low affinity antibodies will be reduced in the tumor tissue. Even if a residualizing radioisotope is used for imaging, much of this

is lost due to diffusion out of the tissue before it can be internalized during the waiting period while clearance is reducing background levels. For pretargeting techniques, a waiting period is again required for normal tissue levels to drop. The surface concentration is the parameter of interest since this is the only antibody accessible to secondary agents. In the retention experiment, diffusion out of the spheroid occurred much more rapidly for the low affinity scFv, resulting in higher surface concentrations for the sm3E antibody than shMFE.

Although antibody fragments rapidly diffuse in and out of spheroids, similar to a micrometastasis, the retention in solid tumors is predicted to be very different. Because the capillary wall is a significant barrier to extravasation, once the antibody has reached the tumor tissue, it is very slow to *intravasate* back into the blood. Thus, for large molecules, this enhanced permeability and retention ('EPR') effect occurs relatively independent of affinity. For smaller molecules with higher permeabilities, binding is predicted to be more important in preventing loss from the tumor due to a lower EPR effect.

Antigen labeling in the IHC experiment shows extensive CEA heterogeneity in the spheroids, as was seen on a per-cell basis in the flow cytometry experiments, and this is an important point for therapy. Looking at the merged images (figure 3.12), the lowest concentration spheroid clearly has antigen in the center that has not been reached by sm3E. At the highest concentration, virtually every area of high antigen concentration has correspondingly high scFv concentrations, indicative of saturation. The middle concentration is more interesting. With this size spheroid, a 3 nM concentration of scFv is predicted to just reach the center, and sm3E has penetrated this far as seen in the green channel. However, there is also a region in the bottom left side with very high antigen concentration that is not completely saturated by scFv. The local increase in antigen concentration (and possibly decrease in void fraction, diffusion coefficient, etc.) has apparently prevented saturation of this region, and this is responsible for the small shoulder on the top portion of the scatter plot. The live cell imaging experiments would not have picked up on the high local antigen density since they only analyze the antibody fragment fluorescence signal. These IHC experiments better capture the local heterogeneities found in solid tumors and metastases by being able to independently detect antibody and antigen. In the live cell experiments, however, the relationship between dose and penetration distance is more clearly established despite the complicating factor of antigen heterogeneity. This antigen heterogeneity can result in antibody heterogeneity even following full antigen saturation.

A small number of fundamental processes dictate the distribution of antibodies and antibody fragments in tumor tissue, and the scaling criteria (Thiele and clearance moduli) capture these rates in order to better understand and predict penetration. The moduli simply relate the supply and demand of free antibody. As a bolus dose clears the plasma and normal tissues, the supply of antibody entering the tumor tissue continually shrinks, and the demand for antibody remains high as more layers of cells are bound. The clearance modulus captures this ratio and predicts the penetration distance prior to clearance. Similarly, even with a steady supply entering from the circulation, demand for antibody to replace molecules that were internalized or degraded may immobilize the free antibody before it can reach every cell. This is in effect the distance that the Thiele modulus predicts.

The implications of these experiments and scaling criteria lend insight into optimizing antibody and antibody fragment imaging and therapy experiments. In order to target all cells with a high affinity binder, the dose must exceed the limitations posed by clearance and internalization as given in the scaling criteria. Decreasing the clearance rate far below the antigen turn-over rate will not increase penetration into the tissue, as antibody metabolism becomes rate limiting. Lower affinity binders result in a more homogenous distribution when the K_d is large enough to reduce the scaling moduli below one. Unfortunately, the total amount entering the tumor is still small, and the fraction that is bound is even less. For pre-vascular metastases and proteins with high permeability, retention of these antibodies will also be poor. For imaging experiments, penetration of antibodies and fragments (and the associated signal) is directly proportional to the AUC. Increasing clearance rates reduces background noise, but it also decreases signal. A more optimal plasma profile would have an extended period of high concentration for tumor uptake followed by rapid clearance, advocating the use of clearing agents. A similar strategy would benefit pretargeting methods.

Understanding the major determinants for antibody and antibody fragment uptake, distribution, and retention in tumors and micrometastases can point to ways of improving and optimizing therapies. The requirements of bound antibody, total antibody uptake, and retention required for successful imaging and therapeutic modalities can be compared to the actual values attainable as predicted by the model based on all the relevant parameters: dose, clearance, internalization, extravasation, diffusion, antigen density, and tumor vascular density. The choice of antigen target, antibody fragment size, and other protein engineering decisions can be made rationally in order to optimize the desired therapeutic or imaging result. Improvements in protein engineering, imaging sensitivity and resolution, toxin

conjugates, Fc effector functions, signal blockade, and other areas relevant to antibody targeting will further push developments in antibody based therapies for the diagnosis and treatment of cancer.

References

1.	Minchinton AI, Tannock IF. Drug penetration in solid tumours. Nature Reviews Cancer 2006;6:583-92.
2.	Sutherland R. Cell and Environment Interactions in Tumor Microregions: The Multicell Spheroid Model. Science 1988;240:177-84.
3.	Kelm J, Timmins N, Brown C, Fussenegger M, Nielsen L. Method for Generation of Homogenous Multicellular Tumor Spheroids Applicable to a Wide Variety of Cell Types. Biotechnology and Bioengineering 2003;83:173-80.
4.	Ivascu A, Kubbies M. Rapid generation of single-tumor spheroids for high-throughput cell function and toxicity analysis. 2006;11:922-32.
5.	Sutherland R, Buchegger F, Schreyer M, Vacca A, Mach J. Penetration and Binding of Radiolabeled Anti-Carcinoembryonic Antigen Monoclonal Antibodies and Their Antigen Binding Fragments in Human Colon Multicellular Tumor Spheroids. Cancer Research 1987;47:1627-33.
6.	Langmuir V, McGann J, Buchegger F, Sutherland R. ^{131}I-Anticarcinoembryonic Antigen Therapy of LS174T Human Colon Adenocarcinoma Spheroids. Cancer Research 1989;49:3401-6.
7.	Langmuir V, McGann J, Buchegger F, Sutherland R. The Effect of Antigen Concentration, Antibody Valency and Size, and Tumor Architecture on Antibody Binding in Multicell Spheroids. Nuclear Medicine and Biology 1991;18:753-64.
8.	Langmuir V, Mendonca H, Woo D. Comparisons between Two Monoclonal Antibodies That Bind to the Same Antigen but Have Differing Affinities: Uptake Kinetics and ^{125}I-Antibody Therapy Efficacy in Multicell Spheroids. Cancer Research 1992;52:4728-34.
9.	Hjelstuen MH, Rasch-Halvorsen K, Bruland O, Davies CD. Uptake, penetration, and binding of monoclonal antibodies with increasing affinity in human osteosarcoma multicell spheroids. Anticancer Research 1998;18:3153-61.
10.	Hjelstuen MH, RaschHalvorsen K, Brekken C, Bruland O, Davies CDL. Penetration and binding of monoclonal antibody in human osteosarcoma multicell spheroids - Comparison of confocal laser scanning microscopy and autoradiography. Acta Oncologica 1996;35:273-9.
11.	Myrdal S, Foster M. Time-Resolved Confocal Analysis of Antibody Penetration into Living, Solid Tumor Spheroids. Scanning 1994;16:155-67.
12.	Ballangrud AM, Yang WH, Charlton DE, et al. Response of LNCaP spheroids after treatment with an alpha-particle emitter (Bi-213)-labeled anti-prostate-specific membrane antigen antibody (J591). Cancer Research 2001;61:2008-14.

13.   Ballangrud AM, Yang WH, Palm S, et al. Alpha-particle emitting atomic generator (actinium-225)-labeled trastuzumab (herceptin) targeting of breast cancer spheroids: Efficacy versus HER2/neu expression. Clinical Cancer Research 2004;10:4489-97.

14.   Graff CP, Wittrup KD. Theoretical analysis of antibody targeting of tumor spheroids: importance of dosage for penetration, and affinity for retention. Cancer Res 2003;63:1288-96.

15.   Carlsson J, Gedda L. Penetration of Tumor Therapy Interesting Substances in Non-Vascularized Metastases: Review of Studies in Multicellular Spheroids. Current Cancer Therapy Reviews 2006;2:293-304.

16.   Devys A, Thedrez P, Gautherot E, et al. Comparative targeting of human colon-carcinoma multicell spheroids using one- and two-step (bispecific antibody) techniques. International Journal of Cancer 1996;67:883-91.

17.   Wenning LA, Murphy RM. Coupled cellular trafficking and diffusional limitations in delivery of immunotoxins to multicell tumor spheroids. Biotechnol Bioeng 1999;62:562-75.

18.   Davies Cde L, Berk DA, Pluen A, Jain RK. Comparison of IgG diffusion and extracellular matrix composition in rhabdomyosarcomas grown in mice versus in vitro as spheroids reveals the role of host stromal cells. Br J Cancer 2002;86:1639-44.

19.   Jain RK. Transport of Molecules, Particles, and Cells in Solid Tumors. Annual Reviews in Biomedical Engineering 1999;01:241-63.

20.   Hammarstrom S. The carcinoembryonic antigen (CEA) family structures, suggested functions and expression in normal and malignant tissues. Cancer Biology 1999;9:67-81.

21.   Aquino A, Formica V, Prete SP, et al. Drug-induced increase of carcinoembryonic antigen expression in cancer cells. Pharmacological Research 2004;49:383-96.

22.   Akamatsu Y, Murphy JC, Nolan KF, et al. A single-chain immunotoxin against carcinoembryonic antigen that suppresses growth of colorectal carcinoma cells. Clinical Cancer Research 1998;4:2825-32.

23.   Pignatelli M, Durbin H, Bodmer W. Carcinoembryonic antigen functions as an accessory adhesion molecule mediating colon epithelial cell-collagen interactions. Proceedings of the National Academy of Science, USA 1989;87:1541-5.

24.   Kinugasa T, Kuroki M, Yamanaka T, et al. Non-proteolytic release of carcinoembryonic antigen from normal human colonic epithelial cells cultured in collagen gel. International Journal of Cancer 1994;58:102-7.

25.   Shi Z, Tsao D, Kim Y. Subcellular Distribution, Synthesis, and Release of Carcinoembryonic Antigen in Cultured Human Colon Adenocarcinoma Cell Lines. Cancer Research 1983;43:4045-9.

26.   Behr T, Behe M, Lohr M, et al. Therapeutic advantages of Auger electron- over beta-emitting radiometals or radioiodine when conjugated to internalizing antibodies. European Journal of Nuclear Medicine 2000;27:753-65.

27.   Liu GZ, He J, Dou SP, Gupta S, Rusckowski M, Hnatowich DJ. Further investigations of morpholino pretargeting in mice - establishing quantitative relations in tumor. European Journal of Nuclear Medicine and Molecular Imaging 2005;32:1115-23.

28.   Bryan JN, Jia F, Mohsin H, et al. Comparative uptakes and biodistributions of internalizing vs. noninternalizing copper-64 radioimmunoconjugates in cell and animal models of colon cancer. Nuclear Medicine and Biology 2005;32:851-8.

29.   Ford C, Tsaltas G, Osbourne P, Addetia K. Novel Flow Cytometric Analysis of the Progress and Route of Internalization of a Monoclonal Anti-Carcinoembryonic Antigen (CEA) Antibody. Cytometry 1996;23:228-40.

30.   Tsaltas G, Ford C, Gallant M. Demonstration of Monoclonal Anti-Carcinoembryonic Antigen (CEA) Antibody Internalization by Electron Microscopy, Western Blotting and Radioimmunoassay. Anticancer Research 1992;12:2133-42.

31.   Bosslet K, Luben G, Schwarz A, et al. Immunohistochemical localization and molecular characteristics of three monoclonal antibody-defined epitopes detectable on carcinoembryonic antigen (CEA). International Journal of Cancer 1985;36:75-84.

32.   Cai W, Olafsen T, Zhang X, et al. PET imaging of colorectal cancer in xenograft-bearing mice by use of an 18F-labeled T84.66 anti-carcinoembryonic antigen diabody. J Nucl Med 2007;48:304-10.

33.   Sharma SK, Pedley RB, Bhatia J, et al. Sustained tumor regression of human colorectal cancer xenografts using a multifunctional mannosylated fusion protein in antibody-directed enzyme prodrug therapy. Clin Cancer Res 2005;11:814-25.

34.   Kraeber-Bodere F, Rousseau C, Bodet-Milin C, et al. Targeting, Toxicity, and Efficacy of 2-Step, Pretargeted Radioimmunotherapy Using a Chimeric Bispecific Antibody and 131I-Labeled Bivalent Hapten in a Phase I Optimization Clinical Trial. J Nucl Med 2006;47:247-55.

35.   Wegener WA, Petrelli N, Serafini A, Goldenberg DM. Safety and efficacy of arcitumomab imaging in colorectal cancer after repeated administration. J Nucl Med 2000;41:1016-20.

36.   Liersch T, Meller J, Kulle B, et al. Phase II Trial of Carcinoembryonic Antigen Radioimmunotherapy With ^{131}I-Labetuzumab After Salvage Resection of Colorectal Metastases in the Liver: Five-Year Safety and Efficacy Results. Journal of Clinical Oncology 2005;23:6763-70.

37.   Wong J, Shibata S, Williams L, et al. A Phase I Trial of ^{90}Y-Anti-Carcinoembryonic Antigen Chimeric T84.66 Radioimmunotherapy with 5-Fluorouracil in Patients with Metastatic Colorectal Cancer. Clinical Cancer Research 2003;9:5842-52.

38.   Willkomm P, Bender H, Bangard M, Decker P, Grunwald F, Biersack H. FDG PET and Immunoscintigraphy with ^{99m}Tc-Labeled Antibody Fragments for Detection of the Recurrence of Colorectal Carcinoma. The Journal of Nuclear Medicine 2000;41:1657-63.

39.   Graff C, Chester K, Begent R, Wittrup KD. Directed Evolution of an Anti-Carcinoembryonic Antigen scFv with a Four-Day Monovalent Dissociation Half-time at 37 °C. Protein Engineering, Design, & Selection 2004;17:293-304.

40.   Crank J. The Mathematics of Diffusion. 2 ed. Oxford: Clarendon Press; 1975.

41.   Schmidt MM, Thurber GM, Wittrup KD. Kinetics of Anti-Carcinoembryonic Antigen (CEA) Antibody Internalization: Effects of Affinity, Bivalency, and Stability. Cancer Immunology and Immunotherapy Submitted.

42.   Kamen B, Smith A. A review of folate receptor alpha cycling and 5-methyltetrahydrofolate accumulation with an emphasis on cell models in vitro. Advanced Drug Delivery Reviews 2004;56:1085-97.

43.   Tom B, Rutzky L, Jakstys M, Oyasu Y, Kaye C, Kahan B. Human Colonic Adenocarcinoma Cells. I. Establishment and Description of a New Line. In Vitro 1976;12:180-91.

44.   Maxfield F, McGraw T. Endocytic Recycling. Nature Reviews Molecular Cell Biology 2004;5:121-32.

45.   Thurber GM, Zajic SC, Wittrup KD. Theoretic criteria for antibody penetration into solid tumors and micrometastases. J Nucl Med 2007;48:995-9.

46.   Lyng H, Haraldseth O, Rofstad EK. Measurement of cell density and necrotic fraction in human melanoma xenografts by diffusion weighted magnetic resonance imaging. Magnetic Resonance in Medicine 2000;43:828-36.

47.   Berk DA, Yuan F, Leunig M, Jain RK. Direct in vivo measurement of targeted binding in a human tumor xenograft. Proc Natl Acad Sci U S A 1997;94:1785-90.

48.   Krol A, Nagaraj S, Dewhirst M, Yuan F. Available volume fraction of macromolecules in tumor tissues. Faseb Journal 2000;14:A167-A.

49.   Brown EB, Boucher Y, Nasser S, Jain RK. Measurement of macromolecular diffusion coefficients in human tumors. Microvasc Res 2004;67:231-6.

50.   Fujimori K, Covell DG, Fletcher JE, Weinstein JN. A modeling analysis of monoclonal antibody percolation through tumors: a binding-site barrier. J Nucl Med 1990;31:1191-8.

51.   Adams G, Schier R, McCall A, et al. High Affinity Restricts the Localization and Tumor Penetration of Single-Chain Fv Antibody Molecules. Cancer Research 2001;61:4750-5.

52.   Thurber G, Schmidt M, Wittrup KD. Poor Antibody Penetration into Tumors: Systemic and Endocytic Clearance Critically Limit Transport. Trends in Pharmacological Sciences 2007, **In Press**.

53.   Pluen A, Boucher Y, Ramanujan S, et al. Role of tumor-host interactions in interstitial diffusion of macromolecules: Cranial vs. subcutaneous tumors. Proceedings of the National Academy of Sciences of the United States of America 2001;98:4628-33.

54.   Yuan F, Dellian M, Fukumura D, et al. Vascular Permeability in a Human Tumor Xenograft: Molecular Size Dependence and Cutoff Size. Cancer Research 1995;55:3752-6.

55.   Thurber G, Schmidt M, Wittrup KD. Factors determining antibody distribution in tumors. Trends in Pharmacological Sciences 2008;29:57-61.

56.   Blumenthal RD, Fand I, Sharkey RM, Boerman OC, Kashi R, Goldenberg DM. The Effect of Antibody Protein Dose on the Uniformity of Tumor Distribution of Radioantibodies - an Autoradiographic Study. Cancer Immunology Immunotherapy 1991;33:351-8.

57.   Mattes MJ, Griffiths G, Diril H, Goldenberg D, Ong G, Shih L. Processing of Antibody-Radioisotope Conjugates after Binding to the Surface of Tumor Cells. Cancer 1994;73:787-93.

Chapter 4 – Theory of the Time Course of Antibody Concentration in Tumors

4.1   Importance of the Time Course of Antibody Concentration in Tumors

The previous chapters focused on the spatial distribution of antibodies in tumor tissue, and these considerations are important from a therapeutic perspective. For some therapies, such as pretargeting, the timing of the dose is important, and the time course for uptake and clearance is crucial for antibody targeted imaging applications. An analysis of the same kinetic rates that determined the spatial distribution can also provide the expected time course of antibody in the tumor.

Similar to the dimensional analysis for the spatial distribution of antibodies, a reductionist approach will be taken to provide the simplest description possible for the time course of uptake. The motivation is to provide a simple model that can describe general trends for antibody localization as a function of dose, clearance, affinity, etc. Uptake for many antibodies takes several days(1) and appears to be non-specific in some cases(2). Even so, some researchers have demonstrated that affinity does yield higher uptake than non-binding molecules(3, 4). This model aims to present these findings as a function of the timing, dose, antibody affinity, and target antigen. From an engineering perspective, the partial differential equations and time-dependent boundary conditions (appendix section 2) that were scaled for the spatial distribution will now be scaled for the temporal component.

4.2   Background on Vascular Distribution and Antibody Uptake

The distribution of antibodies in tumors is an extremely complex, erratic process. Vascularized tumors have a network of poorly formed vessels throughout a highly disorganized, heterogeneous cluster of tumor and multiple other cell types. Due to several biological mediators secreted by local cells, the blood vessels are highly permeable, and, with the lack of efficient lymphatic drainage, this leads to elevated interstitial pressure and collapse of the normal pressure gradients between the tissue and vessel. With the loss of pressure across the capillary wall, these vessels are susceptible to collapse from the growth and solid stress of the surrounding cancerous tissue, causing areas of low vessel density and necrosis. The disrupted pressure gradients and malformed, tortuous paths of vessels interfere with blood flow patterns, causing temporary cessation and even reversal of direction. Poor flow and avascular regions give rise to hypoxia, making some areas more resistant to radiation and chemotherapeutics. Once antibodies exit the blood vessel, they face a variety of other barriers. The

lack of convection means these macromolecular drugs rely primarily on diffusion to extravasate and move through the tissue. Variations in extracellular matrix and cell density cause heterogeneous diffusion in the tumor(5). Rapid binding to their target immobilizes these drugs almost immediately, causing perivascular localization, and differences in local antigen density further vary the local concentration even in regions that are efficiently targeted.

Given the stochastic development of the vasculature and complexity of targeting in tumors, modeling the uptake within tumors is an unwieldy task. There will be intra- and inter-tumor variability, and this will be even greater in the clinic than in animal models. However, a basic understanding of the most important parameters can help in designing experiments, interpreting data, and developing strategies to improve targeting. It is equally useful in determining what assumptions have not been met when tumor uptake is widely different than what is expected, and whether these differences can be exploited.

The purpose of developing this time-dependent model is four-fold. First, this model provides a simple description of the time course of antibody uptake to illustrate the effects of dose, clearance, internalization, affinity, permeability, and vascular density. The model also extends the results of the microscopic modeling around a single capillary(6) to illustrate the effects on total tumor uptake. Given the large spatial heterogeneities present in tumors, treatment of the tumor as a single well mixed compartment is unfounded. This analysis will place these compartmental (i.e. lumped) models of tumor uptake on a more firm theoretical basis by showing the effects of heterogeneity on uptake. Finally, this model provides a mechanistic description of uptake in tumors. Rather than having empirical exchange rates between compartments that are fit to experimental data, the mechanistic description pinpoints areas that can be used to design improved therapies.

4.3   Model Development

Antibody taken up in a tumor enters either from the vasculature or the outer surface from the surrounding tissue. Once in the tumor interstitium, it will bind, dissociate, and be internalized by cells. Signal will be lost from the tumor in much the same way, either by diffusing back into the vasculature, out of the tumor surface, or by being degraded in the cells. During degradation, the label may behave differently than the antibody, either diffusing out of the tumor or being retained in the cells. The

movement of antibody between the plasma, normal tissues, tumor interstitium, and surface complexes is illustrated in figure 4.1.
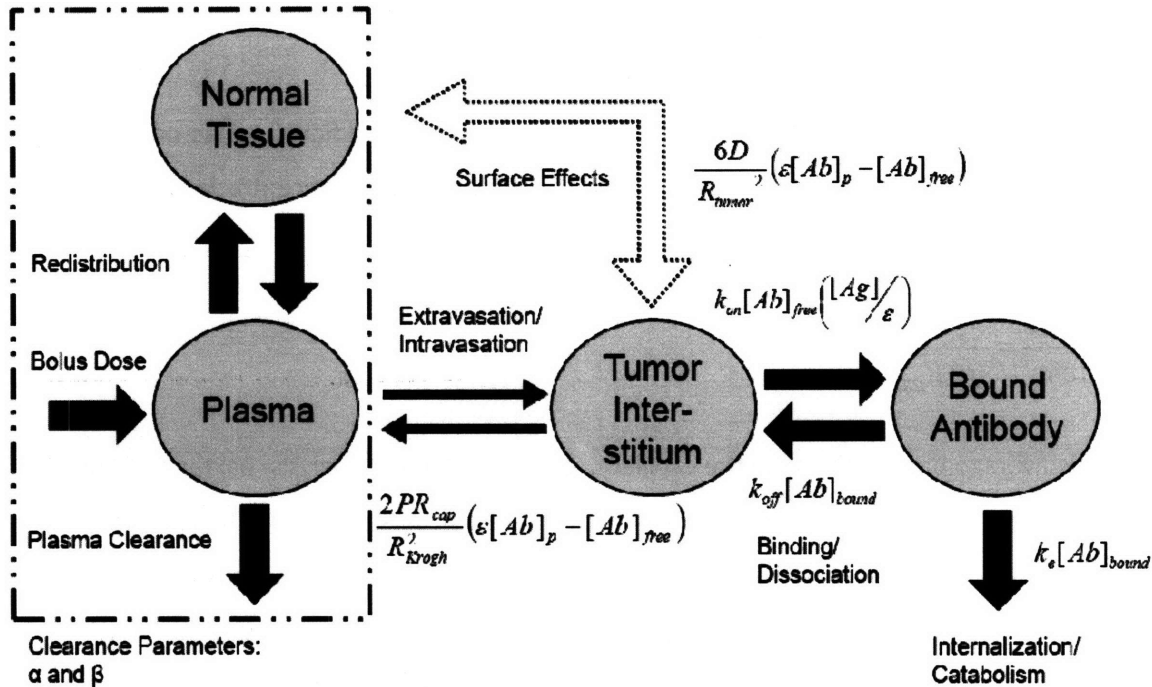

Figure 4.1 – Diagram of compartmental model. The arrows represent the rate of transfer of antibodies from one compartment to the other. A crucial part of this model is the transfer from the plasma to the tumor interstitium, which is the slowest step in uptake.

One of the most important results from the analysis of transport around individual vessels is that the permeability of the vasculature is the slowest and therefore rate-limiting step. The rapid binding and low Biot number indicate permeability is much slower than binding and diffusion. Blood flow is another critical step in transporting molecules to the tumor which was not formally presented in the microscopic model. A comparison between the rate of blood flow to the permeability rate can be used to indicate whether blood flow is limiting for macromolecules.

$$\frac{\text{extravasation rate}}{\text{blood flow rate}} = \frac{PS}{VQ} \qquad 4.1$$

where P is the permeability, S is the capillary surface area for extravasation, V is the tumor volume, and Q is the blood flow rate in units of volume of blood per volume of tissue per time (i.e. inverse time).

113

This ratio can be used to differentiate between a 'flow limited' regime and permeability or 'transfer limited' regime(7). Graff et al. measured permeability and blood flow rates of albumin in melanoma xenografts. Assuming the tissue density is approximately 1 g/mL, and using their reported values(8):

$$\frac{\text{extravasation rate}}{\text{blood flow rate}} = \frac{(1.1x10^{-6} cm/s)(15/cm)}{2.3x10^{-3}/s} = 0.0072 \qquad 4.2$$

This value indicates that in general, permeability is more limiting than blood flow for macromolecules. From a microscopic perspective, the ratio can be related to the depletion in concentration along the length of a Krogh cylinder. The ratio is then(7):

$$\frac{\text{extravasation rate}}{\text{blood flow rate}} = \frac{2PL}{\langle u \rangle R_{cap}} \qquad 4.3$$

where <u> is the average blood velocity in the capillary. Using this type of analysis, Baxter and Jain determined the drop in concentration along the length of a vessel was negligible(9). This also agrees with the perfusion of tissue isolated tumors, where the concentration of a labeled albumin macromolecule exiting the tumor is approximately equal to the concentration entering(10). Like virtually all properties in tumors, the blood flow is very heterogeneous, which is ignored in the above scaling. Some regions around the periphery may be highly perfused, whereas regions in the center may exhibit very poor blood flow. Eskey et al. used a residence time distribution of an isolated perfused tumor to determine the validity of a compartmental flow model(11) and found that a single compartment model did not adequately describe the data. With blood flow heterogeneity, this scaling can be used as an estimate of what steps are limiting in general. Regions in the tumor may exist where there is not adequate blood flow, in which case the above number would be order one or greater.

Previous modeling of antibody distribution around capillaries showed that the Biot number, which is the ratio of the rate of extravasation from the blood to the rate of diffusion between vessels, is very small(6), and the rate of binding is even faster than the rate of diffusion(12). This results in the antibody distribution having little effect on the total uptake and loss within the tumor. Furthermore, the geometry, orientation, and proximity of vessels with each other have little effect on the overall signal localization. The spatial heterogeneity present in tumors is therefore implicitly ignored in the tumor compartment.

To illustrate this point, figure 4.2 (left) shows the difference in plasma and interstitial antibody concentrations as a function of the Biot number. If two vessels are situated very close to each other in the tumor, the local interstitial concentration will be elevated due to the proximity of the two sources. However, with a very low Biot number, in the range of 0.001 for antibodies and antibody fragments, this interstitial concentration is still insignificant compared to the plasma concentration, and the difference between the two drives uptake at virtually the same rate. (The *total* antibody concentration may be very high surrounding the vessels due to binding in this area, but the amount of *unbound* antibody in the tissue is low for tight binders.) Given that the interaction between vessels has little effect on uptake, the influence of the heterogeneity around a single vessel was analyzed. Using a numerical simulation of the binding, diffusion, and internalization of antibody in a Krogh cylinder (see Appendix 2 for equations), the total antibody within the cylinder was compared to the concentration predicted by the compartmental model (Appendix section 13b with no surface terms) in figure 4.2, right. For low Biot numbers (~0.001), the Krogh cylinder simulation results in the same concentration as the compartmental model that ignores spatial heterogeneity, yielding a ratio of one. If the Biot number were large in a tumor, the concentration would quickly equilibrate across the vascular wall, and for a high affinity antibody, the high interstitial concentration prevents more antibody from diffusing into the tumor. Low affinity antibodies do not yield large spatial heterogeneities due to their ability to quickly dissociate and diffuse farther in the tissue(13), so the evenly distributed antibody is equivalent to the well mixed compartmental model at all values of the Biot number. This demonstrates that with a low Biot number, the spatial heterogeneity has little impact on the total tumor uptake.

Gradient Across Blood Vessel Wall

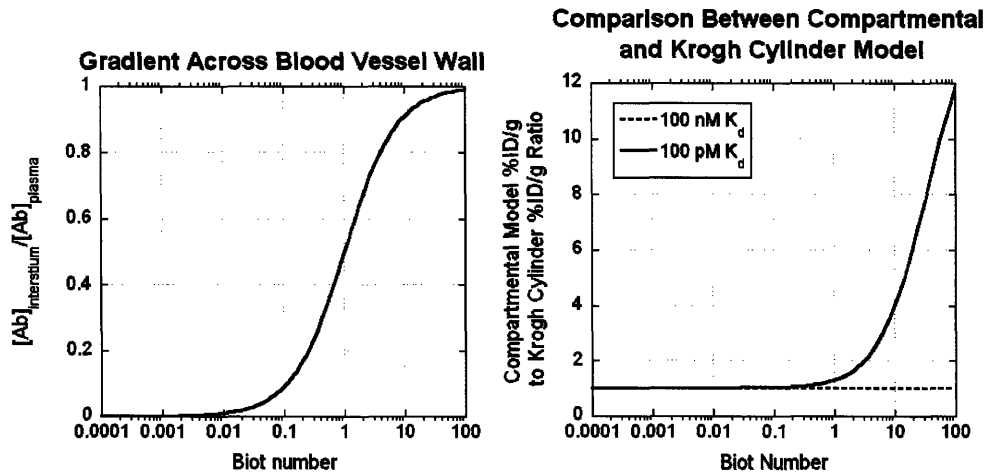**Comparison Between Compartmental and Krogh Cylinder Model**

Figure 4.2 – The use of a compartmental model is justified with a low Biot number. The interstitial concentration is negligible compared to the concentration in the plasma (Appendix section 6), so the proximity of vessels to one another can be ignored (left). Examining vessels individually to determine the effect of spatial heterogeneity, a simple compartmental model with no spatial considerations (Appendix section 13b with no surface terms) yields the same results as a spatially dependent Krogh cylinder model (Appendix section 2 equations) for low Biot numbers (right). This occurs since the diffusion rate over a given distance is much faster than the permeability rate. The parameter values were: $[Ab]_{plasma}$ = 2 nM, [Ag] = 500 nM, ε = 0.1, D = 14 μm^2/s, S/V = 200/cm, k_e = 1.3x10^{-5}/s, and the clearance values are for a human IgG in human(6). The permeability was varied.

The transport of antibody between compartments can occur by both convection and diffusion. For macromolecules, convection typically dominates due to their slow diffusion rates, but in tumors, the elevated interstitial pressure severely restricts convection in the tissue. Models examining interstitial pressure and convection within tumors (9) have shown that due to the uniformly elevated pressure, diffusion is the dominant mode of transport. Measurements of interstitial pressure (14, 15) and estimated velocities from tumor fluid flow(16) are consistent with these results.

This compartmental model assumes only diffusive transport occurs within the tumor and across the tumor surface. To examine the validity of this assumption and the effect that convection may have, a convection-diffusion model was implemented from Baxter and Jain(9) (see also Appendix section 12). This distributed parameter model simulates fluid extravasation, fluid flow, and interstitial pressure as a function of the tumor radius, with individual capillaries being spatially averaged throughout the tissue (i.e. ignoring intercapillary heterogeneity). These values are used to determine diffusive and convective rates of antibody extravasation, interstitial diffusion, and interstitial convection on the length scale of the entire tumor. This model has recently been used to analyze the normalization effects of anti-VEGF treatment on tumors(15). The most notable difference between this implementation and the original is

that tumor permeability measurements made in the center of xenografts (17, 18) were used as the baseline value for permeability, which are 10-fold higher than the original implementation.

Two different scenarios were modeled with the convection-diffusion simulation as outlined in the original paper. An intraperitoneal tumor was simulated where the interstitial pressure is zero at the surface of the tumor (figure 4.3, left). This allows fluid to easily exit the tumor, yielding more convection. A subcutaneous simulation analyzes a tumor surrounded by normal tissue, where this surrounding tissue restricts fluid flow. In the second scenario, the interstitial pressure is elevated even near the tumor periphery, and convection is low throughout the tumor. The interstitial pressure drops in the surrounding tissue, which has been demonstrated experimentally(14), increasing convection in this region. These differences at the tumor surface further illustrate the variability in uptake that can occur within and between tumors.

To capture the relative importance of convection versus diffusion, the model can be used to calculate the Peclet number for transcapillary transport in the tumor. This Peclet number is the ratio of extravasation rate from convection to the extravasation rate from diffusion. Its value is:

$$Pe_{transcapillary} \equiv \frac{J_V(1-\sigma)}{PS}$$
4.4

where J_V is the volumetric rate of fluid leaving the vessels, σ is the reflection coefficient for the molecule of interest, P is the permeability, and S is the capillary surface area. Figure 4.3 (right) shows the transcapillary Peclet number for an intraperitoneal and subcutaneous tumor. For the tumor surrounded by normal tissue (subcutaneous tumor), the Peclet number is always less than one, indicating diffusion dominates. Only at the periphery of the intraperitoneal tumor does the Peclet number increase above one.
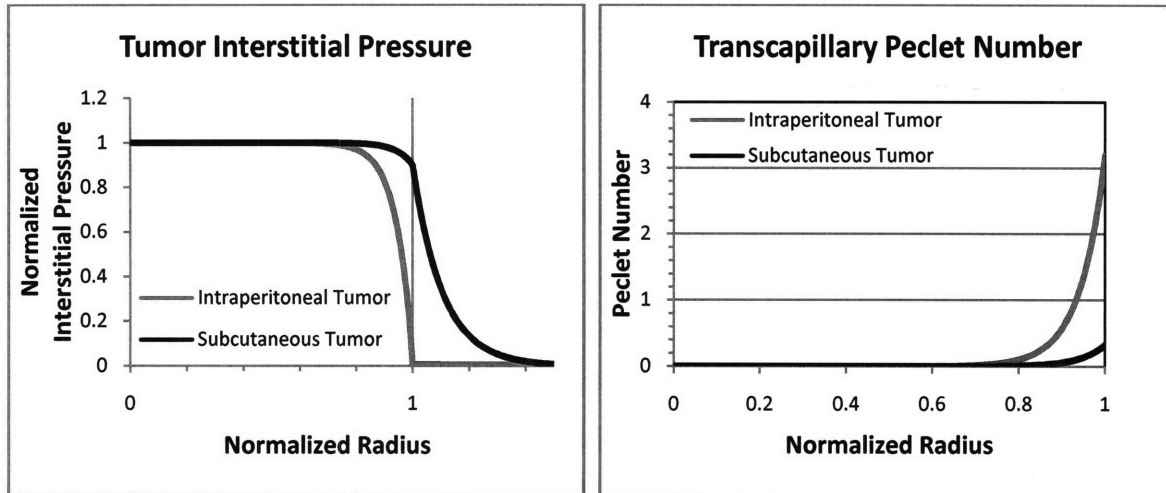
Figure 4.3 – Tumor Interstitial Pressure and Transcapillary Peclet Number. The interstitial pressure is plotted for a 1 cm diameter tumor (left) using a distributed parameter convection diffusion model (Appendix section 12). A normalized radius of 1 marks the edge of the tumor with larger values occurring in the surrounding healthy tissue. When the normalized interstitial pressure reaches one, the value is equal to the hydrostatic and osmotic pressure in the vasculature, so no net fluid leaves the vessel. The transcapillary Peclet number is also plotted as a function of the normalized tumor radius using the same numerical simulation. Values for the subcutaneous tumor are always less than one, but the periphery of the intraperitoneal tumor has significant convection. Here, convection dominates over extravasation for about 25% of the tumor volume (~10% of the tumor radius).

Put in absolute terms of moles of antibody exiting the vasculature per time, figure 4.4 (left) shows the beneficial effect convection has on tumor uptake. As fluid slowly exits the surface of the tumor, the interstitial pressure drops in this region and allows fluid to extravasate from the blood vessels. This fluid carries antibody with it, increasing the rate at which antibodies exit the blood vessels. The result is higher uptake near the surface of the tumor.

Initial Extravasation Rate from Convection and Diffusion
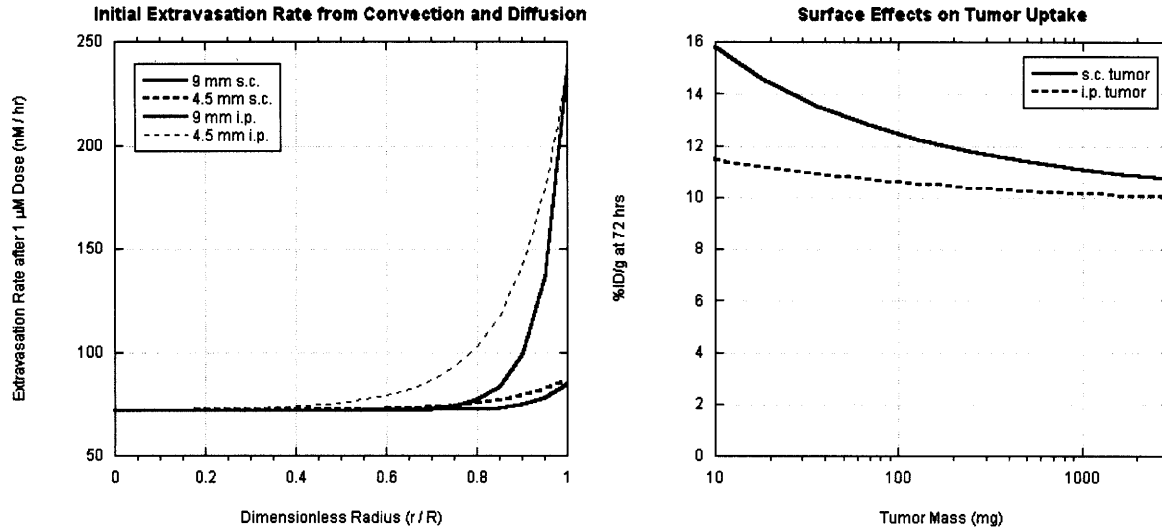
Surface Effects on Tumor Uptake

Figure 4.4 – Convection in the Tumor Periphery and Uptake as a Function of Tumor Size. The extravasation from capillary vessels is increased due to the lower interstitial pressure near the tumor surface (left). The total uptake within the tumor is increased for smaller sizes since these tumors have a larger surface area to volume ratio. For subcutaneous tumors, this occurs directly from diffusion at the tumor surface, and for intraperitoneal tumors, a larger fraction of the tumor is located in the 'convection zone' near the tumor surface as size decreases. Both graphs were generated using a convection diffusion model (Appendix section 12), and the total uptake for the graph on the right was generated by integrating the concentration over the tumor radius.

For smaller tumors, a larger portion is located within this 'convection zone' near the surface of the tumor. Due to higher uptake at the surface, smaller tumors will be impacted more by convection. However, there are competing effects. Although convection is faster than diffusion in most cases, the fluid flow is so slow that diffusion can occur against the direction of flow. The ratio of convection to diffusion between cells in the tumor interstitium is the Peclet number for interstitial transport (which is different than the Peclet number for extravasation given above):

$$Pe_{\text{interstitium}} \equiv \frac{v_i R}{D} \qquad\qquad 4.5$$

where v_i is the interstitial fluid velocity, R is the Krogh cylinder radius, and D is the diffusion coefficient. The maximum velocities occur at the periphery of the tumor and decay rapidly approaching the center. Even at the tumor periphery, using a Krogh cylinder radius of 50 μm, diffusion coefficient of 14 μm^2/s, and interstitial fluid velocity of 0.34 μm/s, the interstitial Peclet number is approximately one. This means even at locations with the highest fluid flow, convection and diffusion are equal in magnitude,

119

and in the rest of the tumor, diffusion dominates. A finite element analysis of antibody transport surrounding a capillary has confirmed these results(19).

Although diffusion rates of macromolecules are slow compared to small molecules, the analysis above demonstrates that they are fast compared to the levels of convection occurring in a solid tumor. Therefore, antibody present in the normal tissue surrounding the tumor can diffuse inward and bind antigen. In a different scenario, an increase in convection would allow more antibody to exit the blood vessels near the tumor surface, but the outward fluid flow would slow down diffusion inward from the surrounding normal tissue. While it is difficult to discern convection versus diffusion at the tumor periphery in experimental tumors, numerical simulations make it possible to simulate different scenarios and determine which mode dominates transport around the tumor surface. For subcutaneous tumors surrounded by normal tissue, the pressure is elevated all the way to the tumor periphery. Simulations for small tumors show an increase in uptake, but if the flux across the tumor outer surface is artificially set to zero, the value collapses back to same uptake as large tumors. This indicates that the increased amount of antibody is entering from the surrounding tissue. If the permeability is set to the constant value from diffusion only (ignoring any increase from convection), the uptake is unchanged, verifying that increased extravasation does not cause higher uptake in these simulated subcutaneous tumors (Appendix section 13f). For intraperitoneal tumors, where the interstitial pressure is zero at the surface, the opposite is true. Smaller tumors still yield higher uptake values than larger tumors, but these small tumors demonstrate higher uptake even when the tumor surface is made impermeable (no flux across the tumor surface). If the permeability is set to a constant value throughout the tumor, though, the uptake collapses back to the level for large tumors. This shows that the higher uptake in the simulated small intraperitoneal tumors is caused by increased extravasation from convection near the tumor periphery (Appendix section 13f).

In the base case for the mechanistic compartmental model (subcutaneous tumor), diffusion is the dominant player. Figure 4.4 (right) shows the effect of convection and diffusion at the surface as a function of tumor size. In general, smaller tumors have higher uptake due to their larger ratio of surface area to total volume. The subcutaneous tumors had higher overall uptake due to diffusion inward from the surrounding tissue. The intraperitoneal tumors had increased convection near their surface from the lower interstitial pressure, but the outward convection countered diffusion inward from the surrounding tissue, lowering the effect of tumor size. These results are extremely dependent on the fluid flow parameters used in the model, however. For example, a reflection coefficient of 0.95 was

120

used for the IgG simulated here, so the vessels filtered 95% of the antibody out of the fluid leaking from the capillaries near the tumor surface. This lowered the relative effect of convection in the small intraperitoneal tumors, since this lowers the number of antibodies that extravasate with the fluid.

The discussion above justifies several assumptions in the model. First, a compartmental model will be used to describe the uptake in the tumor. Although there are large spatial heterogeneities within the tumor, the spatial analysis shows that this does not significantly affect the uptake and loss in the tumor. The transport in the tumor is primarily diffusive, which includes transport across the blood vessel walls and across the outer surface of the tumor. These assumptions will be used in deriving the rate constant for overall uptake and loss in the tumor. As shown in the diagram of tumor uptake (figure 4.1), uptake and loss of antibody (bound and free) in the tumor occurs from the tumor vasculature, across the tumor surface, and from degradation within the tissue.

The tumor vasculature is a major source for uptake and loss within the tissue. Analysis of the transport in tissue demonstrates that binding is much faster than diffusion, and the low Biot number indicates diffusion is much faster than permeability(13). It can then be assumed that binding equilibrium is reached in the tumor tissue. Since sub-saturating doses of antibody are often given, it will be assumed that the concentration in the tumor is much less than the antigen concentration, giving a linear approximation to uptake. Since only free antibody is able to intravasate back into the blood, the rate of transfer between the plasma and tumor compartment is (see Appendix section 13a.i):

$$\frac{d[Ab]_{total}}{dt} = \frac{2PR_{cap}}{R_{Krogh}^2}\left(\varepsilon[Ab]_{plasma} - \left(\frac{K_d}{\left(\frac{[Ag]}{\varepsilon}\right)+K_d}\right)[Ab]_{total}\right) \qquad 4.6$$

Diffusion in and out of the tumor can also occur across the outer surface. For the analysis of spatial distribution, it was assumed antibody in the Krogh cylinder did not leave the outer surface, and a no-flux boundary condition was used at the outer radius of tissue. Either the antibody bound antigen before it reached this distance, or an adjacent capillary had an equal concentration, yielding no net flow across this outer boundary. However, for capillaries near the surface of the tumor, this is not the case. Antibody can diffuse away from the blood vessel and not be reflected back. This is captured in the terms for transport across the tumor surface. Unfortunately, this is a highly non-linear process. The antibody uptake and loss across the tumor surface depends on the total antibody concentration and gradients within the tumor. Local gradients around individual vessels will affect the uptake, as will

121

whole tumor variations, such as increased extravasation near the surface or central necrosis. Even assuming no disruption from the vascular contributions, the term is highly time dependent (see the series solutions in Appendix section 11a.iii and 11d).

Using the series solutions for uptake and loss from a sphere as a guide, an order of magnitude estimate for transport across the tumor surface can be obtained (see Appendix section 13a.ii). The concentration surrounding the tumor is equivalent to the concentration in the normal tissue. However, solving the surface term using this concentration yields a solution that is exceedingly complex. Since antibodies equilibrate across the tumor vasculature during the alpha phase of clearance, it will be assumed that the concentration surrounding the tumor is equal to the plasma concentration. Given that this is an order of magnitude estimate, this assumption is deemed reasonable in order to considerably simplify the result. The term for diffusion across the surface is:

$$\frac{d[Ab]_{total}}{dt} = \frac{6D}{R_{tumor}^2} \left(\varepsilon [Ab]_{plasma} - \left(\frac{K_d}{\left([Ag]/\varepsilon \right) + K_d} \right) [Ab]_{total} \right)$$

4.7

The final term for loss from the tumor is caused by antibody degradation. Care must be taken when measuring labeled antibody. In some scenarios, the surface bound antibody is the parameter of interest, such as with pretargeting experiments. Here, the endocytosis rate is important, as described for the spatial distribution. If a labeled antibody is being tracked, however, it is important to note the difference between the intact antibody and label. If the label is residualizing, it will remain in the tumor for a longer period of time than the antibody. In this case, it is really the slower of the two rates that dictates loss from antibody internalization (see Appendix section 15). Since only bound antibody will be internalized by the cells, the antibody degradation term is:

$$\frac{d[Ab]_{total}}{dt} = -k_e \left(\frac{\left([Ag]/\varepsilon \right)}{\left([Ag]/\varepsilon \right) + K_d} \right) [Ab]_{total}$$

4.8

122

4.4 Compartmental Model Results

With the assumptions and justifications given above, the concentration in the tumor changes with time in the following manner (Appendix section 13b.i):

$$\frac{d[Ab]_{total}}{dt} = \frac{2PR_{cap}}{R^2_{Krogh}}\left(\varepsilon[Ab]_{plasma} - \left(\frac{K_d}{\left([Ag]\!\big/\!\varepsilon\right)+K_d}\right)[Ab]_{total}\right) +$$

$$\frac{6D}{R^2_{tumor}}\left(\varepsilon[Ab]_{plasma} - \left(\frac{K_d}{\left([Ag]\!\big/\!\varepsilon\right)+K_d}\right)[Ab]_{total}\right) - k_e\left(\frac{\left([Ag]\!\big/\!\varepsilon\right)}{\left([Ag]\!\big/\!\varepsilon\right)+K_d}\right)[Ab]_{total} \qquad 4.9$$

where [Ab] is the overall concentration of the antibody in the tumor, t is time, d[Ab]/dt is the change in antibody concentration over time, P is the permeability of antibody across the vessel wall, R_{cap} is the capillary radius in the tumor, R_{Krogh} is the average radius of tissue surrounding each blood vessel, ε is the accessible volume fraction, $[Ab]_{plasma}$ is the plasma concentration of antibody, K_d is the dissociation constant of the antibody, [Ag] is the overall antigen concentration, D is the diffusion coefficient, R_{tumor} is the radius of the tumor, and k_e is the internalization or degradation rate of the bound antibody-antigen complex.

The first set of terms on the right hand side of the equation describes the movement of antibody between the plasma and the tumor. The $2PR_{cap}/R_{Krogh}^2$ is the permeability surface area product per tumor volume. The second set of terms aims to capture some of the surface effects. As described above, this model assumes only diffusion from the surface, which is more appropriate for a subcutaneous tumor with uniformly elevated interstitial pressure. Such effects may be of interest for certain delivery methods, such as intraperitoneal injections and targeting small tumors. The final term describes internalization and degradation of the antibody within the tumor. This is based on the internalization rate of the bound antibody-antigen complex, which is often similar to the intrinsic antigen turn-over rate. The ratio of the dissociation constant and antigen density describes the fraction of antibody within the tumor that is bound.

The plasma clearance of antibodies and their fragments is well described by a biexponential decay. Implicit in this assumption is that the dose is large enough that free antigen in the blood and uptake in the tumor and normal tissues does not significantly affect the clearance(20, 21). With this

assumption, the model can be solved analytically to give an expression of the concentration as a function of time (Appendix section 13b.ii):

$$\frac{[Ab]_{total}}{[Ab]_{plasma,0}} = \varepsilon \left(\frac{2PR_{cap}}{R_{Krogh}^2} + \frac{6D}{R_{tumor}^2} \right) \left\{ \frac{A}{(\Omega - k_\alpha)} \left[e^{-k_\alpha t} - e^{-\Omega t} \right] + \frac{B}{(\Omega - k_\beta)} \left[e^{-k_\beta t} - e^{-\Omega t} \right] \right\}$$

4.10

$$\text{where: } \Omega = \frac{2PR_{cap}}{R_{Krogh}^2} \left(\frac{K_d}{\left([Ag]/\varepsilon \right) + K_d} \right) + \frac{6D}{R_{tumor}^2} \left(\frac{K_d}{\left([Ag]/\varepsilon \right) + K_d} \right) + k_e \left(\frac{\left([Ag]/\varepsilon \right)}{\left([Ag]/\varepsilon \right) + K_d} \right)$$

4.11

$$\text{and: } \quad [Ab]_{plasma} = [Ab]_{plasma,0} \left(A \cdot \exp(-k_\alpha t) + B \cdot \exp(-k_\beta t) \right)$$

4.12

This provides an analytical solution to the time course within the tumor. Values can be entered manually or plotting software such as a spreadsheet program yield the concentration profile as a function of time.

This expression captures all the elements described above for large and small tumors of varying affinity. However, this expression can be simplified when looking at larger tumors. The influence of uptake and loss from the tumor surface to uptake and loss from the vasculature can be expressed as a ratio, indicating which term dominates for different tumor sizes. When this ratio is equal to unity, both are of equal importance (Appendix section 13c).

$$\frac{\text{vasculature transport}}{\text{surface transport}} = \frac{Bi}{6} \left(\frac{R_{tumor}^2}{R_{Krogh}^2} \right)$$

4.13

Using typical values for the Biot number and vascular density, this expression indicates that for tumors larger than about 50 mg (approximately 4.6 mm in diameter), the blood vessels are more important than uptake from the surface, and for values significantly larger than this, the surface effects can be ignored.

Simplifications can also be made based on affinity. The fraction of bound antibody is based on the ratio between the antigen concentration and antibody affinity. With interstitial antigen concentrations typically in the low micromolar range, K_d values in the double digit nanomolar range and below will behave similarly, although their spatial distribution within the tumor may vary. These

antibodies will be cleared primarily due to internalization, so the intravasation and surface loss terms can be ignored. These assumptions can be justified by comparing the relative rates of intravasation and surface loss to internalization (Appendix section 13c):

The ratio of loss from intravasation to internalization is:

$$\frac{\text{internalization}}{\text{intravasation}} = \frac{k_e R_{Krogh}^2 \left([Ag]\middle/ \varepsilon \right)}{2PR_{cap}K_d}$$

4.14

The ratio of loss from internalization to surface loss is:

$$\frac{\text{internalization}}{\text{surface loss}} = \frac{k_e R_{tumor}^2 \left([Ag]\middle/ \varepsilon \right)}{6DK_d}$$

4.15

If both of these values are much greater than 1, internalization dominates the loss from the tumor. This yields the simplified version for a high affinity antibody in a large tumor:

$$\frac{\partial [Ab]_{total}}{\partial t} = \frac{2PR_{cap}}{R_{Krogh}^2} \varepsilon [Ab]_{plasma} - k_e [Ab]_{total}$$

4.16

and

$$\frac{[Ab]_{total}}{[Ab]_{plasma,0}} = \varepsilon \left(\frac{2PR_{cap}}{R_{Krogh}^2} \right) \left\{ \frac{A}{(k_e - k_\alpha)} \left[e^{-k_\alpha t} - e^{-k_e t} \right] + \frac{B}{(k_e - k_\beta)} \left[e^{-k_\beta t} - e^{-k_e t} \right] \right\}$$

4.17

For comparison, a non-binding antibody can also be simplified. Here, $K_d \gg [Ag]/\varepsilon$.

$$\frac{\partial [Ab]_{total}}{\partial t} = \frac{2PR_{cap}}{R_{Krogh}^2} \left(\varepsilon [Ab]_{plasma} - [Ab]_{total} \right)$$

4.18

and

$$\frac{[Ab]_{total}}{[Ab]_{plasma,0}} = \varepsilon \left(\frac{2PR_{cap}}{R_{Krogh}^2} \right) \left\{ \frac{A}{(\Omega - k_\alpha)} \left[e^{-k_\alpha t} - e^{-\Omega t} \right] + \frac{B}{(\Omega - k_\beta)} \left[e^{-k_\beta t} - e^{-\Omega t} \right] \right\}$$

4.19

where: $\Omega = \dfrac{2PR_{cap}}{R_{Krogh}^2}$ 4.20

Even these non-binding molecules will accumulate to some extent within the tumor. While the uptake of these antibodies in the tumor interstitium is slow due to the transport across the vascular wall, the loss of antibody is equally slow, resulting in non-specific retention. (As a technical note, if transport out of the vasculature is biased, which is possible for some parameter values using a two-pore model, non-specific retention can be even more significant.)

Unfortunately, the biexponential decay in the plasma prohibits an analytical expression for the time of maximum uptake in the tumor. Making further assumptions is useful for understanding the qualitative behavior of uptake, however. If a single exponential decay is assumed in the plasma, an analytical expression is possible, and the time for maximum uptake is (Appendix section 13c):

$$t_{max} = \frac{\ln\left(\dfrac{k_\alpha}{\Omega}\right)}{\left(k_\alpha - \Omega\right)}$$ 4.21

Note that for a high affinity antibody, Ω is simply the internalization rate, k_e, for the antibody. Looking at this term for the time of maximum uptake, if either plasma clearance or tumor loss occurs rapidly, the time of maximum uptake will occur quickly. This is typical for scFvs with fast plasma clearance, and to a lesser extent, anti-HER2 antibodies that have an internalization rate of several hours. However, if both the clearance and internalization rates are very slow, the maximum uptake will occur after an extended incubation period. This is typical for slowly clearing IgGs that target persistent antigens, such as A33. Here, the maximum uptake may not occur for several days. From a mathematical standpoint, the plasma profile is the forcing function(22), and uptake and loss from the tumor provides the system response.

The time of maximum uptake can be used to determine the maximum concentration in the tumor. Entering this value in the expression for antibody concentration in the tumor:

$$[Ab]_{max} = \left[\frac{\varepsilon[Ab]_{plasma,0}}{k_\alpha}\left(\frac{2PR_{cap}}{R_{Krogh}^2} + \frac{6D}{R_{tumor}^2}\right)\right]\left[\left(\frac{\Omega}{k_\alpha}\right)^{\frac{\Omega}{k_\alpha - \Omega}}\right]$$ 4.22

The first term in square brackets indicates the maximum amount of antibody that can be taken up into the tumor prior to clearance from the plasma. The second square bracket expression, the 'tumor loss term,' adjusts the maximum uptake by taking into account antibody that leaves the tumor. This value ranges from 0 to 1 depending on the ratio of antibody loss from the tumor (Ω) to clearance from the plasma (k_α). It approaches the maximum value of 1 when loss from the tumor is much less than the clearance rate and approaches 0 when antibody is lost faster than it can be taken up (i.e. $\Omega \gg k_\alpha$). The value of this loss term is represented graphically in figure 4.5:
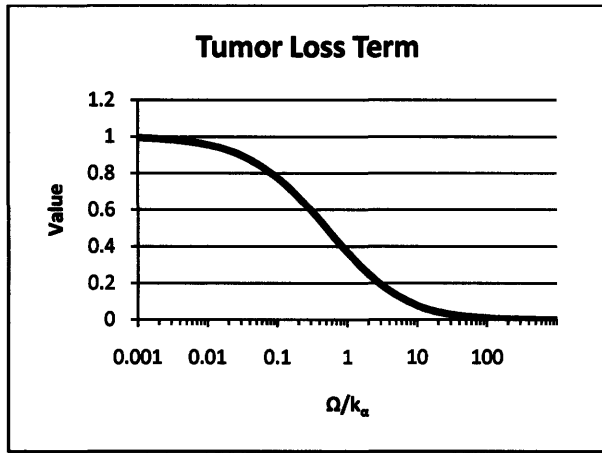

Figure 4.5 – Loss term for maximum uptake. As the term for loss from the tumor becomes small relative to the clearance from the plasma, less antibody leaves the tissue, and the uptake approaches the maximum amount that can enter the tumor prior to plasma clearance. This tumor loss term is the square bracket term on the right in equation 4.22.

For a large tumor with a high affinity antibody:

$$[Ab]_{max} = \left[\frac{\varepsilon[Ab]_{plasma,0}}{k_\alpha} \frac{2PR_{cap}}{R_{Krogh}^2} \right] \left[\left(\frac{k_e}{k_\alpha} \right)^{\frac{k_e}{k_\alpha - k_e}} \right]$$

$$\text{4.23}$$

Because antibody uptake in tumors is often expressed as a percentage of the injected dose per gram of tumor mass, it is useful to define the localization in these terms (Appendix section 13d).

$$\%ID/g = \frac{[Ab]\cdot 100\%}{[Ab]_{plasma,0} V_{plasma} \rho_{tissue}}$$

$$\text{4.24}$$

where the plasma volume is in mL, and the tumor density is $\sim$1 g/mL.

The concentration of antibody within the tumor divided by the tumor tissue density gives the amount of antibody per gram of tumor tissue. This is divided by the initial plasma concentration times the total plasma volume, giving the initial dose, multiplied by 100%. Since the concentration is the pertinent parameter for uptake, a dose diluted in a larger plasma volume gives a much lower efficiency of uptake. This results in a three order of magnitude lower %ID/g for humans (~3.5 L plasma volume) than mice (~2 mL).

To illustrate some typical results for antibody uptake, several plots are shown in Figure 4.6 with the parameter values in Table 4.1. The top graphs show the predicted time course for a typical scFv, and those on the bottom are for an IgG. Notice the difference in time scales on the x-axis. The plots on the left compare the convection-diffusion numerical simulations with the compartmental model. Both a high affinity binder and non-specific antibody are simulated. These non-specific antibodies describe localization based on an EPR-like effect. The transport across the blood vessel wall is very slow, so once the molecule is in the tumor interstitium, it takes a long time for it to clear back to the blood. For these simulations, a small tumor was chosen (~100 mg in size), where surface effects still play a role. It is this uptake that causes the numerical simulations to give slightly higher uptake than the compartmental model. The graphs on the right compare tumors where the assumption of a sub-saturating dose is not achieved. Antibody that enters the tumor after saturation has no free antigen to bind, so it behaves in general as a non-binding antibody. The compartmental model over-predicts the uptake, since it still assumes antibody that enters the tumor will bind antigen. The numerical simulations show two periods of loss, the first being the rapid loss of unbound antibody that has no unoccupied sites to bind, and the second period where bound antibody is cleared from the tumor. This may be important in tumors with low or down-regulated antigen density because these will become saturated more easily.

	Figure 4.6 (scFv)	Figure 4.6 (IgG)	Figure 4.7	Figure 4.8	A33 Clinical Trial
Dose	500 nM (unsat.) 20 µM (sat.)	500 nM (unsat.) 5 µM (sat.)	2 µM	67 nM	167 nM (max)
S/V	200/cm	200/cm	200/cm	200/cm	200/cm
K_d	High Affinity: 1 nM Non-specific: 10 µM	High Affinity: 1 nM Non-specific: 10 µM	Varied	2.6 nM (436) 27 pM (9.2.27) 3.0 nM (IND1) ∞ (B72.3)	1.8 nM
D	80 µm^2/s	14 µm^2/s	80 µm^2/s	14 µm^2/s	14 µm^2/s
P	5×10^{-3} µm/s	3×10^{-3} µm/s	5×10^{-3} µm/s	3×10^{-3} µm/s	3×10^{-3} µm/s
[Ag]	500 nM	500 nM	150 nM	SK-MEL-2 Cells: 580 nM (125 kDa) 51 nM (HMW-MAA) M21 Cells: 230 nM (125 kDa) 210 nM (HMW-MAA)	500 nM
ε	0.3	0.1	0.3	0.1	0.1
k_e	1.3×10^{-5}/s	1.3×10^{-5}/s	1.3×10^{-5}/s	5×10^{-6}/s	3.4×10^{-6}/s
clearance	α: 13.9/hr β: 0.23/hr fraction α: 0.8	α: 1.3/day β: 0.19/day fraction α: 0.43	α: 13.9/hr β: 0.23/hr fraction α: 0.8	Table 2 ref. (3)	α: 1.3/day β: 0.19/day fraction α: 0.43
R_{tumor}	3 mm	3 mm	2.9 mm	1.4 mm	5 mm
ε_{fluid}	0.5	0.5	NA	NA	NA
V_{plasma}	2 mL	2 mL	2 mL	2 mL (23, 24)	3.5 L (25)
time	Varied	Varied	24 hrs	Varied	7 days

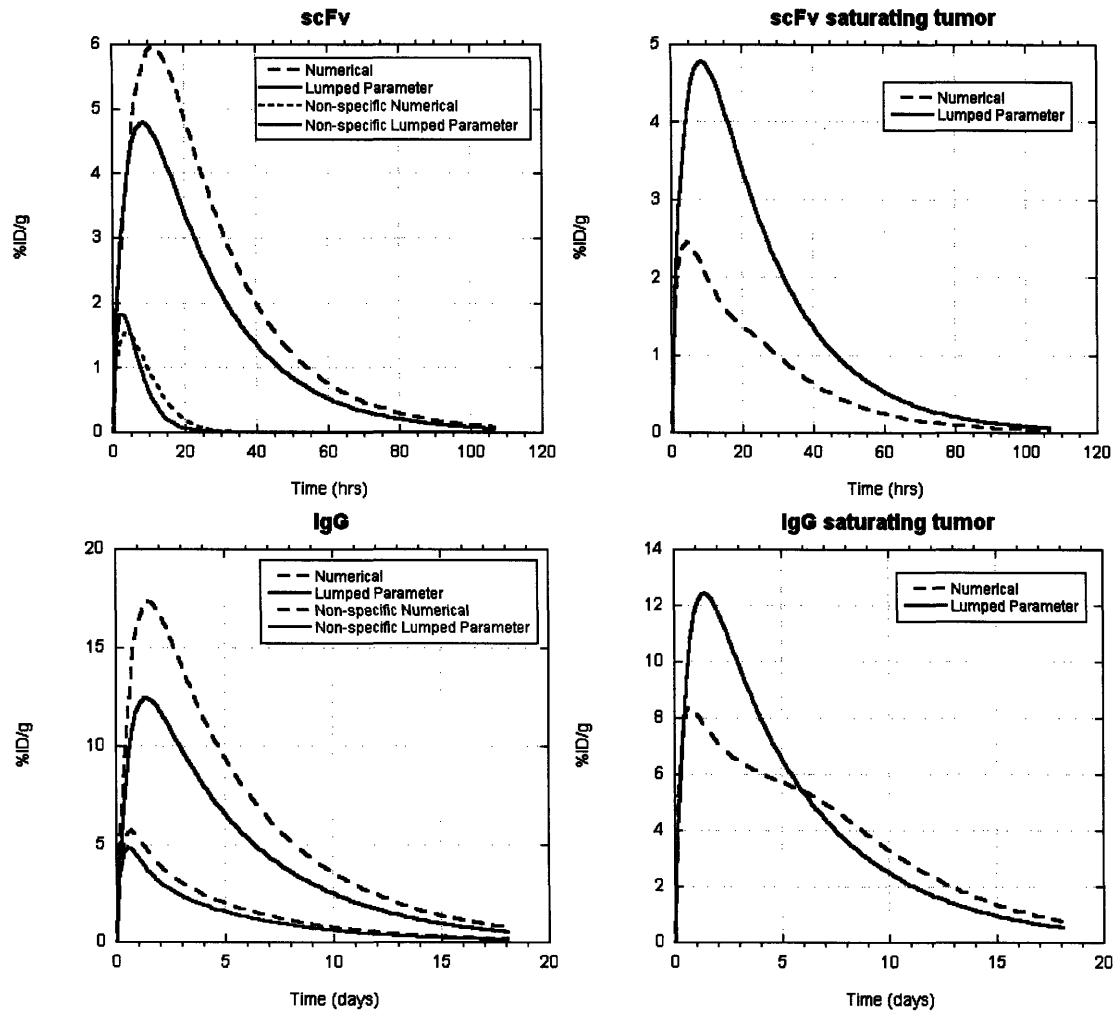Table 4.1 – Parameter values for numerical and compartmental simulations.

Figure 4.6 – Time profiles for a specific and non-specific scFv and IgG in mouse. The profile for an scFv matches closely the full convection-diffusion model simulation for a high affinity (1 nM K_d) and non-specific binder (top left). If a saturating dose is used, the compartmental model assumptions are not met. The numerical simulation shows that antibody clears more rapidly once the binding sites are completely occupied in the tumor. This gives a lower overall uptake (top right). For an IgG, the time scale is much longer (bottom left). The same behavior applies to a saturating dose of an IgG, where the %ID/g is lower than predicted due to saturation of all the binding sites (bottom right). The numerical simulation lines in all the graphs were generated by integrating over the tumor volume using the convection diffusion model (Appendix section 12), and the lumped parameter lines are given by the compartmental model (Appendix section 13b). Parameter values are in table 4.1.

4.5 Compartmental Model Validation

The compartmental model is consistent with the spatial distribution model in tumor tissue. In the spatial distribution theory, variations in time are excluded by examining the steady state for the Thiele modulus, or integrating over time for the clearance modulus. Using the compartmental model

130

and assuming a high affinity binder and steady state for the compartmental model, the fractional antigen saturation is (Appendix section 13e):

$$\frac{[Ab]_{total}}{[Ag]} = \frac{1}{\phi_{tumor}^2} + \frac{6}{\phi_{met}^2}$$

4.25

If either the Thiele modulus based on uptake from the surface or the vasculature is less than one, the tumor will be saturated. Similarly, for a high affinity antibody, if catabolism is ignored, and the compartmental model is integrated from the time of the dose to infinity, the fractional antigen saturation is (Appendix section 13e):

$$\frac{[Ab]_{total}}{[Ag]} = \frac{1}{\Gamma_{tumor}} + \frac{6}{\Gamma_{met}}$$

4.26

If the clearance modulus for uptake from the vasculature or surface is less than one, then the antigen will be saturated.

Other compartmental models have been developed that describe the uptake and loss from antibody in tumors. Many of these models directly connect antibody in the plasma with bound antibody in the tumor, by-passing the critical extravasation step to the tumor interstitium. Comparisons with these models are not relevant since a variety of rate constants were fit that do not match processes in the current model. Several models have been published that are similar enough to make comparisons. Sung et al. used a comparable model to fit rate parameters between compartments of an immunotoxin, although these rates were assumed to be completely convective, and degradation within the tumor was ignored(26). Baxter et al. used a similar model for the tumor compartment in their physiology based pharmacokinetic model, although transport to and from the tumor was assumed to be both diffusive and convective in nature(27). Finally, Ferl et al. have used compartmental models to analyze the uptake of both IgGs(28) and scFv-Fc(29) molecules. Because the loss terms can come from intravasation, internalization, and exit through the tumor surface, it is more direct to compare uptake from the plasma. Table 4.2 compares the uptake rate predicted in this model to the rates that were fit from experimental data in these papers. In all cases, the rates were similar, indicating consistency between the mechanistic compartmental model and uptake in these systems.

131

Model	Extravasation Rate (per day)	Molecule
Current Mechanistic Model	0.476	IgG
Sung et al. 1990	0.187	IgG-immunotoxin
Baxter et al. 1994	0.191	IgG
Ferl et al. 2005	0.730	IgG
Ferl et al. 2006	0.888	scFv-Fc

Table 4.2 – Comparison between uptake rates of current model and fit parameters in previous compartmental models

To analyze the effect affinity has on total tumor retention, model predictions were compared to the experimental results on a series of HER-2 binding scFvs(4). The model inputs were the same as used in the microscopic analysis surrounding each capillary(6) with two exceptions. The surface area to volume ratio of the vasculature as measured by Hilmas and Gillette(30) was used to estimate $2R_{cap}/R_{Krogh}^2$, since it is the average value over the whole tumor that will determine uptake. This value of 200/cm differs from the conservative estimates typically used in the microscopic model to ensure targeting of all cells. The second difference in parameters is the loss rate of antibody signal from the tumor. For the microscopic analysis, the internalization rate of the antigen determines the distribution of antibody surrounding the vessel. However, after degradation, the radioactive iodine tag may remain in the cell for an extended period of time. Other papers show the loss of this isotope occurs with a roughly 15 hour half life (31, 32). Therefore, since the experimental setup cannot distinguish between intact and degraded antibody, the slowest loss rate is the pertinent parameter, which in this case is loss of the label (Appendix section 15).

The top two panels in figure 4.7 show the experimental results on the left and the model prediction on the right. All data points and model results were taken at 24 hours. Using only literature estimates of the various parameters in the model, the shape and order of magnitude of uptake agree roughly with the experimental results. As the affinity decreased to levels similar to the antigen density, more antibody remained unbound and could diffuse out of the tumor. The high affinity antibodies were rapidly internalized, and the loss of signal occurred as iodine left the tumor.
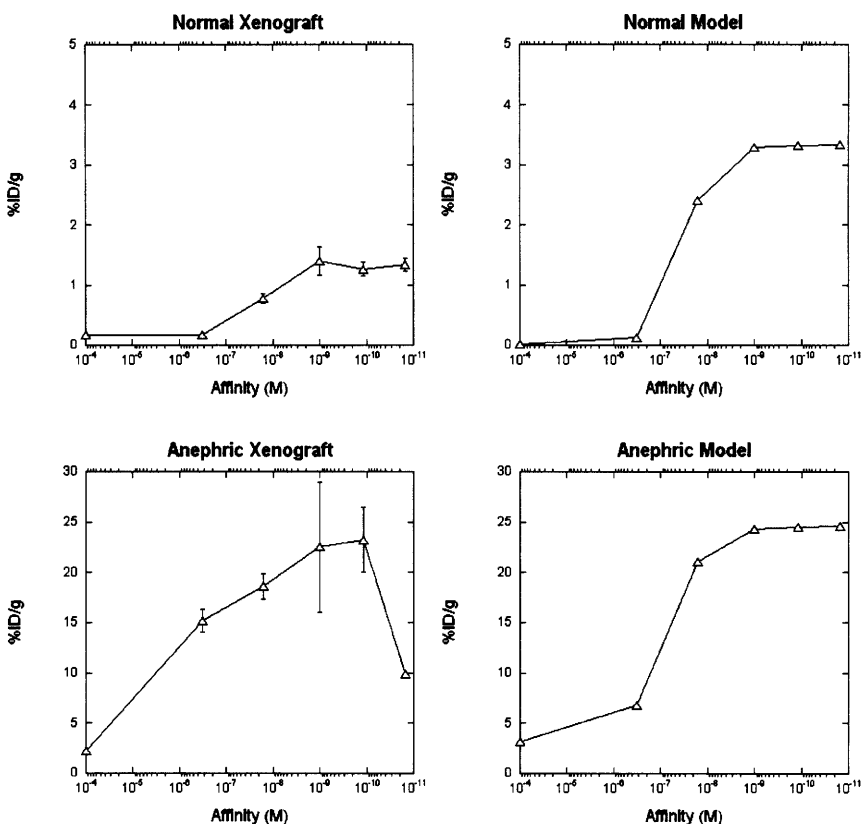
Figure 4.7 – Effects of Affinity and Clearance on Uptake of HER2 binding scFvs. The model predictions based on parameter estimates from the literature (right) are compared with experimental data (left). The top graphs are for scFvs in a normal mouse, whereas the bottom panel had the kidneys removed to reduce renal filtration. The longer retention in the plasma increases uptake (bottom panels). Model predictions are given by the compartmental model (Appendix section 13b), and parameter values are indicated in table 4.1.

In this paper, the authors performed a second experiment where the kidneys were removed in order to eliminate rapid renal clearance. This was simulated in the model by setting the beta phase clearance rate to zero. Essentially, the antibody distributes between the plasma and normal tissue, but then remains at that level indefinitely. With the extended plasma half-life, the uptake in the tumor is much higher. The model predicts roughly the same level of uptake without fitting any parameters. Interestingly, the final experimental point actually decreases. This is likely due to lower plasma persistence, either by uptake in a different organ or lower serum stability. Given the rapid renal clearance in the first experiment, any differences in serum stability would not have been evident. If a mechanism other than clearance plays a role, the possibilities are limited by the fact that this difference was not apparent in the first experiment when the kidneys were intact.

There is some additional error in the model that is created by using a single tumor compartment to describe surface and internalized antibody. In the above case, the internalization rate is much faster than the degradation rate, so k_e was set equal to the degradation and loss rate for iodine. However, antibody that is rapidly internalized will be trapped inside the cell and cannot leave the tumor surface or vasculature. This will be most important for lower affinity antibodies, where these other loss terms (surface loss and intravasation) are significant, and when the internalization rate is much faster than the loss of radioisotope. This is the case for the 320 nM K_d binder in the anephric mice (bottom) of Figure 4.7. The model under-predicts the amount of signal since the antibody is trapped in the cells and cannot leave the tumor. The error is not significant for non-binders, since the antibody must have some affinity for the antigen to bind antigen and be internalized in the first place.

A second model comparison was chosen that differs widely from the above experiment. Whereas the above experiment was a HER-2 binding scFv analyzed after 24 hours in ~100 mg tumors, Shockley et al. have analyzed the time course of uptake of four different monoclonal antibodies that target two separate melanoma antigens in very small tumors (~4-12 mg) using two cell lines with differing antigen densities(3). With this small tumor size, the surface terms account for over a third of the uptake within the tumor. Every single model parameter is different for this experiment except for the S/V ratio ($2R_{cap}/R_{Krogh}^2$) as seen in table 4.1. The authors measured the plasma time course, fitting it to a biexponential decay, which was used as a model input. The paper also provided the antibody affinities for the four different IgGs used in the experiment, along with the maximum number of binding sites per cell for both antigens in each cell line. The mass of the tumors was used to estimate their size and obtain R_{tumor}. The cell density of melanoma cell xenografts is approximately 2.9×10^8 cells/mL(33), and the void fraction, permeability, and diffusion coefficient for IgG were used as given before(6). The internalization rates of these antibodies were estimated at 5×10^{-6}/s based on experiments done by Chan and Murphy(34). Without an explicit internalization rate measurement for the low molecular weight melanoma associated antigen (LMW-MAA), it was assumed to be the same as the high molecular weight melanoma associated antigen (HMW-MAA). Since this rate is slower than the loss of the radioisotope, the internalization rate is the relevant parameter.

The top panel of figure 4.8 shows the experimental time course of antibody in a SK-MEL-2 cell line on the left and the model predictions on the right. All parameters were estimated from the literature, so no values were fit to the experimental results. The LWM-MAA binding 436 IgG, HMW-MAA binding 9.2.27 IgG, and non-specific B72.3 IgG all have %ID/g and time courses similar to those

predicted by the model. However, the HMW-MAA binding IND1 IgG is predicted to bind at higher levels than found in the experiment. Moving to the lower panels, the experimental results in the M21 cell line are given on the left with model predictions on the right. Here, all the values are in reasonable agreement with the model predictions. In this second cell line, the prediction for the IND1 antibody is more in line with the model predictions, raising the question of the difference between the two cell lines. Looking closely at the model, the antigen density on the surface of the SK-MEL-2 cell line is 4 times lower than the M21 cell line. While the model is fairly insensitive to the antigen density for high affinity binders prior to saturation, the apparent affinity of an IgG can be highly sensitive to this surface density if it has a low intrinsic affinity. The authors assumed that the affinity of IND1 on the surface of SK-MEL-2 cells was equivalent to that on the surface of M21 cells, although it was not measured. Tang et al. have shown that if the intrinsic affinity of an antibody is low, even for antibodies with sub-nanomolar apparent affinity, the antibody may have no affinity for cell with a low antigen density on the surface(35). The low intrinsic affinity antibodies must bind bivalently to be retained on the cell, which is easy for cells with a million copies on the surface. However, if the antigen density drops such that only one arm of the antibody can bind, retention is low. The low antigen copy number on the surface of SK-MEL-2 cells may have caused a higher proportion of IND1 antibody to be lost from the tumor due to a lower apparent affinity. It is also evident that the drop in %ID/g at the later time points occurs faster than what is predicted by internalization. Given that these antigens are shed in the tumor(36), some of the antibody may be lost since the complex is not anchored in a cell membrane.
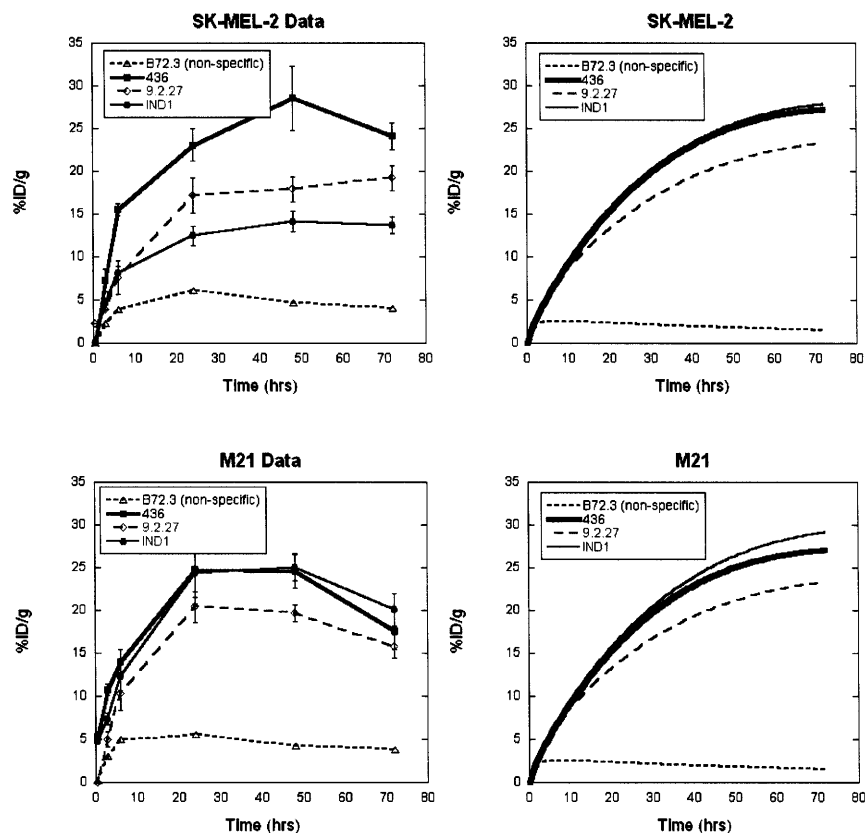
Figure 4.8 – Model Comparison to IgG Uptake in Melanoma Xenografts. The experimental data (left) is compared to the model predictions (right) for the SK-MEL-2 melanoma cell line (top) and M21 cell line (bottom). Model predictions are using the compartmental model for uptake (Appendix section 13b), and parameter values are given in table 4.1.

Although the surface terms in these tumors accounted for a third of the uptake given the 2.8 mm diameter tumor that was simulated, the actual influence may have been even higher. The largest dimension in these tumors ranged from 3-5 mm. Given the oblong shape of the tumors, more surface area is exposed, making the surface uptake more important. This is in agreement with the histology of these tumors, showing a time-dependent labeling from the tumor surface inward(37). If the tumor is secreting VEGF, vessels adjacent to the tumor may become hyperpermeable, providing a large antibody source near the surface.

Because this compartmental model is based on specific mechanisms, the results can be extended from mouse to humans. Model predictions for uptake of an anti-A33 IgG in humans were compared to a phase I clinical trial in which 12 patients received varying doses of humanized monoclonal antibody A33(1). For the model prediction, a 1 cm diameter tumor was assumed, so surface effects

136

were negligible. The affinity for antigen is roughly 1.8 nM (38), and a dose of 167 nM was assumed, although at these sub-saturating levels, the %ID/g is relatively independent of dose. The void fraction, diffusion coefficient, and permeability were as given before(6). Although larger tumors have more necrosis and likely lower surface area to tumor volume ratios, in the absence of better data, the surface area to volume ratio for viable tumor tissue from Hilmas and Gillette was used(30). Given that there is likely necrosis in these tumors, this may over-predict the uptake from the vasculature. The clearance values were measured and reported in the paper. A33 antigen associates with tight junctions on the surface of cells, giving it an extended half-life on the surface of 56 hrs(39). After 7 days, the compartmental model predicts 12.4×10^{-3} %ID/g in the tumor. While data in the clinic varies widely, the average value for all 12 patients was 5.03×10^{-3} %ID/g and ranged from 2.1 to 11.1×10^{-3} %ID/g, in reasonable agreement with the model prediction.

4.6   Discussion

This paper presents a simple, predictive, mechanistic model for simulating the uptake and retention of antibodies in tumor tissue. The parameters that determine uptake can be measured *in vitro* (antibody affinity, antigen density, internalization rate, etc.) or estimated from the literature (permeability, clearance, etc.). Certain properties will vary with conditions; for example a large charge on the antibody drug may affect the clearance, permeability, and/or diffusion(40-42). Local biological mediators can also influence properties such as decreased diffusion and permeability of tumor vasculature in the brain due to blood brain barrier type effects(43). This mechanistic model is useful in determining how changing tumor properties will likely affect the overall uptake without the need for complex computer simulations, and it can easily be used to help in experimental design, interpretation of *in vivo* data, and strategies to improve targeting.

One of the reasons the model reduces to such a simple result is that one of the steps in uptake, extravasation across the blood vessel wall, is so much slower than all the other steps. Uptake is then simply a function of the total permeability and surface area product. If this were not the case and diffusion were limiting, uptake would be dependent on the distribution of distances around each capillary. Plots such as those found by Baish and colleagues(44) would indicate what fraction of the tumor was targeted with different doses. To give an idea of how these frequencies translate into Krogh cylinder radii, fitting this distribution data to a collection of Krogh cylinders that are 20 μm, 50 μm, and

137

100 μm in radius, the results in Baish et al. indicate the respective fractions are 89%, 10%, and 1%. This means that although there are regions far from the vasculature, the majority of the tumor in this model is within several cell diameters of a capillary.

Targeting of systemically delivered antibody involves four major steps: 1) flow to the tumor, 2) transport across the capillary wall, 3) diffusion through the tissue, and 4) binding/metabolism. Of these four steps, extravasation of macromolecules is by far the slowest process. Binding occurs on the order of seconds, diffusion takes minutes, and extravasation takes hours(13). The rate that molecules cross the capillary is so slow that even with poor blood flow, perfusion is sufficient to avoid depletion in the plasma. In three of the models discussed in table 4.2 (27-29), the blood flow to the tumor was treated explicitly, and this rate was 100 to 1000 times faster than the rate of extravasation. Experimentally measured rates of blood flow are much faster than the rates of extravasation(16), and the plasma concentration of macromolecules exiting a tumor is approximately equal to that entering, indicating significant depletion does not occur(10). These studies verify that in general, the plasma concentration is not depleted along the length of the blood vessels, and flow is not the limiting step in uptake. When antibody binding occurs in the tumor, it can mask the low levels of unbound antibody in the tumor. For non-binding macromolecules, however, the concentration in the blood is much higher at early times before the interstitium has equilibrated and the plasma level drops, indicating poor extravasation(18).

For comparison, permeability is not the limiting step for oxygen and many small molecules. The concentration of oxygen just outside the blood vessel is very close to that in the blood(45), indicating a large Biot number. In the cases where the trans-capillary transport rate of oxygen is defined, it is typically dropped by assuming rapid exchange across the vessel wall(7). Problems with oxygen transport occur in the 1st and 3rd steps in uptake, which are blood flow and diffusion limitations(46). Because oxygen can transport across the blood vessel wall and diffuse into the tissue so quickly, the concentration in the blood can drop along the length of the capillary bed. Poor blood flow can then result in lack of oxygen transport to certain regions (e.g. transient hypoxia). Other regions of the tumor are located very far away from the blood vessel, and diffusion is too slow to keep up with metabolism in the tissue, giving rise to chronic hypoxia. These results can be seen in similar Krogh cylinder analyses of oxygen uptake and consumption(47). Oxygen concentration profiles in tumors demonstrate these phenomena. In some regions, the concentration in the capillary is low due to poor blood flow, while other regions have a sufficient concentration in the vessel, but the oxygen tension drops to hypoxic levels at large distances from the vessel in hypovascularized regions(45). In well oxygenated tissue, the

4th step, binding/metabolism, is 'limiting.' If a larger consumption is needed in the tissue, the cells must metabolize more oxygen, since blood flow, transport across the vessel wall, and diffusion to the cells are all sufficient to supply the tissue at the current level of consumption.

Small molecule drugs also have transport limitations in tumors, distributing heterogeneously in tumor tissue(48). While lots of research focuses on cellular mechanisms of drug resistance, such as multi-drug resistance proteins(49), limitations in transport could play an equal or even dominant role(48). Heijn et al. studied a series of anthracyclines with different cellular permeabilities using a perfused isolated tumor. Despite the large differences in plasma membrane permeability, the variants showed similar uptake in tumors. Increasing the perfusion rate did not increase drug uptake, so blood flow was not limiting. Estimates for transport across the capillary wall gave predictions that were much higher than the experimental one-pass fractional uptake (which was approximately 0.4 with a range from 0.3 to 0.7), indicating that permeability was not limiting either. A one-dimensional diffusion model of drug transport gave the closest agreement between prediction and the experimental results, as evidence that these drugs were limited by diffusion(10). Interestingly, the authors used albumin as a non-extravasating marker, since the concentration leaving the tumor was indistinguishable from the concentration entering. They note that although the vessels walls are permeable to albumin, the loss from the vascular compartment is negligible. Other small molecule drugs appear to be flow limited. Kristjansen et al. used a similar ex vivo perfused setup to study the transport of gemcitabine. The authors found an inverse correlation between flow resistance and drug uptake in two small cell lung cancer tumor lines, where the tumor with better blood flow characteristics had higher drug uptake(50). Jain et al. analyzed the uptake of methotrexate and found it was flow limited in some tumor preparations, while it was limited by permeability or diffusion in others(51).

Understanding the limitations on drug transport is critical in determining the best approach to circumvent these problems. Drugs such as bevacizumab decrease blood vessel permeability and normalize blood flow within the tumor, which is beneficial for oxygen and small molecules(52). Since permeability is limiting for macromolecules, this therapy is predicted to lower the overall uptake in tumors. Only if there were regions with extremely poor blood flow, as indicated by equation 4.3, would the improved distribution of blood flow benefit the uptake of this type of drug. However, there may be pharmacodynamic effects that are beneficial, since better oxygenated cells may be more susceptible to treatment, and steadier flow patters may ensure there is no disconnect between cells that are treated and cells that are viable from oxygen and nutrient delivery. Experiments varying other transport

parameters yield ambiguous results on limitations, since multiple effects may be occurring. For example, pharmacological agents that increase arterial blood pressure have been used to improve tumor uptake(53, 54). This could indicate that blood flow is limiting in some regions of the tumor, and higher pressure can force better perfusion. Although permeability is generally the limiting factor, the properties of tumors are heterogeneous. Blood flow is typically 100-1000 times faster than extravasation, but the stochastic development in tumors could reverse this trend in some local environments. For example, it is possible that a particular region may have 100-fold higher permeability and 100-fold lower blood flow. In this case, the regional limitation is caused by poor blood flow, and improving the flow by increasing arterial pressure will help augment local uptake. While the higher arterial blood pressure improves blood flow, it has other effects as well. Tumor capillary pressure is closely tied to the arterial pressure(55), and an increase in tumor vessel pressure may reopen collapsed vessels. While this perfuses areas of the tumor that were previously cut-off, it also increases the total surface area for transport, which is important in permeability limiting cases. The increased pressure may also cause more convection near the tumor periphery, increasing the effective permeability by supplementing extravasation. Therefore, more experiments are necessary to make definitive conclusions as to the benefit of this type of treatment.

This model captures the trend that smaller tumors have higher uptake, and generally uptake is greater near the tumor surface. There are 3 main reasons for this, however, and it is sometimes difficult to discern the difference. For smaller tumors, the shorter dimensions mean noticeable uptake could occur directly from the surface by diffusion inward from the surrounding tissue, and this is the mechanism captured in the current mechanistic model. Depending on the pressure surrounding the tumor, fluid leaving the surface may prevent this diffusion from occurring. The increased fluid flow near the surface will cause more antibody to extravasate, however, resulting in higher peripheral uptake. This scenario was explored with numerical simulations of tumor interstitial pressure and convection. In large tumors, the vascular density is often higher near the surface and there may be extensive central necrosis(56). With the vasculature being the major source of antibody entering the tumor, localization is greater in these outer regions, although the overall vessel surface area to tumor volume ratio is lowered due to necrosis. All three cases likely contribute to increased peripheral uptake in different scenarios.

The compartmental analysis explicitly ignores spatial variations surrounding each vessel in order to examine the time course of total tumor uptake. The microscale distribution around vessels is very

140

important for therapy, however, and should be taken into consideration. For example, 'cold' doses of antibody that lack a radioisotope or toxin conjugate can be delivered prior to the therapeutic agent in order to saturate easily accessible antigen in the blood or normal tissues(57). The compartmental model only indicates the average levels of both antibodies in the tumor. By analyzing the microdistribution, it can be shown that the cold antibody will help the therapeutic antibody target more cells by increasing the distance of penetration. If equal doses are given of each agent, twice as many cells will be targeted with half the antigen on the surface bound by each. As long as the therapeutic antibody is still effective at 50% saturation, the total number of targeted cells will double with no increased in the dose of therapeutic agent.

One of the major limitations of this model is the lack of treatment of convection. In a convection dominated tumor, the time course of uptake may differ from that given here. Baxter and Jain(9) assumed that diffusion made up 0%, 1%, or 10% of the overall permeability across the vessel wall, resulting in a convection dominated tumor. While this convection doesn't affect the distribution around the vessels significantly(19), it would affect the rate at which antibodies extravasate into the interstitium. The elevated interstitial pressure found in most tumors severely limits convection, but in some tumors, convection may play a larger role in antibody uptake. Convection in the tumor is caused by a pressure difference between the vasculature and interstitium, and since most tumors have elevated interstitial pressure, fluid flow is minimal. However, some neoplasias may be more prone to lower interstitial pressure, and anecdotal evidence exists for brain tumors and lymphomas. The permeability of blood vessels in brain tumors is lower than other types of tumors(43), which would lower the amount of fluid flowing into the interstitium and lower IP. Lymphomas may have higher tissue fluid permeability due to less cell-cell adhesion, allowing the fluid that leaks from tumor vessels to flow out of the tumor more easily, lowering IP. Although these pressures are highly variable, the interstitial pressure is slightly lower in these tumor types than others(15).

This compartmental model describes the major rates determining antibody uptake in tumors. Since most antibodies have dissociation rates well below the antigen concentration in the tumor, and many tumors that are targeted are larger than 100 mg (most xenografts and clinically identifiable disease), the model can often be simplified. Approximating the clearance using a single exponential, the maximum uptake is given analytically by equation 4.23. Examining this expression indicates the major factors that determine uptake and potential ways of improving localization. One of the most straight-forward ways of increasing the tumor concentration is to increase the dose. There is a one-to-one

correlation with administered dose and tumor uptake prior to saturation, as demonstrated by a constant %ID/g until all antigen is bound(58-61). Uptake is also increased by lowering the clearance rate or increasing permeability. The size of the targeting molecule often has opposite effects on these parameters, since larger molecules persist in the blood for longer times(62) but extravasate across the vasculature more slowly(18). Antibody uptake can also be maximized by increasing the vascular density $(2R_{cap}/R_{Krogh}^2)$ and the void fraction (ϵ). These parameters may be enhanced by debulking the tumor through traditional chemotherapy and/or radiation, which can increase the void fraction and allow previously collapsed, non-functional vessels to transport blood(30). Finally, targeting antigens with longer surface persistence will increase the maximum uptake in the tumor by lowering the amount lost from internalization.

There are trade-offs in varying many of these parameters. For example, a larger dose will drive greater tumor localization, but increased uptake in normal tissues may make this unfeasible due to increased background in imaging and toxicity with therapeutics. While choosing a slowly internalizing antigen will increase retention, this will decrease efficacy for immunotoxins that must be internalized(63). One area that will increase specificity to the tumor is increasing the permeability. This will allow faster and more selective uptake in the tumor, since any increase in permeability in normal tissues will be minimized by lymphatic drainage. Attempts at this strategy have been made, but changing the vessel permeability is a difficult balance, since too much disruption of the vascular wall can lead to collapse, completely cutting the blood supply to the tumor and limiting uptake(64). Ideally, the increased permeability could be maintained for days to allow the slow uptake from the blood. Methods currently being developed for monitoring the vasculature in tumors for use with anti-VEGF therapies could be adopted to monitor conditions for improved antibody uptake.

In conclusion, certain fundamental principles determine the overall time course of the pharmacokinetic distribution of antibodies in tumors. Since many of these parameters are known or can be obtained from the literature, this simple mechanistic model can give a rough estimate of the time course of antibody concentration in tumors in order to aid with experimental design, data interpretation, and strategies to improve uptake.

References

1.   Scott AM, Lee FT, Jones R, et al. A phase I trial of humanized monoclonal antibody A33 in patients with colorectal carcinoma: Biodistribution, pharmacokinetics, and quantitative tumor uptake. Clinical Cancer Research 2005;11:4810-7.

2.   Williams LE, Duda RB, Proffitt RT, et al. TUMOR UPTAKE AS A FUNCTION OF TUMOR MASS - A MATHEMATIC MODEL. Journal of Nuclear Medicine 1988;29:103-9.

3.   Shockley TR, Lin K, Sung C, et al. A QUANTITATIVE-ANALYSIS OF TUMOR SPECIFIC MONOCLONAL-ANTIBODY UPTAKE BY HUMAN-MELANOMA XENOGRAFTS - EFFECTS OF ANTIBODY IMMUNOLOGICAL PROPERTIES AND TUMOR-ANTIGEN EXPRESSION LEVELS. Cancer Research 1992;52:357-66.

4.   Adams G, Schier R, McCall A, et al. High Affinity Restricts the Localization and Tumor Penetration of Single-Chain Fv Antibody Molecules. Cancer Research 2001;61:4750-5.

5.   Jain RK. Transport of Molecules, Particles, and Cells in Solid Tumors. Annual Reviews in Biomedical Engineering 1999;01:241-63.

6.   Thurber GM, Zajic SC, Wittrup KD. Theoretic criteria for antibody penetration into solid tumors and micrometastases. J Nucl Med 2007;48:995-9.

7.   Middleman S. Transport Phenomena in the Cardiovascular System. New York: Wiley-Interscience; 1972.

8.   Graff BA, Bjornaes I, Rofstad EK. Macromolecule uptake in human melanoma xenografts. relationships to blood supply, vascular density, microvessel permeability and extracellular volume fraction. Eur J Cancer 2000;36:1433-40.

9.   Baxter L, Jain RK. Transport of Fluid and Macromolecules in Tumors: 1. Role of Interstitial Pressure and Convection. Microvascular Research 1989;37:77-104.

10.   Heijn M, Roberge S, Jain RK. Cellular membrane permeability of anthracyclines does not correlate with their delivery in a tissue-isolated tumor. 1999;59:4458-63.

11.   Eskey CJ, Wolmark N, McDowell CL, Domach MM, Jain RK. RESIDENCE TIME DISTRIBUTIONS OF VARIOUS TRACERS IN TUMORS - IMPLICATIONS FOR DRUG-DELIVERY AND BLOOD-FLOW MEASUREMENT. Journal of the National Cancer Institute 1994;86:293-9.

12.   Graff CP, Wittrup KD. Theoretical analysis of antibody targeting of tumor spheroids: importance of dosage for penetration, and affinity for retention. Cancer Res 2003;63:1288-96.

13.   Thurber G, Schmidt M, Wittrup KD. Factors determining antibody distribution in tumors. Trends in Pharmacological Sciences 2008;29:57-61.

14.   Boucher Y, Baxter LT, Jain RK. INTERSTITIAL PRESSURE-GRADIENTS IN TISSUE-ISOLATED AND SUBCUTANEOUS TUMORS - IMPLICATIONS FOR THERAPY. Cancer Research 1990;50:4478-84.

15.   Jain RK, Tong RT, Munn LL. Effect of vascular normalization, by antiangiogenic therapy on interstitial hypertension, peritumor edema, and lymphatic metastasis: Insights from a mathematical model. Cancer Research 2007;67:2729-35.

16.   Butler TP, Grantham FH, Gullino PM. BULK TRANSFER OF FLUID IN INTERSTITIAL COMPARTMENT OF MAMMARY-TUMORS. Cancer Research 1975;35:3084-8.

17.   Yuan F, Dellian M, Fukumura D, et al. Vascular Permeability in a Human Tumor Xenograft: Molecular Size Dependence and Cutoff Size. Cancer Research 1995;55:3752-6.

18.   Dreher MR, Liu WG, Michelich CR, Dewhirst MW, Yuan F, Chilkoti A. Tumor vascular permeability, accumulation, and penetration of macromolecular drug carriers. Journal of the National Cancer Institute 2006;98:335-44.

19.   Baxter LT, Jain RK. TRANSPORT OF FLUID AND MACROMOLECULES IN TUMORS: 4. A MICROSCOPIC MODEL OF THE PERIVASCULAR DISTRIBUTION. Microvascular Research 1991;41:252-72.

20.   Mager DE. Target-mediated drug disposition and dynamics. Biochemical Pharmacology 2006;72:1-10.

21.   Mager DE, Jusko WJ. General pharmacokinetic model for drugs exhibiting target-mediated drug disposition. J Pharmacokinet Pharmacodyn 2001;28:507-32.

22.   Deen W. Analysis of Transport Phenomena: Oxford University Press; 1998.

23.   Green E. Biology of the Laboratory Mouse. New York: Dover Publications & The Jackson Laboratory; 1966.

24.   Kaliss N, Pressman D. Plasma and blood volumes of mouse organs as determined with radioactive iodoproteins. Proceedings of the Society for Experimental Biology and Medicine 1950;75:16-20.

25.   Yang SSL, Nickoloff EL, McIntyre PA, et al. TC-99M HUMAN-SERUM ALBUMIN - SUITABLE AGENT FOR PLASMA-VOLUME MEASUREMENTS IN MAN. Journal of Nuclear Medicine 1978;19:804-7.

26.   Sung C, Youle RJ, Dedrick RL. PHARMACOKINETIC ANALYSIS OF IMMUNOTOXIN UPTAKE IN SOLID TUMORS - ROLE OF PLASMA KINETICS, CAPILLARY-PERMEABILITY, AND BINDING. Cancer Research 1990;50:7382-92.

27.   Baxter L, Zhu H, Mackensen D, Jain RK. Physiologically Based Pharmacokinetic Model for Specific and Nonspecific Monoclonal Antibodies and Fragments in Normal Tissues and Human Tumor Xenografts in Nude Mice. Cancer Research 1994;54:1517-28.

28.   Ferl GZ, Wu AM, DiStefano JJ. A predictive model of therapeutic monoclonal antibody dynamics and regulation by the neonatal fc receptor (FcRn). Annals of Biomedical Engineering 2005;33:1640-52.

29.   Ferl GZ, Kenanova V, Wu AM, DiStefano JJ. A two-tiered physiologically based model for dually labeled single-chain Fv-Fc antibody fragments. 2006;5:1550-8.

30.   Hilmas D, Gillette E. MORPHOMETRIC ANALYSES OF THE MICROVASCULATURE OF TUMORS DURING GROWTH AND AFTER X-IRRADIATION. Cancer 1974;33:103-10.

31.   Press OW, Shan D, HowellClark J, et al. Comparative metabolism and retention of iodine-125, yttrium-90, and indium-111 radioimmunoconjugates by cancer cells. Cancer Research 1996;56:2123-9.

32.   Mattes MJ, Griffiths G, Diril H, Goldenberg D, Ong G, Shih L. Processing of Antibody-Radioisotope Conjugates after Binding to the Surface of Tumor Cells. Cancer 1994;73:787-93.

33.   Lyng H, Haraldseth O, Rofstad EK. Measurement of cell density and necrotic fraction in human melanoma xenografts by diffusion weighted magnetic resonance imaging. Magnetic Resonance in Medicine 2000;43:828-36.

34.   Chan MC, Murphy RM. Kinetics of cellular trafficking and cytotoxicity of 9.2.27-gelonin immunotoxins targeted against the high-molecular-weight melanoma-associated antigen. Cancer Immunology Immunotherapy 1999;47:321-9.

35.   Tang Y, Lou J, Alpaugh RK, Robinson MK, Marks JD, Weiner LM. Regulation of antibody-dependent cellular cytotoxicity by IgG intrinsic and apparent affinity for target antigen. 2007;179:2815-23.

36.   Lin K, Nagy JA, Xu HH, Shockley TR, Yarmush ML, Dvorak HF. COMPARTMENTAL DISTRIBUTION OF TUMOR-SPECIFIC MONOCLONAL-ANTIBODIES IN HUMAN-MELANOMA XENOGRAFTS. Cancer Research 1994;54:2269-77.

37.   Shockley TR, Lin JK, Nagy JA, Tompkins RG, Yarmush ML, Dvorak HF. SPATIAL-DISTRIBUTION OF TUMOR-SPECIFIC MONOCLONAL-ANTIBODIES IN HUMAN-MELANOMA XENOGRAFTS. Cancer Research 1992;52:367-76.

38.   Almqvist Y, Orlova A, Sjostrom A, et al. In vitro characterization of At-211-labeled antibody A33 - a potential therapeutic agent against metastatic colorectal carcinoma. Cancer Biotherapy and Radiopharmaceuticals 2005;20:514-23.

39.   Ackerman M, Chalouni C, Schmidt M, et al. A33 antigen displays persistent surface expression. Cancer Immunology, Immunotherapy 2008.

40.   Rippe B, Haraldsson B. Fluid and protein fluxes across small and large pores in the microvasculature. Application of two-pore equations. Acta Physiol Scand 1987;131:411-28.

41.   Melkko S, Halin C, Borsi L, Zardi L, Neri D. An antibody-calmodulin fusion protein reveals a functional dependence between macromolecular isoelectric point and tumor targeting performance. 2002;54:1485-90.

42.   Dellian M, Yuan F, Trubetskoy VS, Torchilin VP, Jain RK. Vascular permeability in a human tumour xenograft: molecular charge dependence. British journal of cancer 2000;82:1513-8.

43.   Hobbs S, Monsky W, Yuan F, et al. Regulation of transport pathways in tumor vessels: Role of tumor type and microenvironment. Proceedings of the National Academy of Science, USA 1998;95:4607-12.

44.   Baish JW, Gazit Y, Berk DA, Nozue M, Baxter LT, Jain RK. Role of tumor vascular architecture in nutrient and drug delivery: an invasion percolation-based network model. Microvasc Res 1996;51:327-46.

45.   Torres IP, Leunig M, Yuan F, Intaglietta M, Jain RK. Noninvasive Measurement of Microvascular and Interstitial Oxygen Profiles in a Human Tumor in Scid Mice. 1994;91:2081-5.

46.   Dewhirst MW, Kimura H, Rehmus SWE, et al. Microvascular studies on the origins of perfusion-limited hypoxia. British Journal of Cancer 1996;74:S247-S51.

47.   Kirkpatrick JP, Brizel DM, Dewhirst MW. A mathematical model of tumor oxygen and glucose mass transport and metabolism with complex reaction kinetics. Radiation Research 2003;159:336-44.

48.   Minchinton AI, Tannock IF. Drug penetration in solid tumours. Nature Reviews Cancer 2006;6:583-92.

49.   Perez-Tomas R. Multidrug resistance: Retrospect and prospects in anti-cancer drug treatment. Current Medicinal Chemistry 2006;13:1859-76.

50.   Kristjansen PEG, Brown TJ, Shipley LA, Jain RK. Intratumor pharmacokinetics, flow resistance, and metabolism during gemcitabine infusion in ex vivo perfused human small cell lung cancer. Clinical Cancer Research 1996;2:359-67.

51.   Jain RK, Wei J, Gullino PM. PHARMACOKINETICS OF METHOTREXATE IN SOLID TUMORS. Journal of Pharmacokinetics and Biopharmaceutics 1979;7:181-94.

52.   Jain RK. Normalization of tumor vasculature: An emerging concept in antiangiogenic therapy. Science 2005;307:58-62.

53.   Burke D, Davies MM, Zweit J, et al. Continuous angiotensin II infusion increases tumour: normal blood flow ratio in colo-rectal liver metastases. 2001;85:1640-5.

54.   Kinuya S, Yokoyama K, Kawashima A, et al. Pharmacologic intervention with angiotensin II and kininase inhibitor enhanced efficacy of radioimmunotherapy in human colon cancer xenografts. 2000;41:1244-+.

55.   Boucher Y, Jain RK. Microvascular Pressure Is the Principal Driving Force for Interstitial Hypertension in Solid Tumors: Implications for Vascular Collapse. Cancer Research 1992;52:5110-4.

56.   Ahlstrom H, Christofferson R, Lorelius L. Vascularization of the continuous human colonic cancer cell line LS 174 T deposited subcutaneously in nude rats. APMIS 1988;96:701-10.

57.   Hernandez M, Knox S. Radiobiology of radioimmunotherapy: targeting CD20 B-cell antigen in non-Hodgkin's lymphoma. International Journal of Radiation Oncology Biology Physics 2004;59:1274-87.

58.   Sharkey RM, Karacay H, Richel H, et al. Optimizing bispecific antibody pretargeting for use in radioimmunotherapy. Clinical Cancer Research 2003;9:3897S-913S.

59.   Liu GZ, He J, Dou SP, Gupta S, Rusckowski M, Hnatowich DJ. Further investigations of morpholino pretargeting in mice - establishing quantitative relations in tumor. European Journal of Nuclear Medicine and Molecular Imaging 2005;32:1115-23.

60.   Koppe E, Soede AC, Pels W, et al. Experimental radioimmunotherapy of small peritoneal metastases of colorectal origin. International Journal of Cancer 2003;106:965-72.

61.   Kranenborg M, Boerman OC, Oosterwijk-Wakka JC, De Weijert MCA, Corstens FHM, Oosrterwijk E. Two-step radio-immunotargeting of renal-cell carcinoma xenografts in nude mice with anti-renal-cell-carcinoma X anti-DTPA bispecific monoclonal antibodies. International Journal of Cancer 1998;75:74-80.

62.   Wu AM, Senter PD. Arming antibodies: prospects and challenges for immunoconjugates. Nature Biotechnology 2005;23:1137-46.

63.   Wenning LA, Murphy RM. Coupled cellular trafficking and diffusional limitations in delivery of immunotoxins to multicell tumor spheroids. Biotechnol Bioeng 1999;62:562-75.

64.   Zhao LL, Ching LM, Kestell P, Kelland LR, Baguley BC. Mechanisms of tumor vascular shutdown induced by 5,6-dimethylxanthenone-4-acetic acid (DMXAA): Increased tumor vascular permeability. 2005;116:322-6.

Chapter 5 – Experimental Uptake in Mouse Xenografts

5.1   Introduction

In vitro methods for studying antibody transport are extremely useful to parse out the different mechanisms and parameters for tumor localization. Ultimately, testing with an *in vivo* model demonstrates the conclusions in a more realistic, non-ideal system. Typically, these experimental systems involve mice due to their small size, ease of care, low expense, and availability of a variety of transgenic model systems.

There are many different mouse model systems and detection methods available for measuring *in vivo* distribution. Some of the earliest and most widely used models are mouse xenograft models. These involve the injection of human cancer cell lines into immunocompromised mice, where the deficient immune system allows the human cells to escape rejection. Within this class of models, there are ectopic xenografts, where the tumor cell line is not normally found at the site of injection (e.g. breast cancer cells injected subcutaneously). This is typical for many subcutaneous tumors, where the injection under the skin is easily performed, and the surface location allows quick monitoring of the tumor size and easy identification during imaging. Alternatively, orthotopic models (e.g. breast cancer cells in the mammary fat pad) may better replicate certain aspects of tumor physiology, cell signaling, and metastasis(1). Depending on the tumor site, development and experimentation on these types of tumors may be more involved, such as requiring surgery for implantation. While these models typically generate a single tumor per injection site, other models mimic disseminated disease, for example, injecting cells intravenously or intrasplenically and allowing them to form tumors in the lung or liver(2).

Xenograft mouse models are capable of rapidly generating tumors (often in a week or two) at defined locations. However, for therapy, results in these models differ widely than in the clinic. In general, xenograft models are much easier to treat and cure than clinical tumors(3). The xenografts are in a different host, and all the cells are genetically similar. This means the cells are often dependent on the same signaling pathways, and they may lack the genetic diversity capable of mounting resistance against a variety of treatments. In contrast, clinical cancers are often able to escape therapy in an analogous manner to antibiotic resistance. Although therapies may be able to kill 99% of the tumor cells initially, eliminating clinically detectable disease, a resistant population of cells remains that can repopulate the tumor, and it is often no longer responsive to the primary treatment(4). In order to simulate this type of genetic diversity, chemical induced tumor models use mutagens on healthy tissue

in order to mimic the clinical situation. While the results are more realistic than xenografts, the method is also more time consuming.

As our understanding of the genetic basis of cancer develops, researchers are able to better mimic the natural pathways for various cancers. By directly manipulating proto-oncogenes and tumor suppressor genes that are affected in human cancers, more realistic transgenic mouse models are being developed(5). For colon cancer, early models were discovered using random mutagenesis, such as the APC-MIN transgenic mouse(6). Heterozygous mice from this line develop approximately 30 adenomas in the small intestine by 4 months of age(7). This model, crossed with a CEA expressing transgenic, has been used to look at antibody targeting of CEA(8). More recent models include the activation of the RAS oncogene and p53 tumor suppressor gene. Although there are multitudes of oncogenes and tumor suppressor genes that are mutated in human cancers, these are two of the most common implicated genes in their respective categories.

For initial experiments, a subcutaneous xenograft model was used. Since these were not therapeutic experiments, development of the tumor from an established cancer cell line was not a concern. The rapid generation of tumors in a defined location allowed imaging and histology to easily be performed, which outweighed the benefits of orthotopic or transgenic models for this set of experiments. CEA does not have a mouse equivalent, so the target antigen played a role in the choice of model system. In order to use a transgenic system, a mouse model expressing a CEA transgene would be required(7, 9).

While there are many different mouse models for tumor generation, each with benefits and drawbacks, there are also several imaging and detection modalities to track antibodies (and other drugs) delivered to the tumor. Some of these involve destructive sampling, but others offer the capability to follow the same animal in time. Radiolabeling is one of the most common methods for tracking molecules in the body. There are imaging systems for tracking radiolabeled antibodies, but a common method employed is the 'cut-and-count' method, where mice are sacrificed at various time points after injection of the antibody, the tissues of interest are removed, and signal intensity is measured in a gamma counter(10). This technique enables the measurement of uptake in any organ of interest, although it is obviously a destructive method. Histological samples can be taken to look at the local distribution, although the resolution with autoradiographic techniques is limited(11). These same types of tissue samples can be taken using fluorescently tagged or even untagged antibodies(12-14), and fluorescent microscopy techniques have allowed detailed spatial information to be collected. In the

148

case of untagged antibodies, indirect detection methods, such as antibodies against epitope tags or Fc regions, can be used to determine the local distribution of antibody. Without a radioisotope or far-red fluorescent tag, it is more difficult to get information on total tumor uptake, however. A final non-imaging method for indirectly obtaining tumor uptake involves pharmacodynamic measurements, such as tumor size. For example, a therapeutic agent can be delivered to a mouse with an established subcutaneous tumor, and caliper measurements can be taken over time to track tumor growth versus a control(15).

Several imaging techniques have been used to track antibody distribution in mice. Research is active within all of these fields, and currently, no single imaging modality really dominates over the others in the clinic(16). The two techniques for detecting radiolabeled antibodies are single photon emission computed tomography (SPECT) and positron emission tomography (PET). SPECT can be used to detect gamma emissions, for example from radioactive indium or iodine labeling. The method does not have great spatial resolution, and no anatomical data is available. However, it is a convenient method for imaging localized antibodies(17, 18). PET is one of the most sensitive imaging modalities. Like, SPECT, the spatial resolution in humans is several millimeters(16), but small animal devices are being developed with superior resolution. Increasingly, PET is being paired with computed tomography (CT) scanners to combine the exquisite sensitivity of PET with the high spatial resolution of CT. One drawback for PET is that some positron emitting isotopes, such as fluorine-18, have short half lives (e.g. 110 min(16)). While this is okay for small molecules like fluorodeoxyglucose (FDG-PET), the current imaging agent of choice for cancer(18), it is not compatible with the slow accumulation of macromolecules. Some researchers have combined these PET emitters with pretargeting methods(19) to circumvent this problem. Compared to high energy radioisotopes, fluorescence imaging certainly has limitations in detection; the body is fairly impenetrable to visible light. However, light in the far red spectrum does have appreciable penetration in tissue, and several far red fluorochromes have been developed for *in vivo* imaging(20). These methods are generally safer than radioactive tags and are compatible with fluorescence microscopy of histological samples. Fluorescence molecular tomography (FMT) uses sequential images with varying location of the excitation light to develop three-dimensional reconstructions of fluorescent label in mice(21). Finally, magnetic resonance imaging (MRI) can be used by tagging antibodies with certain contrast agents. The major strengths of MRI in the clinic are excellent resolution and contrast of soft tissues and a great safety profile with the use of non-ionizing radiation. A major drawback is the limited sensitivity of contrast agents; for Gd-DTPA, the agent is typically injected in millimolar concentrations(22) and may require 10-100 μM for detection(23, 24).

For this series of experiments, a combination of FMT imaging and fluorescence microscopy on histology sections was chosen for analysis. The detection of antibodies with micrometer resolution in the histology sections was a major factor in choosing these methods, since fluorescent labeling can be used to detect the antibody, antigen, and blood vessels in the tumor.

5.2   Methods

To generate identical antigen positive and negative tumors, the cell line HT-1080 was transfected with a pIRES-CEA expression plasmid(25) using Lipofectamine. This plasmid contains a CMV promoter driving CEA expression, followed by an internal ribosome binding site and neomycin resistance gene. The single promoter for the two sites increases the chances that a resistant clone is expressing the transgene. The transfection protocol was adapted from the manufacturer's instructions; briefly, 6 μg of plasmid DNA and 18 μL Lipofectamine, each diluted in 300 μL OptiMEM, were mixed and incubated 30 min at room temperature. This was further diluted to a volume of 1.2 mL in OptiMEM and added to 80% confluent HT-1080 cells in a T-25 flask (~3.6×10^5 cells) that had been washed with 5 mL OptiMEM. The cells were incubated for 6 hours in a 37^0C incubator. The media was removed, and cells were washed and incubated with EMEM media under normal conditions for 72 hours.

For selection of stable clones, 3 days after the transfection, the cells were subcultured into 3 separate 6-well dishes to monitor the surviving clones. A concentration of 0.75 mg/mL of G418 was added to the media for selection, and the media was replaced every 2-3 days. After 7 days, 9 of 18 wells contained viable cells. Most colonies were single cells, one contained 32 cells, and no viable cells were apparent in the mock transfected flask. To increase cell growth, the selection pressure was reduced from 0.75 mg/mL G418 to 0.25 mg/mL on day 7. After 2 weeks of selection, one colony was growing at an appreciable rate, and this was eventually subcultured into additional plates.

The *in vivo* plasma decay curves of antibody and dextran were tracked with one of two methods. Mice were anesthetized with 2-3% isoflurane, and 5 or 10 μg of ds-sm3E-750 and/or 40 kDa dextran-Cy5.5 in a 100 μL volume was given by tail vein injection. Blood samples were taken by retro-orbital puncture on anesthetized mice with a heparin coated capillary tube. The fluorescence intensity was taken directly from these capillary tubes using an Odyssey infrared imager (LI-COR, Lincoln, NE). Alternatively, 20 μL of whole blood was diluted with 40 μL of SPDP buffer (phosphate buffered saline (PBS) with 10 mM EDTA) to prevent clotting. The samples were spun briefly to remove red blood cells,

placed in a 384 well plate, and imaged on the Odyssey IR imager. A control sample was added where the concentration was identical to the injected dose diluted in 2 mL mouse plasma volume.

Tumors were grown by injecting 3×10^6 cells (HT-1080, HT-CEA, or LS174T) in 50 µL volume of PBS or 50% Matrigel / 50% EMEM media subcutaneously in the left or right flank of anesthetized athymic (nude) mice. Tumors developed after 1-2 weeks of growth. The LS174T cell line grew rapidly, forming tumors ~1 g in size after 1-2 weeks, while the HT-1080 and HT-CEA cell lines grew to about 100-200 mg after 1-2 weeks of growth.

For histological analysis of tumors, mice were anesthetized at various time points after injection and euthanized by cervical dislocation. The tumors were removed from the flanks, weighed, placed in optimal cutting temperature (OCT) compound, and frozen at -70^0C. The MIT Center for Cancer Research Histology facility processed the samples by frozen sectioning. Slides were processed by three 5 min washes (3x5 min washes) in phosphate buffered saline to remove the OCT, 20 min blocking in 100 µL of PBG (PBS with 0.15% glycine, 0.5% bovine serum albumin (BSA)) with 20% goat serum, and additional 3x5 min washes in PBS. The slides were stained overnight at 4^0C using 50-100 µL of 10 µg/mL anti-CD31 antibody (MAB 1398Z, Millipore, Billerica, MA) in PBS with 0.1% BSA (PBS-BSA). After 3x5 min washes in PBS, slides were labeled for 1 hr at room temperature in PBS-BSA with 50 µL of 10 µg/mL goat anti-hamster Alexa-546 (Invitrogen, Carlsbad, CA) and/or 10 nM Alexa-488 conjugated anti-CEA antibody (M85151a, Fitzgerald Industries, Concord, MA). The slides were washed (3x5 min) in PBS and sealed with 0.0003% Hoechst 33342 in PBS for nuclear staining. Slides were imaged on an Olympus widefield fluorescence scope with the appropriate fluorophore filters.

5.3   Results

The pathological physiology of tumors causes increased uptake in tumors compared to healthy tissue for a variety of molecules. In order to distinguish between this non-specific uptake and antibody binding mediated specificity, an antigen negative tumor was injected in the opposite flank of the antigen positive tumor in the same mouse. However, differences in vascularization, permeability, cell growth, and cell density all affect the uptake, so using a different cell lines is prone to errors from these effects. In order to have two tumors that are identical in as many facets as possible, an antigen negative cell line was transfected with CEA so the two lines would differ only by antigen expression.

For the background line, a human fibrosarcoma cell line, HT-1080, was selected. This cell line shows high permeability similar to colon cancer cell lines (Bhatia lab, personal communication), and its origin as a fibroblast cell line made it unlikely to express CEA. Subsequent testing with antibodies and scFvs against CEA showed no staining, indicating a lack of CEA expression (figure 5.2). Using Lipofectamine, HT-1080 cells were transfected with a CEA expression plasmid containing a neomycin resistance gene. Control tests using serial dilutions of G418 showed that 0.75 mg/mL was sufficient to kill cells after day 2, and 0.25 mg/mL would suppress viability after 6 days (figure 5.1).

G418 Toxicity
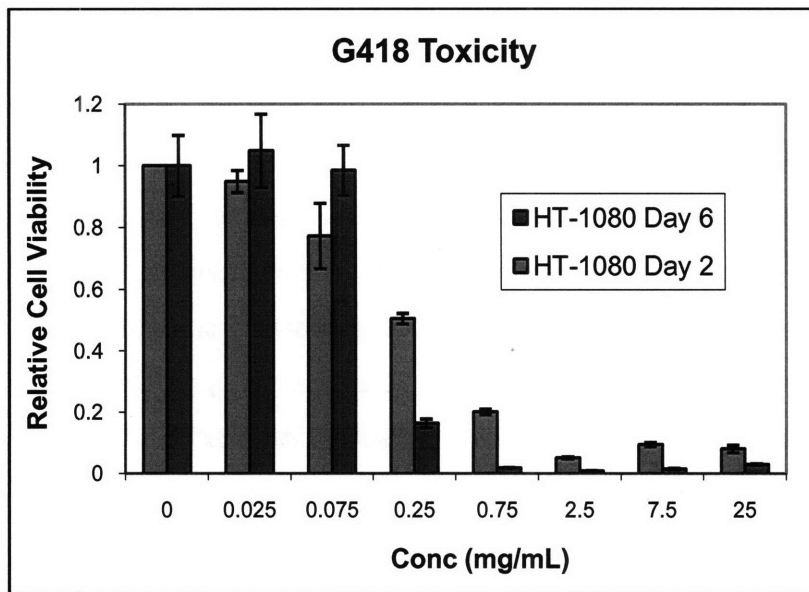
Figure 5.1 – HT-1080 cells were grown in EMEM with varying concentrations of G418 in the media. After 2 and 6 days, viability was tested using a crystal violet assay. From these results, a 0.75 mg/mL concentration was used for initial selection of transfected cells, followed by 0.25 mg/mL for maintenance.

Only one apparent colony was isolated after 2 weeks of selection. This may have been due to the stringent selection conditions using high concentrations of G418 on the cells. This colony was continually grown under selective pressure and analyzed by flow cytometry and fluorescence imaging to detect the presence of surface CEA. With a roughly 1 day doubling time, it took approximately 3 weeks to go from a single transfected cell to 10^6 cells for experiments. This initial colony was given the name HT-1080-CEA. Figure 5.2 shows positive staining with an anti-CEA scFv using flow cytometry and fluorescence microscopy.
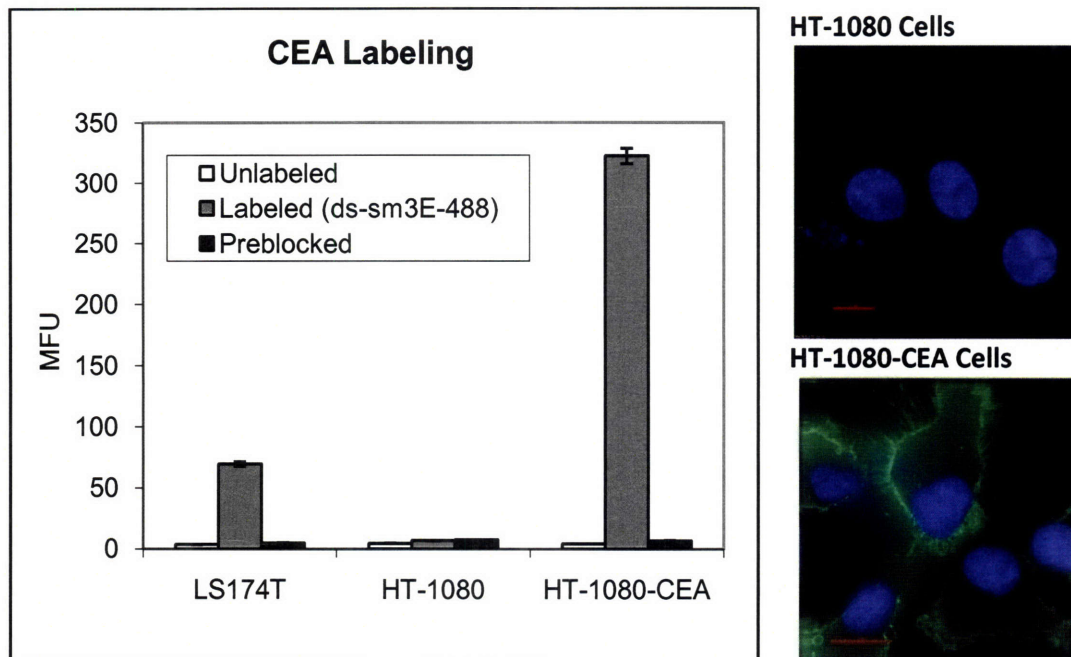
Figure 5.2 – Surface labeling of CEA. Cells were incubated with 20 nM ds-sm3E-488 for 1 hr on ice and analyzed by flow cytometry (left). The preblocked cells were incubated overnight with 100 nM non-fluorescent ds-sm3E, and 100 nM of non-fluorescent ds-sm3E was included during the labeling step to block all specific binding sites. The HT-1080-CEA cells show higher staining than LS174T cells, which have approximately 400,000 CEA molecules per cell. This may be due in part to the larger size of the HT-1080 cells. Cells were labeled similarly and imaged using a fluorescence microscope (right). The surface staining of CEA is readily apparent by the green fluorescence on the transfected cells. The nuclei were stained with Hoechst 33342 (blue). Red scale bar = 10 μm

The transfected cell line was frozen for storage in liquid nitrogen, and these aliquots continued to express CEA after they were thawed, providing an immortalized transfected cell line. Unexpectedly, the flow cytometry histograms demonstrated 2 peaks of labeled HT-1080-CEA cells. This was repeatable, and a sort was carried out to isolate the high expressing cells. However, after 6 months of growth in selection media, only 1 peak was present during the sort. Figure 5.3 shows a comparison between the original transfected cell line, HT-1080-CEA, and the continuously cultured cell line, named HT-CEA. It is likely that the cells growing at the fringe of the original colony after transfection, which were thought to have migrated to this area, must have constituted another viable colony with lower expression adjacent to the original one. These were grown in culture together, but after months of selection, only the higher expressing cell line remained. The other line likely had lower expression due to the location of the inserted gene(s), number of copies, or a combination of the two. The single colony clone, HT-CEA, was subsequently frozen for storage.
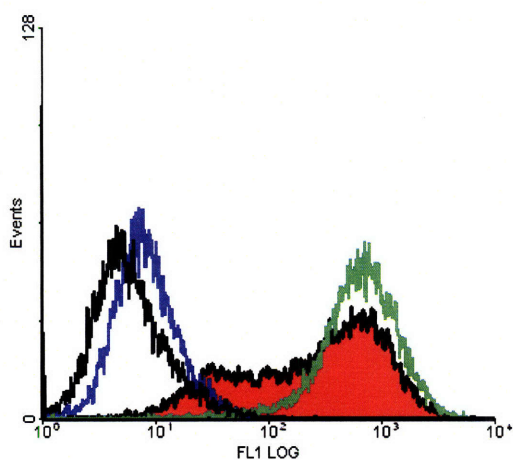
Figure 5.3 – Histogram of HT-1080-CEA and HT-CEA cell lines. 20 nM ds-sm3E-488 was used to label HT-1080-CEA cells (red) or HT-CEA cells (green) on ice for 1 hr. The unlabelled negative controls are shown in black (HT-1080-CEA) and blue (HT-CEA).

Disulfide stabilized sm3E was secreted from yeast as described in Chapter 3. Approximately 2 liters of yeast culture yielded 1.1 mg of purified disulfide stabilized monomer. To label the scFv with Alexa-750, 35 µL of 1M sodium bicarbonate was added to the antibody to yield a final concentration of approximately 3 mg/mL protein. 1 mg of Alexa Fluor 750 carboxylic acid, succinimidyl ester was dissolved in 100 µL DMSO. 50 µL of the dissolved dye was added to the protein and incubated for 30 min at room temperature. After 30 min, the degree of labeling was greater than 3 dye/protein, so the reaction was stopped by separation of the unreacted dye using Bio-gel P-6 gel (Bio-Rad, Hercules, CA). The protein was then dialyzed overnight in PBS to remove any remaining free dye. SDS-PAGE shows a single band of the correct molecular weight for the ds-sm3E-750, and the shift under reducing conditions indicates the disulfide bond holding the two domains together is correctly formed (figure 5.4). Using TLC and an Odyssey infrared imager, > 90% of the Alexa-750 dye was attached to protein. To test the reactive fraction of labeled scFv, analytical gel filtration was performed on the conjugate. 5 µg of ds-sm3E-750 at a concentration of 1.85 µM was incubated overnight at 37^0C with 133 µg CEA (7.4 µM, or 4x excess) to allow the active fraction to form complexes. 5 µg of ds-sm3E-750 was injected into a Pharmacia Biotech FPLC system with Superdex 75 and Superdex 200 columns in series to obtain a unbound scFv control peak, and the mixture was then run to determine the fraction in complexes versus unbound. No detectable protein appeared in the free scFv fractions (data not shown), indicating that virtually all of the labeled protein was still reactive with CEA.
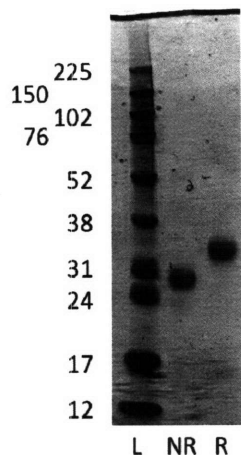
Figure 5.4 – SDS-PAGE of ds-sm3E-750 protein. 1 μg of ds-sm3E-750 protein was loaded in a 12% Bis-Tris gel and run at 200V for 50 min, followed by staining with Coomassie Blue. The first lane is a protein ladder, followed by the scFv under non-reducing conditions (lane 2) and reducing conditions (lane 3). The unreduced protein runs faster due to the extra disulfide bond maintaining a more compact shape.

To test the clearance of the scFv from the mouse plasma after injection, two mice without tumors, and two tumor bearing mice, were injected with 5-10 μg of ds-sm3E-750 and 40 kDa dextran-Cy5.5 (Nanocs, New York, NY). The plasma fluorescence in the 680 and 750 channels was either taken directly in capillary tubes used for whole blood sampling, or it was diluted, separated from the red blood cells, and imaged. The signal was normalized to the 1 minute time point, and the results are shown in figure 5.5. A control well showed that the initial fluorescence intensity for the scFv was similar to the total injected dose dissolved in a 2 mL plasma volume, indicating that the antibody rapidly distributed in the plasma volume but was not sequestered in any other regions (e.g. binding red blood cells, plasma membrane, etc.).
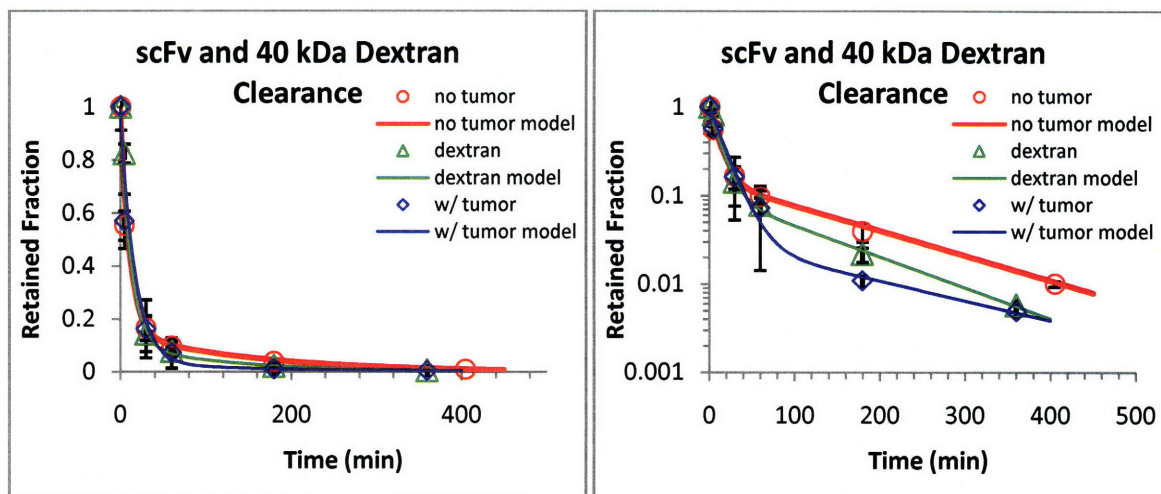
Figure 5.5 – Plasma clearance of ds-sm3E-750 and 40 kDa dextran-Cy5.5 from tumor and non-tumor bearing mice. The same data is plotted on a linear axis (left) to show the qualitatively similar clearance, and a log axis (right) to show minor differences in the beta phase clearance. 5-10 µg of scFv or dextran was injected into nude mice, and plasma samples were taken at 1 min, 5 min, 30 min, 1 hr, 3 hr, and 6 hrs. The dextran clearance was only measured in tumor bearing mice. Over 90% of the plasma level is gone after 1 hr, as expected by the 30 and 40 kDa sizes, which are below the renal filtration limit.

Using least squares fitting, the data were fit to a biexponential decay. Table 5.1 shows the fitted values for a biexponential decay of the scFv in tumor and non-tumor bearing mice and the 40 kDa dextran. Qualitatively, clearance from the plasma follows a similar profile to other scFvs(26), where approximately 90% of the antibody is cleared with a half life of several minutes, followed by a beta phase clearance of a couple hours. The variation in fitted parameters arises from differences in only a couple time points, so it is difficult to know if these are real or results of experimental variation.

Expt	% α	Alpha half-life	Beta half life
ds-sm3E-750 no tumor	86	7.4 min	1 hr 47 min
ds-sm3E-750 tumor bearing	97	12 min	2 hr 15 min
40 kDa dextran-Cy5.5 tumor bearing	90	8 min	1 hr 26 min

Table 5.1 – Fitted clearance rates for dextran and scFv. The clearance curves were fit to a biexponential decay using least squares and weighting the error by the inverse of the square signal intensity (so early time points were not over-emphasized). The model profiles are shown in figure 5.5.

CEA has been shown to be internalized with an approximately 15 hr half life on the surface of LS174T colon cancer cells(27). Studies on the HT-CEA transfected cell line show that these cells

156

internalize the antigen even faster, with a 3 hour half life (Mike Schmidt, data not shown). With this short internalization half life, the residualizing nature of the dye is important in determining the signal retention. If the dye from degraded antibody leaves the cells quickly, the signal intensity will drop over time. However, if the dye stays within the cells for an extended length of time, the total signal within the tumor will not decrease due to internalization. To test this, HT-CEA cells were incubated for 2 hrs at 37^0C with 10 nM ds-sm3E-750. The antibody was then removed, and the wells were incubated at 37^0C in media for 30 min, 1 hr, 3 hrs, 5 hrs, and 24 hrs. At each time point, the cellular fluorescence was taken using flow cytometry. The results are shown in figure 5.6. Even after 24 hours, the signal intensity only dropped to roughly 90% of the initial signal, indicating the dye remains in the cells for an extended period of time. Similar results were obtained using shMFE-750.
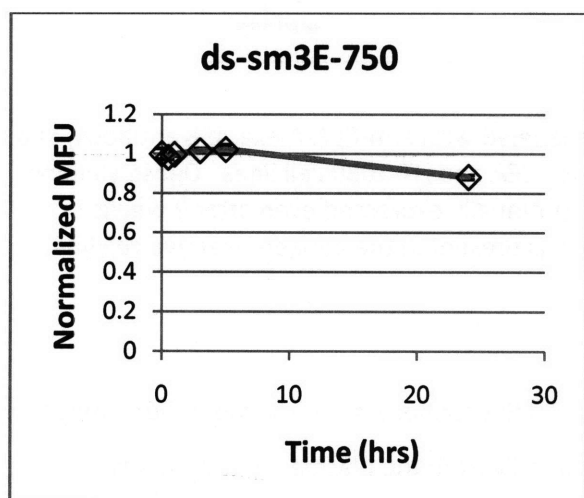

Figure 5.6 – Residualization of Alexa-750 dye in HT-CEA cells. Cells were labeled for 2 hr in 10 nM ds-sm3E-750, then incubated for various times at 37^0C. The total cellular fluorescent was measured using flow cytometry.

Using the system developed above, the localization of systemically delivered scFv was tested in mice bearing HT-1080 and HT-CEA flank and mammary fat pad tumors. Mice were anesthetized, injected with 50 µg of ds-sm3E-750, and euthanized by cervical dislocation at 3, 7, and 24 hrs. The tumors were weighed and frozen in OCT for sectioning. *In vivo* expression of CEA antigen was tested by labeling the tumors with anti-CEA IgG conjugated to Alexa-488. Figure 5.7 shows that only the antigen positive cell lines labeled for CEA. While expression on the cellular level is heterogeneous, expression on a 100-200 µm scale is fairly uniform throughout the tumor.

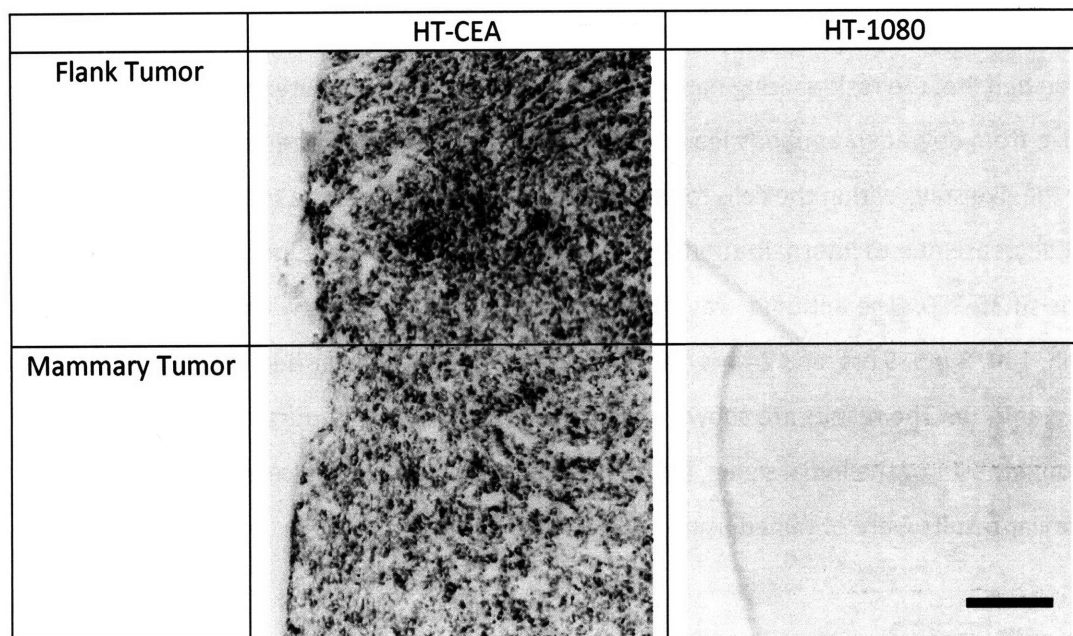|	HT-CEA	HT-1080
Flank Tumor		
Mammary Tumor		

Figure 5.7 – CEA expression *in vivo*. Frozen sections were labeled with anti-CEA-Alexa-488 antibody, and the contrast was adjusted to identical levels for both the HT-CEA and HT-1080 cell lines. Dense staining in the antigen positive tumors (left) indicates that CEA is continually expressed even after 2 weeks *in vivo* without G418 selection. As expected, no expression was present in the antigen negative cell line (right). Scale bar = 200 μm

The injected scFv was directly labeled with Alexa-750 fluorophore, so the sections were imaged for the localization of ds-sm3E. With the rapid clearance of scFv from the plasma, little antibody extravasates into the tumor interstitium, and the antibody signal was close to the limit of detection. However, with little autofluorescence in the 750 channel and no detectable signal in the antigen negative tumors, the staining in the antigen positive tumors was clearly specific. Figure 5.8 shows punctuate spots throughout the tumor where binding increased the local concentration of extravasated antibody. Although no signal was detectable in the antigen negative tumor, there likely is non-specific uptake in this tissue. Without binding, the diffuse signal is either too faint to be detected, or the unbound molecule was lost in processing.
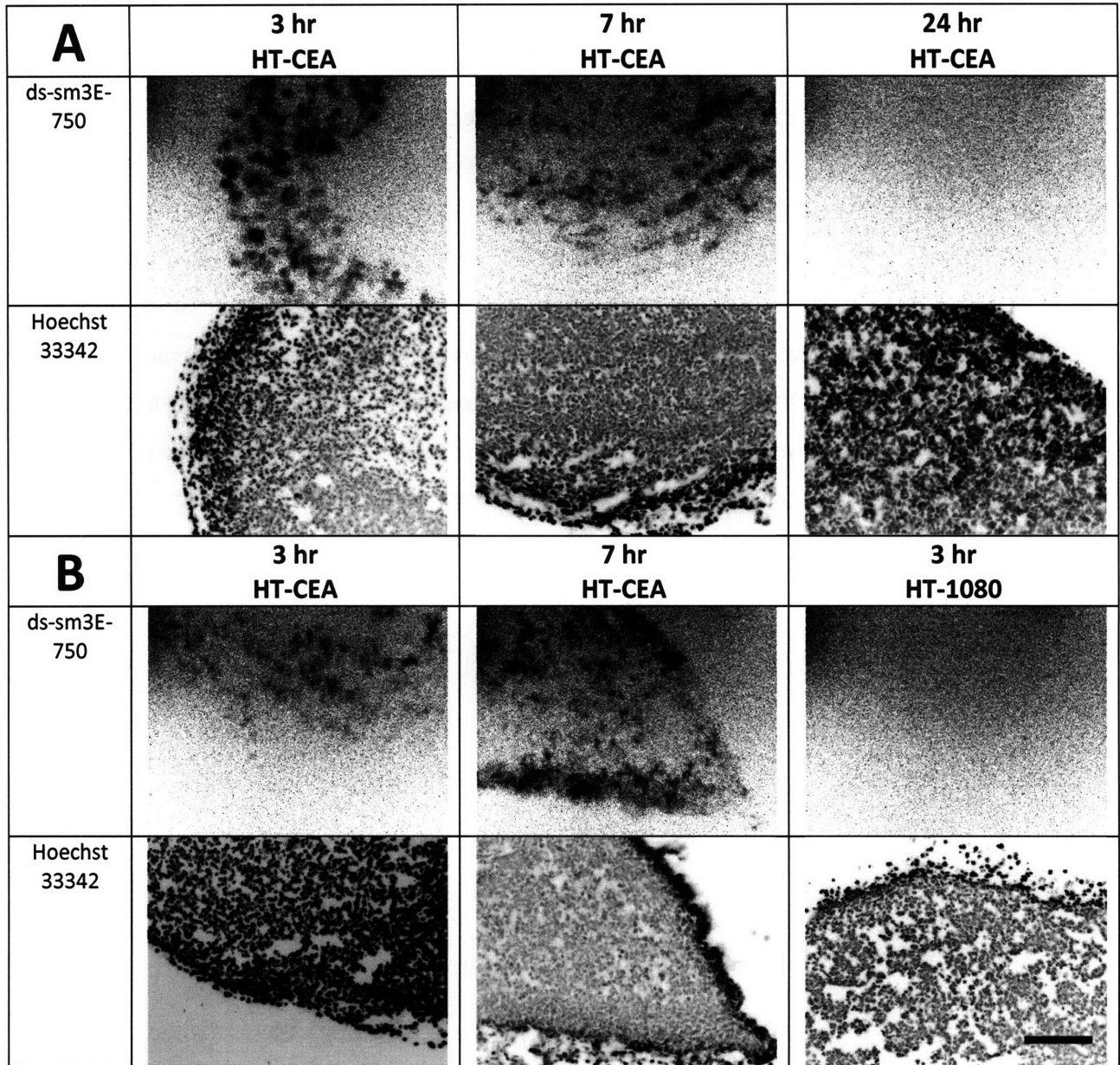
Figure 5.8 – (A) Localization of ds-sm3E-750 in HT-CEA and HT-1080 tumors after 3, 7, and 24 hrs. The Hoechst 33342 stained nuclei are shown for the same section. (B) Additional images of localization after 3 and 7 hrs. The antigen negative HT-1080 tumor shows no localization even at 3 hrs due to the lack of binding. Scale Bar = 200 μm

The vasculature of the tumor sections was labeled with an anti-CD31 antibody to detect any differences in vascular density throughout the tumor. Given the transient flow(28, 29) and collapsed vessels(30) present in many tumors, a marker was used for the functional vasculature. Fluorescent images of tumor vasculature did not show detectable staining after injecting 100 μg of Texas-red labeled *Lycopersicon esculentum* (tomato) lectin(31) (Vector laboratories, Burlingame, CA), although doses up to

500 μg have been used with low power (e.g. 10x) imaging in other studies(32). Hoechst 33342 can also be used to label functional vasculature (e.g. 15 mg/kg(33, 34)), but this precludes the use of this stain for labeling nuclei. The lipophilic carbocyanine dye, $DiOC_7$, has been used to label functional vasculature(14, 33), and the green fluorescence is compatible with a number of other fluorophores. Mice were injected with 25 μg of $DiOC_7$ (1 mg/kg) dissolved in 75% DMSO and 25% water 5 min before cervical dislocation. Although the staining is faint, the functional vasculature colocalizes with some, but not all, of the positive CD31 stained vessels (figure 5.9). Because labeling with the $DiOC_7$ was limited to 5 min, some functional vasculature may not be labeled if it was not flowing during that period. Studies in other tumors indicate that 20% of functional vessels are transiently closed over this time interval(28). Images using systemically delivered Hoechst 33342 and $DiOC_7$ should always be interpreted with some caution, since the levels used can exhibit vasoactive effects, such as reduced blood flow and arterial pressure in mice(34).
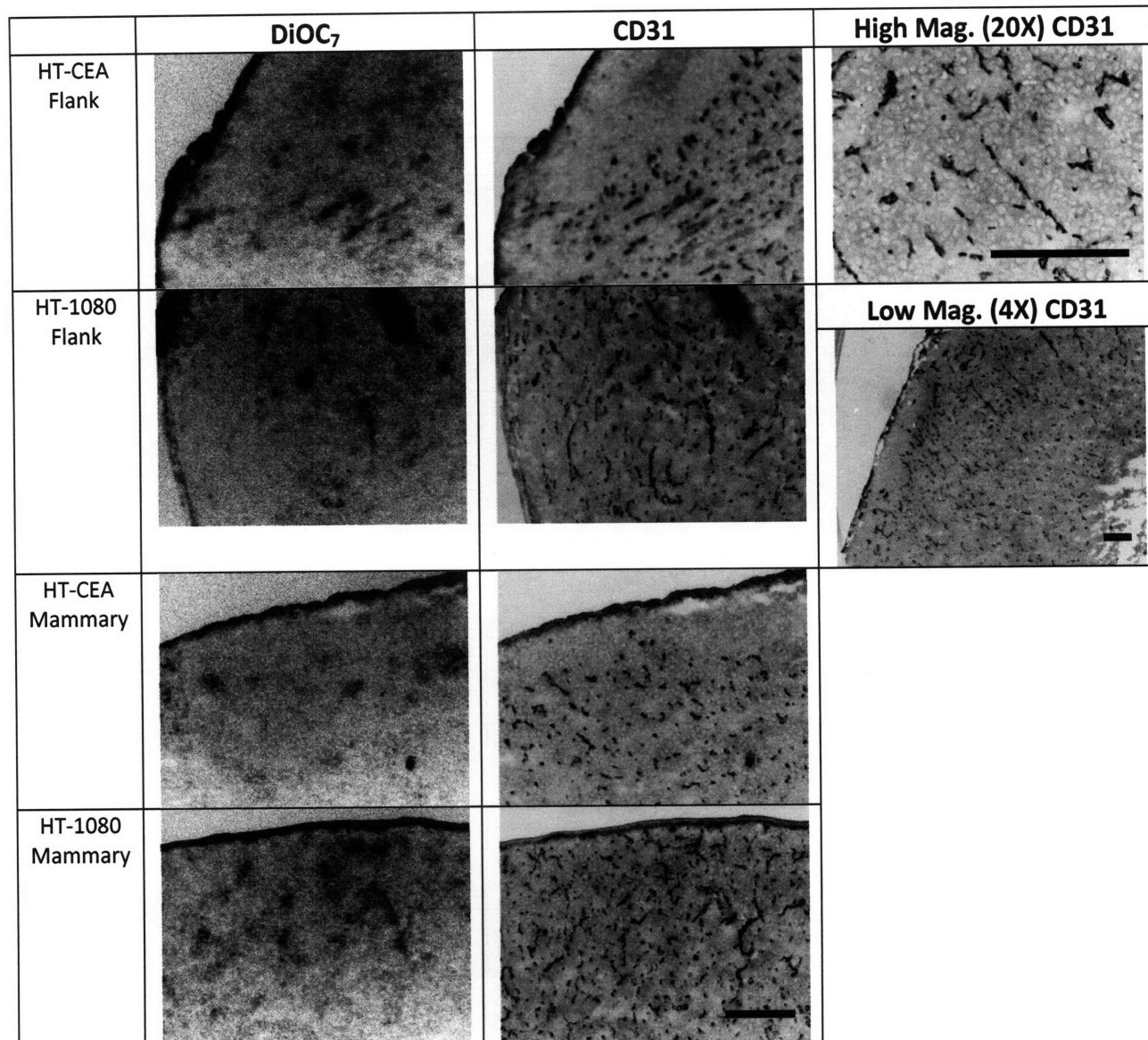
Figure 5.9 – Tumor Vasculature. DiOC$_7$ dye was used to indicate which vessels were functional 5 min prior to harvesting the tumor (left), and the tumor endothelium was labeled with an anti-CD31 antibody on the same slide to mark the total vasculature (middle). Images of CD31 staining were taken using 20X and 4X magnification (right) to see individual vessels and large scale trends in vascularization, respectively. Scale bar = 200 μm. All images at 10X magnification unless otherwise noted.

Comparisons between CD31 positive vessels and localized scFv uptake were made at 3 and 7 hrs after injection of ds-sm3E-750 (figure 5.10). The results show that uptake is very high around some vessels, but others have no detectable signal. Less light is captured with a low power (10x) objective, so there may be a small amount of uptake around these vessels that is not apparent with the low fluorescence intensity. Alternatively, this could be caused by heterogeneity in the capillary permeability, or the vessels may be transiently closed during the first hour after injection, while the majority of scFv is

161

cleared from the plasma. These images demonstrate the heterogeneity between vessels in the same tumor.

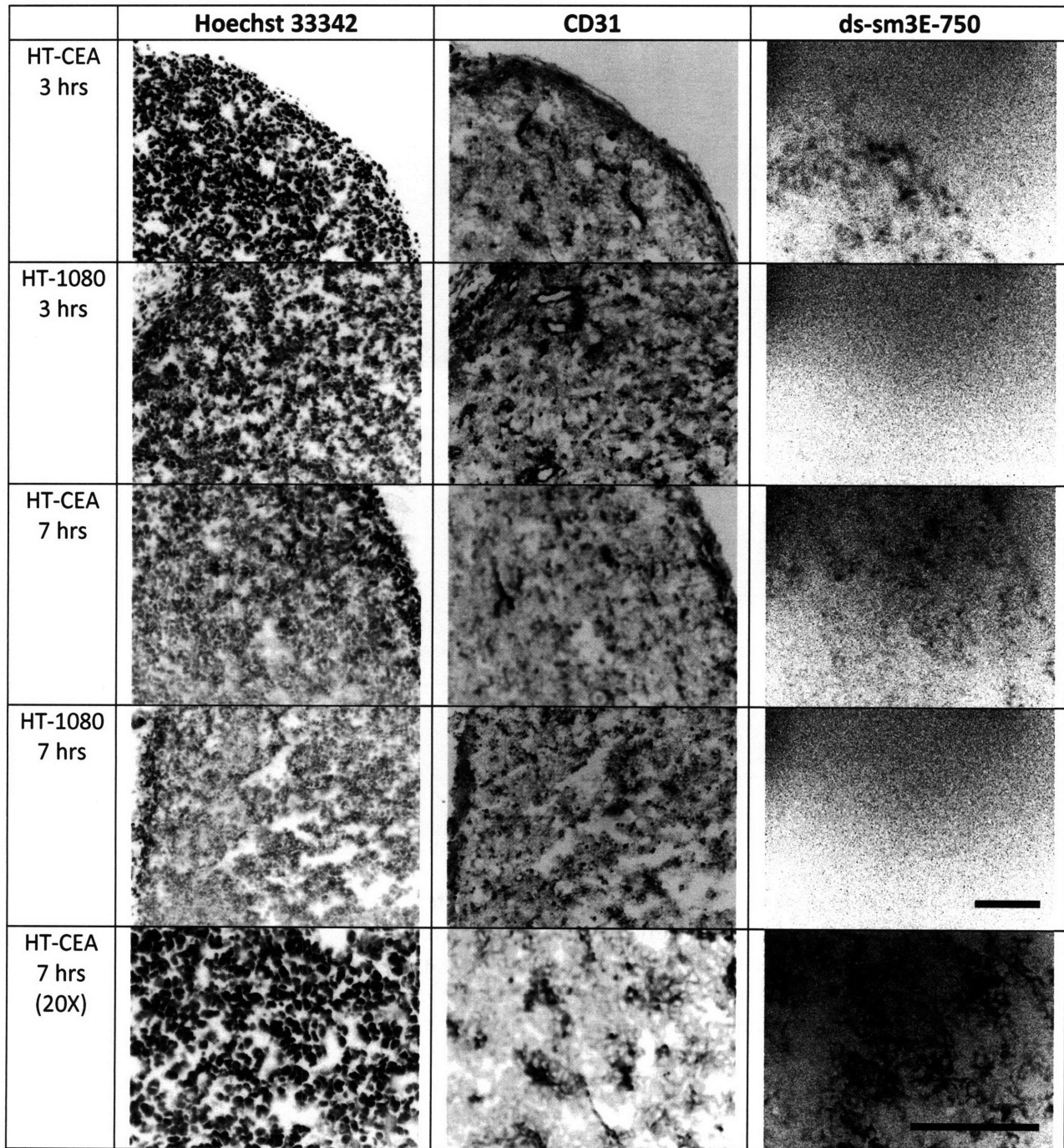|	Hoechst 33342	CD31	ds-sm3E-750
HT-CEA 3 hrs			
HT-1080 3 hrs			
HT-CEA 7 hrs			
HT-1080 7 hrs			
HT-CEA 7 hrs (20X)			

Figure 5.10 – Colocalization of Vasculature and ds-sm3E-750. The ds-sm3E-750 colocalizes with some of the vessels, but not all CD31 positive capillaries have perivascular scFv. The higher magnification (20X) gives better signal, showing the labeling surrounding several vessels. Scale bar = 200 µm. All images are at 10X unless otherwise noted.

To quantify the total fluorescence within the tumors, fluorescence molecular tomography (FMT) was used to image the flank tumors. Due to the rapid clearance of scFv from the plasma into normal tissues and filtered by the kidney, the efficiency of uptake for scFvs is low, as indicated by low percent injected dose per gram (%ID/g)(35-37). The signal to noise for the tumor was poor at early time points, with values fluctuating up and down over the first 1-9 hours. Background fluorescence in the kidneys, bladder, and presumably intestines made it difficult to discern tumor specific antibody versus background or peripheral contributions. Figure 5.11 shows the tumor concentrations at 24 hours for three different experiments. In all experiments, 40 μg of ds-sm3E-750 was injected via the tail vein. The first experiment compares uptake in a large (~1.1 g) LS174T tumor in the left flank versus a smaller (~160 mg) HT-CEA tumor on the right. The second group of 3 mice contained HT-1080 tumors (~75 mg) in the left flank and HT-CEA tumors in the right flank (~140 mg). Finally, 3 mice were injected with 100 μg of M11147 and 100 μg of M85151a anti-CEA IgGs 3 days prior to injection of the scFv. These antibodies do not compete with ds-sm3E (data not shown). If shedding is an issue in these tumors, the mixture of these IgGs should cross-link some of the shed antigen, increasing persistence in the tumor. M85151a also downregulates the surface concentration of CEA, allowing penetration farther from the vessel. If there is shed antigen in the plasma, these IgGs should also complex this CEA and lower the amount in the blood. The same dose of ds-sm3E-750 was delivered, and the fluorescence at 24 hrs was taken. Uptake in both the large LS174T and smaller HT-CEA tumors was similar (group 1). For the mice with antigen positive and antigen negative tumor, the uptake was higher in the antigen positive tumor, with total localization in the HT-CEA tumor approximately double that found in the HT-1080 tumor (group 2). When the non-fluorescent IgGs were delivered before the scFv, uptake increased over the 1st group of mice, although total localization was similar to that with the antigen negative tumor group (group 3). Due to poor signal to noiseand the large variation between mice, it is difficult to conclusively compare uptake between experiments. While the localization is around the same order of magnitude as radiolabeling experiments, with 20 nM uptake corresponding to 1.4 %ID/g and 80 nM equally 5.4 %ID/g, further experiments will be required to see if the data reflect specific trends or experimental variation.
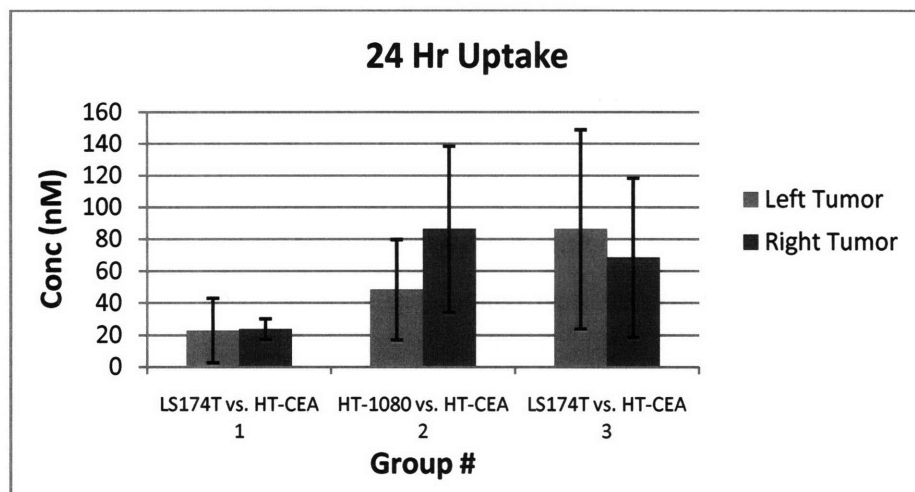
24 Hr Uptake

Figure 5.11 – FMT Uptake at 24 hrs. 24 hrs before imaging by FMT, mice received 40 μg of ds-sm3E-750 by tail vein injection. In the third group of mice, 72 hrs prior to injection of the scFv, the mice were given 100 μg doses each of anti-CEA IgG M11147 and M85151a. 80 nM tumor concentration corresponds to 5.4% ID/g. The right tumor is HT-CEA in each group.

Figure 5.12 shows two images of compressed z-stacks, showing the total fluorescence in the mouse from FMT. Since the scFv is below the renal filtration limit(38), this molecule is primarily cleared by the kidney, as seen by the two bright areas at the top of the field of view on the left, and goes to the bladder, which is the bright region in the center of the image on the right. While some fluorescence is clearly localized to the tumor (e.g. signal in the large LS174T tumor in the mouse on the left), other areas of fluorescence bleed between the tumor and normal tissue. This is likely due to the lower targeting efficiency from rapid plasma clearance.

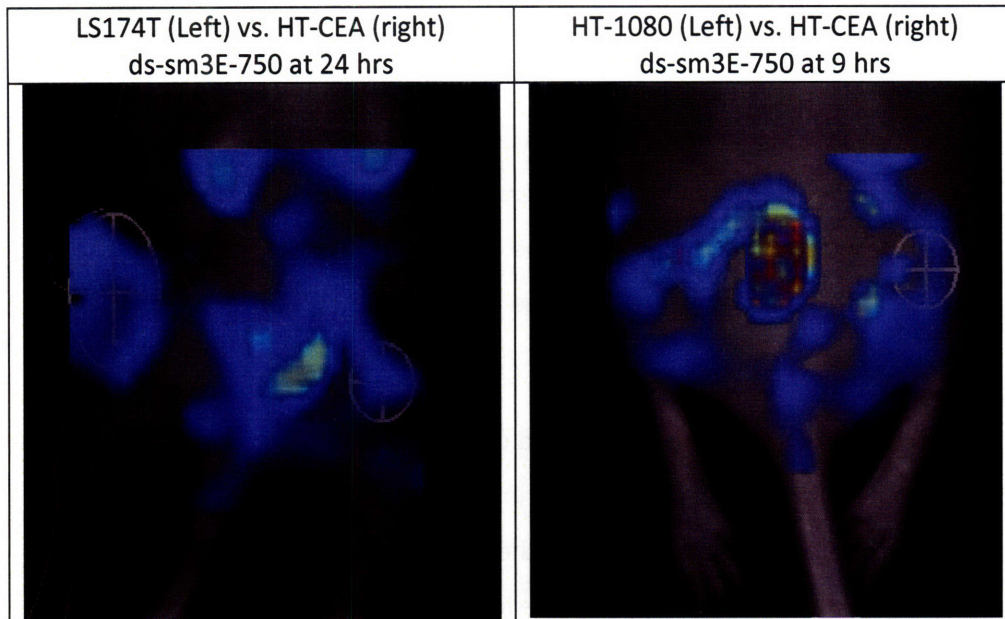| LS174T (Left) vs. HT-CEA (right) ds-sm3E-750 at 24 hrs	HT-1080 (Left) vs. HT-CEA (right) ds-sm3E-750 at 9 hrs

Figure 5.12 – Sample FMT Images. The 750 fluorescence is picture over the outline of the mouse. The two kidneys are just in the fluorescent field of view at the top of the image on the left, and the bladder fluorescence is readily apparent at the bright region on the left. Other regions of fluorescence likely indicate uptake in normal tissues such as the intestine. The ellipsoid regions of interest where the tumor concentration was quantified are pictured for both images.

5.4 Discussion

The uptake and retention of antibodies in tumor tissue is a function of both the intrinsic antibody properties as well as the physiological characteristics of the tumor. This study used a CEA expression plasmid to generate identical cell lines differing only by antigen expression. The pathological physiology of tumors causes non-specific uptake of macromolecules, so the two cell lines could be used to establish binding-mediated effects. Figure 5.2 shows the high level of antigen expression in the transgenic cell line, with over a million copies per cell, compared to no detectable expression on the antigen negative line. This high level of antigen expression persists *in vivo* (figure 5.8).

Although scFvs have rapid renal clearance, an advantage of using this type of molecule is the rapid pulse in tumor uptake. Previous data show that the sm3E signal in tumors drops rapidly between the first few hours and 1 day (data not shown). By using a pulse followed by sequential analysis, the drop in signal can be determined more explicitly. In contrast, if an IgG were used, the plasma persistence would cause a pseudo-steady state to develop. Rapid loss from the tumor would only be apparent as a lower total signal. The maximum signal is dependent on a variety of factors, such as dose,

permeability, and vascular density, so it is difficult to attribute a lower signal to poor retention. Figure 5.5 shows the quick exit of the scFv from the plasma, where greater than 90% of the scFv is gone after 1 hr. While this rapid clearance is an advantage from a pulse-chase perspective, the major drawback is low signal to noise. Model predictions using a simple normal tissue compartment indicate that the concentration in the normal tissue exceeds the tumor at all time points except for 24 hrs. The bright fluorescence in non-tumor tissue is apparent in figure 5.13. Due to their rapid clearance, scFvs will likely not likely play a role in targeted therapies.

Signal can be lost from the tumor by internalization and degradation, intravasation, or loss from the tumor surface. Antigen binding shifts the balance towards internalization, since antibody anchored to the surface of a cell cannot enter the bloodstream or leave the tumor periphery. In order to understand the fate of the label after internalization, cells were incubated with labeled scFv, incubated at 37^0C, and analyzed by flow cytometry. Figure 5.7 demonstrates that the label persists within the cell for an extended period of time. If the scFv is internalized *in vivo*, the label should remain within the tumor well beyond the 24 hr time point, eliminating internalization as a compounding factor in loss of signal.

Figure 5.9 shows patchy labeling of ds-sm3E-750 throughout the tumor. As the scFv binds antigen, the local antibody concentration is increased, giving rise to the signal in the image. There is no detectable signal in the antigen negative tumor. Since the time required for diffusion between vessels situated 100 μm apart is only 5 min, it is expected that scFv in these tumors is homogeneously distributed and therefore below the limit of detection. Since it is not bound to antigen, it may also be lost during histological sectioning and processing.

Images of the vasculature in these tumors show fairly uniform vessel density throughout the majority of the tumor (figure 5.10). However, the label for functional vasculature stains some vessels much brighter than others, indicating that many of these capillaries could be transiently perfused. This is consistent when comparing scFv labeling versus vasculature (CD31) staining (figure 5.11).

Several scFvs targeting CEA show increased uptake at early times (e.g. 1-3 hrs), followed by a decrease after 24 hrs. For example, two scFvs targeting CEA showed %ID/g of 3.04 and 6.57 at 1 hr and then dropped to 0.3 and 0.94 %ID/g by 24 hrs(35). These studies were using radioiodinated antibodies, so internalization and catabolism could have eliminated the label. However, similar phenomena are seen with Tc-99 labeled scFvs, which should be retained in the cells after internalization. A different

anti-CEA scFv dropped from 5.4 %ID/g at 4 hrs to approximately 1 %ID/g after 24 hrs(10). This type of decrease is not apparent with a Tc-99 labeled scFv targeting HER2, where the %ID/g dropped from 1.5 to 1 over 48 hrs in two separate experiments(36, 37). While this could be a property of the tumor cell line used (LS174T in the CEA targeting studies versus SK-OV-3 for HER2), it could also be a function of the antigen.

Several explanations for the drop in specific targeting between 3-7 hrs and 24 hrs can be ruled out given the available data. First, internalization does not completely describe the lack in retention of this scFv. If the scFv were significantly internalized, *in vitro* experiments indicate that it should be retained in the cell for several days. This is consistent with data showing sm3E localization is higher with a residualizing technetium-99 label than iodine label after 24 hrs, but the signal still drops from the level at 3 hrs (data not shown). The heterogeneous distribution in HT-CEA tumors and lack of signal in HT-1080 tumors indicates it is binding antigen in the tumor interstitium and is not complexed with antigen in the plasma, for example. Dissociation does not explain the rapid decrease, either. The dissociation rate for sm3E is on the order of 4 days and is relatively insensitive to pH (data not shown), so greater than 80% of the scFv would remain bound at 24 hrs, and this completely ignores the large amount of rebinding that would take place. Finally, if the 3-4 hr internalization half life on HT-CEA cells continues *in vivo*, extracellular proteases would not have a significant amount of time to degrade the scFv on the cell surface. The additional disulfide bond also helps stabilize the scFv from protease degradation(27).

Two major explanations remain for the drop in tumor signal in the CEA positive tumors. First, there may be no real drop in specific signal, but rather the high signal at early time points could be an artifact from the surrounding stromal tissue. When dissecting the tumors, if all the surrounding tissue is not removed, any scFv present in this tissue will contribute to the overall signal, even though it is not in the tumor interstitial compartment. Hemorrhaging and rapid extravasation in stromal tissue compared to slow uptake in the tumor could cause a large increase in the surrounding tissue at these early time points. Visible hemorrhaging was apparent near the tumor surface in many of the tumors imaged in this study (data not shown). Uptake in normal tissue is high over the first several hours, then drops(35), as seen with the FMT imaging (data not shown). While this result cannot be completely ruled out, there was no apparent signal in the surrounding stromal tissue in any of the histology samples that were imaged. Combined with the fact that the specific labeling decreases between the first few hours and 24 hours (figure 5.8), this explanation is not required to explain the data.

The other explanation for the drop in tumor signal is shed antigen. If the scFv enters the tumor interstitial space and binds previously shed antigen or the CEA is shed after the binding event, the entire complex would be free to intravasate or exit the tumor surface. CEA is approximately 180 kDa in molecular weight(39), so a complex with scFv would be approximately 210 kDa in size. While the permeability of the vasculature is lower for this size molecule than the scFv, the rate is only reduced by half(40). Instead of the scFv anchoring into the cell membrane upon association, it may be binding a moving target. It is well established that CEA is shed antigen, and in humans, this antigen ends up in the plasma(39). This explanation would also account for the difference between binders to HER2, which is not shed at an appreciable rate, and the shed antigen CEA.

In summary, histological images demonstrate that the ds-sm3E-750 binds antigen in the tumor, as indicated by punctuate staining on the slides. Cell culture studies show that the dye is retained within cells if it is internalization, so loss from catabolism is negligible. With a dissociation rate that has a 4 day half life(41), release from the antigen is also not an issue. The drop in signal from the first few hours to 24 hours is likely due to antigen shedding. Methods to anchor the antibody in the tumor, such as by extensive cross-linking of antigen with multiple antibodies that bind different epitopes, could improve uptake and retention. However, depending on the therapy, this may not be beneficial. Immunotoxins bound to the shed antigen would not be internalized, and therefore they would be ineffective.

References

1. Kubota T. METASTATIC MODELS OF HUMAN CANCER XENOGRAFTED IN THE NUDE-MOUSE - THE IMPORTANCE OF ORTHOTOPIC TRANSPLANTATION. Journal of Cellular Biochemistry 1994;56:4-8.
2. Behr TM, Behe M, Stabin MG, et al. High-linear energy transfer (LET) alpha versus low-LET beta emitters in radioimmunotherapy of solid tumors: Therapeutic efficacy and dose-limiting toxicity of Bi-213- versus Y-90-labeled CO17-1A Fab ' fragments in a human colonic cancer model. Cancer Research 1999;59:2635-43.

3.   Kerbel RS. Human tumor xenografts as predictive preclinical models for anticancer drug activity in humans - Better than commonly perceived - But they can be improved. Cancer Biology & Therapy 2003;2:S134-S9.

4.   Kim JJ, Tannock IF. Repopulation of cancer cells during therapy: An important cause of treatment failure. Nature Reviews Cancer 2005;5:516-25.

5.   Van Dyke T, Jacks T. Cancer Modeling in the modern era: Progress and challenges. Cell 2002;108:135-44.

6.   Moser AR, Pitot HC, Dove WF. A DOMINANT MUTATION THAT PREDISPOSES TO MULTIPLE INTESTINAL NEOPLASIA IN THE MOUSE. Science 1990;247:322-4.

7.   Hance KW, Zeytin HE, Greiner JW. Mouse models expressing human carcinoembryonic antigen (CEA) as a transgene: Evaluation of CEA-based cancer vaccines. Mutation Research-Fundamental and Molecular Mechanisms of Mutagenesis 2005;576:132-54.

8.   Wilkinson RW, Ross EL, Poulsom R, et al. Antibody targeting studies in a transgenic murine model of spontaneous colorectal tumors. Proceedings of the National Academy of Sciences of the United States of America 2001;98:10256-60.

9.   Clarke P, Mann J, Simpson JF, Rickard-Dickson K, Primus FJ. Mice transgenic for human carcinoembryonic antigen as a model for immunotherapy. Cancer Research 1998;58:1469-77.

10.   Pietersz GA, Patrick MR, Chester KA. Preclinical characterization and in vivo imaging studies of an engineered recombinant technetium-99m-labeled metallothionein-containing anti-carcinoembryonic antigen single-chain antibody. Journal of Nuclear Medicine 1998;39:47-56.

11.   Flynn A, Green A, Boxer G, Casey J, Pedley R, Begent R. A Novel Technique, Using Radioluminography, for the Measurement of Uniformity of Radiolabelled Antibody Distribution in a Colorectal Cancer Xenograft Model. International Journal of Radiation Oncology Biology Physics 1998;43:183-9.

12.   Adams G, Schier R, McCall A, et al. High Affinity Restricts the Localization and Tumor Penetration of Single-Chain Fv Antibody Molecules. Cancer Research 2001;61:4750-5.

13.   Dennis MS, Jin HK, Dugger D, et al. Imaging tumors with an albumin-binding Fab, a novel tumor-targeting agent. 2007;67:254-61.

14.   Baker J, Lindquist K, Huxham L, Kyle A, Sy J, Minchinton A. Direct Visualization of Heterogeneous Extravascular Distribution of Trastuzumab in Human Epidermal Growth Factor Receptor Type 2 Overexpressing Xenografts. Clinical Cancer Research 2008;14:2171-9.

15.   Baselga J, Norton L, Albanell J, Kim YM, Mendelsohn J. Recombinant humanized anti-HER2 antibody (Herceptin (TM)) enhances the antitumor activity of paclitaxel and doxorubicin against HER2/neu overexpressing human breast cancer xenografts. Cancer Research 1998;58:2825-31.

16.   Bushberg J, Seibert J, Leidholdt E, Boone J. The Essential Physics of Medical Imaging. 2nd ed. Philadelphia: Lippincott Williams and Wilkins; 2002.

17.   Welt S, Divgi CR, Real FX, et al. QUANTITATIVE-ANALYSIS OF ANTIBODY LOCALIZATION IN HUMAN METASTATIC COLON CANCER - A PHASE-I STUDY OF MONOCLONAL ANTIBODY-A33. Journal of Clinical Oncology 1990;8:1894-906.

18.   Sharkey RM, Karacay H, Cardillo TM, et al. Improving the delivery of radionuclides for imaging and therapy of cancer using pretargeting methods. Clinical Cancer Research 2005;11:7109S-21S.

19.   Sharkey RM, Karacay H, Vallabhajosula S, et al. Metastatic human colonic carcinoma: Molecular imaging with pretargeted SPECT and PET in a mouse model. Radiology 2008;246:497-507.

20.   Ballou B, Fisher G, Hakala T, Farkas D. Tumor Detection and Visualization Using Cyanine Fluorochrome-Labeled Antibodies. Biotechnology Progress 1997;13:649-58.

21.   Nuiachristos V. Fluorescence molecular imaging. Annual Review of Biomedical Engineering 2006;8:1-33.

22.	Tofts PS. Modeling tracer kinetics in dynamic Gd-DTPA MR imaging. Jmri-Journal of Magnetic Resonance Imaging 1997;7:91-101.

23.	Ahrens ET, Rothbacher U, Jacobs RE, Fraser SE. A model for MRI contrast enhancement using T-1 agents. Proceedings of the National Academy of Sciences of the United States of America 1998;95:8443-8.

24.	Gustafsson B, Youens S, Louie AY. Development of contrast agents targeted to macrophage scavenger receptors for MRI of vascular inflammation. Bioconjugate Chemistry 2006;17:538-47.

25.	Song K, Chang Y, Prud'homme GJ. IL-12 plasmid-enhanced DNA vaccination against carcinoembryonic antigen (CEA) studied in immune-gene knockout mice. Gene Therapy 2000;7:1527-35.

26.	Milenic DE, Yokota T, Filpula DR, et al. Construction, Binding-Properties, Metabolism, and Tumor Targeting of a Single-Chain Fv Derived from the Pancarcinoma Monoclonal-Antibody Cc49. Cancer Research 1991;51:6363-71.

27.	Schmidt MM, Thurber GM, Wittrup KD. Kinetics of Anti-Carcinoembryonic Antigen (CEA) Antibody Internalization: Effects of Affinity, Bivalency, and Stability. Cancer Immunology and Immunotherapy Submitted.

28.	Chaplin DJ, Olive PL, Durand RE. Intermittent Blood-Flow in a Murine Tumor - Radiobiological Effects. Cancer Research 1987;47:597-601.

29.	Eskey CJ, Koretsky AP, Domach MM, Jain RK. H-2-Nuclear Magnetic-Resonance-Imaging of Tumor Blood-Flow - Spatial and Temporal Heterogeneity in a Tissue-Isolated Mammary Adenocarcinoma. Cancer Research 1992;52:6010-9.

30.	Hilmas D, Gillette E. MORPHOMETRIC ANALYSES OF THE MICROVASCULATURE OF TUMORS DURING GROWTH AND AFTER X-IRRADIATION. Cancer 1974;33:103-10.

31.	Inai T, Mancuso M, Hashizume H, et al. Inhibition of vascular endothelial growth factor (VEGF) signaling in cancer causes loss of endothelial fenestrations, regression of tumor vessels, and appearance of basement membrane ghosts. 2004;165:35-52.

32.	Debbage PL, Griebel J, Ried M, Gneiting T, DeVries A, Hutzler P. Lectin intravital perfusion studies in tumor-bearing mice: Micrometer-resolution, wide-area mapping of microvascular labeling, distinguishing efficiently and inefficiently perfused microregions in the tumor. Journal of Histochemistry & Cytochemistry 1998;46:627-39.

33.	Trotter MJ, Chaplin DJ, Olive PL. Use of a Carbocyanine Dye as a Marker of Functional Vasculature in Murine Tumors. 1989;59:706-9.

34.	Trotter MJ, Olive PL, Chaplin DJ. Effect of Vascular Marker Hoechst-33342 on Tumor Perfusion and Cardiovascular Function in the Mouse. 1990;62:903-8.

35.	Wu AM, Chen WG, Raubitschek A, et al. Tumor localization of anti-CEA single-chain Fvs: Improved targeting by non-covalent dimers. Immunotechnology 1996;2:21-36.

36.	Kubetzko S, Balic E, Waibel R, Zangemeister-Wittke U, Pluckthun A. PEGylation and multimerization of the anti-p185(HER-2) single chain Fv fragment 4D5 - Effects on tumor targeting. Journal of Biological Chemistry 2006;281:35186-201.

37.	Willuda J, Kubetzko S, Waibel R, Schubiger PA, Zangemeister-Wittke U, Pluckthun A. Tumor targeting of mono-, di-, and tetravalent Anti-p185(HER-2) miniantibodies multimerized by self-associating peptides. Journal of Biological Chemistry 2001;276:14385-92.

38.	Deen WM, Lazzara MJ, Myers BD. Structural determinants of glomerular permeability. 2001;281:F579-F96.

39.	Hammarstrom S. The carcinoembryonic antigen (CEA) family structures, suggested functions and expression in normal and malignant tissues. Cancer Biology 1999;9:67-81.

40.	Dreher MR, Liu WG, Michelich CR, Dewhirst MW, Yuan F, Chilkoti A. Tumor vascular permeability, accumulation, and penetration of macromolecular drug carriers. Journal of the National Cancer Institute 2006;98:335-44.

41.   Graff C, Chester K, Begent R, Wittrup KD. Directed Evolution of an Anti-Carcinoembryonic Antigen scFv with a Four-Day Monovalent Dissociation Half-time at 37 °C. Protein Engineering, Design, & Selection 2004;17:293-304.

Appendix – Mathematical Derivations

A.1   List of Symbols

The following symbols are used in the appendix:

A = fraction (0-1) of alpha phase clearance
a_0, a_1, a_2 = constants used in numerical simulation boundary conditions
Ab = normalized antibody concentration
[Ab] = Free antibody concentration
$[Ab]_{cap}$ = Antibody concentration on the abluminal side of the capillary using overall tissue volume
$[Ab]_n$ = Normal tissue compartment (interstitial) antibody concentration (for micrometastases)
$[Ab]_{n,0}$ = Initial antibody concentration in normal tissue compartment
$[Ab]_{plasma}$ = Concentration of free antibody in blood plasma
$[Ab]_{plasma,0}$ = Initial concentration of free antibody in blood plasma

$[Ab]_{surf}$ = Interstitial antibody concentration on abluminal side of capillary or surface of micrometastasis (using interstitial volume) = $[Ab]_{cap} / \varepsilon$

$[Ab]_{total}$ = total antibody concentration in the tumor

Ag = normalized antigen concentration

[Ag] = Antigen concentration per total tumor volume

$[Ag]_0$ = Initial antigen concentration per total tumor volume

AUC = area under curve, used for the integral of plasma concentration over time

[B] = concentration of bound antibody-antigen complex using total tissue volume

B = fraction (0-1) of beta phase clearance

Bd = normalized bound antibody-antigen complex concentration

Bi = mass transfer Biot number, the ratio of capillary transport to diffusive transport

C_1 = integration constant

C_2 = integration constant

D = (effective) diffusion coefficient

[D] = degraded antibody in cell compartment model

ε = effective void fraction (antibody accessible volume / total volume) – e.g. 0.5 for small molecule (salts), 0.3 for scFv, and 0.1 for IgG

γ = normal tissue lymphatic clearance rate coefficient for two compartment model

Γ_{met} = clearance modulus defined for metastasis

Γ_{tumor} = clearance modulus defined for solid tumor

[I] = internal antibody concentration in cell compartment model

∇ = gradient operator

∇^2 = Laplacian

κ = normal tissue capillary extravasation rate coefficient for two compartment model

k_α = alpha phase clearance rate constant = $\ln(2)/t_{1/2,\alpha}$

k_β = beta phase clearance rate constant = = $\ln(2)/t_{1/2,\beta}$

K_d = equilibrium dissociation constant

k_{deg} = degradation rate constant

k_e = endocytosis rate constant

k_i = internalization rate constant

k_{loss} = rate of loss of signal from degraded antibody for cell compartment model

k_{on} = antibody binding rate constant

k_{off} = antibody dissociation rate constant

k_r = recycle rate constant

λ = normalized radius

λ_e = extinction radius, the concentration drops to zero, normalized saturation radius

L = length of Krogh cylinder

[L] = antibody lost from cell in cell compartment model

P = capillary permeability

r = radius

R = radius of reacting front/radius of saturation in shrinking core derivation or an arbitrary radius of interest as used in the clearance and Thiele modulus

R_{cap} = capillary radius

R_{Krogh} = average radius of tissue around vessel such that $2R_{cap}/R_{Krogh}^2$ yields the overall capillary surface area to tumor volume ratio

R_{max} = the maximum radius that would be saturated under the given conditions

R_{met} = micrometastasis radius

R_s = antigen synthesis rate

R_{sat} = radius of reacting front/saturation radius in Thiele modulus derivation

R_{tumor} = tumor radius

S = total surface area of capillaries able to transport molecules

S_{tumor} = outer surface area of a spherical tumor

[S] = surface antibody concentration in cell compartment model

$[S]_0$ = initial surface antibody concentration

t = time

$t_{1/2}$ = half life

$t_{clearance}$ = the plasma clearance time; a lumped value incorporating both alpha and beta phases

$t_{infusion}$ = length of time for constant infusion/constant blood plasma concentration

t_{sat} = saturation time

τ = normalized time

θ = normalized radius of reaction front (e.g. R/R_{met})

u = fluid velocity

Φ = Basis function for FFT method for solving partial differential equations

ϕ_{met} = Thiele modulus defined for metastasis

ϕ_{sat} = value of Thiele modulus at which point saturation occurs

ϕ_{tumor} = Thiele modulus defined for solid tumor

V = total tumor volume

V_{plasma} = total plasma volume

%ID/g = percent injected dose per gram of tissue

A.2 Equations for Microscopic Distribution of Antibodies

The model assumes diffusion through a pseudo-homogenous tissue.

$$\frac{\partial [Ab]}{\partial t} = D\nabla^2 [Ab] - \frac{k_{on}}{\varepsilon}[Ab][Ag] + k_{off}[B]$$

$$\frac{\partial [B]}{\partial t} = \frac{k_{on}}{\varepsilon}[Ab][Ag] - k_{off}[B] - k_e[B]$$

$$\frac{\partial [Ag]}{\partial t} = R_s - \frac{k_{on}}{\varepsilon}[Ab][Ag] + k_{off}[B] - k_e[Ag]$$

These equations can be simulated using a finite difference approach and the method of lines.

a. Micrometastasis

Assuming only radial gradients due to symmetry, the antibody concentration becomes:

$$\frac{\partial [Ab]}{\partial t} = D\frac{1}{r^2}\frac{\partial}{\partial r}\left(r^2 \frac{\partial [Ab]}{\partial r}\right) - \frac{k_{on}}{\varepsilon}[Ab][Ag] + k_{off}[B]$$

The time-dependent boundary conditions are given by the antibody concentration in the surrounding normal tissue. A Dirichlet boundary condition, where the concentration is defined at the metastasis surface is used:

$$[Ab]_n = [Ab]_{plasma,0}\left(\kappa\left(\frac{Ae^{-k_\alpha t}}{\gamma - k_\alpha} + \frac{Be^{-k_\beta t}}{\gamma - k_\beta}\right) - \kappa\left(\frac{A}{\gamma - k_\alpha} + \frac{B}{\gamma - k_\beta}\right)e^{-\kappa}\right) = [Ab]_{surf}$$

b. Vascularized Tumor

Assuming only radial gradients due to symmetry, the antibody concentration becomes:

$$\frac{\partial[Ab]}{\partial t} = D\frac{1}{r}\frac{\partial}{\partial r}\left(r\frac{\partial[Ab]}{\partial r}\right) - \frac{k_{on}}{\varepsilon}[Ab][Ag] + k_{off}[B]$$

The time-dependent boundary conditions are given by the plasma concentration, with a mixed, or Robin boundary condition at the surface:

$$P\left(\left(\varepsilon\cdot[Ab]_{plasma}\right) - [Ab]_{cap}\right) = -D\left(\frac{d[Ab]}{dr}\right) \qquad \text{where: } [Ab]_{surf} = [Ab]_{cap}/\varepsilon \qquad \text{and}$$

$$[Ab]_{plasma} = [Ab]_{plasma,0}\left(A\exp(-k_\alpha t) + B\exp(-k_\beta t)\right)$$

c. Note on Concentrations, Void Fraction, and Effective Diffusion Coefficient

All the concentrations used above are overall concentrations, meaning they are the concentration in the entire tumor volume (e.g. mol antibody per total volume of tumor tissue). Since these molecules are hydrophilic, they do not readily cross cell membranes. Therefore, the actual concentration in the interstitial spaces between cells is higher due to the limited volume (e.g. mols antibody per accessible space). This is why the void fraction appears in the reaction terms above; the binding reaction proceeds faster than if both molecules were diluted in the entire tissue volume. An alternative way of defining the equations is to use interstitial concentrations, which can be obtained by dividing both sides of the equation by the void fraction. When epsilon is paired with each concentration, all terms will be expressed as effective (interstitial) concentrations. For example:

$$[Ab]_{interstitial} = \frac{[Ab]}{\varepsilon}$$

The diffusion coefficient used in the equations is an effective diffusion coefficient and differs from free diffusion in several manners. First, the diffusion will be slower than diffusion in water due to

extracellular matrix components present in the interstitium. Free diffusion coefficients, such as those measured by FCS in the small volume between cells(1), take this into account. However, because diffusion must occur between and around cells, the effective diffusion coefficient used must account for these changes. The tortuosity and constriction factors are a way of measuring these influences(2). This effective diffusion coefficient can be measured, for example, by using FRAP over an area that spans several cell diameters or measuring uptake over an entire spheroid(3). The recovery time of signal includes the effects of antibody diffusing between and around cells. The void fraction does not affect this diffusion coefficient; it only slows penetration when binding occurs.

d. Numerical Simulation Boundary Conditions for Eroding Cylinder Model

Using the central difference approximation for the internal points in the finite difference simulation, the error scales as Δx^2. This is because the lower terms cancel out in the Taylor series approximation. For the end points in this simulation, however, the central difference method cannot be used due to the lack of a point on one side. There is a Robin boundary condition next to the capillary wall and Neumann boundary condition at the outer edge of the Krogh cylinder. Both of these require estimates of the first derivative. If a one-sided difference is used, the error will scale as Δx. To try to lower this error, instead of two points yielding a linear approximation of the derivative, a third point will be used to construct a quadratic approximation of the concentration at both points. The derivative of this quadratic will provide a more accurate approximation at the edges of the cylinder.

Neumann Boundary at Edge of Cylinder

The concentration profile between the outer edge and the two preceding points will be defined using a quadratic equation. The distances will be redefined with the origin at the outer surface to simplify the solution.

$$[Ab] = a_0 + a_1 \cdot r + a_2 \cdot r^2$$

where the 'a' values are constants to be determined at r = the distance from the origin/edge.

$$[Ab] = [Ab]_{param\_num\_pts} = [Ab]_{p-0} \quad \text{at} \quad r = 0 \qquad \text{i.}$$

$$[Ab] = [Ab]_{param\_num\_pts-1} = [Ab]_{p-1} \quad \text{at} \quad r = \Delta x = x \qquad \text{ii.}$$

178

$$[Ab] = [Ab]_{param\_num\_pts-2} = [Ab]_{p-2} \quad \text{at} \quad r = 2\Delta x = 2x \quad \quad \text{iii.}$$

where x is the finite difference length used in the simulation. This is assuming uniform spacing of the lines at the outer edge. To determine the flux:

$$\frac{d[Ab]}{dr} = a_1 + 2a_2 \cdot r$$

$$\frac{d[Ab]}{dr}\bigg|_{r=0} = a_1 \quad \quad \text{with the origin at the edge.}$$

Using the initial conditions to solve for the constants:

$$[Ab]_{p-0} = a_0 \quad \quad \quad \text{i'}$$

$$[Ab]_{p-1} = [Ab]_{p-0} + a_1 x + a_2 x^2 \quad \quad \text{ii'}$$

$$[Ab]_{p-2} = [Ab]_{p-0} + a_1 2x + a_2 (2x)^2 \quad \quad \text{iii'}$$

From ii':

$$a_2 = \frac{[Ab]_{p-1} - [Ab]_{p-0} - a_1 x}{x^2} \quad \quad \text{ii''}$$

Pluggin ii'' into iii':

$$a_1 = \frac{4[Ab]_{p-1} - 3[Ab]_{p-0} - [Ab]_{p-2}}{2x}$$

Plugging back into the flux:

$$\frac{d[Ab]}{dr}\bigg|_{r=0} = \frac{4[Ab]_{p-1} - 3[Ab]_{p-0} - [Ab]_{p-2}}{2x}$$

where x is the distance between points, and the [Ab] values are at the antibody concentrations at the three points adjacent to the edge. With a Neumann boundary condition:

$$\frac{d[Ab]}{dr}\bigg|_{r=0} = 0 = \frac{4[Ab]_{p-1} - 3[Ab]_{p-0} - [Ab]_{p-2}}{2x}$$

$$[Ab]_{p-0} = \frac{4}{3}[Ab]_{p-1} - \frac{1}{3}[Ab]_{p-2}$$

Robin Boundary Condition at Edge of Capillary

Similar to the Neumann boundary condition, the concentration profile between the outer edge and the two preceding points will be defined using a quadratic equation, with the origin at the capillary surface.

$$[Ab] = a_0 + a_1 \cdot r + a_2 \cdot r^2$$

where the 'a' values are constants to be determined at r = the distance from the capillary edge.

$$[Ab] = [Ab]_{wall} = [Ab]_w \qquad \text{at} \qquad r = 0 \qquad\qquad \text{i.}$$

$$[Ab] = [Ab]_{wall+1} = [Ab]_{w+1} \qquad \text{at} \qquad r = \Delta x = x \qquad\qquad \text{ii.}$$

$$[Ab] = [Ab]_{wall+2} = [Ab]_{w+2} \qquad \text{at} \qquad r = 2\Delta x = 2x \qquad\qquad \text{iii.}$$

This is assuming uniform spacing of the lines at the capillary wall. To determine the flux:

$$\frac{d[Ab]}{dr} = a_1 + 2a_2 \cdot r$$

$$\frac{d[Ab]}{dr}\bigg|_{r=0} = a_1 \qquad\qquad \text{because we defined the origin at the wall.}$$

Using the initial conditions to solve for the constants:

$$[Ab]_w = a_0 \qquad\qquad\qquad\qquad\qquad \text{i'}$$

$$[Ab]_{w+1} = [Ab]_w + a_1 x + a_2 x^2 \qquad\qquad \text{ii'}$$

$$[Ab]_{w+2} = [Ab]_w + a_1 2x + a_2 (2x)^2 \qquad\qquad \text{iii'}$$

From ii':

$$[Ab]_{w+1} - [Ab]_w - a_1 x = a_2 x^2$$

$$a_2 = \frac{[Ab]_{w+1} - [Ab]_w - a_1 x}{x^2} \qquad\qquad \text{ii''}$$

Pluggin ii'' into iii':

$$a_1 = \frac{4[Ab]_{w+1} - 3[Ab]_w - [Ab]_{w+2}}{2x}$$

Plugging back into the flux:

$$\left.\frac{d[Ab]}{dr}\right|_{r=0} = \frac{4[Ab]_{w+1} - 3[Ab]_w - [Ab]_{w+2}}{2x}$$

where x is the distance between points, and the [Ab] values are the antibody concentrations at the three points adjacent to the capillary wall. With a Robin boundary condition:

$$flux\big|_{capillary\_wall\_+} = flux\big|_{capillary\_wall\_-}$$

The concentrations are defined in terms of overall tumor volume. Also, the partition coefficient within the plasma is assumed to be one. From equation 7(4).

$$P\left(\varepsilon[Ab]_{plasma} - [Ab]_w\right) = -D\left.\frac{d[Ab]}{dr}\right|_{capillary\_wall}$$

$$[Ab]_w = \varepsilon[Ab]_{plasma} + \left(\frac{D}{P}\right)\left.\frac{d[Ab]}{dr}\right|_{capillary\_wall}$$

$$[Ab]_w = \varepsilon[Ab]_{plasma} + \left(\frac{D}{P}\right)\left(\frac{4[Ab]_{w+1} - 3[Ab]_w - [Ab]_{w+2}}{2x}\right)$$

The above boundary condition can be used with the previous [Ab]$_w$ point in calculating the new point. Alternatively, the equation can be algebraically solved for [Ab]$_w$, and only the previous two inner points will be used for the calculation.

$$[Ab]_w = \frac{2Px\left(\varepsilon[Ab]_{plasma}\right) + D\left(4[Ab]_{w+1} - [Ab]_{w+2}\right)}{2Px + 3D}$$

Testing the signs, units, and logic of the above expression:

The limits for this equation are the following: If the capillary is not permeable (P = 0), then the equation simplifies to the no flux Neumann condition listed above. If the permeability is much greater than diffusion (Px >> D), then the wall concentration approaches the plasma concentration.

The signs are all positive except for the difference between the two internal points. If the interior concentration is much much greater than that near the wall and the plasma concentration is zero, then the wall concentration could appear to be negative. This is the same situation that occurs with the Neumann boundary condition above, which should not occur unless the points are too far apart. The 'smoothing' action of diffusion should minimize this risk.

The units work out correctly, since Px has the same units as D, and these cancel with each other on the top and bottom to leave the two terms on the top in concentration.

A.3   Binding Modulus

The derivation of the binding modulus will be done for a micrometastasis (spherical geometry), but the procedure is identical for a vascularized tumor (cylindrical geometry). The derivation shows that for high affinity antibodies, the binding rate is much faster than diffusion, and therefore antibodies can be assumed to bind immediately to available antigen. This justifies using the shrinking core analysis.

With high affinity antibodies, the dissociation rate is negligible:

$$\frac{\partial[Ab]}{\partial t} = D\frac{1}{r^2}\frac{\partial}{\partial r}\left(r^2\frac{\partial[Ab]}{\partial r}\right) - \frac{k_{on}}{\varepsilon}[Ab][Ag]$$

Non-dimensionalizing the equation:

$$\frac{\partial Ab}{\partial \tau} = \frac{1}{\lambda^2}\frac{\partial}{\partial \lambda}\left(\lambda^2\frac{\partial Ab}{\partial \lambda}\right) - \left\{\frac{k_{on}\left(\frac{[Ag]}{\varepsilon}\right)R^2}{D}\right\}Ab$$

where $\quad Ab \equiv \dfrac{[Ab]}{[Ab]_{surf}} \qquad\qquad \lambda \equiv \dfrac{r}{R} \qquad\qquad \tau \equiv \dfrac{tR^2}{D}$

The dimensionless term in brackets is defined as the binding modulus. This term represents the distance an antibody can diffuse before binding to a free antigen. The association rate and antigen concentration determine the length of time an antibody takes to bind antigen, and the length squared divided by the diffusion coefficient defines the distance an antibody will diffuse in this time. Using typical parameters for an IgG of $k_{on} = 10^5$ /M/s, D = 14 μm^2/s, [Ag] = 10^{-6} M, and ε = 0.1, the characteristic distance before binding is 3.7 μm. This distance is less than the diameter of a cell, indicating that the antibody will bind any antigen in its immediate vicinity before diffusing to the next layer of cells. This rapid binding justifies the shrinking core assumptions used for high affinity antibodies. If the binding rate is slow or the local antigen concentration is low (which is possible due to heterogeneity in antigen expression), this assumption may not apply and antibody can diffuse beyond the shrinking core limit.

From an engineering perspective, this dimensionless group is a type of Damköhler number. It differs from the Thiele modulus in that the reaction in this case is the association (binding) reaction. For the Thiele modulus, the reaction is the irreversible internalization and degradation of the antibody by the cancer cell.

A.4   Clearance Modulus – High Affinity

a. Micrometastasis

The binding modulus for high affinity antibodies indicates that the binding reaction proceeds much faster than diffusion. It is therefore assumed that antibody diffuses into the micrometastasis saturating layer after layer. The concentration at the binding front is assumed to be zero, and the diffusion within the tissue is assumed to proceed much faster than changes in the plasma concentration and the radius of the reaction front, resulting in a pseudo-steady state. (This second assumption is equivalent to assuming that the antibody concentration is small compared to the antigen concentration.) This encompasses the shrinking core assumptions(2, 5). Consumption (endocytosis) within the tissue is ignored in this derivation.

Assuming a pseudo steady state, the reaction-diffusion equation is:

$$0 = D \frac{1}{r^2} \frac{d}{dr} \left(r^2 \frac{d[Ab]}{dr} \right)$$

$$0 = \frac{d}{d\lambda} \left(\lambda^2 \frac{dAb}{d\lambda} \right) \qquad \lambda = \frac{r}{R_{met}} \qquad Ab = \frac{[Ab]}{\varepsilon[Ab]_{surf}}$$

$$Ab = \frac{-C_1}{\lambda} + C_2$$

Boundary Conditions

$$Ab \big|_{\lambda=\theta} = 0 \qquad \text{where } \theta = \frac{R(t)}{R_{met}} \qquad \text{The concentration is zero at the reaction front.}$$

$$Ab \big|_{\lambda=1} = 1 \qquad \text{Dirichlet boundary condition at the surface.}$$

Concentration Profile:

$$Ab = \left(\frac{\lambda - \theta}{(1-\theta)\lambda} \right)$$

To determine the movement of the reaction front into the micrometastasis (i.e. the radius of saturation), the flux of antibody into the metastasis must be calculated:

$$\frac{dAb}{d\lambda} \bigg|_{\lambda=\theta} = \frac{1}{(\theta - \theta^2)}$$

$$\frac{d[Ab]}{dr} \bigg|_{r=R(t)} = \frac{\varepsilon[Ab]_{surf}(t)}{\left(R(t) - \frac{(R(t))^2}{R_{met}} \right)} \qquad \text{the (t) denotes variables that are functions of time}$$

Calculating change in radius of the reaction front from the mass balance:

$$\frac{d}{dt} \left(\frac{4}{3} \pi R^3 [Ag] \right) = -4\pi R^2 D \frac{d[Ab]}{dr} \bigg|_{r=R(t)} = -4\pi R^2 D \frac{\varepsilon[Ab]_{surf}(t)}{\left(R(t) - \frac{(R(t))^2}{R_{met}} \right)}$$

$$\frac{dR}{dt} = -\frac{D}{[Ag]} \frac{\varepsilon[Ab]_{surf}(t)}{\left(R(t) - \frac{(R(t))^2}{R_{met}}\right)}$$

$$\left(R(t) - \frac{(R(t))^2}{R_{met}}\right)dR = -\frac{D}{\left(\frac{[Ag]}{\varepsilon}\right)}[Ab]_{surf}(t)dt \qquad \text{Separable assuming pseudo-steady state}$$

i. Constant Surface Concentration

If a constant infusion of antibody is given, the plasma and normal tissue concentrations equilibrate and remain steady. Under these circumstances, the metastasis will take a given time to saturate. This solution is also useful for calculating the time necessary for saturating a spheroid in a dish (where the surface concentration is constant and not depleted).

$$1 - 3\lambda^2 + 2\lambda^3 = -\frac{6D}{R_{met}^2\left(\frac{[Ag]}{\varepsilon}\right)}[Ab]_{surf}t_{sat}$$

$$t_{sat} = \frac{R_{met}^2\left(\frac{[Ag]}{\varepsilon}\right)}{6D[Ab]_{surf}}\left(1 - 3\left(\frac{R}{R_{met}}\right)^2 + 2\left(\frac{R}{R_{met}}\right)^3\right)$$

ii. Clearance Modulus for Decaying Boundary Conditions

The concentration at the surface of the micrometastasis is assumed to be equal to the normal tissue concentration, which is calculated using a simple two-compartment model.

The plasma concentration is given by a biexponential decay:

$$[Ab]_{plasma} = [Ab]_{plasma,0}\left(A\exp(-k_\alpha t) + B\exp(-k_\beta t)\right)$$

The normal tissue concentration is:

$$[Ab]_n = [Ab]_{plasma,0}\left(\kappa\left(\frac{Ae^{-k_\alpha t}}{\gamma - k_\alpha} + \frac{Be^{-k_\beta t}}{\gamma - k_\beta}\right) - \kappa\left(\frac{A}{\gamma - k_\alpha} + \frac{B}{\gamma - k_\beta}\right)e^{-\gamma t}\right) = [Ab]_{surf}$$

Note: γ is used to avoid confusion with λ, which has been used before(6).

185

It is necessary to assume that the plasma concentration changes slowly compared to the rate of free diffusion in order to achieve a pseudo-steady state, which is generally the case. With the shrinking core model, there is no reaction outside the core, so the pertinent time scale is R^2/D. The time scale for plasma decay is the half life.

Assuming:

$$t_{1/2,\alpha} > \frac{R^2}{D}$$

For a small antibody fragment with $D = 80 \ \mu m^2/s$ and $R = 100 \ \mu m$, the alpha phase clearance must have a half time greater than 2 minutes. For large fragment with $D = 14 \ \mu m^2/s$, the half life must be greater than 12 minutes. For a scFv and IgG respectively, these assumptions are generally true. It is also not as strict as it initially appears, since the relevant R value is initially small before much of the metastasis is saturated. This corresponds with the most rapid drop in plasma concentration. Therefore, when the boundary conditions are changing the most rapidly, the system responds much faster than at later time points.

$$\left(R(t) - \frac{(R(t))^2}{R_{met}} \right) dR = -\frac{D}{\left([Ag] \middle/ \varepsilon \right)} \left([Ab]_{plasma,0} \left(\kappa \left(\frac{Ae^{-k_\alpha t}}{\gamma - k_\alpha} + \frac{Be^{-k_\beta t}}{\gamma - k_\beta} \right) - \kappa \left(\frac{A}{\gamma - k_\alpha} + \frac{B}{\gamma - k_\beta} \right) e^{-\gamma t} \right) \right) dt$$

Integrating from zero to infinity to determine the minimum possible core of unbound antigen:

$$\int_{R_{met}}^{R_{sat}} \left(x - \frac{x^2}{R_{met}} \right) dx = -\frac{D}{\left([Ag] \middle/ \varepsilon \right)} \int_0^\infty \left([Ab]_{plasma,0} \left(\kappa \left(\frac{Ae^{-k_\alpha t}}{\gamma - k_\alpha} + \frac{Be^{-k_\beta t}}{\gamma - k_\beta} \right) - \kappa \left(\frac{A}{\gamma - k_\alpha} + \frac{B}{\gamma - k_\beta} \right) e^{-\gamma t} \right) \right) dt$$

$$3 \left(1 - \left(\frac{R_{sat}}{R_{met}} \right)^2 \right) - 2 \left(1 - \left(\frac{R_{sat}}{R_{met}} \right)^3 \right) = \frac{6D[Ab]_{plasma,0}}{R_{met}^2 \left([Ag] \middle/ \varepsilon \right)} \left(\frac{\kappa}{\gamma} \right) \left[\frac{A}{k_\alpha} + \frac{B}{k_\beta} \right]$$

$$\frac{R_{met}^2 \left([Ag] \middle/ \varepsilon \right)}{6D[Ab]_{plasma,0} \left(\frac{\kappa}{\gamma} \right) \left(\frac{A}{k_\alpha} + \frac{B}{k_\beta} \right)} = \frac{1}{1 - 3\lambda^2 + 2\lambda^3} \qquad \text{where } \lambda = \frac{R_{sat}}{R_{met}}$$

$$\Gamma_{met} \equiv \frac{R^2\left([Ag]\Big/\varepsilon\right)}{6D[Ab]_{plasma,0}\left(\dfrac{\kappa}{\gamma}\right)\left(\dfrac{A}{k_\alpha}+\dfrac{B}{k_\beta}\right)} \qquad \text{and } \Gamma = 1 \text{ when } \lambda = 0 \text{ (saturation)}$$

b. Vascularized Tumor

This derivation applies the shrinking core model in an 'inside-out' cylindrical geometry. As was assumed for the micrometastasis case, there is no catabolism in the tissue, the binding reaction occurs much faster than diffusion, and the antigen is in excess over the free antibody, causing a slow moving reaction front. This results in a pseudo-steady state concentration of antibody in the Krogh cylinder. The analysis is carried out for high affinity antibodies where the dissociation rate is slow enough to assume irreversible binding. In this model, a mixed or Robin boundary condition is used to incorporate the large resistance across the capillary wall at the center of the cylinder.

Assuming a pseudo-steady state, the reaction-diffusion equation is:

$$\frac{D}{r}\frac{d}{dr}r\frac{d[Ab]}{dr} = 0$$

$$\int \frac{d}{dr}r\frac{d[Ab]}{dr} = \int 0$$

$$[Ab] = K_1\ln(r) + K_2$$

<u>Boundary conditions</u>

$$Ab\big|_{r=R(t)} = 0 \qquad\qquad \text{The concentration is zero at the reaction front.}$$

Flux across capillary wall = Flux just outside capillary wall

$$P\left(\left(\varepsilon\cdot[Ab]_{plasma}\right)-[Ab]_{cap}\right) = -D\left(\frac{d[Ab]}{dr}\right)$$

This second boundary condition is a mixed or Robin boundary condition where both the value and derivative are involved. Using these, the concentration profile is:

$$[Ab]_{cap} = \frac{\varepsilon \cdot [Ab]_{plasma}}{\left(\dfrac{D}{P \cdot R_{cap}} + \ln\left(\dfrac{R}{R_{cap}}\right)\right)} \ln\left(\frac{R}{r}\right)$$
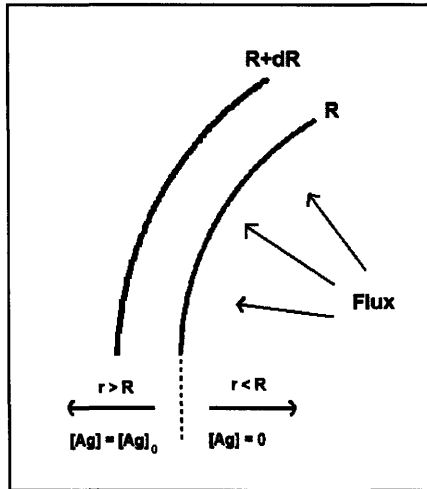
Figure A.1 – Geometry for Eroding Cylinder. Antigen is saturated inside the reaction front at radius R.

To determine the rate of 'erosion' of the cylinder, a differential volume at the radius of saturation is defined. Assuming instantaneous reaction/binding, the number of molecules entering the volume (product of flux and area) in a differential time is equal to the number of molecules reacting/binding in that volume. Since this occurs instantaneously, the number of reacting molecules is equal to the total number of binding sites within the volume (the initial antigen concentration).

Using overall concentration for both sides of the equation:

# of binding sites = # of binding antibodies

$$[Ag](2\pi RL)dR = flux\big|_{r=R}(2\pi RL)dt$$

$$[Ag]\frac{dR}{dt} = -D\frac{d[Ab]}{dr}\bigg|_{r=R}$$

Taking the derivative of the concentration profile (above):

188

$$R\frac{dR}{dt} = \frac{\varepsilon D[Ab]_{plasma}}{[Ag]\left(\dfrac{D}{P \cdot R_{cap}} + \ln\left(\dfrac{R}{R_{cap}}\right)\right)}$$

i. Constant Plasma Concentration

The derivation will first be carried out for a constant plasma concentration. This yields the saturation time when there is no clearance from the blood. For low Biot number scenarios, the second term (containing $\ln(R/R_{cap})$) is negligible, and the integration can be carried out neglecting this term. (e.g. for R/R_{cap}=10 and the Biot number = 0.004 or 0.001 for IgG and scFv, this is assuming 467 >> 2.3 for IgG and 1600 >> 2.3 for scFv). However, for completeness, we will include this term for now.

$$\left(\frac{D}{P \cdot R_{cap}} + \ln\left(\frac{R}{R_{cap}}\right)\right)R \cdot dR = \frac{\varepsilon D[Ab]_{plasma}}{[Ag]}dt$$

with a dummy variable (x) for R:

$$\frac{D}{P \cdot R_{cap}}\int_{R_{cap}}^{R}x \cdot dx + \int_{R_{cap}}^{R}\ln\left(\frac{x}{R_{cap}}\right)x \cdot dx = \frac{\varepsilon D[Ab]_{plasma}}{[Ag]}\int_{0}^{t_{sat}}dt$$

$$\left(\frac{D}{P \cdot R_{cap}}\right)\left(R^2 - R_{cap}^{2}\right) + R^2\ln\left(\frac{R}{R_{cap}}\right) - \frac{R^2}{2} + \frac{R_{cap}^{2}}{2} = \frac{2D \cdot [Ab]_{plasma}}{\left([Ag]\big/\varepsilon\right)}t_{sat}$$

Making assumptions to simplify:

1. If R >> R_{cap}, will integrate from 0 to R instead of R_{cap} to R. (Assuming negligible vascular volume.)

$$\left(\frac{D}{P \cdot R_{cap}} + \ln(\frac{R}{R_{cap}}) - \frac{1}{2}\right) = \frac{2D[Ab]_{plasma}}{R^2\left([Ag]\big/\varepsilon\right)}t_{sat}$$

2. If $\dfrac{D}{P \cdot R_{cap}} >> \ln\left(\dfrac{R}{R_{cap}}\right)$ and >> 1/2 as shown above, then it simplifies to one term:

$$t_{sat} = \frac{\left([Ag]/\varepsilon\right)R^2}{\left(2PR_{cap}[Ab]_{plasma}\right)}$$

ii. Clearance Modulus for Decaying Boundary Conditions

For decaying boundary conditions, it will be assumed that the plasma concentration decays slowly compared to the free diffusion between the capillary and reaction front, similar to the assumption for micrometastases. The results will also include an initial infusion period to show the effects of maintaining a constant plasma concentration initially, followed by decay. It will be simplified for the case of a bolus dose at the end.

The boundary conditions for infusion and decay vary over time:

$$[Ab]_{plasma} = [Ab]_{plasma,0} \qquad\qquad 0 < t < t_{\text{inf usion}}$$

$$[Ab]_{plasma} = [Ab]_{plasma,0}\left(A\exp(-k_\alpha t) + B\exp(-k_\beta t)\right) \quad t_{\text{inf usion}} < t < \infty$$

In the previous section, the equation was integrated before making simplifying assumptions. Here it will be simplified before integration.

$$R\frac{dR}{dt} = \frac{\varepsilon D[Ab]_{plasma}}{[Ag]\left(\dfrac{D}{P \cdot R_{cap}} + \ln\left(\dfrac{R}{R_{cap}}\right)\right)}$$

Using an estimate for the second term in the denominator:

$$\ln\left(\frac{R}{R_{cap}}\right) = 2.3 \ll 467 = \frac{D}{P \cdot R_{cap}}$$

as shown in the previous section.

$$R\frac{dR}{dt} = \frac{\varepsilon D[Ab]_{plasma}(t)}{[Ag]\left(\dfrac{D}{PR_{cap}}\right)} = \frac{[Ab]_{plasma}(t)PR_{cap}}{\left([Ag]/\varepsilon\right)}$$

where the (t) indicates that [Ab]$_{plasma}$ is a function of time.

Using the simplified equation from above and integrating over the infusion period:

$$\int_{R_{cap}}^{R_{temp}} RdR = \int_{0}^{t_{inf usion}} \frac{[Ab]_{plasma}(t)PR_{cap}}{\left([Ag]\middle/\varepsilon\right)} dt$$

where R_{temp} is the radius of saturation after the infusion period before decay.

Integrating from 0 to R_{temp} while $[Ab]_{plasma}$ is constant to simplify the result:

$$\frac{R_{temp}^{2}}{2} = \frac{[Ab]_{plasma}PR_{cap}}{\left([Ag]\middle/\varepsilon\right)} t_{inf usion}$$

The second period occurs when the antibody decays from the plasma. To obtain the maximum radius that could be saturated assuming no catabolism and irreversible binding, the right hand side (RHS) is integrated to infinity. The LHS is then integrated to R_{max}, the maximum achievable radius of saturation.

Integrating over the second time period:

$$\int_{R_{temp}}^{R_{max}} RdR = \int_{t_{inf usion}}^{\infty} \frac{[Ab]_{plasma}(t)PR_{cap}}{\left([Ag]\middle/\varepsilon\right)} dt$$

$$\int_{R_{temp}}^{R_{max}} RdR = \frac{[Ab]_{plasma,0}PR_{cap}}{\left([Ag]\middle/\varepsilon\right)} \int_{t_{inf usion}}^{\infty} \left(A\exp(-k_{\alpha}t) + B\exp(-k_{\beta}t)\right) dt$$

$$\frac{R_{max}^{2}}{2} - \frac{R_{temp}^{2}}{2} = \frac{[Ab]_{plasma,0}PR_{cap}}{\left([Ag]\middle/\varepsilon\right)} \left(\frac{A}{k_{\alpha}}\exp(-k_{\alpha}t_{inf usion}) + \frac{B}{k_{\beta}}\exp(-k_{\beta}t_{inf usion})\right)$$

Combining:

$$\frac{R_{max}^{2}}{2} = \frac{[Ab]_{plasma,0}PR_{cap}}{\left([Ag]\middle/\varepsilon\right)} \left(t_{inf usion} + \frac{A}{k_{\alpha}}\exp(-k_{\alpha}t_{inf usion}) + \frac{B}{k_{\beta}}\exp(-k_{\beta}t_{inf usion})\right)$$

191

$$1 = \frac{R_{max}{}^2 \left([Ag] \Big/ \varepsilon \right)}{2PR_{cap}[Ab]_{plasma,0} \left(t_{inf\ usion} + \dfrac{A}{k_\alpha} \exp(-k_\alpha t_{inf\ usion}) + \dfrac{B}{k_\beta} \exp(-k_\beta t_{inf\ usion}) \right)}$$

The clearance modulus is then defined as:

$$\Gamma_{tumor} \equiv \frac{R^2 \left([Ag] \Big/ \varepsilon \right)}{2PR_{cap}[Ab]_{plasma,0} \left(t_{inf\ usion} + \dfrac{A}{k_\alpha} \exp(-k_\alpha t_{inf\ usion}) + \dfrac{B}{k_\beta} \exp(-k_\beta t_{inf\ usion}) \right)}$$

Comparing the solution to the defined clearance modulus, it is apparent that if R is larger than the R_{max} given the other conditions, the clearance modulus will be greater than 1 and the tissue of radius R will not be saturated. If R < R_{max} (i.e. the cylinder of tissue is smaller than the maximum cylinder of tissue that could be saturated), then the clearance modulus will be less than one. Notice that over an infinite period, the assumptions about no catabolism and irreversible binding will break down. This is one reason why the clearance modulus must be less than and not equal to one.

Simplifying for a bolus dose with no infusion:

$$\Gamma_{tumor} \equiv \frac{R^2 \left([Ag] \Big/ \varepsilon \right)}{2PR_{cap}[Ab]_{plasma,0} \left(\dfrac{A}{k_\alpha} + \dfrac{B}{k_\beta} \right)}$$

A.5   Thiele Modulus – High Affinity

a. Micrometastasis

i.   Scaling Analysis

The Thiele modulus described the penetration of antibodies in tumor tissue versus the degradation of the molecules due to binding, internalization, and irreversible degradation. For this derivation, the plasma concentration is held constant until a steady state develops in the tissue. This is valid for an infusion or with very slow clearance times, such as IgGs. Since the antibody, bound complex, and free antigen concentrations are not changing over time, a steady state will be invoked. The reaction front is

stationary due to the fact that the antibody extravasating from the capillary or diffusing into the metastasis is degraded before reaching the reaction front.

The dimensionless steady state transport equations in a spherical micrometastasis (section A.2) are:

$$0 = \frac{1}{\lambda^2}\frac{d}{d\lambda}\left(\lambda^2\frac{dAb}{d\lambda}\right) - \frac{k_{on}R^2[Ag]_0}{\varepsilon D}AbAg + \frac{k_{off}R^2[Ag]_0}{D[Ab]_{cap}}Bd \qquad \text{i.}$$

$$0 = \frac{k_{on}}{\varepsilon}AbAg - \frac{k_{off}}{[Ab]_{cap}}Bd - \frac{k_e}{[Ab]_{cap}}Bd \qquad \text{ii.}$$

$$0 = \frac{R_s}{[Ag]_0[Ab]_{cap}} - \frac{k_{on}}{\varepsilon}AbAg + \frac{k_{off}}{[Ab]_{cap}}Bd - \frac{k_e}{[Ab]_{cap}}Ag \qquad \text{iii.}$$

where $Ab = \dfrac{[Ab]}{[Ab]_{cap}}$, $Ag = \dfrac{[Ag]}{[Ag]_0}$, $Bd = \dfrac{[B]}{[Ag]_0}$, and $\lambda = \dfrac{r}{R}$

Non-dimensionalize and simplify ii.

$$Bd = \left(\frac{k_{on}}{k_{off}+k_e}\right)\frac{[Ab]_{cap}}{\varepsilon}AbAg \qquad\qquad K_d' \equiv \frac{k_e + k_{off}}{k_{on}}$$

$$Bd = \left(\frac{[Ab]_{cap}}{\varepsilon \cdot K_d'}\right)AbAg \qquad \text{ii'.}$$

Non-dimensionalize and simplify iii.

$$0 = k_e[Ag]_0 R - \frac{k_{on}[Ab]_{cap}[Ag]_0}{\varepsilon}AbAg + k_{off}[Ag]_0 Bd - k_e[Ag]_0 Ag \qquad\qquad R \equiv \frac{R_s}{k_e[Ag]_0}$$

$$0 = k_e R - \frac{k_{on}[Ab]_{cap}}{\varepsilon}AbAg + k_{off}Bd - k_e Ag \qquad \text{iii'.}$$

Plug ii' into i

$$0 = \nabla^2 Ab - \frac{k_{on}R^2[Ag]_0}{\varepsilon D}AbAg + \frac{k_{off}R^2[Ag]_0}{D[Ab]_{cap}}\left(\frac{[Ab]_{cap}}{\varepsilon \cdot K_d'}AbAg\right)$$

$$0 = \nabla^2 Ab - \left[\left(\frac{R^2 [Ag]_0}{\varepsilon D} AbAg \right) \left(\frac{k_e}{K_d'} \right) \right]$$ ii'+i'

Plug ii' into iii'

$$0 = k_e R - \frac{k_{on}}{\varepsilon} [Ab]_{cap} AbAg + k_{off} \left(\frac{[Ab]_{cap}}{\varepsilon \cdot K_d'} \right) AbAg - k_e Ag$$

$$R = Ag \left(\frac{[Ab]_{cap} Ab}{\varepsilon \cdot K_d'} + 1 \right)$$ Assume surface conc. is constant at steady state: R=1

$$Ag = \frac{1}{\left(\frac{[Ab]_{cap} Ab}{\varepsilon \cdot K_d'} + 1 \right)}$$ ii'+iii'

Combine ii'+iii' and ii'+i

$$0 = \nabla^2 Ab - \left(\frac{R^2 [Ag] k_e}{D [Ab]_{cap}} \frac{Ab}{\left(Ab + \frac{\varepsilon K d'}{[Ab]_{cap}} \right)} \right)$$

$$0 = \nabla^2 Ab - \phi^2 \left[\frac{Ab}{\left[\left(Ab + \frac{Kd'}{[Ab]_{surf}} \right) \right]} \right]$$ since $[Ab]_{surf} = \frac{[Ab]_{cap}}{\varepsilon}$

$$\phi^2 \equiv \left(\frac{k_e R^2 \left(\frac{[Ag]}{\varepsilon} \right)}{D [Ab]_{surf}} \right)$$

$[Ab]_{surf}$ is the interstitial antibody concentration at the surface of the tissue. For micrometastases, $[Ab]_{surf}$ is the concentration at the surface of the spheroid. For a constant infusion:

$$[Ab]_{surf} = \frac{\kappa}{\gamma} [Ab]_{plasma}$$

ii.   High Affinity Antibodies – Zero Order Reaction in a Sphere

If $K_d' << [Ab]_{surf}$, which is true for high affinity binders, then the equation becomes:

194

$$0 = \nabla^2 Ab - \left(\frac{k_e R^2 \left([Ag]/\varepsilon \right)}{D[Ab]_{surf}} \right)$$

$$\frac{1}{\lambda^2} \frac{d}{d\lambda} \lambda^2 \frac{dAb}{d\lambda} - \left(\frac{k_e R^2 \left([Ag]/\varepsilon \right)}{D[Ab]_{surf}} \right) = 0$$

$$\frac{d}{d\lambda} \lambda^2 \frac{dAb}{d\lambda} - \phi^2 \lambda^2 = 0$$

$$\lambda^2 \frac{dAb}{d\lambda} - \frac{\phi^2}{3} \lambda^3 = C_1$$

Boundary Condition 1 – No flux at the extinction radius (where the concentration goes to zero)

$$\frac{dAb}{d\lambda}\bigg|_{\lambda=\lambda_e} = 0$$

Substituting in BC 1:

$$C_1 = -\frac{\phi^2}{3} \lambda_e^{\ 3}$$

$$\frac{dAb}{d\lambda} - \frac{\phi^2}{3} \lambda + \lambda_e^{\ 3} \frac{\phi^2}{3} \frac{1}{\lambda^2} = 0 \qquad \text{Integrate:}$$

$$Ab - \frac{\phi^2}{6} \lambda^2 - \lambda_e^{\ 3} \frac{\phi^2}{3} \frac{1}{\lambda} = C_2$$

Boundary Condition 2 – Dirichlet boundary at surface

$$Ab\big|_{\lambda=1} = 1$$

$$C_2 = 1 - \frac{\varphi^2}{6} - \lambda_e^{\ 3} \frac{\varphi^2}{3}$$

$$Ab - \frac{\phi^2}{6}\lambda^2 + \lambda_e^3 \frac{\phi^2}{3}\left(1 - \frac{1}{\lambda}\right) = 1 - \frac{\phi^2}{6}$$ defines the antibody concentration profile.

The extinction radius (maximum radius of penetration) must be known in order to determine the concentration profile. This can be found by finding where the concentration goes to zero.

$$Ab\big|_{\lambda=\lambda_e} = 0$$

$$\phi^2 = \frac{6}{\left(1 + 2\lambda_e^3 - 3\lambda_e^2\right)}$$

Saturation of the micrometastasis or spheroid occurs when the extinction radius reaches the center, since all the antigen will be targeted at this point.

$$\phi^2 = 6 \text{ when } \lambda_e = 0$$

With a high affinity antibody, a micrometastasis will be saturated when the Thiele modulus is equal or less than 6. This solution is in agreement with previous derivations for zero order reaction in a sphere(7).

b. Vascularized Tumor

i. Scaling Analysis with Biot Number

The scaling analysis for high affinity antibodies surrounding a capillary in a vascularized tumor is virtually identical to that for a micrometastasis, but the Laplacian is different due to the geometry. The antibody balance is:

$$\frac{\partial[Ab]}{\partial t} = D\frac{1}{r}\frac{\partial}{\partial r}\left(r\frac{\partial[Ab]}{\partial r}\right) - \frac{k_{on}}{\varepsilon}[Ab][Ag] + k_{off}[B]$$

The same scaling analysis leads to:

$$0 = \nabla^2 Ab - \phi^2 \left[\frac{Ab}{\left(Ab + \dfrac{Kd'}{[Ab]_{surf}} \right)} \right] \qquad \text{and} \qquad \phi^2 \equiv \left(\frac{k_e R^2 \left(\dfrac{[Ag]}{\varepsilon} \right)}{D[Ab]_{surf}} \right)$$

However, there is a major difference in the boundary conditions between a micrometastasis and vascularized tumor. While diffusion from the normal tissue determines uptake in micrometastases, the permeability of the tumor vasculature is important in solid tumors. Instead of a Dirichlet boundary condition that defines the surface concentration, a mixed, or Robin, boundary condition is necessary. Because the surface concentration (just outside the capillary wall) is not known, a Thiele modulus in terms of the plasma concentration is more useful.

To define the Thiele modulus in terms of the plasma concentration, a total mass balance will be performed on the Krogh cylinder. At steady state, after the reaction front has reached its maximum value, the flux of antibody across the capillary wall will be equal to the consumption within the radius of saturated tissue. Because the antibody is assumed not to diffuse beyond this reaction front, the no-flux boundary at the outer Krogh radius is not necessary to define the volume of interest. However, it does reinforce the idea that no antibody leaves the system other than what is catabolized.

At steady state:

Flux across the capillary wall = Catabolism in the tissue

$$flux\big|_{r=R_{cap}} S = k_e [B] V$$

$$flux\big|_{r=R_{cap}} = \frac{k_e [Ag]}{S \big/ V_{sat}}$$

where V_{sat} is the volume of tissue that is saturated with antibody. Because all the antigen in this region is saturated, the bound complex concentration is equal to the initial antigen concentration.

The Robin boundary condition at the capillary wall yields:

$$flux\big|_{r=R_{cap}} = P\left([Ab]\big|_{r=R_{cap}-} - [Ab]\big|_{r=R_{cap}+} \right) = P\left(\left(\varepsilon [Ab]_{plasma} \right) - [Ab]_{cap} \right)$$

where P is the vascular permeability(4). Note that ε is required so both concentrations are on an overall tumor volume basis.

Combining:

$$P\left([Ab]_{plasma} - [Ab]_{surf}\right) = k_e \frac{[Ag]}{\varepsilon} \frac{V_{sat}}{S}$$

The saturated volume to surface ratio for the Krogh cylinder is:

$$\frac{V_{sat}}{S} = \frac{\pi(R_{sat}^2 - R_{cap}^2)L}{2\pi R_{cap}L} = \frac{R_{sat}^2 - R_{cap}^2}{2R_{cap}} \approx \frac{R_{sat}^2}{2R_{cap}}$$

A hexagonal (array) geometry can be assumed, but this decreases the volume by less than 20%. (A_hexagon/A_circle > 0.8) Combining:

$$P\left([Ab]_{plasma} - [Ab]_{surf}\right) = \frac{k_e R_{sat}^2 \left(\frac{[Ag]}{\varepsilon}\right)}{2R_{cap}}$$

$$\frac{2PR_{cap}}{D}\left(\frac{[Ab]_{plasma}}{[Ab]_{surf}} - 1\right) = \frac{k_e R_{sat}^2 \left(\frac{[Ag]}{\varepsilon}\right)}{D[Ab]_{surf}}$$

As was shown for the micrometastases, the RHS is the Thiele modulus defined in terms of the concentration just outside the capillary wall. The right hand side is approximately equal to one, since the radius is defined at the saturation distance and the Thiele modulus is approximately one at the saturation radius (shown below). This yields:

$$\frac{2PR_{cap}}{D}\left(\frac{[Ab]_{plasma}}{[Ab]_{surf}} - 1\right) = 1$$

$$[Ab]_{surf} = \frac{[Ab]_{plasma}}{\frac{1}{Bi} + 1}$$

$$Bi \equiv \frac{2PR_{cap}}{D}$$

The Biot number relates the surface concentration to the plasma concentration, so substituting back into the Thiele modulus:

$$\phi_{tumor}^2 \equiv \left(\frac{k_e R^2 \left([Ag] \Big/ \varepsilon \right)}{D \left(\dfrac{[Ab]_{plasma}}{1 \Big/ Bi + 1} \right)} \right)$$

ii.   High Affinity Antibodies – Zero Order Reaction in a Cylindrical Annulus

The previous derivation assumed that the Thiele modulus is approximately equal to one when the saturation radius is used. With a few more assumptions, an exact solution can be obtained. For a zero order reaction, the reaction rate is independent of the concentration, so this concentration will drop until it is identically zero at some finite distance. This is the saturation distance within the tissue, R. At steady state, this is not changing, so the distances will be normalized with this value. When binding is assumed to occur instantaneously, such that all antigen within the saturation front (R_{sat}) is completely complexed with antibody:

$$\frac{1}{r}\frac{d}{dr} r \frac{d[Ab]}{dr} - \frac{k_e[Ag]}{D} = 0 \qquad \text{for } R_{cap} < r < R$$

$$\frac{1}{\lambda}\frac{d}{d\lambda} \lambda \frac{dAb}{d\lambda} - \frac{k_e[Ag]R^2}{D[Ab]_{cap}} = 0 \qquad \text{where } Ab = \frac{[Ab]}{[Ab]_{cap}} \quad \text{and } \lambda = \frac{r}{R}$$

$$\frac{1}{\lambda}\frac{d}{d\lambda} \lambda \frac{dAb}{d\lambda} - \phi^2 = 0 \qquad \text{where } \phi^2 = \frac{k_e[Ag]R^2}{D[Ab]_{cap}} = \frac{k_e\left([Ag] \Big/ \varepsilon \right)R^2}{D[Ab]_{surf}}$$

$$\int \frac{d}{d\lambda} \lambda \frac{dAb}{d\lambda} - \phi^2 \lambda = \int 0 \qquad \text{(Note that R in the Thiele modulus is unknown at this point.)}$$

$$\lambda \frac{dAb}{d\lambda} - \frac{\phi^2}{2} \lambda^2 = C_1$$

Boundary Condition 1 – No flux at the extinction radius (Neumann condition)

$$\frac{dAb}{d\lambda}\bigg|_{\lambda=1} = 0$$

$$C_1 = -\frac{\phi^2}{2}$$

$$\frac{dAb}{d\lambda} - \frac{\phi^2}{2}\lambda + \frac{\phi^2}{2\lambda} = 0$$

$$\int \frac{dAb}{d\lambda} - \frac{\phi^2}{2}\lambda + \frac{\phi^2}{2\lambda} = \int 0$$

$$Ab - \frac{\phi^2}{4}\lambda^2 + \frac{\phi^2}{2}\ln\lambda = C_2$$

Boundary Condition 2 – Dirichlet condition at the capillary wall

$$Ab\big|_{\lambda=\frac{R_{cap}}{R}} = 1$$

$$1 - \frac{\phi^2}{4}\left(\frac{R_{cap}}{R}\right)^2 + \frac{\phi^2}{2}\ln\left(\frac{R_{cap}}{R}\right) = C_2$$

$$\boxed{Ab = 1 + \frac{\phi^2}{4}\left(\lambda^2 - \left(\frac{R_{cap}}{R}\right)^2 - 2\left(\ln\left(\frac{r}{R_{cap}}\right)\right)\right)}$$

The saturation radius must be found before the concentration profile is determined. At the saturation radius, the concentration is zero, and the Thiele modulus is at the critical value of saturation:

$$0 = 1 + \frac{\phi^2}{4}\left(1 - \left(\frac{R_{cap}}{R}\right)^2 - 2\left(\ln\left(\frac{R}{R_{cap}}\right)\right)\right) \qquad \text{when Ab = 0 at r = R}$$

$$\phi^2 = \frac{4}{\left(\left(\frac{R_{cap}}{R}\right)^2 - 1 + 2\ln\left(\frac{R}{R_{cap}}\right)\right)}$$

This equation, combined with the Thiele modulus definition, defines the saturation radius R. This could be solved for R, and the concentration profile is then given by the boxed equation. However, the solution requires the knowledge of $[Ab]_{surf}$, and $[Ab]_{plasma}$ is typically known. This will be revisited below, but the scaling assumption in A.5b.i will first be justified using this solution.

Because the Krogh cylinder is not a simple cylinder but rather an annulus with the capillary in the center and saturation radius at the outside, the value of the Thiele modulus at saturation is dependent on the geometry ratio (R/R_{cap}). (Essentially the Thiele modulus definition lacks a geometry factor for the cylindrical annulus.) For the scaling derivation, it was assumed that this value was approximately equal to 1. A general rule of thumb for scaling a variable as order one is that it stays between 0.3 and 3(8). The Thiele modulus at saturation (given by the above equation) is graphed versus R/R_{cap} below, and it is within these limits when R/R_{cap} ranges from 3 to 1300. For a 20 micron diameter tumor vessel, the assumption is valid for intercapillary distances ranging from 40 μm to 2.6 cm, spanning the range of a well vascularized tumor(9) to large necrotic regions(10).
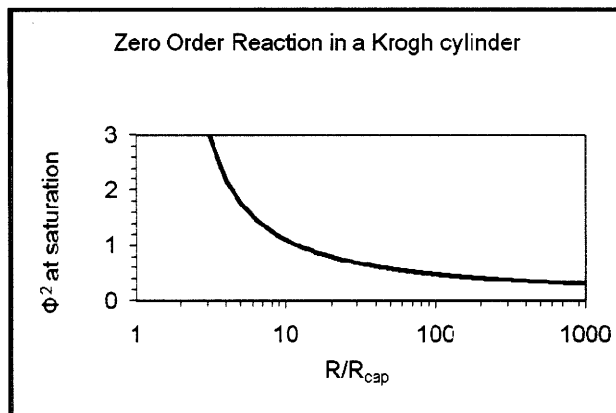
Figure A.2 – Graph of the Thiele modulus versus R/R_{cap}. The Thiele modulus is order of magnitude one for all physiologically relevant values of R/R_{cap}, validating the assumption in A.5b.i.

The derivation above was carried out knowing the concentration at the outer surface of the capillary ($[Ab]_{surf}$), but now it will be directly related to $[Ab]_{plasma}$ using the mixed boundary condition. After the first integration above:

$$\frac{dAb}{d\lambda} - \frac{\phi^2}{2}\lambda + \frac{\phi^2}{2}\frac{1}{\lambda} = 0$$

The mixed boundary condition is:

$$\frac{dAb}{d\lambda}\bigg|_{\lambda=\frac{R_{cap}}{R}} = \frac{PR}{D}\left(1 - \frac{\varepsilon[Ab]_{plasma}}{[Ab]_{cap}}\right)$$

Yielding:

$$Bi\left(1 - \frac{\varepsilon[Ab]_{plasma}}{[Ab]_{cap}}\right) - \phi^2\left(\frac{R_{cap}}{R}\right)^2 + \phi^2 = 0 \qquad \text{where} \quad Bi \equiv \frac{2PR_{cap}}{D}$$

Using this boundary condition, the definition of Φ^2, and the value at saturation, e.g.

$$\phi^2 = \frac{k_e\left([Ag]/\varepsilon\right)R^2}{D[Ab]_{surf}} \qquad\qquad \text{i.} \qquad \text{Thiele modulus definition}$$

$$\phi^2 = \frac{4}{\left(\frac{R_{cap}^2}{R^2} - 1 + \ln\left(\frac{R^2}{R_{cap}^2}\right)\right)} \qquad\qquad \text{ii.} \qquad \text{Material balance solution}$$

$$Bi\left(1 - \frac{\varepsilon[Ab]_{plasma}}{[Ab]_{cap}}\right) + \frac{k_e\left([Ag]/\varepsilon\right)\left(R^2 - R_{cap}^2\right)}{D[Ab]_{surf}} = 0 \qquad \text{iii.} \qquad \text{Mixed boundary condition}$$

the 3 unknowns in the 3 equations above are ϕ^2, R, and [Ab]$_{surf}$. Combining the equations, the saturation radius, R, is a function of [Ab]$_{plasma}$ given the known parameters k$_e$, [Ag], ε, P, R$_{cap}$, and D (Bi):

$$[Ab]_{plasma} = \frac{k_e\,[Ag]/\varepsilon\,(R^2)}{D}\left[\frac{1}{Bi}\left(\frac{R^2 - R_{cap}^2}{R^2}\right) + \frac{\left(\frac{R_{cap}^2}{R^2} - 1 + \ln\left(\frac{R^2}{R_{cap}^2}\right)\right)}{4}\right]$$

This is the exact solution for a zero order reaction in a cylindrical annulus. The solution can be scaled like in the previous section to give a much simpler solution. Equation ii was shown to be approximately equal to 1 over the relevant range, so:

202

$$\phi^2 = \frac{k_e\left(\frac{[Ag]}{\varepsilon}\right)R^2}{D[Ab]_{surf}} \approx 1 \qquad \text{and} \qquad \frac{1}{\phi^2} = \frac{\left(\frac{R_{cap}^2}{R^2} - 1 + \ln\left(\frac{R^2}{R_{cap}^2}\right)\right)}{4} \approx 1$$

Combined with the assumption $R^2 - R_{cap}^2 \approx R^2$:

$$[Ab]_{plasma} = [Ab]_{surf}\left[\frac{1}{Bi} + 1\right]$$

$$[Ab]_{surf} = \frac{[Ab]_{plasma}}{1 + \frac{1}{Bi}}$$

Using this relationship, the Thiele modulus can be defined in terms of the plasma concentration:

$$\phi_{tumor}^2 \equiv \frac{k_e\left(\frac{[Ag]}{\varepsilon}\right)R^2}{D\left(\frac{[Ab]_{plasma}}{1 + \frac{1}{Bi}}\right)}$$

A.6   Biot Number and Other Boundary Conditions

The Biot number is useful to define the concentration just outside the capillary wall in terms of the plasma concentration. If transport across the vessel wall was rapid, then the concentration outside the vessel would be equivalent to the plasma concentration once it was adjusted by the void fraction. However, from rates measured in tumors, it is a significant barrier. The surface concentration will be scaled during shrinking core uptake (from the clearance modulus), during steady state (Thiele modulus), and based on a simple change of variables where no assumptions in the tissue are made. Finally, the analytical predictions are compared to numerical simulations.

a.   Shrinking Core Biot Number Scaling

From the shrinking core derivation for a solid tumor, right after the mixed boundary condition is introduced:

$$[Ab]_{cap} = \frac{\varepsilon \cdot [Ab]_{plasma}}{\left(\dfrac{D}{P \cdot R_{cap}} + \ln\left(\dfrac{R}{R_{cap}} \right) \right)} \ln\left(\frac{R}{r} \right)$$

The initial derivation looked at the flux at the reacting surface. However, at r=R$_{cap}$:

$$[Ab]_{surf} = \frac{[Ab]_{plasma}}{\left(\dfrac{D}{2PR_{cap}} \dfrac{2}{\ln\left(\dfrac{R}{R_{cap}} \right)} + 1 \right)}$$

Defining the Biot number as Bi = 2PR$_{cap}$/D:

$$[Ab]_{surf} = \frac{[Ab]_{plasma}}{\left(\dfrac{1}{Bi} \dfrac{2}{\ln\left(\dfrac{R}{R_{cap}} \right)} + 1 \right)}$$

Since:

$$0.3 < \frac{2}{\ln\left(\dfrac{R}{R_{cap}} \right)} < 3 \quad \text{or} \quad \frac{2}{\ln\left(\dfrac{R}{R_{cap}} \right)} \approx 1 \quad \text{when} \quad 2 < \frac{R}{R_{cap}} < 785$$

$$[Ab]_{surf} \approx \frac{[Ab]_{plasma}}{\left(\dfrac{1}{Bi} + 1 \right)}$$

For large Bi: $[Ab]_{surf} \approx [Ab]_{plasma}$

For small Bi: $[Ab]_{surf} \approx Bi[Ab]_{plasma}$

The constraints on the assumption make it valid from ~1 cell diameter outside of the capillary to almost 8 mm away from the nearest vessel for a 10 μm radius capillary. Therefore, the above surface

204

concentration as a function of the plasma is valid for most cases with shrinking core assumptions used to derive the clearance modulus.

The boundary condition can be scaled to show the proper form of the Biot number. All terms must be scaled according to their maximum value.

$$P\left(\left(\varepsilon \cdot [Ab]_{plasma}\right) - [Ab]_{cap}\right) = -D\left(\frac{d[Ab]}{dr}\right)$$

$$\frac{P}{D}\left(1 - \left(\frac{[Ab]_{plasma}}{[Ab]_{surf}}\right)\right) = \frac{dAb}{dr}\Big|_{r=R_{cap}}$$

The derivative from the shrinking core analysis is:

$$\frac{dAb}{dr}\Big|_{r=R_{cap}} = \frac{1}{R_{cap}\ln\left(\dfrac{R_{cap}}{R}\right)}$$

The proper distance must be chosen to normalize the radius. The two obvious choses are R_{cap} and R. While the choice of R_{cap} was shown above to stay between 0.3 and 3 over a useful range, the magnitude of the derivative exceeds 3 for $R/R_{cap} > 5$. Since cells are found at distances greater than 50 µm away from vessels(10), R_{cap} is the proper length scale. Using insight from the exact solution, the length scale of $2R_{cap}$ is used to normalize the boundary condition:

$$\frac{2PR_{cap}}{D}\left(1 - \left(\frac{[Ab]_{plasma}}{[Ab]_{surf}}\right)\right) = \frac{dAb}{d\lambda}\Big|_{\lambda=\frac{1}{2}} \sim 1 \qquad \text{and} \qquad \lambda = \frac{r}{2R_{cap}}$$

b. Thiele Modulus Biot Number Scaling

The total mass balance, useful for defining the Thiele modulus, can be used to scale the boundary conditions. Starting with an overall mass balance at steady state for a high affinity antibody:

Flux entering Krogh cylinder = Total consumption

$$\left(2\pi R_{cap}L\right)\left(-D\frac{d[Ab]}{dr}\Big|_{r=R_{cap}}\right) = \int_{R_{cap}}^{\infty} k_e\left([Ag]/\varepsilon\right)L \cdot 2\pi R dR$$

205

With a high affinity antibody, the concentration is zero at distances greater than R, and it is assumed that R>>R_{cap}, simplifying the limits of integration:

$$\left(2\pi R_{cap}L\right)\left(-D\frac{d[Ab]}{dr}\bigg|_{r=R_{cap}}\right)=k_e\left([Ag]\Big/\varepsilon\right)2\pi L\int_0^R x\,dx$$

$$-R_{cap}D\frac{d[Ab]}{dr}\bigg|_{r=R_{cap}}=\frac{k_e}{2}\left([Ag]\Big/\varepsilon\right)R^2$$

$$-\frac{d[Ab]}{dr}\bigg|_{r=R_{cap}}=\frac{k_e\left([Ag]\Big/\varepsilon\right)R^2}{2R_{cap}D}$$

$$-\frac{dAb}{dr}\bigg|_{r=R_{cap}}=\frac{1}{2R_{cap}}\left(\frac{k_e\left([Ag]\Big/\varepsilon\right)R^2}{D[Ab]_{surf}}\right)$$

The Thiele modulus term in brackets has already been shown to be order 1 when R is the radius of saturation. The derivative must be normalized by $2R_{cap}$ in order for both sides to be properly scaled.

$$-\frac{dAb}{d\lambda}\bigg|_{\lambda=\frac{1}{2}}=\left(\frac{k_e\left([Ag]\Big/\varepsilon\right)R^2}{D[Ab]_{surf}}\right)\sim 1$$

Using the mixed boundary condition:

$$flux\big|_{r=R_{capillary}{}^+}=flux\big|_{r=R_{capillary}{}^-}$$

$$-D\frac{d[Ab]}{dr}\bigg|_{r=R_{cap}}=P\left([Ab]_{plasma}-[Ab]_{surf}\right)$$

$$-\frac{dAb}{d\lambda}\bigg|_{\lambda=\frac{1}{2}}=\frac{2R_{cap}P}{D}\left(\frac{[Ab]_{plasma}}{[Ab]_{surf}}-1\right)\sim 1$$

The derivative has already been shown to be order of magnitude 1, so the RHS must also be order of magnitude 1.

$$\frac{2R_{cap}P}{D}\left(\frac{[Ab]_{plasma}}{[Ab]_{surf}}-1\right)\approx 1$$

$$Bi\left(\frac{[Ab]_{plasma}}{[Ab]_{surf}}-1\right)=1 \qquad\qquad Bi\equiv\frac{2PR_{cap}}{D}$$

$$[Ab]_{surf}=\frac{[Ab]_{plasma}}{\left(1+\frac{1}{Bi}\right)}$$

A Note on Krogh Cylinder Geometry:

This scaling is facilitated by the divergent geometry of diffusion outward from a cylinder. For example, antibody diffusing into the center of a spheroid is affected by the curvature and hence the overall size of the spheroid. Antibody diffusing into a boundary layer that is 10 microns thick in a 1 cm spheroid has very little curvature; antibody diffusing 10 microns into a spheroid of radius 15 microns has lots of curvature. This is not the case for divergent geometry from a cylinder with constant inner radius. Antibody diffusing into a boundary layer 10 microns thick has the same curvature regardless of whether the outer Krogh cylinder radius (e.g. half distance between capillaries) is 30 microns or 300 microns. This is the reason it is easier to give a simple formula for the penetration distance outside a capillary without needing the maximum half distance, whereas the exact solution for a sphere contains polynomials that include the total radius.

c. Biot Number in Infinite Medium

A simple change of variables can be used to demonstrate that the capillary radius is the appropriate length scale for the Biot number. The scaling is only valid prior to saturation of the tumor, since once all binding sites are occupied, the free antibody concentration in the tumor rapidly increases. In order to guarantee that antibody has not reached the outer radius, a change of variables can be used to examine antibody diffusing outward into infinite surrounding tissue. This scaling requires no assumptions as to the affinity, internalization, or even the presence of binding in the tissue.

207

Boundary condition 1 – mixed boundary at capillary wall

$$-D\frac{d[Ab]}{dr}\bigg|_{r=R_{cap}} = P\big([Ab]_{plasma} - [Ab]_{surf}\big)$$

Boundary condition 2 – zero concentration at infinite distance from the capillary

$$[Ab]\big|_{r=\infty} = 0$$

<u>Change in variables:</u>

To facilitate scaling of a cylinder in infinite medium, a change of variables is invoked:

$$n = \frac{1}{r} \qquad \text{and} \qquad dr = \frac{-dn}{n^2}$$
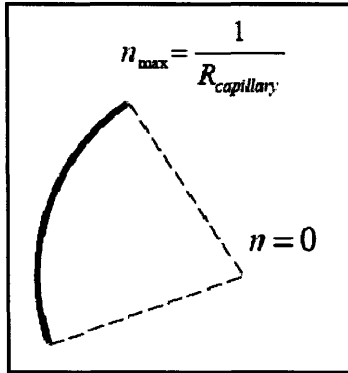
Figure A.3 – Geometry after the change in variables for Biot number scaling.

Focusing on the first boundary condition:

$$D\left(n^2\frac{d[Ab]}{dn}\right)\bigg|_{n=n_{max}} = P\big([Ab]_{plasma} - [Ab]_{surf}\big) \qquad \text{where } n_{max} = \frac{1}{R_{cap}}$$

The magnitude of the derivative is equal to the magnitude of the change in $[Ab]_{surf}$ divided by the magnitude of the change in n:

$$n \sim (n_{max} - 0) \sim n_{max} \qquad\qquad \text{since n ranges from } n_{max} \text{ at surface to zero at center (infinite r)}$$

$$[Ab] \sim \left([Ab]_{surf} - 0\right)\frac{1}{2} \sim \frac{1}{2}[Ab]_{surf}$$ since [Ab] ranges from [Ab]$_{surf}$ at the capillary surface to zero at center (infinite r) according to boundary condition 2. The geometric factor of ½ is included from knowledge of the exact solution for a zero-order reaction at steady state in cylindrical geometry. Scaling only indicates the proper length scale, not any shape factors.

Using these order of magnitude estimates for the boundary condition:

$$Dn_{max}^{2}\frac{[Ab]_{surf}\dfrac{1}{2}}{n_{max}} \sim P\left([Ab]_{plasma} - [Ab]_{surf}\right)$$

Changing back to normal cylindrical coordinates with the correct scale:

$$[Ab]_{surf} = \frac{2PR_{cap}}{D}\left([Ab]_{plasma} - [Ab]_{surf}\right)$$

$$[Ab]_{surf} = \frac{[Ab]_{plasma}}{\left(1 + \dfrac{1}{Bi}\right)} \qquad \text{where } Bi = \frac{2PR_{cap}}{D}$$

The change of variables is very simple, but it removes the requirement for a saturation (dynamic) radius, R, to scale the boundary condition. Without the requirement for R, or any binding, internalization, etc., it provides a much more general rule at the capillary wall.

d. Ab$_{surf}$ from Numerical Simulations

Numerical simulations in a Krogh cylinder (using Appendix section 2) were performed to verify the Biot scaling at the capillary wall. The equations as given for the Krogh cylinder were implemented, and the concentration at the outer surface of the vessel was compared to the analytical prediction. The doses used had to be small enough that the concentration in the cylinder was well below saturation. As mentioned before, if the cylinder becomes saturated, the free antibody concentration rapidly increases as the newly extravasated antibody lacks free binding sites.

Simulations were run for permeability values of 1×10^{-3} µm/s, 5×10^{-3} µm/s, and 20×10^{-3} µm/s. The diffusion coefficient was set at 1, 14, or 80 µm²/s, and R_{cap} was 5 or 10 µm. The ratio of predicted $[Ab]_{surf}$ to the numerical value for $[Ab]_{surf}$ ranged from 0.61 to 3.2 over all 18 simulations. The numerical simulations, therefore, are in reasonable agreement with the analytical predictions. It is important to note that $[Ab]_{surf}$ is the free antibody concentration. When binding occurs in the tumor, the total concentration (bound + free) is much higher, and it is difficult to measure the only the free antibody concentration.

A.7 Shrinking Core Derivation with Catabolism – Spherical Geometry

The initial shrinking core analysis was solved assuming no catabolism in the tissue. This assumption can be relaxed, although the resulting solution is more complex. The reaction-diffusion equation is:

$$D\frac{1}{r^2}\frac{d}{dr}\left(r^2\frac{d[Ab]}{dr}\right) - k_e[Ag] = 0$$

$$\frac{1}{\lambda^2}\frac{d}{d\lambda}\left(\lambda^2\frac{dAb}{d\lambda}\right) - \frac{k_e\left([Ag]\big/\varepsilon\right)R_{met}^2}{D[Ab]_{surf}} = 0 \qquad \lambda = \frac{r}{R_{met}} \qquad Ab = \frac{[Ab]}{\varepsilon[Ab]_{surf}}$$

$$\frac{1}{\lambda^2}\frac{d}{d\lambda}\left(\lambda^2\frac{dAb}{d\lambda}\right) - \phi^2 = 0 \qquad\qquad \phi^2 = \frac{k_e\left([Ag]\big/\varepsilon\right)R_{met}^2}{D[Ab]_{surf}}$$

$$\int\frac{d}{d\lambda}\left(\lambda^2\frac{dAb}{d\lambda}\right) - \phi^2\lambda^2 = \int 0$$

$$\lambda^2\frac{dAb}{d\lambda} - \frac{\phi^2}{3}\lambda^3 = C_1$$

$$\int\frac{dAb}{d\lambda} - \frac{\phi^2}{3}\lambda = \int\frac{C_1}{\lambda^2}$$

$$Ab - \frac{\phi^2}{6}\lambda^2 = \frac{-C_1}{\lambda} + C_2$$

Boundary Conditions:

$$Ab\big|_{\lambda=\theta} = 0 \qquad\qquad \text{where } \theta = \frac{R(t)}{R_{sphere}} \qquad \text{Instantaneous binding reaction}$$

$$Ab\big|_{\lambda=1} = 1 \qquad \text{Dirichlet condition at surface}$$

$$C_1 = \frac{\dfrac{\phi^2}{6}\left(\theta^3 - \theta\right) + \theta}{\left(1-\theta\right)}$$

$$C_2 = \frac{1 + \dfrac{\phi^2}{6}\left(\theta^3 - 1\right)}{\left(1-\theta\right)}$$

Concentration Profile

$$Ab - \frac{\phi^2}{6}\lambda^2 = \frac{-1}{\lambda}\left(\frac{\dfrac{\phi^2}{6}\left(\theta^3 - \theta\right) + \theta}{\left(1-\theta\right)}\right) + \frac{1 + \dfrac{\phi^2}{6}\left(\theta^3 - 1\right)}{\left(1-\theta\right)}$$

Finding the flux at the reaction surface:

$$\frac{dAb}{d\lambda}\bigg|_{\lambda=\theta} = \frac{\phi^2}{3}\theta + \left(\frac{1 + \dfrac{\phi^2}{6}\left(\theta^2 - 1\right)}{\left(\theta - \theta^2\right)}\right)$$

Calculating the change in radius:

$$\frac{d}{dt}\left(\frac{4}{3}\pi R^3 [Ag]\right) = -4\pi R^2 D\frac{\varepsilon[Ab]_{surf}}{R_{met}}\left(\frac{dAb}{d\lambda}\bigg|_{\lambda=\theta}\right)$$

$$\frac{d\theta}{dt} = \frac{-D[Ab]_{surf}}{\left([Ag]\!\big/\!\varepsilon\right)R_{met}^2}\left(\frac{dAb}{d\lambda}\bigg|_{\lambda=\theta}\right)$$

$$\frac{d\theta}{dt} = \frac{-D[Ab]_{surf}}{\left([Ag]\!\big/\!\varepsilon\right)R_{met}^2}\left(\frac{1 - \dfrac{\phi^2}{6}\left(1 - 3\theta^2 + 2\theta^3\right)}{\left(\theta - \theta^2\right)}\right)$$

Examining the derivative, the Thiele modulus term lowers the magnitude of the derivative, slowing down the change in radius as antibody is consumed. For very small values of the Thiele modulus, the solution matches that result when catabolism is ignored. For large values, the change in

radius of the reaction front may become zero prior to saturation. Setting the derivative to zero, the metastasis becomes saturated when $\phi^2 = 6$, in agreement with the steady state solution.

$$0 = 1 + \frac{\phi^2}{6}\left(3\theta^2 - 2\theta^3 - 1\right)$$

A.8   Low Affinity Antibodies

Low and high affinity are arbitrary terms, since the effect of varying dissociation constants is highly application dependent. For the purposes of this analysis, as will be shown below, antibody targeting is considered low affinity in any case where $[Ab]_{surf}$ (the concentration in contact with the tumor tissue) is less than K_d. This is important, since the same affinity (e.g. 10 nM) may be considered low affinity with a low dose (e.g. $[Ab]_{surf}$ = 1 nM) but penetrate as a high affinity antibody saturating layer after layer in shrinking core fashion at a high dose (e.g. $[Ab]_{surf}$ = 100 nM).

a. Thiele Modulus

i. Low Affinity Scaling

Starting from the scaling derivation for micrometastases, and assuming the dissociation rate is faster than internalization, $K_d{}' \approx \dfrac{k_{off}}{k_{on}} = K_d$:

$$0 = \nabla^2 Ab - \left(\frac{k_e R^2\left([Ag]/\varepsilon\right)}{D[Ab]_{surf}}\right)\left[\frac{Ab}{\left(Kd'/[Ab]_{surf}\right)}\right]$$

$$0 = \nabla^2 Ab - \left(\frac{k_e R^2\left([Ag]/\varepsilon\right)}{D \cdot Kd}\right)Ab = \nabla^2 Ab - \phi^2 Ab \quad \text{where} \quad \phi^2 \equiv \left(\frac{k_e R^2\left([Ag]/\varepsilon\right)}{D \cdot Kd}\right)$$

This scaling yields a Thiele modulus similar to the high affinity case defined earlier, but with K_d in the denominator instead of the surface concentration. The dimensionless antibody concentration still exists outside the modulus, indicating that it is a 1st order Thiele modulus instead of a zero order term. This is due to the antibody binding in the linear regime instead of the saturation regime.

ii. Low Affinity Thiele Modulus for Micrometastases – 1st Order Reaction in a Sphere

The solution for a 1st order reaction in a sphere can be solved exactly to show that the Thiele modulus is approximately equal to 1 when there are no spatial gradients in the tissue. This does not indicate that all the cells are saturated but rather that the cells near the surface contain the same concentration of antibody as those in the center. Assuming that the dissociation rate is faster than the internalization rate, the binding is in the linear regime, and steady state has been achieved:

$$D\frac{1}{r^2}\frac{d}{dr}r^2\frac{d[Ab]}{dr}-\frac{k_e\left([Ag]/\varepsilon\right)}{K_d}[Ab]=0$$

Notice that the ratio is between the K_d and the interstitial antigen concentration, since this is the relevant concentration between cells where binding occurs.

$$\frac{1}{\lambda^2}\frac{d}{d\lambda}\lambda^2\frac{dAb}{d\lambda}-\frac{k_e\left([Ag]/\varepsilon\right)R_{met}^2}{D\cdot K_d}Ab=0$$

$$\frac{d^2Ab}{d\lambda^2}+\frac{2}{\lambda}\frac{dAb}{d\lambda}-\phi^2 Ab=0 \qquad \text{where} \quad \phi^2\equiv\frac{k_e\left([Ag]/\varepsilon\right)R_{met}^2}{D\cdot K_d}$$

Change of variables, $x = Ab\cdot\lambda$:

$$\frac{dAb}{d\lambda}=\frac{1}{\lambda}\frac{dx}{d\lambda}-\frac{x}{\lambda^2} \qquad \text{and} \qquad \frac{d^2Ab}{d\lambda^2}=\frac{1}{\lambda}\frac{d^2x}{d\lambda^2}-\frac{2}{\lambda^2}\frac{dx}{d\lambda}+\frac{2x}{\lambda^3}$$

Yielding:

$$\frac{1}{\lambda}\frac{d^2x}{d\lambda^2}-\frac{2}{\lambda^2}\frac{dx}{d\lambda}+\frac{2x}{\lambda^3}+\frac{2}{\lambda}\left(\frac{1}{\lambda}\frac{dx}{d\lambda}-\frac{x}{\lambda^2}\right)-\phi^2\frac{x}{\lambda}=0$$

$$\frac{d^2x}{d\lambda^2}-\phi^2 x=0$$

Solving:

$$x = A_1\cosh(\phi\lambda)+B_1\sinh(\phi\lambda) \qquad \text{so} \qquad Ab=\frac{A_1}{\lambda}\cosh(\phi\lambda)+\frac{B_1}{\lambda}\sinh(\phi\lambda)$$

Boundary condition 1 - finite concentration at center

Ab = finite   at $\lambda = 0$ yielding $A_1 = 0$

Boundary condition 2 – Dirichlet condition at surface

Ab = 1   at $\lambda = 1$ yielding $B_1 = \dfrac{1}{\sinh(\phi)}$

$$Ab = \frac{1}{\lambda}\frac{\sinh(\phi\lambda)}{\sinh(\phi)}$$

Notice that the Thiele modulus appears in the solution without being squared. Historically, this is why the Thiele modulus is defined with the square term; it eliminates any square root in the solution to the first order equation.

Concentration profiles:
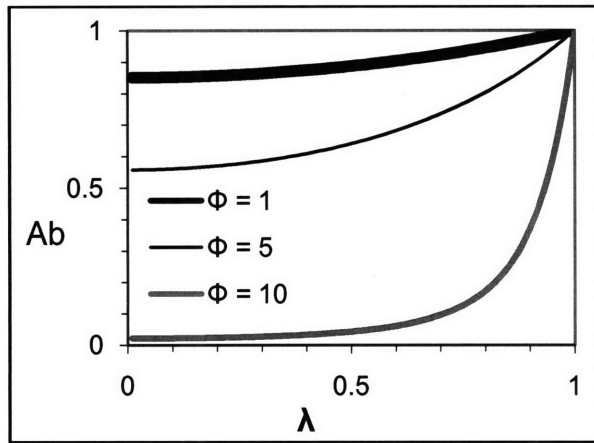
Figure A.4 – Graph of low affinity antibody concentration in a micrometastasis. As the low affinity Thiele modulus value approaches 1, the antibody concentration approaches the level found at the surface. This only means the concentration is uniform and equal to the surface value; it has nothing to do with the saturation level of antigen.

iii.   Low Affinity Thiele Modulus for Vascularized Tumors

The solution for a first order reaction in a cylindrical annulus (Krogh cylinder) is complicated and unintuitive (see appendix section A.11c). However, the scaling analysis still holds, giving the distance low affinity binders penetrate beyond the capillary wall. The scaling is similar to the metastasis with the Laplacian for cylindrical coordinates instead of spherical:

$$\frac{1}{\lambda}\frac{d}{d\lambda}\lambda\frac{dAb}{d\lambda}-\phi^2 Ab = 0 \qquad \text{where} \quad \phi^2 \equiv \frac{k_e\left(\frac{[Ag]}{\varepsilon}\right)R^2}{D\cdot K_d}$$

Examining the limiting behavior, as K_d approaches infinity, the material balance becomes:

$$\frac{1}{\lambda}\frac{d}{d\lambda}\lambda\frac{dAb}{d\lambda}=0$$

Boundary condition 1 – no flux at Krogh cylinder outer surface:

$$\left.\frac{dAb}{d\lambda}\right|_{\lambda=1}=0$$

Solving:

$$0=\frac{d}{d\lambda}\lambda\frac{dAb}{d\lambda}$$

$$\lambda\frac{dAb}{d\lambda}=C_1=0 \qquad\qquad \text{Using BC 1}$$

$$Ab=C_2$$

The concentration in the tumor is equal to a constant, so it is not a function of radius. Therefore, as the low affinity Thiele modulus for solid tumors drops below one, the concentration in the tumor ceases to be a function of the radius. The actual concentration in the tumor depends on the dose and boundary condition at the capillary wall. Using a mass balance to determine this concentration, and assuming that the concentration is constant throughout the cylinder (e.g. [Ab] = [Ab]$_{surf}$):

Extravastation from the capillary = Catabolism in the tissue

$$2\pi R_{cap}LP\left([Ab]_{plasma}-[Ab]_{surf}\right)=\pi R^2 L k_e\left(\frac{[Ag]}{\varepsilon}\right)\left(\frac{[Ab]_{surf}}{K_d}\right)$$

$$[Ab]_{surf}=\frac{[Ab]_{plasma}}{\dfrac{k_e R^2\left(\frac{[Ag]}{\varepsilon}\right)}{2PR_{cap}K_d}+1}$$

215

$$[Ab]_{surf} = \frac{[Ab]_{plasma}}{\dfrac{1}{Bi}\left(\dfrac{k_e R^2\left([Ag]/\varepsilon\right)}{DK_d}\right)+1}$$

As $K_d \to \infty$, $[Ab]_{surf} \to [Ab]_{plasma}$

For low affinity binders, the concentration in the tumor approaches that in the plasma after steady state has been reached. This is because with very little binding and internalization in the tumor, the antibody is not being consumed in the tissue, so with a constant concentration in the plasma, eventually equilibration across the capillary wall will occur.

iv. Slow-binding

Starting from the scaling derivation for micrometastases:

$$0 = \nabla^2 Ab - \phi^2 \left[\frac{Ab}{\left(Ab + Kd'/[Ab]_{surf}\right)}\right]$$

where $K_d' \equiv \dfrac{k_e + k_{off}}{k_{on}}$ and $\phi^2 \equiv \left(\dfrac{k_e R^2\left([Ag]/\varepsilon\right)}{D[Ab]_{surf}}\right)$

For high affinity interactions, the K_d' term was assumed to be much less than the antibody concentration. For lower affinity interactions, this is not necessarily true. Examining the case where Kd' is greater than [Ab]:

$$0 = \nabla^2 Ab - \left(\frac{k_e R^2\left([Ag]/\varepsilon\right)}{D[Ab]_{surf}}\right)\left[\frac{Ab}{\left(Kd'/[Ab]_{surf}\right)}\right]$$

If the endocytosis rate is much faster than the dissociation rate, then $K_d' \approx \dfrac{k_e}{k_{on}}$

$$0 = \nabla^2 Ab - \left(\frac{k_e R^2\left([Ag]/\varepsilon\right)}{D\left(k_e/k_{on}\right)}\right)Ab$$

$$0 = \nabla^2 Ab - \left(\frac{k_{on} R^2 \left([Ag] / \varepsilon \right)}{D} \right) Ab$$

This yields the binding modulus as defined before. For lower affinity interactions (fast-off and slow-on binders), the behavior is determined by the difference between internalization and dissociation. An antibody bound to the cell surface will either be internalized or dissociate to diffuse farther in the tissue. The above case looks at the situation where internalization dominates.

b. Clearance Modulus

i. Low Affinity Scaling

Similar to the high affinity binders, it is assumed there is no catabolism for the clearance modulus. Assuming $[Ab]_{surf} \ll K_d$ (low affinity interaction):

$$\frac{[B]}{[Ag]_0} = \frac{[Ab] / \varepsilon}{[Ab] / \varepsilon + K_d} \approx \frac{[Ab] / \varepsilon}{K_d} \qquad \text{(Assuming linear adsorption isotherm)}$$

The interstitial concentration of antibody is used because the concentration within the interstitial space determines the fraction of antigen bound. The antibody concentration given above is the free antibody concentration.

$$[B] = \frac{\left([Ag] / \varepsilon \right)}{K_d} [Ab]$$

With a linear binding isotherm, the equations behave exactly as a non-binder but with the diffusion coefficient scaled by the binding constant(11):

$$\frac{\partial [Ab]}{\partial t} = \frac{D}{\left(\frac{\left([Ag] / \varepsilon \right)}{K_d} + 1 \right)} \nabla^2 [Ab]$$

If $\dfrac{\left([Ag] / \varepsilon \right)}{K_d} \ll 1$ (and already assumed $[Ab]_{surf} \ll K_d$) then the antibody behaves as a non-binder, since

both the antibody and antigen concentrations are less than the dissociation constant.

217

If $\dfrac{\left(\dfrac{[Ag]}{\varepsilon}\right)}{K_d} >> 1$:

$$\frac{\partial [Ab]}{\partial t} = \frac{D \cdot K_d}{\left(\dfrac{[Ag]}{\varepsilon}\right)} \nabla^2 [Ab]$$

Non-dimensionalize:

$$\frac{\partial Ab}{\partial \tau} = \frac{D \cdot K_d \left(\dfrac{A}{k_\alpha} + \dfrac{B}{k_\beta}\right)}{R^2 \left(\dfrac{[Ag]}{\varepsilon}\right)} \nabla^2 Ab$$

$$\left(\frac{R^2 \left(\dfrac{[Ag]}{\varepsilon}\right)}{D \cdot K_d \left(\dfrac{A}{k_\alpha} + \dfrac{B}{k_\beta}\right)}\right) = \frac{\nabla^2 Ab}{\left(\dfrac{\partial Ab}{\partial \tau}\right)} = \frac{diffusive \quad gradient}{temporal \quad gradient}$$

If the scaling parameter on the left hand side is small, diffusive gradients (along r) are much less than temporal gradients, and a pseudo-steady state approximation can be invoked(8).

ii. Low Affinity Clearance Modulus for Micrometastases

The above analysis showed that a pseudo-steady state approximation can be used when the low affinity clearance modulus is small. Solving the equation for a micrometastasis:

$$0 = \frac{D \cdot K_d \left(\dfrac{A}{k_\alpha} + \dfrac{B}{k_\beta}\right)}{R^2 \left(\dfrac{[Ag]}{\varepsilon}\right)} \frac{1}{\lambda^2} \frac{d}{d\lambda}\left(\lambda^2 \frac{dAb}{d\lambda}\right)$$

$$0 = \frac{d}{d\lambda}\left(\lambda^2 \frac{dAb}{d\lambda}\right)$$

$$\frac{dAb}{d\lambda} = \frac{C_1}{\lambda^2}$$

Boundary condition 1 – no flux at center

$$\left.\frac{dAb}{d\lambda}\right|_{\lambda=0} = 0$$

$$\frac{dAb}{d\lambda} = 0 \qquad \text{and} \qquad Ab = C_2$$

The concentration in the spheroid is independent of the radius. Using a normal tissue compartment:

Boundary condition 2 – Dirichlet condition at surface

$$\frac{dAb}{dt} = \kappa \frac{[Ab]_{plasma}(t)}{[Ab]_{surf}} - \gamma Ab(t)$$

For biexponential plasma clearance:

$$Ab\big|_{\lambda=1} = \kappa\left(A\frac{\exp(-k_\alpha t) - \exp(-\gamma t)}{\gamma - k_\alpha} + B\frac{\exp(-k_\beta t) - \exp(-\gamma t)}{\gamma - k_\beta} \right)$$

$$Ab = \kappa\left(A\frac{\exp(-k_\alpha t) - \exp(-\gamma t)}{\gamma - k_\alpha} + B\frac{\exp(-k_\beta t) - \exp(-\gamma t)}{\gamma - k_\beta} \right)$$

The end result is that the concentration in the spheroid is equivalent to the normal tissue concentration surrounding the spheroid if the scaling parameter is small. This does not mean that the spheroid is saturated, just that the concentration throughout will be equal to the surface concentration.

iii. Low Affinity Clearance Modulus for Vascularized Tumors

The derivation for vascularized tumors is identical except for the Laplacian and boundary conditions.

$$\frac{\partial Ab}{\partial \tau} = \frac{D \cdot K_d\left(\dfrac{A}{k_\alpha} + \dfrac{B}{k_\beta}\right)}{R^2\left([Ag]\big/\varepsilon\right)} \frac{1}{\lambda}\frac{\partial}{\partial\lambda}\lambda\frac{\partial Ab}{\partial\lambda}$$

Invoking pseudo-steady state hypothesis:

$$0 = \frac{D \cdot K_d\left(\dfrac{A}{k_\alpha} + \dfrac{B}{k_\beta}\right)}{R^2\left([Ag]\big/\varepsilon\right)} \frac{1}{\lambda}\frac{d}{d\lambda}\lambda\frac{dAb}{d\lambda}$$

$$\frac{dAb}{d\lambda} = \frac{C_1}{\lambda}$$

Boundary condition 1 – no flux at the Krogh cylinder radius:

$$\left.\frac{dAb}{d\lambda}\right|_{\lambda=1} = 0 \quad \text{so} \quad \frac{dAb}{d\lambda} = 0$$

$$Ab = C_2$$

The concentration profile is equal to a constant, meaning it is not a function of the radius if the scaling parameter is small. However, this constant is a function of time (from the pseudo-steady state hypothesis). In order to determine this dependence, a compartmental model can be used since there are no spatial gradients.

$$\pi R^2 L \frac{d[Ab]_{total}}{dt} = 2\pi R_{cap} LP[Ab]_{plasma}(t) - 2\pi R_{cap} LP[Ab]_{total}(t)$$

$$\frac{d[Ab]_{total}}{dt} = \frac{2PR_{cap}}{R^2}[Ab]_{plasma}(t) - \frac{2PR_{cap}}{R^2}[Ab]_{total}(t)$$

This is a simple compartmental model where binding and internalization in the tissue is ignored. The more inclusive compartmental model for solid tumors is presented later in the appendix. For this non-binding scenario, the equation is identical to the normal compartment except that the uptake and clearance terms are $2PR_{cap}/R^2$ instead of the healthy capillary extravasation and lymphatic clearance. The solution is identical with this substitution.

iv.   Clearance of Slow-binding Antibodies

<u>Distribution of Slow-on Antibodies</u>

The high affinity (fast-on, slow-off) and low affinity (fast-on, fast-off) cases have been scaled above. The third interesting case is for a slow binding antibody (slow-on, slow-off). The fourth case of slow-on and fast-off is very low affinity and can be treated as a non-binder.

For homogeneous distribution in the tissue, the free diffusion rate must be faster than the antigen binding rate as given by the binding modulus:

$$\frac{k_{on}\left(\frac{[Ag]}{\varepsilon}\right)R^2}{D} \ll 1 \text{ yields homogenous distribution.}$$

This is true for subsaturating doses of antibody when catabolism is limiting, as shown above, and when clearance is limiting, assuming the free diffusion rate is faster than the clearance rate, which is often the case.

Retention of Slow-on Antibodies

Although this type of antibody gives even distribution, the slow binding rate may lower the amount of antibody that is bound and retained within the tissue (e.g. the fraction saturated). To determine the amount retained, the binding rate must be scaled with uptake and clearance. For a solid tumor, if the binding rate is faster than the extravasation/intravasation rate, then the antibody will reach equilibrium in the tissue.

If $\dfrac{k_{on}\left(\frac{[Ag]}{\varepsilon}\right)R^2}{2PR_{cap}} \gg 1$, the antibody will reach equilibrium in the tissue.

Assuming that antigen is in excess, uptake and retention in a solid tumor will follow the simple compartmental model given below, which also assumes equilibrium binding and antigen in excess. If the binding rate is so slow that transport across the capillary is faster than binding, the ratio of interest is the clearance in the plasma versus the binding rate. When an antibody is cleared from the plasma faster than it binds, little will be retained in the tumor. Since the capillary wall is not limiting transport, the ratio for solid tumors and metastases is the same:

If $k_{on}\left(\frac{[Ag]}{\varepsilon}\right)\left(\frac{A}{k_\alpha} + \frac{B}{k_\beta}\right) \gg 1$, a significant fraction of antibody will be retained.

Saturation with Slow Binding Antibodies

With micrometastases, it is often possible to saturate the tissue. In this case, binding must be faster than both clearance and catabolism. The association rate multiplied by the antigen concentration is appropriate for an isolated antibody in a volume of tissue, which is relevant when the antigen concentration is in excess. In order to saturate the antigen, however, the antibody must be supplied in excess over the antigen. In this case, the binding rate is proportional to the antibody concentration in

the tissue, [Ab]$_{surf}$. (From an antigen perspective, this is the bulk antibody concentration that defines the rate of binding to each antigen.) The ratio of binding to clearance is then:

$$k_{on}[Ab]_{surf}\left(\frac{A}{k_\alpha} + \frac{B}{k_\beta}\right)$$

Similar to the high affinity cases presented earlier, saturation can be achieved by increasing the dose. However, the lower the on rate, the higher the dose required.

The binding rate must also be faster than internalization or else a large fraction of the surface will not be saturated. Assuming a pseudo-steady state, the fraction of antibody bound on the cell surface is:

$$[Ag] \underset{k_{off}}{\overset{\overset{k_{on}[Ab]_{surf}}{\rightarrow}}{\leftarrow}} [B] \overset{k_e}{\rightarrow} [I]$$
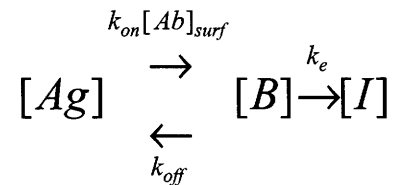
$$\frac{[B]}{[Ag]_0} = \frac{[Ab]_{surf}}{[Ab]_{surf} + \dfrac{k_e + k_{off}}{k_{on}}}$$

For low affinity antibodies, this simplifies to:

$$\frac{[B]}{[Ag]_0} = \frac{[Ab]_{surf}}{[Ab]_{surf} + K_d}$$

For slow binding antibodies, this is:

$$\frac{[B]}{[Ag]_0} = \frac{k_{on}[Ab]_{surf}}{k_{on}[Ab]_{surf} + k_e}$$

c. General Moduli
i. Thiele Modulus

The Thiele modulus has been derived for both high and low affinity cases, and analytical solutions have been provided where possible. A more general presentation of the Thiele modulus can be presented that simplifies to the two cases. Starting with the dimensionless Thiele modulus equation:

222

$$0 = \nabla^2 Ab - \phi^2 \left[\frac{Ab}{\left(Ab + K_d' \Big/ [Ab]_{surf} \right)} \right]$$

where $\quad K_d' \equiv \dfrac{k_e + k_{off}}{k_{on}} \qquad$ and $\qquad \phi^2 \equiv \left(\dfrac{k_e R^2 \left([Ag] \Big/ \varepsilon \right)}{D[Ab]_{surf}} \right)$

To simplify to the general case, it will be assumed that the dissociation rate is faster than internalization. This assumption is generally useful for the following reasons. For most antibodies, the k_{on} rate is very fast (e.g. 10^5 /M/s). As will be shown below, for the low affinity case to be relevant, the K_d' term must be larger than the $[Ab]_{surf}$ term. This requires either a fast dissociation rate or a fast endocytosis rate. Given that this time scale often needs to be less than a couple hours, endocytosis rates in this range are rare. For example, with a 1 nM surface concentration, the endocytosis rate must be less than 2 hrs in order in order to affect the result. Therefore, it is more common for the dissociation rate to be faster than the endocytosis rate when this term is important.

Assuming: $\qquad K_d' = \dfrac{k_{off}}{k_{on}} = K_d$

$$0 = \nabla^2 Ab - \left(\frac{k_e R^2 \left([Ag] \Big/ \varepsilon \right)}{D\left([Ab]_{surf} + K_d \Big/ Ab \right)} \right)$$

Although the K_d term contains the dimensionless antibody concentration, Ab, which changes with radius, this parameter is scaled such that it is order of magnitude 1. Therefore, the general Thiele modulus is written:

$$\phi^2 \equiv \frac{k_e R^2 \left([Ag] \Big/ \varepsilon \right)}{D\left([Ab]_{surf} + K_d \right)}$$

If $[Ab]_{surf}$ is larger than K_d, the modulus simplifies to the high affinity case. If K_d is greater than the surface concentration, it simplifies to the low affinity case. The Ab in the low affinity case makes the scaling parameter a first order Thiele modulus.

ii. Clearance Modulus

A general clearance modulus can be defined by linearizing the binding isotherm in order to obtain a scaled mass balance. Although this is not rigorously valid, the limiting cases collapse to the above derived high and low affinity case:

$$\frac{[B]}{[Ag]_0} = \frac{[Ab]/\varepsilon}{[Ab]/\varepsilon + K_d}$$

$$\frac{\partial[Ab]}{\partial t} = D\nabla^2[Ab] - \frac{\partial[B]}{\partial t} \quad \text{where} \quad [B] = \frac{[Ab]}{[Ab]/\varepsilon + K_d}\left([Ag]/\varepsilon\right)$$

For the linear binding isotherm where $K_d \gg [Ab]/\varepsilon$, the solution holds exactly. If the term in the denominator is treated as a constant $[Ab]_{surf}$, the change in $[Ab]$ becomes linear to a change in $[B]$. (The same analysis can be carried out without this assumption, but the scaled diffusion becomes more complicated with no change in the limiting behavior.) Ignoring catabolism as before:

$$\frac{\partial[B]}{\partial t} \approx \frac{\left([Ag]/\varepsilon\right)}{[Ab]_{surf} + K_d}\frac{\partial[Ab]}{\partial t} \quad \text{which plugging in:}$$

$$\frac{\partial[Ab]}{\partial t} = D\nabla^2[Ab] - \left(\frac{\left([Ag]/\varepsilon\right)}{[Ab]_{surf} + K_d}\right)\frac{\partial[Ab]}{\partial t}$$

$$\frac{\partial[Ab]}{\partial t} = D\left(\frac{[Ab]_{surf} + K_d}{[Ab]_{surf} + K_d + \left([Ag]/\varepsilon\right)}\right)\nabla^2[Ab]$$

Therefore:

$$D_{scaled} = D\left(\frac{[Ab]_{surf} + K_d}{[Ab]_{surf} + K_d + \left([Ag]/\varepsilon\right)}\right)$$

The limiting cases can be examined to show the behavior given different order of magnitudes between $[Ag]/\varepsilon$, K_d, and $[Ab]_{surf}$:

1) If $K_d \gg [Ag]/\varepsilon$: $D_{scaled} = D$ since binding is negligible

2) If $[Ab]_{surf} \gg [Ag]/\varepsilon$: $D_{scaled} = D$ since binding has a negligible effect on $[Ab]$

3) If $[Ag]/\varepsilon \gg [Ab]_{surf} \gg K_d$: $D_{scaled} = \dfrac{[Ab]_{surf}}{\left([Ag]\big/\varepsilon\right)}D$ as shown in shrinking core derivations

4) If $[Ag]/\varepsilon \gg K_d \gg [Ab]_{surf}$: $D_{scaled} = \dfrac{K_d}{\left([Ag]\big/\varepsilon\right)}D$ as shown in low affinity derivations

The latter two scenarios are prevalent in most tumor targeting scenarios due to antigen concentrations typically in the micromolar range. Dissociation constants are usually low nanomolar, making scenario 1 unlikely, and the low Biot number causes $[Ab]_{surf}$ values that are 100-1000 fold below the plasma concentration. With plasma doses in the nanomolar to low micromolar range, $[Ab]_{surf}$ values make scenario 2 unlikely.

Given the above 'correction' of the diffusion coefficient for binding, the general clearance modulus can be presented as follows:

$$\frac{\partial[Ab]}{\partial t} = D\left(\frac{[Ab]_{surf} + K_d}{[Ab]_{surf} + K_d + \left([Ag]\big/\varepsilon\right)}\right)\nabla^2[Ab]$$

Assuming $[Ag]/\varepsilon \gg K_d$ and $[Ab]_{surf}$:

$$\frac{\partial[Ab]}{\partial t} = D\left(\frac{[Ab]_{surf} + K_d}{\left([Ag]\big/\varepsilon\right)}\right)\nabla^2[Ab]$$

Normalizing:

$$\frac{\partial Ab}{\partial \tau} = \frac{D\left([Ab]_{surf} + K_d\right)\left(\dfrac{A}{k_\alpha} + \dfrac{B}{k_\beta}\right)}{R^2\left([Ag]\big/\varepsilon\right)}\nabla^2 Ab \qquad \text{where} \quad \tau \equiv \frac{t}{\left(\dfrac{A}{k_\alpha} + \dfrac{B}{k_\beta}\right)}$$

$$\left(\frac{R^2\left([Ag]/\varepsilon\right)}{D\left([Ab]_{surf} + K_d\right)\left(\dfrac{A}{k_\alpha} + \dfrac{B}{k_\beta}\right)} \right) = \frac{\nabla^2 Ab}{\left(\dfrac{\partial Ab}{\partial \tau}\right)} = \frac{diffusive \quad gradient}{temporal \quad gradient}$$

If the general clearance scaling parameter on the left is less than one, then the diffusive gradients over the distance R are less than the gradients in time. Consequently, the antibody will reach this distance. If $[Ab]_{surf}$ is greater than K_d, antibody will saturate antigen to radius R. If K_d is greater than $[Ab]_{surf}$, antibody will be able to dissociate and diffuse to the distance R, although the dose is not large enough to saturate antigen to this distance. The distance R is the maximum size of a micrometastasis or the outer radius of Krogh cylinder. $[Ab]_{surf}$ depends on the Biot number for vascularized tumors and on the normal tissue concentration for micrometastases.

d. Conceptual Viewpoints

i. Equilibrium Viewpoint

The general Thiele and Clearance modulus have been derived rigorously for high and low affinity cases, and they are scaled above to generate a smooth transition between the two scenarios. Conceptually, this is justified, since the binding isotherm makes a smooth transition from the linear binding regime, where the fraction of antigen bound is proportional to the antibody concentration, to the saturation regime, where the fraction of antigen bound is independent of the antibody concentration. A conceptual argument can be made where the low affinity cases are equivalent to the high affinity scenario scaled by the maximum fraction of antigen bound at equilibrium:

$$\phi^2_{general} = \frac{k_e R^2\left([Ag]/\varepsilon\right)\left(\dfrac{[Ab]_{surf}}{[Ab]_{surf} + K_d}\right)}{D[Ab]_{surf}} = \frac{k_e R^2\left([Ag]/\varepsilon\right)}{D\left([Ab]_{surf} + [K_d]\right)}$$

$$\Gamma_{general} = \frac{R^2\left([Ag]/\varepsilon\right)\left(\dfrac{[Ab]_{surf}}{[Ab]_{surf} + K_d}\right)}{D[Ab]_{surf}\left(\dfrac{A}{k_\alpha} + \dfrac{B}{k_\beta}\right)} = \frac{R^2\left([Ag]/\varepsilon\right)}{D\left([Ab]_{surf} + K_d\right)\left(\dfrac{A}{k_\alpha} + \dfrac{B}{k_\beta}\right)}$$

It is important to note that while this describes the distance antibody penetrates into the tumor, the fraction of antigen on the surface of the targeted cells differs greatly between the saturation and

linear binding regimes. If $[Ab]_{surf}$ is greater than K_d (saturation regime), the each cell layer will be saturated as the antibody front penetrates deeper into the tumor. If K_d is greater than $[Ab]_{surf}$, not all of the binding sites will be filled, since this is a sub-saturating dose (linear regime). A portion of the antibody remains unbound and is able to diffuse deeper into the tissue. The actual fraction bound is still dependent on the dose.

ii. Dynamic Viewpoint

The above presentation looks at low affinity targeting from an equilibrium standpoint. For the Thiele modulus scenario, catabolism in the tissue is lowered because not all of the internalized antigen is bound to antibody. For the clearance modulus case, it is actually a dynamic process for low affinity antibodies, since the binding rate is so rapid. Another way to conceptually picture this is the low affinity antibody making several 'jumps' through the tissue. The length of each of these 'jumps' is described by the binding modulus, since this determines the distance the antibody will diffuse prior to binding. The total number of 'jumps' depends on the time scale of interest and the dissociation rate. If the dissociation time is roughly 15 minutes, an antibody on average will make 4 'jumps' in an hour. This can be described mathematically:

$$\text{Penetration time} = (\text{\# jumps to R})(\text{time per jump}) = \frac{k_{on}\left(\frac{[Ag]}{\varepsilon}\right)R^2}{D}\left(\frac{1}{k_{off}}\right) = \frac{\left(\frac{[Ag]}{\varepsilon}\right)R^2}{D \cdot K_d}$$

Notice that it is not the intrinsic antibody affinity that determines the penetration. The antibody must be able to completely dissociate from the cell surface to diffuse deeper into the tissue, so it is the effective binding affinity that determines uptake. Unfortunately, valency cannot be used to increase binding while still maintaining high penetration of a low intrinsic affinity antibody.

Slow binding antibodies essentially make one large 'leap' into the tissue since they do not dissociate after binding. There penetration is sufficiently described by the binding modulus.

A.9   Buckingham Pi Analysis

The above dimensional analysis yields a variety of dimensionless groups used to understand the transport of antibodies in tumor tissue. Due to the non-linear partial differential equations involved, dimensional analysis is a useful tool to understand the behavior where closed form analytical solutions are not possible. In order to formalize the number of linearly independent dimensionless groups that describe this behavior, the Buckingham Pi Theorem can be used.

The Buckingham Pi Theorem states that given n variables (e.g. D, k_e, R, etc.) that describe a problem that are formed from k fundamental dimensions (e.g. length, time, etc.), the number of linearly independent dimensionless groups that describe the problem (Pi groups's) is $(n-k)$.

The three fundamental dimensions are length, time, and concentration. The mole is really the fundamental dimension, but since it is always lumped per length cubed, concentration will be used. The eleven variables are k_{on}, k_{off}, D, R, ([Ag]/ε), [Ab], R_{cap}, k_e, $t_{clearance}$, P, t_{sample}. For simplicity, ε is lumped with the antigen concentration, since comparisons between antibody and antigen concentrations are always done with both on an interstitial or both on an overall concentration basis. The clearance parameters A, B, α, and β are all lumped into the clearance time, where $t_{clearance} \equiv \left(\dfrac{A}{k_\alpha} + \dfrac{B}{k_\beta} \right)$; if specific inferences were made between the alpha and beta phase of clearance, then these variables would have to be treated separately. The variable t_{sample} is introduced to capture effects that depend on the observation time. For example, the distribution of an IgG will differ depending on whether it is sampled 1 hour or 3 days after the dose is given. Together, the theorem indicates there are 8 dimensionless groups that describe the behavior of the system.

#	Name	Group	Param.	Ratio
1	Thiele modulus	$\dfrac{k_e R^2 \left([Ag] / \varepsilon \right)}{D[Ab]}$	k_e, R, D	$\dfrac{\text{Catabolism rate}}{\text{Penetration rate}}$
2	Clearance modulus	$\dfrac{R^2 \left([Ag] / \varepsilon \right)}{D[Ab] t_{clearance}}$	$t_{clearance}$	$\dfrac{\text{Clearance rate}}{\text{Penetration rate}}$
3	Biot number	$\dfrac{2PR_{cap}}{D}$	P	$\dfrac{\text{Extravasation rate}}{\text{Diffusion rate}}$
4	Low affinity number	$\dfrac{R^2 \left([Ag] / \varepsilon \right)}{D \cdot K_d \cdot t_{clearance}}$	k_{off}	$\dfrac{\text{Clearance rate}}{\text{Low affinity penetration rate}}$
5	Binding modulus	$\dfrac{k_{on} R^2 \left([Ag] / \varepsilon \right)}{D}$	k_{on}	$\dfrac{\text{Binding rate}}{\text{Diffusion rate}}$
6	Geometry ratio	$\dfrac{R}{R_{cap}}$	R_{cap}	$\dfrac{\text{Tumor volume}}{\text{Capillary volume}}$
7	Saturation number	$\dfrac{\left([Ag] / \varepsilon \right)}{[Ab]}$	[Ab], [Ag]	$\dfrac{\text{Antigen conc.}}{\text{Antibody conc.}}$
8	Sampling time ratio	$\dfrac{t_{sample}}{t_{clearance}}$	t_{sample}	$\dfrac{\text{Sampling time}}{\text{Clearance time}}$

Table A.1 - Buckingham Pi Analysis

A matrix with 11 columns representing the parameters and 8 rows representing the dimensionless groups with values equal to the exponent for each group has a rank of 8. This indicates that all the groups are linearly independent. Multiplying the matrix by a vector representing each of the fundamental dimensions gave a zero vector as the result, verifying that all the groups are dimensionless. As given in the theorem and shown below, these groups are not unique. However, all groups can be formed by a combination of this set of 8 groups.

The first five groups have been described explicitly in the dimensionless scaling. The other 3 have been used implicitly. For example, the geometry ratio was used to simplify the limits of integration by assuming that $R^2 \gg R_{cap}^2$, and it will be used later to define the tumor vascular surface area to tumor volume ratio. The saturation number was used when assuming the antigen concentration was greater than the dose, and a linear combination between 2, 4, and 7 gives the same assumption for K_d (i.e.

$[Ag]/\varepsilon \gg K_d$). Finally, the sampling ratio was used to set the limits of integration for the clearance modulus. It was implicitly assumed that $t_{sample} \gg t_{clearance}$ when the solutions were integrated to infinity, allowing adequate time for uptake.

A.10   Pretargeting Number

Although the groups above form the maximum number of linearly independent groups, other parameters may be important in different situations; for example the tumor size is important for surface effects (see the compartmental model with R_{tumor}), and blood flow, Q, is needed to show uptake is not flow limited (see Chapter 4). The groups are also not unique; for example the ratio of the clearance modulus and saturation number describes the competition between clearance and free diffusion for a non-binding antibody. One important group for pretargeting is the ratio of the Thiele modulus and clearance modulus:

$$\frac{\phi^2}{\Gamma} = k_e\left(\frac{A}{k_\alpha} + \frac{B}{k_\beta}\right) = \frac{\text{catabolism rate}}{\text{clearance rate}}$$

The behavior of the system is very different depending on this ratio. First, since both the clearance modulus and Thiele modulus must be less than unity for targeting to a given radius, the ratio describes which parameter is limiting. A small ratio indicates the antibody is cleared too rapidly to target more cells, and a large ratio indicates that catabolism in the tissue is the major barrier to uptake. The second issue is how the distribution changes after the maximum uptake in the tumor. If this ratio is large, catabolism occurs much more rapidly than clearance. As the plasma concentration drops, the antibody distal to the vessel is quickly degraded, whereas the supply from the capillary replenishes antibody near the vessel. The targeting radius will then shrink during clearance, given by the Thiele modulus with the dropping plasma antibody concentration. If the ratio is small, after reaching the maximum radius, the antibody rapidly clears from the plasma before it is degraded in the tissue. The turnover on the cells then occurs uniformly in the tissue. This second scenario is advantageous for pretargeting, since sufficient clearance from the plasma is required before administering a second dose. At this point, all the targeted cells will retain some antibody, whereas the first scenario only targets cells close to the vasculature. In fact, increasing the dose in this first scenario is not beneficial, since the extended waiting period required to allow for sufficient plasma clearance results in the same surface antibody concentration in the tumor when the secondary agent is delivered. Clearing agents may be useful in these scenarios to speed up clearance after targeting.

A.11   Solutions without Closed Forms

The spatial solutions given above ignore time by assuming steady state or integrating over a pseudo-steady state, and the compartmental model presented later ignores spatial distributions by examining the entire tumor as a single compartment. With problems that vary in both space and time, simple closed form analytical solutions generally do not exist. The equations governing transport of antibodies in tumors can be integrated numerically, or with certain assumptions, series solutions are possible. Because a computer is often needed for the series solution, numerical integration is usually preferred since no further assumptions are necessary. However, in certain instances, a series solution is useful, such as when fitting a diffusion coefficient. Other solutions are presented below to show the difficulty in obtaining analytical solutions and their limited utility. This is why numerical solutions and scaling analyses are primarily used in this thesis.

a.   Antibody Free Diffusion in a Sphere

The solution for uptake of a non-binding antibody in a sphere is useful for fitting a diffusion coefficient. Spheroids can be incubated with a non-binding variant, and the fluorescence signal within the spheroid can be followed over time. In order to utilize more common mathematical notation, some new variables are introduced in this section that are not present in the list of symbols. These will be defined the first time they are used.

i.   Finite Fourier Transform (FFT) Method

$$\frac{\partial [Ab]}{\partial t} = D \frac{1}{r^2} \frac{\partial}{\partial r} r^2 \frac{\partial [Ab]}{\partial r}$$ (Assuming no gradients in the phi or theta directions due to symmetry.)

$$\frac{\partial Ab}{\partial \tau} = \frac{1}{\lambda^2} \frac{\partial}{\partial \lambda} \lambda^2 \frac{\partial Ab}{\partial \lambda}$$ where $Ab = \dfrac{[Ab]}{[Ab]_{surf}}$, $\lambda = \dfrac{r}{R_{met}}$, and $\tau = \dfrac{tD}{R_{met}^2}$

Boundary conditions:

$$Ab(1,\tau) = 1 \qquad\qquad \frac{dAb}{d\lambda}(0,\tau) = 0 \qquad\qquad Ab(\lambda,0) = 0$$

The basis functions for this problem are(8):

$$\Phi_n(\lambda) = \sqrt{2} \frac{\sin(n\pi\lambda)}{\lambda}$$

Performing a finite Fourier transform (FFT) on the equation and boundary conditions:

$$Ab_n(\tau) = \int_0^1 \Phi_n(\lambda) Ab(\lambda,\tau) \lambda^2 d\lambda \qquad \text{where } \lambda^2 \text{ is the weighting factor}$$

The first term yields:

$$\int_0^1 \Phi_n(\lambda) \frac{dAb}{d\tau} \lambda^2 d\lambda = \frac{d}{d\tau} \int_0^1 \Phi_n(\lambda) Ab(\lambda,\tau) \lambda^2 d\lambda = \frac{dAb_n}{d\tau}$$

The second term yields:

$$\int_0^1 \Phi_n(\lambda) \left(\frac{1}{\lambda^2} \frac{d}{d\lambda} \lambda^2 \frac{dAb}{d\lambda} \right) \lambda^2 d\lambda$$

From Deen 4.6-6(8), the operator on Ab has $p = w = \lambda^2$ and $q = 0$.

Using 4.6-16:

$$\langle \ell, Ab, \Phi_n \rangle = \lambda^2 \left(\Phi_n \frac{dAb}{d\lambda} - Ab \frac{d\Phi_n}{d\lambda} \right) \Big|_0^1 - \lambda_n Ab_n \qquad \text{Note, to maintain consistency between Deen(8)}$$

and current notation, λ and λ_n are different terms.

$$= \left(-\lambda^2 Ab \frac{d\Phi_n}{d\lambda} \right) \Big|_0^1 - \lambda_n Ab_n = -\lambda^2 Ab \left(\sqrt{2} n\pi \frac{\cos(n\pi\lambda)}{\lambda} + \sqrt{2} \frac{-\sin(n\pi\lambda)}{\lambda^2} \right) \Big|_0^1 - \lambda_n Ab_n$$

$$= \left(-\lambda Ab\sqrt{2} n\pi \cos(n\pi\lambda) + Ab\sqrt{2} \sin(n\pi\lambda) \right) \Big|_0^1 - \lambda_n Ab_n$$

$$= \left(-\sqrt{2} n\pi \cos(n\pi) \right) - (n\pi)^2 Ab_n = -\sqrt{2} n\pi (-1)^n - (n\pi)^2 Ab_n$$

Substituting the transformed functions into the original equation:

$$\frac{dAb_n}{d\tau} = -\sqrt{2} n\pi (-1)^n - (n\pi)^2 Ab_n$$

$$\frac{dAb_n}{d\tau} + (n\pi)^2 Ab_n + \sqrt{2}n\pi(-1)^n = 0$$

The transformed boundary condition is:

$$Ab_n(0) = 0$$

Solving the first order differential equation in time using an integrating factor:

$$Ab_n = \frac{\int \exp\left((n\pi)^2 \tau\right)\left(-\sqrt{2}(-1)^n n\pi\right)d\tau + C_1}{\exp\left((n\pi)^2 \tau\right)}$$

$$Ab_n = \frac{\left(-\sqrt{2}(-1)^n\right)}{(n\pi)} + C_1 \exp\left(-(n\pi)^2 \tau\right)$$

Using $Ab_n(0) = 0$:

$$C_1 = \frac{\sqrt{2}(-1)^n}{(n\pi)}$$

$$Ab_n = \frac{\left(-\sqrt{2}(-1)^n\right)}{(n\pi)} + \frac{\sqrt{2}(-1)^n}{(n\pi)} \exp\left(-(n\pi)^2 \tau\right)$$

$$Ab_n = \frac{-\sqrt{2}(-1)^n}{(n\pi)}\left(1 - \exp\left(-(n\pi)^2 \tau\right)\right)$$

Plugging into the final solution:

$$Ab(\lambda, \tau) = \sum_{n=1}^{\infty} Ab_n(\tau)\Phi_n(\lambda)$$

$$Ab(\lambda, \tau) = -2\sum_{n=1}^{\infty} \frac{(-1)^n}{(n\pi)}\left(1 - \exp\left(-(n\pi)^2 \tau\right)\right)\frac{\sin(n\pi\lambda)}{\lambda}$$

Adding dimensions:

$$\frac{[Ab]}{[Ab]_{surf}} = \frac{-2R_{met}}{\pi \cdot r} \sum_{n=1}^{\infty} \frac{(-1)^n}{n} \left(1 - \exp\left(-\frac{Dn^2\pi^2}{R_{met}^2}t\right)\right) \sin\left(n\pi \frac{r}{R}\right)$$

Using the steady state solution:

$$\frac{[Ab]}{[Ab]_{surf}} = 1 + \frac{2R_{met}}{\pi \cdot r} \sum_{n=1}^{\infty} \frac{(-1)^n}{n} \exp\left(-\frac{Dn^2\pi^2}{R_{met}^2}t\right) \sin\left(n\pi \frac{r}{R}\right)$$

ii. Separation of Variables Method

The antibody concentration for free diffusion in a sphere can also be solved by the separation of variables. Agreement between the results verifies the solution.

$$\frac{\partial[Ab]}{\partial t} = D \frac{1}{r^2} \frac{\partial}{\partial r}\left(r^2 \frac{\partial[Ab]}{\partial r}\right)$$

Making the substitution u = [Ab]r

$$\frac{1}{r}\frac{\partial u}{\partial t} = D \frac{1}{r^2} \frac{\partial}{\partial r}\left(r^2\left(\frac{-u}{r^2} + \frac{1}{r}\frac{\partial u}{\partial r}\right)\right)$$

$$\frac{\partial u}{\partial t} = D \frac{1}{r} \frac{\partial}{\partial r}\left(-u + r\frac{\partial u}{\partial r}\right)$$

$$\frac{\partial u}{\partial t} = D \frac{1}{r}\left(-\frac{\partial u}{\partial r} + r\frac{\partial^2 u}{\partial r^2} + \frac{\partial u}{\partial r}\right)$$

$$\frac{\partial u}{\partial t} = D \frac{\partial^2 u}{\partial r^2}$$ which can be evaluated as free diffusion in a planar sheet.

For the non-steady state solution, the equation is separable. The variable x will be used for the solution in the planar case. A solution is assumed of the form(12):

$$u(x,t) = X(x)T(t)$$

Substituting into the original equation:

$$X\frac{\partial T}{\partial t} = DT\frac{\partial^2 X}{\partial x^2}$$

$$\frac{1}{T}\frac{\partial T}{\partial t} = \frac{D}{X}\frac{\partial^2 X}{\partial x^2} = -\lambda_e^2 D$$ Both sides must be equal to a constant $-\lambda_e^2 D$, where λ_e are the

eigenvalues, yielding two differential equations that must be solved:

$$\frac{1}{T}\frac{dT}{dt} = -\lambda_e^2 D$$

This is a simple 1st order differential equation with solutions of the form:

$$T = \exp\left(-\lambda_e^2 Dt\right)$$

The equation in the radial direction is:

$$\frac{1}{X}\frac{d^2 X}{dx^2} = -\lambda_e^2$$

This is a 2nd order linear differential equation with complex roots having no real parts(12). Solutions are of the form:

$$X = A_m \sin\lambda_m x + B_m \cos\lambda_m x$$ where A_m and B_m are integration constants with λ_m eigenvalues

There is an infinite number of eigenvalues, so the most general form of the solution is:

$$u = \sum_{m=1}^{\infty} \exp\left(-\lambda_m^2 Dt\right)\left(A_m \sin\lambda_m x + B_m \cos\lambda_m x\right)$$

All that remains is to evaluate the constants using the boundary conditions. These conditions are:

$$u = [Ab]r = 0 \quad x = 0 \quad t > 0$$ (In the spherical case, if [Ab] is finite at the center of the spheroid, u = 0 when r = 0)

$$u = [Ab]_{surf} R = u_{surf} \quad x = R \quad t > 0$$

$$u = 0 \quad 0 < x < R \quad t = 0$$

These boundary conditions are non-homogenous. Since the solution will settle down to a steady state after infinite time, the answer will be broken down into the sum of the steady state solution and the transient solution. The steady state solution is subtracted from the original problem, yielding homogenous boundary conditions for the transient problem(12).

For the steady state solution:

$$\frac{d^2 X}{dx^2} = 0 \qquad \text{at long times (steady state)}$$

Boundary conditions:

$$X(0) = 0$$
$$X(R) = u_{surf}$$

$$X(x) = u_{surf}\left(\frac{x}{R}\right) \qquad \text{which is the steady state solution}$$

Breaking the solution into the steady state and transient parts:

$$u(x,t) = X(x) + W(x,t) \qquad \text{where} \quad W(x,t) \text{ is the transient solution.}$$

Substituting in:

$$\frac{\partial u}{\partial t} = D\frac{\partial^2 u}{\partial x^2}$$

$$\frac{\partial}{\partial t}[X(x) + W(x,t)] = D\frac{\partial^2}{\partial x^2}[X(x) + W(x,t)]$$

Since $\dfrac{\partial}{\partial t}[X(x)] = 0$ and $\dfrac{\partial^2}{\partial x^2}[X(x)] = 0$ at steady state:

$$\frac{\partial}{\partial t}[W(x,t)] = D\frac{\partial^2}{\partial x^2}[W(x,t)]$$

This transient problem can be solved using homogenous boundary conditions and subtracting the steady state solution from the initial condition. Since the initial condition was [Ab] = 0 for 0 < x < R, the initial condition for the transient solution is just the negative of the steady state solution.

Solving:

$$\frac{\partial W}{\partial t} = D\frac{\partial^2 W}{\partial x^2}$$

Boundary conditions:

1) $W = [Ab]r = 0 \quad x = 0 \quad t > 0$

2) $W = 0 \quad x = R \quad t > 0$

3) $u = -u_{surf}\left(\dfrac{x}{R}\right) \quad 0 < x < R \quad t = 0$ zero concentration when added to steady state

With homogenous boundary conditions, the problem is solved, with the general solution:

$$W = \sum_{m=1}^{\infty} \exp\left(-\lambda_m{}^2 Dt\right)\left(A_m \sin \lambda_m x + B_m \cos \lambda_m x\right)$$

Using boundary condition 1:

$$0 = \sum_{m=1}^{\infty} \exp\left(-\lambda_m{}^2 Dt\right)\left(A_m \sin(0) + B_m \cos(0)\right)$$

$$B_m = 0$$

$$W = \sum_{m=1}^{\infty} \exp\left(-\lambda_m{}^2 Dt\right)\left(A_m \sin \lambda_m x\right)$$

Using boundary condition 2:

$$0 = \sum_{m=1}^{\infty} \exp\left(-\lambda_m{}^2 Dt\right)\left(A_m \sin \lambda_m R\right)$$

$$\lambda_m = \frac{m\pi}{R}$$

$$W = \sum_{m=1}^{\infty} \exp\left(-\frac{m^2\pi^2 D}{R^2}t\right)\left(A_m \sin\frac{m\pi x}{R}\right)$$

Using boundary condition 3:

$$-u_{surf}\left(\frac{x}{R}\right) = \sum_{m=1}^{\infty} A_m \sin\frac{m\pi x}{R}$$

The coefficients to the Fourier sine series can be found using the Euler-Fourier formula(12):

$$A_m = \frac{2}{R}\int_0^R -u_{surf}\left(\frac{x}{R}\right)\sin\frac{m\pi x}{R}dx \qquad \text{where m is a positive integer constant}$$

$$A_m = \frac{-2u_{surf}}{R^2}\left(\frac{\sin\dfrac{m\pi x}{R}}{\left(\dfrac{m\pi}{R}\right)^2} - \frac{x\cdot\cos\dfrac{m\pi x}{R}}{\dfrac{m\pi}{R}}\right)\Bigg|_0^R$$

$$A_m = \frac{2u_{surf}}{m\pi}\cos m\pi$$

Substituting into the transient solution:

$$W = u_{surf}\frac{2}{\pi}\sum_{m=1}^{\infty}\exp\left(-\frac{m^2\pi^2 D}{R^2}t\right)\left(\frac{\cos m\pi}{m}\right)\left(\sin\frac{m\pi x}{R}\right)$$

$$W = u_{surf}\frac{2}{\pi}\sum_{m=1}^{\infty}\left(\frac{(-1)^m}{m}\right)\exp\left(-\frac{m^2\pi^2 D}{R^2}t\right)\left(\sin\frac{m\pi x}{R}\right)$$

And combining the steady state and transient solutions for the general solution:

$$u(x,t) = X(x) + W(x,t)$$

$$u(x,t) = u_{surf}\left(\frac{x}{R}\right) + u_{surf}\frac{2}{\pi}\sum_{m=1}^{\infty}\left(\frac{(-1)^m}{m}\right)\exp\left(-\frac{m^2\pi^2 D}{R^2}t\right)\left(\sin\frac{m\pi x}{R}\right)$$

Converting back to spherical geometry:

238

$$[Ab]r = [Ab]_{surf} R\left(\frac{r}{R}\right) + [Ab]_{surf} R\frac{2}{\pi}\sum_{m=1}^{\infty}\left(\frac{(-1)^m}{m}\right)\exp\left(-\frac{m^2\pi^2 D}{R^2}t\right)\left(\sin m\pi \frac{r}{R}\right)$$

$$\frac{[Ab]}{[Ab]_{surf}} = 1 + \frac{2R}{\pi r}\sum_{m=1}^{\infty}\left(\frac{(-1)^m}{m}\right)\exp\left(-\frac{Dm^2\pi^2 t}{R^2}\right)\left(\sin m\pi \frac{r}{R}\right)$$

This is in agreement with the FFT method.

iii. Area and Volume Integrals

The area and volume integrals of the above solution are useful for comparison with experimental data. It is easier to measure the total amount of fluorescently tagged antibody in a spheroid or the total fluorescence signal in a confocal image slice rather than fitting radial concentration gradients over time. This averages the radial gradients to smooth the data. The area integral is given as A_t, and the volume integral, or total mass, is given as M_t.

$$A_t = \int_0^R [Ab](2\pi r)dr$$

$$A_t = \int_0^R\left([Ab]_{surf} + \frac{2R[Ab]_{surf}}{\pi r}\sum_{m=1}^{\infty}\left(\frac{(-1)^m}{m}\right)\exp\left(-\frac{Dm^2\pi^2 t}{R^2}\right)\left(\sin\frac{m\pi r}{R}\right)\right)(2\pi r)dr$$

Integrating the first term:

$$A_t = [Ab]_{surf}\pi R^2 + \int_0^R (2\pi r)\left(\frac{2R[Ab]_{surf}}{\pi r}\sum_{m=1}^{\infty}\left(\frac{(-1)^m}{m}\right)\exp\left(-\frac{Dm^2\pi^2 t}{R^2}\right)\left(\sin\frac{m\pi r}{R}\right)\right)dr$$

Integrating term by term:

$$A_t = [Ab]_{surf}\pi R^2 + 4R[Ab]_{surf}\sum_{m=1}^{\infty}\left(\frac{(-1)^m}{m}\right)\exp\left(-\frac{Dm^2\pi^2 t}{R^2}\right)\int_0^R\left(\sin\frac{m\pi r}{R}\right)dr$$

$$A_t = [Ab]_{surf}\pi R^2 + 4R[Ab]_{surf}\sum_{m=1}^{\infty}\left(\frac{(-1)^m}{m}\right)\exp\left(-\frac{Dm^2\pi^2 t}{R^2}\right)\left(\frac{-\cos\frac{m\pi r}{R}}{\frac{m\pi}{R}}\bigg|_0^R\right)$$

$$A_t = [Ab]_{surf} \pi R^2 - \frac{4R^2[Ab]_{surf}}{\pi} \sum_{m=1}^{\infty} \left(\frac{(-1)^m}{m^2} \right) \exp\left(-\frac{Dm^2\pi^2 t}{R^2} \right) (\cos m\pi - 1)$$

Normalizing to the area intensity at infinite time:

$$A_\infty = \int_0^R [Ab]_{surf} (2\pi r) dr$$

$$A_\infty = [Ab]_{surf} \pi R^2$$

Together:

$$\frac{A_t}{A_\infty} = 1 - \frac{4}{\pi^2} \sum_{m=1}^{\infty} \left(\frac{(-1)^m}{m^2} \right) \exp\left(-\frac{Dm^2\pi^2 t}{R^2} \right) (\cos m\pi - 1)$$

Because the final term alternates between 0 and -2, a more computationally efficient way of evaluating the series is:

$$\frac{A_t}{A_\infty} = 1 - \frac{8}{\pi^2} \sum_{n=1}^{\infty} \left(\frac{1}{(2n-1)^2} \right) \exp\left(-\frac{D\pi^2 t}{R^2} (2n-1)^2 \right)$$

The total mass diffusing into the sphere is:

$$M_t = \int_0^R [Ab] (4\pi r^2) dr$$

$$M_t = \int_0^R [Ab]_{surf} (4\pi r^2) dr + \int_0^R (8r) \left(R[Ab]_{surf} \sum_{m=1}^{\infty} \left(\frac{(-1)^m}{m} \right) \exp\left(-\frac{Dm^2\pi^2 t}{R^2} \right) \left(\sin\frac{m\pi r}{R} \right) \right) dr$$

Integrating term by term:

$$M_t = [Ab]_{surf} \frac{4}{3} \pi R^3 + 8R[Ab]_{surf} \sum_{m=1}^{\infty} \left(\frac{(-1)^m}{m} \right) \exp\left(-\frac{Dm^2\pi^2 t}{R^2} \right) \int_0^R (r) \sin\frac{m\pi r}{R} dr$$

$$M_t = [Ab]_{surf} \frac{4}{3} \pi R^3 + 8R[Ab]_{surf} \sum_{m=1}^{\infty} \left(\frac{(-1)^m}{m} \right) \exp\left(-\frac{Dm^2\pi^2 t}{R^2} \right) \left(\frac{\sin\frac{m\pi r}{R}}{\left(\frac{m\pi}{R}\right)^2} - \frac{r\cdot\cos\frac{m\pi r}{R}}{\frac{m\pi}{R}} \right) \Bigg|_0^R$$

$$M_t = [Ab]_{surf} \frac{4}{3} \pi R^3 - 8R^3[Ab]_{surf} \sum_{m=1}^{\infty} \left(\frac{(-1)^m}{m} \right) \exp\left(-\frac{Dm^2\pi^2 t}{R^2} \right) \left(\frac{\cos m\pi}{m\pi} \right)$$

Evaluating total mass after infinite time:

$$M_\infty = \int_0^R [Ab]_{surf}\left(4\pi r^2\right) dr$$

$$M_\infty = [Ab]_{surf} \frac{4}{3} \pi R^3$$

Normalizing concentration:

$$\frac{M_t}{M_\infty} = 1 - \frac{6}{\pi^2} \sum_{n=1}^{\infty} \left(\frac{1}{n^2} \right) \exp\left(-\frac{Dn^2\pi^2 t}{R^2} \right) \qquad \text{in agreement with the published formula(11).}$$

b. Low Affinity Antibody in a Micrometastasis with No Catabolism

As shown above for low affinity binders, the effective diffusion coefficient is:

$$D_{scaled} = \frac{D}{1 + \frac{\left(\left[Ag\right]/\varepsilon\right)}{K_d}} \approx \frac{K_d}{\left(\left[Ag\right]/\varepsilon\right)} D$$

Using the solution for free diffusion in a sphere with no initial concentration and a variable surface concentration(11):

$$[Ab] = \frac{-2D_{scaled}}{rR} \sum_{n=1}^{\infty} (-1)^n \exp\left(\frac{-D_{scaled}n^2\pi^2 t}{R^2} \right) n\pi \sin\left(\frac{n\pi r}{R} \right) \int_0^t \exp\left(\frac{D_{scaled}n^2\pi^2 \tau}{R^2} \right) \varepsilon[Ab]_n(\tau) d\tau$$

The overall concentration in the normal tissue surrounding a micrometastasis is given by:

$$[Ab]_n = [Ab]_{plasma,0}\left(\kappa\left(\frac{Ae^{-k_\alpha t}}{\gamma - k_\alpha} + \frac{Be^{-k_\beta t}}{\gamma - k_\beta}\right) - \kappa\left(\frac{A}{\gamma - k_\alpha} + \frac{B}{\gamma - k_\beta}\right)e^{-\gamma t}\right) = [Ab]_{surf}$$

To simplify the notation, $\chi \equiv \dfrac{Dn^2\pi^2}{R^2}$. Performing the integration:

$$\int_0^t \varepsilon[Ab]_n \exp(\chi\tau)d\tau$$

$$= \varepsilon[Ab]_{plasma,0}\left\{A\kappa\left(\frac{\exp((\chi - \gamma)t) - 1}{(k_\alpha - \gamma)(\chi - \gamma)} - \frac{\exp((\chi - k_\alpha)t) - 1}{(k_\alpha - \gamma)(\chi - k_\alpha)}\right) + B\kappa\left(\frac{\exp((\chi - \gamma)t) - 1}{(k_\beta - \gamma)(\chi - \gamma)} - \frac{\exp((\chi - k_\beta)t) - 1}{(k_\beta - \gamma)(\chi - k_\beta)}\right)\right\}$$

The final solution for transient diffusion of antibody into a metastasis with no catabolism is:

$$[Ab] = \frac{-2K_dD}{rR\left([Ag]/\varepsilon\right)}\sum_{n=1}^\infty (-1)^n \exp\left(\frac{-K_dDn^2\pi^2t}{R^2\left([Ag]/\varepsilon\right)}\right)n\pi\sin\left(\frac{n\pi r}{R}\right)\varepsilon[Ab]_{plasma,0}$$

$$\left\{A\kappa\left(\frac{\exp((\chi - \gamma)t) - 1}{(k_\alpha - \gamma)(\chi - \gamma)} - \frac{\exp((\chi - k_\alpha)t) - 1}{(k_\alpha - \gamma)(\chi - k_\alpha)}\right) + B\kappa\left(\frac{\exp((\chi - \gamma)t) - 1}{(k_\beta - \gamma)(\chi - \gamma)} - \frac{\exp((\chi - k_\beta)t) - 1}{(k_\beta - \gamma)(\chi - k_\beta)}\right)\right\}$$

c. Uptake of a Low Affinity Antibody in a Cylindrical Annulus with Constant Plasma Concentration

The following result is adapted directly from the published solution for diffusion in a cylindrical annulus(11) and used to illustrate the complexity of this type of analytical solution. Note that both plasma clearance and antibody catabolism have to be ignored to obtain this solution.

Boundary condition 1 at the capillary wall:

$$-D_{scaled}\frac{d[Ab]}{dr}\bigg|_{r=R_{cap}} = P\left(\varepsilon \cdot [Ab]_{plasma} - [Ab]\right)$$

and $D_{scaled} = \dfrac{D}{1 + \dfrac{\left([Ag]/\varepsilon\right)}{K_d}} \approx \dfrac{K_d}{\left([Ag]/\varepsilon\right)} D$

Using the notation provided in Crank(11):

$k_1 = 0$, $k_2 = -D_{scaled}$ $k_3 = P$ $k_4 = P[Ab]_{plasma}\varepsilon$

Boundary condition 2 at r = R:

$\left. \dfrac{d[Ab]}{dr} \right|_{r=R} = 0$

Using the notation provided in Crank:

$k_1' = k_3' = k_4' = 0$ and $k_2' = 1$

The concentration profile given the above boundary conditions, no initial antibody in the cylinder, and constant plasma concentration [Ab]$_{plasma}$ is:

$$[Ab] = [Ab]_{plasma}\,\varepsilon - \pi \sum_{n=1}^{\infty} \exp\left(-D_{scaled}\,\alpha_n^2 t\right) F(\alpha_n) C_0(r;\alpha_n)\left[-P[Ab]_{plasma}\,\varepsilon\alpha_n J_1(R\alpha_n)\right]$$

where:

$$F(\alpha_n) = \dfrac{-\alpha_n J_1(R\alpha_n)}{\left(\alpha_n J_1(R\alpha_n)\right)^2\left(P^2 + D_{scaled}^{\;2}\alpha_n^2\right) - \left(PJ_0(R_{cap}\alpha_n) + D_{scaled}\alpha_n J_1(R_{cap}\alpha_n)\right)^2\left(\alpha_n^2\right)}$$

$$C_0(r;\alpha_n) = J_0(r\alpha_n)\left\{PY_0(R_{cap}\alpha_n) + D_{scaled}\,\alpha_n Y_1(R_{cap}\alpha_n)\right\} - Y_0(r\alpha_n)\left\{PJ_0(R_{cap}\alpha_n) + D_{scaled}\,\alpha_n J_1(R_{cap}\alpha_n)\right\}$$

and α_n s are the positive roots of:

$$\left\{PJ_0(R_{cap}\alpha) + D_{scaled}\alpha J_1(R_{cap}\alpha)\right\}\left\{-\alpha Y_1(R\alpha)\right\} - \left\{-\alpha J_1(R\alpha)\right\}\left\{PY_0(R_{cap}\alpha_n) + D_{scaled}\alpha Y_1(R_{cap}\alpha)\right\} = 0$$

For comparison with this solution, the realistic case of reaction in the capillary or biexponential decay from the plasma yield a more complex problem. The reason this solution contains this number of terms is both zero and first order Bessel functions of the first and second kind are required due to the

243

cylindrical annulus, and the Robin boundary condition requires the eigenvalues to be calculated numerically for each case. In comparison, the numerical result can be carried out quite rapidly without the need for assumptions as to the linearity of binding and internalization.

d. Surface Loss of a Low Affinity Antibody in a Sphere

Although the analytical solutions for various cases do not yield simple solutions, they are valuable in verifying the scaling analyses. A final analytical solution is useful for validating the functional form of antibody loss from the surface of a micrometastasis or solid tumor. The problem will be formulated as a sphere saturated with antibody with a zero concentration at the surface.

Starting with the dimensionless equation:

$$\frac{\partial Ab}{\partial \tau} = \frac{1}{\lambda^2}\frac{\partial}{\partial \lambda}\lambda^2\frac{\partial Ab}{\partial \lambda} \qquad \text{where } Ab \equiv \frac{[Ab]}{[Ag]},\ \lambda \equiv \frac{r}{R},\text{ and } \tau \equiv \frac{t \cdot D_{scaled}}{R^2}$$

Boundary and initial conditions:

$$Ab(1,t) = 0, \qquad \frac{\lambda Ab}{\partial \lambda}(0,t) = 0, \qquad Ab(\lambda,0) = 1$$

The basis functions for a Dirichlet boundary condition in spherical coordinates are(8):

$$\Phi_n(\lambda) = \sqrt{2}\frac{\sin(n\pi\lambda)}{\lambda}$$

Transforming the second order operator in the differential equation:

$$\lambda^2\left(\Phi_n\frac{dAb_n}{d\lambda} - Ab_n\frac{d\Phi_n}{d\lambda}\right)\Bigg|_0^1 - \Lambda_n^2 Ab_n \quad \text{where } \Lambda_n = n\pi$$

$$= -\lambda^2 Ab_n\left(\frac{d\Phi_n}{d\lambda}\right)\Bigg|_0^1 - \Lambda_n^2 Ab_n = -\lambda^2 Ab_n\left(\sqrt{2}n\pi\frac{\cos(n\pi\lambda)}{\lambda} + \sqrt{2}\frac{-\sin(n\pi\lambda)}{\lambda^2}\right)\Bigg|_0^1 - \Lambda_n^2 Ab_n$$

$$= -(n\pi)^2 Ab_n$$

The transformed equation is then:

244

$$\frac{dAb_n}{d\tau} = -(n\pi)^2 Ab_n$$

Transforming the initial condition:

$$Ab_n = \int_{\lambda=0}^{\lambda=1} \Phi_n(\lambda)Ab(\lambda,\tau)\lambda^2 d\lambda$$

$$Ab_n(0) = \int_0^1 \sqrt{2}\frac{\sin(n\pi\lambda)}{\lambda}(1)\lambda^2 d\lambda \qquad \text{where } Ab = 1 \text{ for all } \lambda \text{ at } \tau = 0$$

$$Ab_n(0) = \sqrt{2}\left(\frac{1}{(n\pi)^2}\sin(n\pi\lambda) - \frac{\lambda}{(n\pi)}\cos(n\pi\lambda)\right)\Bigg|_0^1$$

$$Ab_n(0) = \frac{-\sqrt{2}(-1)^n}{n\pi}$$

Solving the transformed equation:

$$\frac{dAb_n}{Ab_n} = -(n\pi)^2 d\tau$$

$$Ab_n = C_1 \cdot \exp\left(-(n\pi)^2 \tau\right)$$

$$Ab_n = \frac{-\sqrt{2}(-1)^n}{n\pi}\exp\left(-(n\pi)^2 \tau\right)$$

The analytical solution is:

$$Ab(\lambda,\tau) = \sum_{n=1}^{\infty} \Phi(r)Ab_n(\tau)$$

$$Ab(\lambda,\tau) = \frac{-2}{\pi\lambda}\sum_{n=1}^{\infty}\frac{(-1)^n}{n}\exp\left(-(n\pi)^2 \tau\right)\sin(n\pi\lambda)$$

Plotting the solution (evaluating n = 26 terms, r = 11 terms, and t = 5 terms for a total of 1,430 terms):
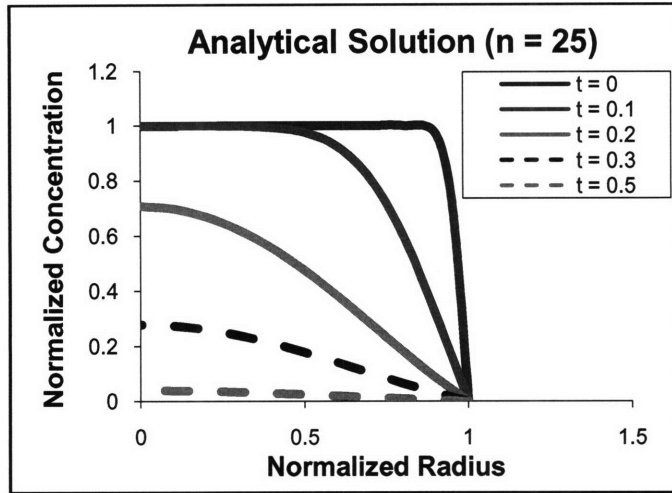
245

Figure A.5 – Antibody Decay from a Sphere

Converting solution back to units:

$$\frac{[Ab]}{[Ag]} = \frac{-2R}{\pi r} \sum_{n=1}^{\infty} \frac{(-1)^n}{n} \exp\left(-(n\pi)^2 \frac{K_d \cdot D}{\left(K_d + \left([Ag]\middle/\varepsilon\right)\right)R^2} t\right) \sin\left(\frac{n\pi r}{R}\right)$$

If the initial concentration of antibody is equal to the antigen concentration:

$$M_0 = [Ag]\frac{4}{3}\pi R^3$$

The integration for total antibody in the sphere is similar to the integration for uptake yielding:

$$M_t = \int_0^R (-8r)\left(R[Ag]\sum_{n=1}^{\infty}\left(\frac{(-1)^n}{n}\right)\exp\left(-(n\pi)^2 \frac{K_d \cdot D}{\left(K_d + \left([Ag]\middle/\varepsilon\right)\right)R^2} t\right)\left(\sin\frac{n\pi r}{R}\right)\right)dr$$

$$\frac{M_t}{M_0} = \frac{6}{\pi^2} \sum_{n=1}^{\infty}\left(\frac{1}{n^2}\right)\exp\left(-(n\pi)^2 \frac{K_d \cdot D}{\left(K_d + \left([Ag]\middle/\varepsilon\right)\right)R^2} t\right)$$

The time scale present in the exponent is useful for scaling the loss of antibody from a spherical mass of tumor cells.

246

A.12 Convection-Diffusion Model

a. Equations for Convection-Diffusion Model

The transport of antibodies in tumor tissue occurs both by convection and diffusion. Although diffusion is very slow for these molecules, convection is severely inhibited in solid tumors, so diffusion dominates in many regions. In order to model the effect of convection in a whole tumor setting, a previously published model of convection in tumors by Baxter and Jain(13) was implemented.

Briefly, the current implementation of this model treats a spherical tumor, with radius R_{tumor}, surrounded by an adjustable thickness of normal tissue. The boundary condition at the edge of this explicitly modeled normal tissue is a defined concentration given by a two compartmental model similar to that surrounding a micrometastasis. Extravasation of fluid and antibodies is assumed to occur uniformly within the tissue (i.e. individual capillaries are averaged over the tissue), so perivascular gradients are ignored. Steady state pressure profiles (as a function of the tumor radius) are calculated using Darcy's law for flow through the tissue. Both the extravasation rate and velocity profiles within the tumor, which impact the distribution of antibody, are calculated from this pressure profile. The implementation was carried out using the method of lines with finite differences (versus the original model which used a finite element method).

Notation similar to Baxter and Jain was used, and to avoid confusion, the parameters in this section will be defined when they are first used rather than defined in the list of symbols.

<u>Fluid Flow Equations</u>

Darcy's law for axisymmetric flow

$$u_i = -K\nabla p_i = -K\frac{dp_i}{dr}$$
where K is Darcy's law permeability coefficient and p_i is interstitial pressure

To simplify the equations, it is assumed that there are no lymphatics in the tumor.

Continuity equation:

$$\nabla \cdot u_i = \frac{1}{r^2}\frac{\partial}{\partial r}r^2 u_r + \frac{1}{r\sin\theta}\frac{\partial}{\partial \theta}u_\theta \sin\theta + \frac{1}{r\sin\theta}\frac{\partial u_\phi}{\partial \phi} = \phi_V$$

where:

$$\phi_V = \frac{J_V}{V} = \frac{L_p S}{V}\left(p_V - p_i - \sigma_T\left(\pi_V - \pi_i\right)\right)$$

where ϕ_V is the fluid source term (not to be confused with the Thiele modulus), J_v is the volumetric fluid extravasation rate for the vasculature, L_p is the vascular fluid permeability, p_v is the capillary pressure, σ_T is the total vascular reflection coefficient, and π_v and π_i are the plasma and interstitial osmotic pressures.

Combining the above and assuming axisymmetric flow:

$$-\nabla \cdot K \nabla p_i = \phi_V$$

For constant K, L_p, S/V, π_v, π_i and σ:

$$\nabla^2 p_i = \frac{\alpha^2}{R_{tumor}^2}\left(p_i - p_e\right) \qquad \text{(R}_{tumor}^2 \text{ needed to balance units in derivative)}$$

where:

$$\alpha^2 \equiv R_{tumor}^2\left(\frac{L_p S}{KV}\right)$$

$p_e = p_V - \sigma_T\left(\pi_V - \pi_i\right)$ = effective pressure (interstitial P where vascular efflux = 0)

The boundary conditions are:

$$\nabla p_i\big|_{r=0} = 0 \qquad \text{No flux BC at center of the tumor}$$

$$p_i\big|_{r=large} = p_\infty \qquad \text{At a large distance, the pressure gradients have decayed}$$

$$-K_T \frac{dp_i}{dr}\bigg|_{r=R^-} = -K_N \frac{dp_i}{dr}\bigg|_{r=R^+} \qquad \text{BC where tumor meets normal tissue}$$

$$p_i\big|_{r=R^-} = p_i\big|_{r=R^+}$$

The steady-state interstitial pressure solution is(13):

$$\hat{p} \equiv \frac{p_i - p_e}{p_\infty - p_e} = 1 - \frac{1}{\hat{r}} \frac{(1 + \alpha_N)\sinh\{\alpha_T \hat{r}\}}{(1 + \alpha_N)\sinh\{\alpha_T\} + \hat{K}(\alpha_T \cosh\{\alpha_T\} - \sinh\{\alpha_T\})} \qquad r < R$$

$$\hat{p} \equiv \frac{1}{\hat{r}} \frac{\hat{K}(\alpha_T \cosh\{\alpha_T\} - \sinh\{\alpha_T\})(\sinh\{\alpha_N \hat{r}\} - \cosh\{\alpha_N \hat{r}\})}{((1 + \alpha_N)\sinh\{\alpha_T\} + \hat{K}(\alpha_T \cosh\{\alpha_T\} - \sinh\{\alpha_T\}))(\sinh\{\alpha_N\} - \cosh\{\alpha_N\})} \qquad r > R$$

The fluid flow velocity can be determined from Darcy's law.

Antibody Transport Equations

Assuming constant D and axisymmetric transport:

Free antibody:

$$\frac{\partial[Ab]}{\partial t} + u_i \frac{\partial[Ab]}{\partial r} = D \frac{1}{r^2} \frac{\partial}{\partial r}\left(r^2 \frac{\partial[Ab]}{\partial r}\right) + \phi_{extravasate} - \phi_{bind} + \phi_{dissociate}$$

Bound antibody:

$$\frac{\partial[B]}{\partial t} = \phi_{bind} - \phi_{dissociate} - \phi_{internalization}$$

Free antigen:

$$\frac{\partial[Ag]}{\partial t} = -\phi_{bind} + \phi_{dissociate} - \phi_{internalization} + \phi_{synthesis}$$

where $\phi_{extravasate}$, ϕ_{bind}, $\phi_{dissociate}$, $\phi_{internalization}$, and $\phi_{synthesis}$ are the volume averaged extravasation, binding, dissociation, internalization, and antigen synthesis rates. Note that these terms are different than the Thiele modulus.

$$\phi_{extravasate} = \frac{J_V(1 - \sigma)}{V}[Ab]_{plasma} + \frac{PS}{V}\left([Ab]_{plasma} - [Ab]\right)\left(\frac{Pe_V}{e^{Pe_V} - 1}\right)$$

$$\phi_{extravasate} = \frac{J_V(1-\sigma)}{V}\frac{[Ab]_{plasma}e^{Pe_V}-[Ab]}{e^{Pe_V}-1}$$

where:

$$Pe_V = \frac{J_V(1-\sigma)}{PS} = \text{Peclet number}$$

The Peclet number is the ratio of convection to diffusion across the capillary wall. Note that in this use, P is strictly the diffusive permeability. When used elsewhere, it often refers to the effective permeability, where P is simply a mass transfer coefficient at the capillary wall. σ is the reflection coefficient for the molecule of interest.

The reaction terms are:

$$\phi_{bind} = \frac{k_{on}}{\varepsilon}[Ab][Ag]$$

$$\phi_{dissociate} = k_{off}[B]$$

$$\phi_{internalization} = k_e[B] \quad \text{for complex and} \quad \phi_{internalization} = k_e[Ag] \quad \text{for antigen}$$

$$\phi_{synthesis} = k_e[Ag]_0$$

The boundary conditions for free antibody are:

1) $\quad -D\frac{\partial[Ab]}{\partial r}\bigg|_{r=0} + u_i[Ab]\big|_{r=0} = 0 \qquad$ no flux at tumor center

2) $\quad [Ab]\big|_{r=R_{tumor}^-} = [Ab]\big|_{r=R_{tumor}^+} \qquad$ antibody continuity at tumor edge

3) $\quad -D_T\frac{\partial[Ab]}{\partial r}\bigg|_{r=R_{tumor}^-} + u_i[Ab]\big|_{r=R_{tumor}^-} = -D_N\frac{\partial[Ab]}{\partial r}\bigg|_{r=R_{tumor}^+} + u_i[Ab]\big|_{r=R_{tumor}^+} \qquad$ flux continuity

4) $\quad [Ab] = [Ab]_{normal\_tissue} \qquad$ At an unspecified distal point where [Ab]normal tissue is equal to the normal tissue compartment. The normal tissue compartment is that used for metastases. The

thickness of the explicitly modeled normal tissue surrounding the tumor can be changed in numerical simulations so that the gradients in this tissue have decayed.

The initial conditions for all 3 equations are:

$$[Ab] = 0 \qquad [B] = 0 \qquad [Ag] = [Ag]_0$$

b. Note on Interstitial Fluid Velocity

The fluid velocities calculated in Baxter and Jain[13] and measured by Butler et al.[14] are averaged over the entire tumor volume. Since this volume of fluid is only traveling between the interstitial spaces, the actual fluid velocity will be faster by a factor of the fluid void volume. It is assumed that the void volume for this fluid is equivalent to that measured for small molecules, which is ~0.5 when measured in tumors. Filtration effects from the extracellular matrix are ignored.

As an example, in a given small volume of tumor tissue, the overall antibody concentration is 1 nM. If the tissue void fraction, ε, is 0.1, then the interstitial concentration is 10 nM (6 Ab/μm^3). Given an overall velocity of 0.17 μm/s at the tumor surface and accessible fluid volume of 0.5, the interstitial velocity must be 0.34 μm/s since it is assumed no fluid travels through the cell. The interstitial flux is the 10 nM concentration multiplied by the 0.34 μm/s velocity, giving 2.04 Ab/μm^2/s. Multiplying this by the 0.1 void fraction results in an overall flux 0.20 Ab/μm^2/s. If the overall fluid flow rate were simply multiplied by the overall antibody concentration, the flux would appear to be 0.1 Ab/μm^2/s, which is only ½ of the actual rate. Therefore, the fluid accessible volume must be taken into account when looking at convection in the tissue.

c. Note on Numerical Integration with Upwind Differencing

The finite difference method uses the central difference approximation so the error scales with the square of the length between points. This can result in numerical instabilities when convection is introduced into the equations. Only the upwind difference is used for the convection term, so the error scales linearly with the difference, but the code is more stable.

A.13 Compartmental Model

a. Justification of Material Balance Terms

A tumor has two major interfaces with the surrounding tissue, the vascular surface area within the tumor and the tumor surface area on the outside exposed to surrounding tissue. Antibody entering

or leaving the tumor must cross one of these two surfaces. In order to understand the magnitude and timing of this transport, a simplified compartmental mathematical model is used to determine the overall tumor uptake as a function of time.

The overall (volume averaged) concentration of antibody in the tumor is a function of extravasation from the plasma and intravasation across the vascular surface area, uptake and loss from the surface of the tumor, and internalization throughout the tissue. Internalization does not occur across either of the previously mentioned surfaces. However, the antibody will be degraded and no longer in the initial form. Degradation products, such as a radioisotope attached to the antibody, may pass across these surfaces or be retained within the cell, and this will have to be considered when determining tracer signal versus actual cell bound antibody.

The above terms can also be considered in relation to the spatial tumor model surrounding a capillary vessel. Trans-capillary transport occurs across the capillary wall, described by the permeability at the vessel surface, and internalization occurs within the tissue due to antigen turn-over. Loss from the surface of the tumor does not have a direct analogy in the Krogh cylinder, but it relates to antibody crossing the outer Krogh cylinder radius. This is typically treated as a no-flux boundary, either because a high affinity antibody binds and never reaches this distance (isolated cylinder) or antibody from the surrounding vessels in the middle of a tumor opposes the concentration gradient, so no antibody crosses this barrier ("mirror" boundary condition). While this is acceptable under these two circumstances, lower affinity antibodies near the surface of a tumor will not have any adjacent capillaries to oppose their diffusion out of the cylinder. Therefore, surface uptake and loss must be accounted for separately in this compartmental model.

i. Vascular Terms

One of the major terms for antibody uptake is from the tumor vasculature. The low permeability of the capillaries (low Biot number) reduces the dependence of transport on the microscopic distribution surrounding each vessel. For instance, capillaries close to one another will not reduce extravasation very much since the gradient between the plasma and interstitium is still large. A slight increase in the local concentration in the interstitium has a negligible effect on the difference in concentration. Similarly, loss from the blood vessels is also not very dependent on the local distribution. Since the binding modulus indicates binding is much faster than diffusion, and the Biot number shows diffusion is faster than extravasation, binding occurs much more rapidly than extravasation in the tumor.

252

This means an assumption of equilibrium in the tissue is justified, although this does not mean the antibody will be spatially uniform. For example, a high affinity antibody that distributes close to the blood vessel at early times will diffuse both toward and away from the vessel. The low permeability will 'reflect' most of the perivascular antibody, allowing it to diffuse deeper into the tissue and bind new antigen.

Assuming equilibrium within the tissue:

$$K_d = \frac{\left([Ab]\middle/\varepsilon\right)\left([Ag]\middle/\varepsilon\right)}{[B]\middle/\varepsilon}$$

Assuming a sub-saturating dose, such that [Ab] << [Ag]:

$$K_d = \frac{([Ab]_{total} - [B])[Ag]}{\varepsilon[B]} \qquad \text{so:}$$

$$[B] = \frac{\left([Ag]\middle/\varepsilon\right)}{\left([Ag]\middle/\varepsilon\right) + K_d}[Ab]_{total} \qquad \text{and} \qquad [Ab] = \frac{K_d}{\left([Ag]\middle/\varepsilon\right) + K_d}[Ab]_{total}$$

Assuming a small Biot number, the vascular uptake and loss terms are:

$$\frac{d[Ab]_{total}}{dt} = \frac{2PR_{cap}}{R_{Krogh}^2}\left(\varepsilon[Ab]_{plasma} - \left(\frac{K_d}{\left([Ag]\middle/\varepsilon\right) + K_d}\right)[Ab]_{total}\right)$$

ii. Surface Terms

To scale the surface uptake and loss, a spherical geometry is assumed for the solid tumor. It is really the distance from the surface that affects this term, so surface effects would be greater for an elongated or flat tumor where more of the cells are located near a surface. The radius, r, is the distance from the center and R_{tumor} is the average radius of the mass. The magnitude of antibody transport across the surface will be determined in a manner similar to the scaling used to simplify the micrometastasis model. The equation for radial gradients in a sphere with no reaction terms:

253

$$\frac{\partial[Ab]}{\partial t} + u_r \frac{\partial[Ab]}{\partial r} = D_{scaled} \frac{1}{r^2} \frac{\partial}{\partial r} r^2 \frac{\partial[Ab]}{\partial r}$$

Assuming convection is negligible throughout the majority of the tumor (e.g. low Peclet number):

$$\frac{\partial[Ab]}{\partial t} = D_{scaled} \frac{1}{r^2} \frac{\partial}{\partial r} r^2 \frac{\partial[Ab]}{\partial r}$$

The dimensionless equation is:

$$\frac{\partial Ab}{\partial \tau} = \frac{1}{\lambda^2} \frac{\partial}{\partial \lambda} \lambda^2 \frac{\partial Ab}{\partial \lambda}$$
where $Ab \equiv \dfrac{[Ab]}{\varepsilon[Ab]_{plasma,0}}$, $\lambda \equiv \dfrac{r}{R_{tumor}}$, and $\tau \equiv \dfrac{tD_{scaled}}{R_{tumor}^2}$

Uptake from the tumor surface (low affinity)

An exact solution for low affinity uptake given a constant surface concentration was presented above using a series solution.

$$\frac{M_t}{M_\infty} = 1 - \frac{6}{\pi^2} \sum_{n=1}^{\infty} \left(\frac{1}{n^2}\right) \exp\left(-\frac{D_{scaled} n^2 \pi^2 t}{R_{tumor}^2}\right)$$

Taking the derivative with respect to time to get an estimate of the uptake rate at early times (prior to saturation):

$$\frac{d}{dt}\left(\frac{M_t}{M_\infty}\right) = \frac{d}{dt}\left(1 - \frac{6}{\pi^2} \sum_{n=1}^{\infty} \left(\frac{1}{n^2}\right) \exp\left(-\frac{D_{scaled} n^2 \pi^2 t}{R_{tumor}^2}\right)\right)$$

$$\frac{d[Ab]_{total}}{dt} = [Ab]_\infty \frac{6 D_{scaled}}{R_{tumor}^2} \left(\sum_{n=1}^{\infty} \exp\left(-\frac{D_{scaled} n^2 \pi^2 t}{R_{tumor}^2}\right)\right)$$

Since the fraction of free antibody will be in equilibrium with the surface concentration at long times:

$$[Ab]_\infty = \varepsilon[Ab]_{surf}\left(\frac{K_d + \left([Ag]/\varepsilon\right)}{K_d}\right)$$ at subsaturating concentrations and:

254

$$D_{scaled} = D\left(\dfrac{K_d}{K_d + \left([Ag]\Big/\varepsilon\right)}\right)$$

$$\dfrac{d[Ab]_{total}}{dt} = \dfrac{6D\varepsilon[Ab]_{surf}}{R_{tumor}^2}\left(\sum_{n=1}^{\infty}\exp\left(-\dfrac{D_{scaled}n^2\pi^2 t}{R_{tumor}^2}\right)\right)$$

Although the derivative is not a constant, starting very large as antibody is taken up near the surface and slowing with time, the coefficient in front of the summation is not a function of affinity. This term outside the summation will be used as the surface uptake rate constant.

Uptake from the tumor surface (high affinity)

A high affinity antibody is not taken up by diffusion slowed by binding but rather by saturating each cell layer and diffusing beyond the saturated front. This type of transport was modeled in a micrometastasis and can be extended here. The change in antibody concentration is:

$$\dfrac{d[Ab]_{total}}{dt} = \dfrac{D\left(\dfrac{d[Ab]}{dr}\Big|_{r=R_{tumor}}\right)S_{tumor}}{V} = \dfrac{D\left(\dfrac{d[Ab]}{dr}\Big|_{r=R_{tumor}}\right)\left(4\pi R_{tumor}^2\right)}{\tfrac{4}{3}\pi R_{tumor}^3}$$

$$\dfrac{d[Ab]_{total}}{dt} = \dfrac{3D\varepsilon\left(\dfrac{d[Ab]}{dr}\Big|_{r=R_{tumor}}\right)}{R_{tumor}}$$

For a shrinking core in a sphere:

$$\dfrac{d[Ab]}{dr}\Big|_{r=R_{tumor}} = \dfrac{R[Ab]_{surf}}{\left(R_{tumor} - R\right)R_{tumor}}$$

So:

$$\dfrac{d[Ab]_{total}}{dt} = \dfrac{3D\varepsilon[Ab]_{surf}}{R_{tumor}^2}\left(\dfrac{R}{R_{tumor} - R}\right)$$

255

Similar to the low affinity antibody, uptake from the surface is not a simple first order term but depends on the time. Uptake is rapid at early times due to saturation of the cells very near the surface and then slows as antibody must diffuse farther into the tissue. For an order of magnitude analysis, the uptake will be calculated when the reaction front, R, has reached 1/3 of the way to the center:

$$\frac{d[Ab]_{total}}{dt} = \frac{3D\varepsilon[Ab]_{surf}}{R_{tumor}^2}\left(\frac{\frac{2}{3}R_{tumor}}{R_{tumor}-\frac{2}{3}R_{tumor}}\right) = \frac{6D\varepsilon[Ab]_{surf}}{R_{tumor}^2}$$

With this estimate, the shape factor and uptake term agree with the low affinity scaling. Uptake from the tumor for both high and low affinity antibodies is:

$$\frac{d[Ab]_{total}}{dt} = \frac{6D}{R_{tumor}^2}\varepsilon[Ab]_{surf}$$

Loss from the tumor surface

Loss from the tumor surface can be scaled by assuming a zero concentration at the tumor surface. This was solved exactly with a series solution above, with loss depending on the scaled diffusion:

$$D_{scaled} = D\left(\frac{[Ab]_{surf}+K_d}{[Ab]_{surf}+K_d+\left([Ag]/\varepsilon\right)}\right) = D\left(\frac{K_d}{K_d+\left([Ag]/\varepsilon\right)}\right)$$

since $[Ab]_{surf}$ is zero for the loss term and $[Ag] \gg [Ab]$. While local areas may be saturated in the case of a high affinity antibody due to shrinking core type penetration into the tissue, the loss of these antibodies will be dominated by the catabolism term, so any error will have a minimal effect.

Numerical simulations of free diffusion in a spherical tumor mass show surface loss is not a simple 1st order function of antibody concentration. However, all the simulations collapse to a single curve when the time is normalized by:

$$\left(\left(\frac{K_d}{K_d+\left([Ag]/\varepsilon\right)}\right)\frac{D}{R_{tumor}^2}\right)$$

This decay will vary depending on the initial antibody concentration and distribution within the tumor. It is also dependent on the addition of antibody from internal and surface sources and loss due to intravasation. As such, the surface loss, like uptake from the surface, is not a simple linear term. However, a pseudo-1st order decay constant will provide an order of magnitude estimate for the surface loss without requiring detailed spatial information within the tumor.

Using the base case scenario from the above simulations, the pseudo-1st order rate constant is:

$$k_{surface\ loss} = \frac{\{SF\}K_d}{\left(\frac{[Ag]}{\varepsilon}\right) + K_d} \frac{D}{R_{tumor}^2}$$

where SF is the pseudo-1st order shape factor for loss from a sphere. Because a large portion of the antibody is near the surface, a large initial drop occurs while the gradient forms near the surface of the sphere. After this, the curve levels out as antibody must diffuse farther from the interior of the tumor to the surface.

$$\frac{M_t}{M_0} = \frac{6}{\pi^2} \sum_{n=1}^{\infty} \left(\frac{1}{n^2}\right) \exp\left(-(n\pi)^2 \frac{K_d \cdot D}{\left(K_d + \left(\frac{[Ag]}{\varepsilon}\right)\right)R^2} t\right)$$

$$\frac{d}{dt}\left(\frac{M_t}{M_0}\right) = \frac{d}{dt}\left(\frac{6}{\pi^2} \sum_{n=1}^{\infty} \left(\frac{1}{n^2}\right) \exp\left(-(n\pi)^2 \frac{K_d \cdot D}{\left(K_d + \left(\frac{[Ag]}{\varepsilon}\right)\right)R^2} t\right)\right)$$

$$\frac{d[Ab]_{total}}{dt} = \frac{-6DK_d}{R_{tumor}^2\left(K_d + \left(\frac{[Ag]}{\varepsilon}\right)\right)}[Ab]_0 \left(\sum_{n=1}^{\infty} \exp\left(-(n\pi)^2 \frac{K_d \cdot D}{\left(K_d + \left(\frac{[Ag]}{\varepsilon}\right)\right)R^2} t\right)\right)$$

The summation is dependent on time, but the coefficient in front is used for the scaled antibody loss from the surface, resulting in a shape factor (SF) of 6. This loss rate is multiplied by the initial antibody concentration, so it is dependent on the amount of antibody in the sphere.

iii. Catabolism Term

Catabolism occurs in the tumor for antibody bound to the surface of cancer cells. Assuming binding equilibrium has occurred, the loss of antibody from catabolism is the antigen turn-over rate on the cells multiplied by the fraction of total antibody in the tumor that is bound.

$$\frac{d[Ab]_{total}}{dt} = -k_e \left(\frac{\left([Ag]/\varepsilon \right)}{\left([Ag]/\varepsilon \right) + K_d} \right) [Ab]_{total}$$

A quick comparison can be made between catabolism in the tissue and uptake from the surface. The shape factor of 6 is in agreement with the surface uptake for micrometastases.

$$\frac{d[Ab]_{total}}{dt} = \frac{6D}{R_{tumor}^2} \varepsilon [Ab]_{surf} - k_e \left(\frac{\left([Ag]/\varepsilon \right)}{\left([Ag]/\varepsilon \right) + K_d} \right) [Ab]_{total}$$

Assuming steady state is reached for a high affinity antibody:

$$\frac{k_e \left([Ab]_{total}/\varepsilon \right) R_{tumor}^2}{6D[Ab]_{surf}} = 1$$

The left hand side of this equation is identical to the Thiele modulus for micrometastases except that [Ag] in the Thiele modulus is replaced with [Ab] in the tumor. This matches the saturation condition since [Ab] = [Ag] when the Thiele modulus equals 1 at saturation. Therefore, the shape factor of 6 for surface effects matches the saturation condition for micrometastases.

One final consideration before laying out the lumped parameter model is the uptake from the surface. First, for small tumors, the outward convection may be strong enough to oppose any inward diffusion from the surrounding tissue. Second, it is really the normal tissue concentration surrounding the tumor that is the relevant concentration for uptake. However, for IgGs, the rapid equilibration of the plasma to normal tissue levels results in parallel normal tissue and plasma curves. On top of this, the uptake from the surface is an order of magnitude estimate. Therefore, surface uptake is assumed to occur directly from the plasma. This assumption results in a large simplification of the analytical solution, since uptake is then from a single (plasma) compartment.

b. Final Forms

i. Differential Form

Combining the free and bound antibody concentrations and the surface loss terms into the original 1st order lumped parameter model, the defining equation is:

$$\frac{d[Ab]_{total}}{dt} = \frac{2PR_{cap}}{R_{Krogh}^2}\left(\varepsilon[Ab]_{plasma} - \left(\frac{K_d}{\left(\frac{[Ag]}{\varepsilon}\right) + K_d}\right)[Ab]_{total}\right) + \frac{6D}{R_{tumor}^2}\left(\varepsilon[Ab]_{plasma} - \left(\frac{K_d}{\left(\frac{[Ag]}{\varepsilon}\right) + K_d}\right)[Ab]_{total}\right)$$
$$- k_e\left(\frac{\left(\frac{[Ag]}{\varepsilon}\right)}{\left(\frac{[Ag]}{\varepsilon}\right) + K_d}\right)[Ab]_{total}$$

All antibody is either bound and internalizing or free to intravasate or diffuse out of the tumor surface. Antibody enters the tumor according to the plasma concentration profile. All loss terms are 1st order, making an analytical solution possible.

ii. Integral Form - Closed-form Analytical Solution to the Compartmental Model

Grouped by Gain/Loss

$$\frac{d[Ab]_{total}}{dt} = \left(\frac{2PR_{cap}}{R_{Krogh}^2} + \frac{6D}{R_{tumor}^2}\right)\varepsilon[Ab]_{plasma}$$

$$-\left(\frac{2PR_{cap}}{R_{Krogh}^2}\left(\frac{K_d}{\left(\frac{[Ag]}{\varepsilon}\right) + K_d}\right) + \frac{6D}{R_{tumor}^2}\left(\frac{K_d}{\left(\frac{[Ag]}{\varepsilon}\right) + K_d}\right) + k_e\left(\frac{\left(\frac{[Ag]}{\varepsilon}\right)}{\left(\frac{[Ag]}{\varepsilon}\right) + K_d}\right)\right)[Ab]_{total}$$

or:

$$\frac{d[Ab]_{total}}{dt} = \left(\frac{2PR_{cap}}{R_{Krogh}^2} + \frac{6D}{R_{tumor}^2}\right)\varepsilon[Ab]_{plasma} - \Omega[Ab]_{total}$$

where:

$$\Omega = \frac{2PR_{cap}}{R_{Krogh}^2}\left(\frac{K_d}{\left(\frac{[Ag]}{\varepsilon}\right) + K_d}\right) + \frac{6D}{R_{tumor}^2}\left(\frac{K_d}{\left(\frac{[Ag]}{\varepsilon}\right) + K_d}\right) + k_e\left(\frac{\left(\frac{[Ag]}{\varepsilon}\right)}{\left(\frac{[Ag]}{\varepsilon}\right) + K_d}\right)$$

Solving:

$$\frac{d[Ab]_{total}}{dt} + \Omega[Ab]_{total} = \left(\frac{2PR_{cap}}{R_{Krogh}^2} + \frac{6D}{R_{tumor}^2}\right)\varepsilon[Ab]_{plasma,0}\left(A\cdot\exp(-k_\alpha t) + B\cdot\exp(-k_\beta t)\right)$$

Using the integrating factor $\mu = \exp(\Omega t)$

$$[Ab]_{total} = \frac{\int\exp(\Omega t)\left\{\left(\frac{2PR_{cap}}{R_{Krogh}^2} + \frac{6D}{R_{tumor}^2}\right)\varepsilon[Ab]_{plasma,0}\left(A\cdot\exp(-k_\alpha t) + B\cdot\exp(-k_\beta t)\right)\right\}dt + C_1}{\exp(\Omega t)}$$

$$[Ab]_{total} = \frac{A\left(\frac{2PR_{cap}}{R_{Krogh}^2} + \frac{6D}{R_{tumor}^2}\right)\varepsilon[Ab]_{plasma,0}\exp((\Omega - k_\alpha)t)}{(\Omega - k_\alpha)\exp(\Omega t)} +$$

$$\frac{B\left(\frac{2PR_{cap}}{R_{Krogh}^2} + \frac{6D}{R_{tumor}^2}\right)\varepsilon[Ab]_{plasma,0}\exp((\Omega - k_\beta)t)}{(\Omega - k_\beta)\exp(\Omega t)} + \frac{C_1}{\exp(\Omega t)}$$

Initial condition: $\quad [Ab]_{total}(0) = 0$

$$C_1 = \frac{-A\left(\frac{2PR_{cap}}{R_{Krogh}^2} + \frac{6D}{R_{tumor}^2}\right)\varepsilon[Ab]_{plasma,0}}{(\Omega - k_\alpha)} + \frac{-B\left(\frac{2PR_{cap}}{R_{Krogh}^2} + \frac{6D}{R_{tumor}^2}\right)\varepsilon[Ab]_{plasma,0}}{(\Omega - k_\beta)}$$

Yielding:

$$\frac{[Ab]}{[Ab]_{plasma,0}} = \varepsilon\left(\frac{2PR_{cap}}{R_{Krogh}^2} + \frac{6D}{R_{tumor}^2}\right)\left\{\frac{A}{(\Omega - k_\alpha)}\left[e^{-k_\alpha t} - e^{-\Omega t}\right] + \frac{B}{(\Omega - k_\beta)}\left[e^{-k_\beta t} - e^{-\Omega t}\right]\right\}$$

where: $\Omega = \frac{2PR_{cap}}{R_{Krogh}^2}\left(\frac{K_d}{\left([Ag]\big/\varepsilon\right) + K_d}\right) + \frac{6D}{R_{tumor}^2}\left(\frac{K_d}{\left([Ag]\big/\varepsilon\right) + K_d}\right) + k_e\left(\frac{\left([Ag]\big/\varepsilon\right)}{\left([Ag]\big/\varepsilon\right) + K_d}\right)$

c. Simplifications Based on Scaling

The uptake and loss terms can be simplified under certain conditions, which are presented here in differential form:

Case 1 – High affinity antibody in large tumor ($K_d \ll [Ag]/\varepsilon$)

$$\frac{d[Ab]_{total}}{dt} = \frac{2PR_{cap}}{R_{Krogh}^2} \varepsilon[Ab]_{plasma} - k_e[Ab]_{total}$$

Case 2 – Negligible affinity in large tumor ($[Ab]$ and $[Ag] \ll K_d$)

$$\frac{d[Ab]}{dt} = \frac{2PR_{cap}}{R_{Krogh}^2} \varepsilon[Ab]_{plasma} - \frac{2PR_{cap}}{R_{Krogh}^2}[Ab]$$

The three terms describing loss of antibody from the tumor, either from the surface, intravasation, or internalization, can also be compared to determine which term dominates in a given scenario.

The ratio of loss from intravasation to loss from the surface is (and uptake from extravasation to uptake from surface):

$$\frac{\text{intravasation}}{\text{surface loss}} = \frac{Bi}{6}\left(\frac{R_{tumor}^2}{R_{Krogh}^2}\right)$$

For small tumors, which are often well vascularized, the surface loss terms start becoming negligible around 4-5 mm diameter tumor. This corresponds to ~50 mm^3 tumor volume or 50 mg. A typical xenograft is 100-200 mg (small), 400-500 mg (medium) or > 1000 mg (large). This means diffusion from the surface, although it may affect the overall distribution, does not have a major impact on total uptake in a larger tumor. Note that this ratio is not dependent on affinity since both mechanisms require unbound antibody. The Biot number appears in the ratio, but in the lumped parameter model, it is used to compare the rate of intravasation to diffusion out of the tumor surface rather than extravasation to diffusion away from the vessel wall as in the microscopic model. It is assumed that the permeability due to diffusion is equal in both directions.

The ratio of loss from intravasation to internalization is:

$$\frac{\text{internalization}}{\text{intravasation}} = \frac{k_e R_{Krogh}^2 \left([Ag]\big/\varepsilon\right)}{2PR_{cap}K_d}$$

The ratio of loss from internalization to surface loss is:

$$\frac{\text{internalization}}{\text{surface loss}} = \frac{k_e R_{tumor}^2 \left([Ag]\big/\varepsilon\right)}{6DK_d}$$

If one of the terms dominates, the analytical solution can be simplified accordingly.

Time can also be scaled to understand the broader behavior of clearance versus localization. Because the plasma clearance is biexponential, explicit terms for the maximum concentration and the time of maximum concentration are not able to be obtained. However, if a single exponential decay is assumed, the equation simplifies considerably and explicit maximum can be found. This can be useful in understanding what affects the time of maximum uptake.

Assuming single exponential decay from the plasma (e.g. B = 0):

$$\frac{[Ab]_{total}}{[Ab]_{plasma,0}} = \varepsilon \left(\frac{2PR_{cap}}{R_{Krogh}^2} + \frac{6D}{R_{tumor}^2}\right) \frac{\left(e^{-k_\alpha t} - e^{-\Omega t}\right)}{\left(\Omega - k_\alpha\right)}$$

Taking the derivative and setting to zero, the time of maximum uptake is:

$$t_{max} = \frac{\ln\left(\frac{k_\alpha}{\Omega}\right)}{\left(k_\alpha - \Omega\right)}$$

Examining the time for maximum uptake more closely, if clearance form the plasma, loss from the tumor, or both are rapid, the time of maximum uptake occurs early. Only if both are slow does the maximum uptake time occur later. This also does not include normal tissue considerations, so even if the maximum uptake occurs early, the best tumor to normal tissue ratio may occur much later.

Substituting this expression into the concentration:

$$[Ab]_{\max} = \varepsilon[Ab]_{plasma,0} \left(\frac{2PR_{cap}}{R_{Krogh}^2} + \frac{6D}{R_{tumor}^2} \right) \frac{1}{(k_\alpha - \Omega)} \left[\exp\left(-\Omega \frac{\ln\left(\frac{\Omega}{k_\alpha}\right)}{\Omega - k_\alpha} \right) - \exp\left(-k_\alpha \frac{\ln\left(\frac{\Omega}{k_\alpha}\right)}{\Omega - k_\alpha} \right) \right]$$

$$[Ab]_{\max} = \varepsilon[Ab]_{plasma,0} \left(\frac{2PR_{cap}}{R_{Krogh}^2} + \frac{6D}{R_{tumor}^2} \right) \frac{1}{(k_\alpha - \Omega)} \left[\left(\frac{\Omega}{k_\alpha} \right)^{\frac{-\Omega}{\Omega-k_\alpha}} - \left(\frac{\Omega}{k_\alpha} \right)^{\frac{-k_\alpha}{\Omega-k_\alpha}} \right]$$

$$[Ab]_{\max} = \varepsilon[Ab]_{plasma,0} \left(\frac{2PR_{cap}}{R_{Krogh}^2} + \frac{6D}{R_{tumor}^2} \right) \frac{\left(\frac{\Omega}{k_\alpha} \right)^{\frac{-\Omega}{\Omega-k_\alpha}}}{(k_\alpha - \Omega)} \left[1 - \frac{\Omega}{k_\alpha} \right]$$

$$[Ab]_{\max} = \left[\frac{\varepsilon[Ab]_{plasma,0}}{k_\alpha} \left(\frac{2PR_{cap}}{R_{Krogh}^2} + \frac{6D}{R_{tumor}^2} \right) \right] \left[\left(\frac{\Omega}{k_\alpha} \right)^{\frac{\Omega}{k_\alpha-\Omega}} \right]$$

The first term in square brackets indicates the maximum amount of antibody that can enter the tumor prior to it being cleared from the plasma. The second term in square brackets ranges between 0 and 1, and this term adjusts the maximum uptake for loss of the antibody; this approaches the maximum value of 1 as the loss term, Ω, becomes very small relative to clearance from the plasma, k_α. For a high affinity antibody, Ω is simply k_e.
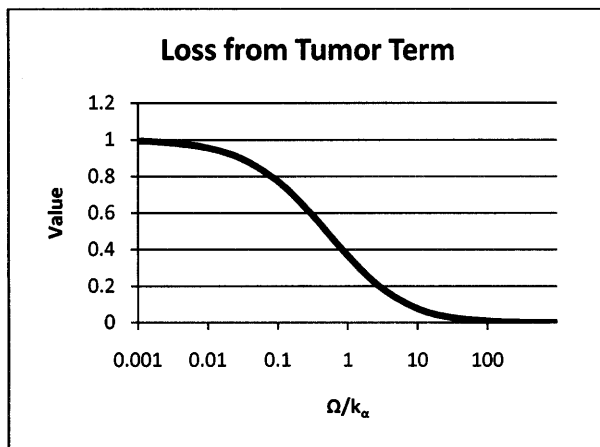

Figure A.6 – Fractional Loss of Antibody from Catabolism

d. Percent Injected Dose per Gram

Whole tumor localization is often expressed as a percentage of the injected dose per gram of tissue. The conversion from antibody concentration in the tumor to %ID/g is:

$$\%ID/g = \frac{\text{mass per gram tumor}}{\text{total mass injected}}100\%$$

$$\%ID/g = \frac{\left(MW_{antibody}\,[Ab]\Big/\rho_{tissue}\right)}{\left(MW_{antibody}[Ab]_{plasma,0}V_{plasma}\right)}100\%$$

$$\%ID/g = \frac{[Ab]\cdot100\%}{[Ab]_{plasma,0}V_{plasma}\rho_{tissue}}$$

e. Consistency Between Compartmental Model and Spatial Distribution

The compartmental model and spatial distribution theory are both derived from the same set of differential equations. The compartmental model ignores the spatial distribution to yield an expression for total uptake. The spatial distribution ignores the temporal distribution examining the steady state or integrating over time. Using the compartmental model, the consistency between the two analyses can be shown.

$$\frac{d[Ab]_{total}}{dt} = \frac{2PR_{cap}}{R_{Krogh}^2}\left(\varepsilon[Ab]_{plasma} - \left(\frac{K_d}{\left(\left[Ag\right]\big/\varepsilon\right)+K_d}\right)[Ab]_{total}\right) + \frac{6D}{R_{tumor}^2}\left(\varepsilon[Ab]_{plasma} - \left(\frac{K_d}{\left(\left[Ag\right]\big/\varepsilon\right)+K_d}\right)[Ab]_{total}\right)$$
$$- k_e\left(\frac{\left(\left[Ag\right]\big/\varepsilon\right)}{\left(\left[Ag\right]\big/\varepsilon\right)+K_d}\right)[Ab]_{total}$$

For the Thiele modulus:

1) Assume steady state, $\dfrac{\partial[Ab]_{total}}{\partial t} = 0$

2) Assume high affinity, $K_d \ll \left(\left[Ag\right]\big/\varepsilon\right)$

$$\frac{[Ab]_{total}}{[Ag]} = \frac{2PR_{cap}[Ab]_{plasma}}{k_e R_{Krogh}^2\left(\left[Ag\right]\big/\varepsilon\right)} + \frac{6D[Ab]_{plasma}}{k_e R_{tumor}^2\left(\left[Ag\right]\big/\varepsilon\right)}$$

$$\frac{[Ab]_{total}}{[Ag]} = \frac{1}{\phi_{tumor}^2} + \frac{6}{\phi_{met}^2}$$

For the clearance modulus:

1) Assume no catabolism, $k_e = 0$

2) Assume high affinity, $K_d << \left([Ag]/\varepsilon\right)$

$$\frac{\partial[Ab]}{\partial t} = \frac{2PR_{cap}}{R_{Krogh}^2}\left(\varepsilon[Ab]_{plasma}\right) + \frac{6D}{R_{tumor}^2}\left(\varepsilon[Ab]_{plasma}\right)$$

Integrate from t = 0 to infinity and from Ab = 0 initially to Ab = [Ab]$_{total}$:

$$\int_0^{[Ab]_{total}} d[Ab] = \int_0^\infty \left\{\frac{2PR_{cap}}{R_{Krogh}^2}\left(\varepsilon[Ab]_{plasma}\right) + \frac{6D}{R_{tumor}^2}\left(\varepsilon[Ab]_{plasma}\right)\right\} dt$$

$$[Ab]_{total} = \left\{\frac{2PR_{cap}\varepsilon}{R_{Krogh}^2} + \frac{6D\varepsilon}{R_{tumor}^2}\right\}\int_0^\infty [Ab]_{plasma} dt$$

For biexponential decay:

$$[Ab]_{total} = \left\{\frac{2PR_{cap}\varepsilon}{R_{Krogh}^2} + \frac{6D\varepsilon}{R_{tumor}^2}\right\}[Ab]_{plasma,0}\left(\frac{A}{k_\alpha} + \frac{B}{k_\beta}\right)$$

$$\frac{[Ab]_{total}}{[Ag]} = \frac{2PR_{cap}[Ab]_{plasma,0}\left(\dfrac{A}{k_\alpha} + \dfrac{B}{k_\beta}\right)}{R_{Krogh}^2\left(\dfrac{[Ag]}{\varepsilon}\right)} + \frac{6D[Ab]_{plasma,0}\left(\dfrac{A}{k_\alpha} + \dfrac{B}{k_\beta}\right)}{R_{tumor}^2\left(\dfrac{[Ag]}{\varepsilon}\right)}$$

$$\frac{[Ab]_{total}}{[Ag]} = \frac{1}{\Gamma_{tumor}} + \frac{6}{\Gamma_{met}}$$

f. Importance of Surface Terms

Surface effects come into play both directly and indirectly, depending on the conditions surrounding the tumor. First, uptake and loss can occur directly from the surface by diffusion into and out of the tumor. The indirect effect occurs through fluid flow and convection. Since tumors do not have functional lymphatics, the fluid that crosses the blood vessels seeps out of the surface of the tumor. This causes lower pressure near the tumor periphery, more fluid can extravasate in this region, and this increased convection carries with it more antibody near the surface.

The two effects are mutually exclusive, however. With low pressure near the tumor surface, such as a tissue isolated in a body cavity, the large pressure gradient near the surface causes significant extravasation of fluid. The outward flow of antibody causes an indirect increase in uptake near the surface. However, this increased convection causes an outward flow of fluid in the tumor periphery. Although the actual fluid velocities are low (on the order of 1 or 2 cell lengths per minute), these are significant compared with the slow diffusion rates of macromolecules. Therefore, the outward diffusion from the surface reduces the inward diffusion of antibody from the surrounding tissue. If, however, the tumor is imbedded in the surrounding tissue, the pressure gradients decay slowly outside of the tumor. The velocity within the tumor is very low, but the interstitial pressure is elevated to the periphery. In this scenario, there is no outward flow to block the inward diffusion from the surrounding tissue. The elevated interstitial pressure blocks convection throughout the entire tumor, so there is no increase in convective uptake near the surface.

These scenarios are extremely difficult to compare *in vivo*. However, numerical simulations allow aphysical constraints to be placed on the transport. A series of simulations was run with the convection-diffusion model with a 200 nM bolus dose of a 1 nM IgG for various tumor sizes, and the maximum percent injected dose per gram was recorded. To determine the extent of uptake from diffusion inward from the surface versus extravasated from the peripheral tumor vessels, two artificial simulations were run. First, a tumor with an impermeable surface was simulated by using a no-flux boundary condition at the tumor-stromal interface. This blocks all diffusion inward from the surface but allows increased uptake due to extravasation. The second scenario was simulated by invoking a constant permeability in the whole tumor. Normally, this effective permeability has contributions from convection and diffusion, but this simulation set the value to diffusive extravasation only. For a tumor surrounded by normal tissue, where the pressure is elevated almost entirely throughout the tumor, the results were as follows:

Scenario	%ID/g
1 cm diameter tumor	15.1
2 mm diameter tumor	34.0
2 mm diameter tumor impermeable surface	16.7
2 mm diameter tumor constant permeability	30.1

Table A.2 – Direct Surface Uptake vs. Increased Peripheral Extravasation in a Subcutaneous Tumor

266

This set of simulations shows that as the tumor size decreases, the uptake increases primarily by diffusion inward from the surface. Making the surface impermeable cuts the uptake almost in half and decreases it close to the level of the larger tumor. Invoking constant permeability, however, only slightly decreases the %ID/g, indicating that convection plays a smaller role in uptake here.

Running the identical simulation but increasing the hydraulic permeability of the surrounding normal tissue by 1000-fold causes the interstitial pressure to drop to virtually zero at the tumor surface. This represents a tissue-isolated tumor, where the fluid at the tumor surface is under zero pressure, such as in the lumen of the colon or a body cavity. The results for this tumor are:

Scenario	%ID/g
1 cm diameter tumor	16.6
2 mm diameter tumor	49.7
2 mm diameter tumor impermeable surface	43.7
2 mm diameter tumor constant permeability	19.4

Table A.3 – Direct Surface Uptake vs. Increased Peripheral Extravasation in an Intraperitoneal Tumor

These results show that convection dominates for this type of small tumor. The %ID/g increases 3-fold with the smaller size due to convection in the tumor surface. If the tumor surface is impermeable, uptake is still well above the large tumor. However, if the extravasation from the blood vessels is set to a constant value, ignoring the increased convective extravasation near the surface, the %ID/g drops to nearly the level of the large tumor. In this situation, convection dominates the surface effects, caused by fluid flow near the surface which indirectly increases uptake.

A.14 Effective Endocytosis Rate with Recycling

Using a simple compartmental model for internalization from the cell surface:

$$[S] \underset{k_r}{\overset{k_i}{\rightleftarrows}} [I] \xrightarrow{k_{deg}} [D]$$
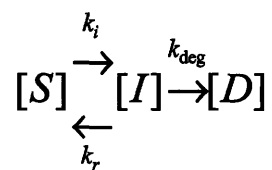
$$\frac{d[I]}{dt} = k_i[S] - k_r[I] - k_{\text{deg}}[I]$$

$$\frac{d[D]}{dt} = k_{\text{deg}}[I]$$

Using a pseudo-steady state approximation where $\dfrac{d[I]}{dt} = 0$

$$\frac{d[D]}{dt} = \frac{k_i k_{\text{deg}}}{k_r + k_{\text{deg}}}[S]$$

This gives an 'effective' endocytosis rate:

$$k_e = \frac{k_i k_{\text{deg}}}{k_r + k_{\text{deg}}} = \frac{k_i}{\left(\dfrac{k_r}{k_{\text{deg}}}\right) + 1}$$

For Herceptin, 85% recycled and 15% degraded for each pass (15), so:

$$k_e = \frac{k_i}{\left(0.85 \middle/ 0.15\right) + 1} = \frac{k_i}{6.7}$$

$$k_e = (0.15)k_i = 0.15 \cdot 2.2 x 10^{-4} / s = 3.3 x 10^{-5} / s$$

This type of analysis does not account for any large internal antigen compartments. In that case, the internalization rate would occur quickly at first until the pseudo-steady state developed.

A.15   Compartmental Model – Internalization versus Degradation

When measuring the total signal in a tumor for the compartmental time-scale model, some signal will be lost from internalization and degradation of the antibody. However, the signal may be retained or quickly lost from the cell(16). With a simple cellular compartmental model, it can be shown that the slower of the two rates (endocytosis vs. loss) is the relevant rate for the tumor compartment model.
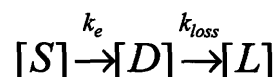
$$[S] \xrightarrow{k_e} [D] \xrightarrow{k_{loss}} [L]$$ where internalization and recycling are represented by k_e

$$\frac{d[L]}{dt} = k_{loss}[D]$$ where [L] represents the lost signal from the cell. It is easier to discuss loss of signal in terms of [L] rather than [S] or [D] since both [S] and [D] contribute to the overall signal.

For reaction in series, the middle product concentration is given by (e.g. (2)):

$$[D] = k_e[S]_0 \left(\frac{\exp(-k_e t) - \exp(-k_{loss}t)}{k_{loss} - k_e} \right)$$

$$\frac{d[L]}{dt} = \frac{k_{loss}k_e}{k_{loss} - k_e}[S]_0 \left(\exp(-k_e t) - \exp(-k_{loss}t) \right)$$

If $k_{loss} \gg k_e$

$$\frac{d[L]}{dt} = k_e[S]_0 \exp(-k_e t)$$

$$[L] = [S]_0 \left(1 - e^{-k_e t}\right)$$

Since

$$[S] + [D] + [L] = [S]_0$$

$$([S] + [D]) = [S]_0 e^{-k_e t}$$

If $k_e \gg k_{loss}$

$$\frac{d[L]}{dt} = k_{loss}[S]_0 \exp(-k_{loss}t)$$

And

$$[L] = [S]_0 \left(1 - e^{-k_{loss}t}\right)$$

$$([S] + [D]) = [S]_0 e^{-k_{loss}t}$$

Appendix References

1.   Alexandrakis G, Brown E, Tong R, et al. Two-photon fluorescence correlation microscopy reveals the two-phase nature of transport in tumors. Nature Medicine 2004;10:203-7.

2.   Fogler HS. Elements of Chemical Reaction Engineering. 3rd ed: Prentice-Hall; 1999.

3.   Thurber GM, Wittrup KD. Quantitative spatiotemporal analysis of antibody fragment diffusion and endocytic consumption in tumor spheroids. Cancer Research 2008;68:3334-41.

4.   Gerlowski L, Jain RK. Microvascular Permeability of Normal and Neoplastic Tissues. Microvascular Research 1986;31:288-305.

5.   Graff CP, Wittrup KD. Theoretical analysis of antibody targeting of tumor spheroids: importance of dosage for penetration, and affinity for retention. Cancer Res 2003;63:1288-96.

6.   Thurber GM, Zajic SC, Wittrup KD. Theoretic criteria for antibody penetration into solid tumors and micrometastases. J Nucl Med 2007;48:995-9.

7.   Weekman VW, Gorring RL. Influence of Volume Change on Gas-Phase Reactions in Porous Catalysts. Journal of Catalysis 1965;4:260-70.

8.   Deen W. Analysis of Transport Phenomena: Oxford University Press; 1998.

9.   Hilmas D, Gillette E. MORPHOMETRIC ANALYSES OF THE MICROVASCULATURE OF TUMORS DURING GROWTH AND AFTER X-IRRADIATION. Cancer 1974;33:103-10.

10.   Baish JW, Gazit Y, Berk DA, Nozue M, Baxter LT, Jain RK. Role of tumor vascular architecture in nutrient and drug delivery: an invasion percolation-based network model. Microvasc Res 1996;51:327-46.

11.   Crank J. The Mathematics of Diffusion. 2 ed. Oxford: Clarendon Press; 1975.

12.   Boyce W, DiPrima R. Elementary Differential Equations and Boundary Value Problems. 7th ed. New York: John Wiley and Sons, Inc.; 2001.

13.   Baxter L, Jain RK. Transport of Fluid and Macromolecules in Tumors: 1. Role of Interstitial Pressure and Convection. Microvascular Research 1989;37:77-104.

14.   Butler TP, Grantham FH, Gullino PM. BULK TRANSFER OF FLUID IN INTERSTITIAL COMPARTMENT OF MAMMARY-TUMORS. Cancer Research 1975;35:3084-8.

15.   Austin C, Maziere A, Pisacane P, et al. Endocytosis and Sorting of ErbB2 and the Site of Action of Cancer Therapeutics Trastuzumab and Geldanamycin. Molecular Biology of the Cell 2004;15:5268-82.

16.   Press OW, Shan D, HowellClark J, et al. Comparative metabolism and retention of iodine-125, yttrium-90, and indium-111 radioimmunoconjugates by cancer cells. Cancer Research 1996;56:2123-9.

Greg M. Thurber

gthurber@mit.edu

Office address:
MIT
77 Massachusetts Ave.
Room E19-556
Cambridge, MA 02139

Laboratory address:
MIT
50 Ames St.
Room E19-563
Cambridge, MA 02139
617-258-7261

Education

Massachusetts Institute of Technology, Cambridge, MA
Doctoral Candidate in Chemical Engineering, 2003 - Present
Thesis Title: Distribution and Metabolism of Antibodies and Macromolecules in Tumor Tissue

Pennsylvania State University, University Park, PA
Bachelor of Science: *Summa Cum Laude*, May, 2003
Major: Chemical Engineering
Minor: Biochemistry and Molecular Biology

Honors and Awards

2006   Ludwig Fellowship in Cancer Research
2003   MIT Presidential Fellow
      Chemical Engineering Student Marshall, Pennsylvania State University
      Hertz Fellowship Finalist
      1st place AIChE Regional Conference Paper Competition, Philadelphia, PA
      Howard Hughes Medical Institute Graduate Fellowship Alternate
      National Science Foundation Graduate Fellowship Honorable Mention
2002   Golden Key International Honour Society
2001   National Society of Collegiate Scholars
2000   Phi Eta Sigma National Honor Society

Research Experience

Massachusetts Institute of Technology, Department of Chemical Engineering
Dr. K. Dane Wittrup Laboratory, 2003 - Present

- Determined that the internalization rate of anti-CEA antibodies was sufficient to limit uptake
- Developed and verified a general theory for antibody transport in tumor tissue
- Verified theoretical predictions using two-photon imaging of antibodies in a tumor spheroid system
- Provided protein engineering strategies to improve antibody tumor targeting and total uptake

Pennsylvania State University, Department of Chemical Engineering
Dr. Wayne Curtis Laboratory, 2001 - 2003

- Developed several lines of transgenic plant species to test assistance of viral genes in protein production
- Characterized gene insertion, inheritance, and expression in plant, root, and cell tissue culture
- Optimized a co-transformation procedure to cut production time in half of transgenic root cultures
- Verified transcription of viral genes designed to increase protein production with reverse transcriptase PCR

Adhesives Research, York, PA
Intern in R&D Department, summer 2000, 2001
- Optimized solvent-free process conditions for transitioning adhesives to production in a more energy efficient and environmentally friendly twin-screw extruder
- Produced novel adhesives with various fibers and fillers using extrusion
- Verified utility of unique blends through physical testing of mechanical and surface properties

Teaching Experience

MIT, Dept. of Chemical Engineering, Cambridge, MA
Chemical Kinetics and Reactor Design, Teaching Assistant.
- Responsible for running office hours, answering student questions on current class topics
- Held review sessions, graded, and provided feedback on exams
- In charge of preparing and delivering a lecture on non-ideal reactor design

MIT, Dept. of Chemical Engineering, Cambridge, MA
Advisor for undergraduate research assistant
- Develop appropriate problems for undergraduate research participation
- Teach student basic elements of research project and laboratory techniques

MIT Museum, Cambridge, MA
Volunteer for 2004 MIT FAST program (Family Adventures in Science and Technology)
- Design short presentation and demo on scientific topics of interest to the general public
- Answer questions on science and technology from middle school children and their parents

Publications

Thurber, G.M., S.C. Zajic, and K.D. Wittrup, *Theoretic Criteria for Antibody Penetration into Solid Tumors and Micrometastases.* Journal of Nuclear Medicine, 2007. 48(6): p. 995-999.

Thurber, G.M., M.M. Schmidt, and K.D. Wittrup, *Factors determining antibody distribution in tumors.* Trends in Pharmacological Sciences, 2008. 29(2): p. 57-61.

Thurber, G.M. and K.D. Wittrup, *Quantitative spatiotemporal analysis of antibody diffusion and endocytic consumption in tumor spheroids.* Cancer Research, 2008. 68(9): p. 3334-3341.

Thurber, G.M., M.M. Schmidt, and K.D. Wittrup, *Antibody tumor penetration: transport opposed by systemic and antigen-mediated clearance.* Advanced Drug Delivery Reviews, In Press.

Schmidt, M.M., **G.M. Thurber**, and K.D. Wittrup, *Kinetics of anti-CEA antibody internalization: negligible effects of affinity, bivalency, or stability.* Cancer Immunology and Immunotherapy, Submitted.

Thurber, G.M. and K.D. Wittrup, *A mechanistic compartmental model for antibody uptake in tumors.* Annals of Biomedical Engineering, Submitted.

Presentations

Thurber, G, Wittrup KD, *"Targeting Cancer Cells with Antibodies – Theory and Experiment"* presentation at the Biomedical Engineering Society 2007 Conference, Los Angeles, CA

Thurber, G, *"Internalization and Clearance Limit Antibody Uptake – An Experimental and Theoretical Analysis,"* presentation at 2007 Keystone Conference on Antibodies as Drugs, Lake Louise, Alberta, CAN

Thurber, G, *"Antibody Targeting – Theory and Experiment,"* presentation at 11th Conference on Cancer Therapy with Antibodies and Immunoconjugates, 2006, Parsippany, NJ

Thurber, G, Wittrup KD, *"Tumor Targeting with Anti-CEA Antibodies and scFvs"* poster presented at 2006 Focus on Microscopy Conference, Perth, AUS

Thurber, G, Wittrup KD, *"Antibody Metabolism in Tumor Tissue"* poster presented at 2005 Keystone Conference on Antibody-Based Therapeutics for Cancer, Santa Fe, NM

Thurber, G, *"Genetic Engineering of Plant Tissue for Use in a Plant Bioreactor Protein Production Platform,"* presentation at the 2003 American Institute of Chemical Engineers National Conference, San Francisco, CA

Thurber, G, Curtis, W, *"Addition of Viral REP Gene to Plant Tissue Culture,"* poster entered in 2003 Undergraduate Research Exhibition, State College, PA. 1st place

Thurber, G., *"Cotransformation of Glycine max,"* poster presentation for 2002 Life Sciences Consortium Summer Research Program, State College, PA

Skills

- Fluorescence microscopy – deconvolution, confocal, and multi-photon imaging
- Analytical and numerical simulations (Matlab) of transport
- Flow cytometry analysis of surface labeled yeast and mammalian cells
- Basic recombinant DNA techniques (cloning, PCR, reverse transcription)
- Protein secretion and purification in yeast
- Transfection of mammalian, plant, yeast, and bacteria cells
- *In vivo* analysis – mouse imaging, dissection, and histology